

**THE INFLUENCE OF AGGREGATE PACKING CHARACTERISTICS ON THE
COMPACTION, VOLUMETRICS AND RUTTING RESISTANCE OF ASPHALT MIXES**

JULIUS JOSEPH KOMBA

**A thesis submitted in partial fulfilment of the requirements of the
degree of**

PHILOSOPHIAE DOCTOR (CIVIL ENGINEERING)

in the

**FACULTY OF ENGINEERING, BUILT ENVIRONMENT AND INFORMATION
TECHNOLOGY**

UNIVERSITY OF PRETORIA

June 2021

THESIS SUMMARY

THE INFLUENCE OF AGGREGATE PACKING CHARACTERISTICS ON THE COMPACTION, VOLUMETRICS AND RUTTING RESISTANCE OF ASPHALT MIXES

JULIUS JOSEPH KOMBA

Supervisor: Professor J.W. Maina
Co- Supervisor: Doctor E. Horak
Department: Civil Engineering
University: University of Pretoria
Degree: Philosophiae Doctor (Civil Engineering)

SUMMARY

Hot-Mix Asphalt (HMA) compaction is required to be undertaken during the laboratory design of asphalt mixes and asphalt pavements construction. Adequate HMA compaction is required to enable the asphalt mix to achieve stability, reduce water permeability, provide resistance against rutting and fatigue cracking, as well as to enhance the overall performance of the pavement structure. In HMA pavement layers, the aggregate structure is responsible for load transfer and providing resistance against pavement distresses. A strong aggregate structure relies on the optimal packing of the aggregates. Among other factors, the aggregate packing characteristics, binder volume and stiffness, and the air void distribution define the internal structure of the HMA, which in turn plays a significant role in the mechanical and volumetric properties of HMA. The internal structure of compacted HMA also depends on the compaction process or method.

With the above background, this thesis aimed to relate aggregate packing characteristics with HMA compactability, the resulting HMA volumetric properties, and the ability of the compacted asphalt mix to resist rutting. To ensure the achievement of the aim of the thesis, the study was divided into three specific objectives.

The first objective was geared towards understanding how the aggregate packing characteristics influence the compactability of HMA mixes. Six aggregate gradations were analysed to determine eight packing parameters, including two gradation parameters (shape factor and gravel to sand ratio), three traditional Bailey ratios, three rational Bailey ratios. It was established that the rational Bailey

ratios provided a better description of the packing characteristics of the aggregate gradations. Subsequently, a gyratory compactor was used to compact HMA mixes that were prepared using each of the six gradations. The compaction data was analysed to determine HMA compactability parameters, namely: locking point, compaction energy index, compaction slope, traffic densification index and area under shear stress compaction curve. Subsequently, the compactability parameters were correlated to rational Bailey ratios. It was found that the traffic densification index, locking point, and compaction slope are related more logically to the aggregate packing.

The second objective investigated the air voids distribution in laboratory-compacted HMA samples and cores extracted from actual field road sections. The laboratory experiments were designed to also investigate the influence of sample height and compaction density. It was found that the smaller the sample height and the higher the compaction density, the higher the variation of air voids. The results also showed that the vertical distribution of air voids differs, with the middle part of the HMA samples found to exhibit higher compaction density than the bottom and top.

The third objective investigated the influence of the compaction method and compaction density on the HMA rutting resistance, using two different rutting tests: repeated simple shear test at a constant height and uniaxial repeated shear test. The two tests were used to compare the rutting resistance of samples compacting using gyratory and slab roller compactors. The results showed that the gyratory compacted samples had better rutting resistance than the slab roller-compacted samples, suggesting that the compaction method influenced the internal structure of the resulting samples and, consequently, the HMA rutting resistance. For the influence of density, the study found that HMA samples compacted to higher density had better rutting resistance than those compacted to lower density.

DECLARATION

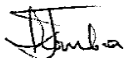
I, the undersigned hereby declare that

- I understand what plagiarism is and I am aware of the University's policy in this regard;
- the work contained in this thesis is my own original work;
- I did not refer to work of current or previous students, lecture notes, handbooks or any other study material without proper referencing;
- where other people's work has been used, this has been properly acknowledged and referenced;
- I have not allowed anyone to copy any part of my thesis, and
- I have not previously – in its entirety or in part – submitted this thesis at any university for degree purposes.

DISCLAIMER:

The work presented in this thesis is that of the student alone. Students were encouraged to take ownership of their projects and to develop and execute their experiments with limited guidance and assistance. The content of the research does not necessarily represent the views of the supervisor or any staff member of the University of Pretoria, Department of Civil Engineering. The supervisor did not read or edit the final report and is not responsible for any technical inaccuracies, statements or errors. The conclusions and recommendations given in the report are also not necessarily that of the supervisor, sponsors or companies involved in the research.

Signature of student



Name of student

Julius Joseph Komba

Student number

26431620

Date

June 2021

ACKNOWLEDGEMENT

I wish to express my appreciation to the following individuals and institutions who in one way or another contributed to the completion of my PhD research.

- a) Prof. James W. Maina, my supervisor, for his guidance, advice, and financial support to participate at conferences during the study.
- b) Dr Emile Horak, my co-supervisor, for his guidance, constructive ideas and encouragement during the study.
- c) The Council for Scientific and Industrial Research (CSIR), for funding this PhD research through Parliamentary Grant (PG).
- d) Dr Martin Mgangira (CSIR), Mr Benoit Verhaeghe (CSIR), Dr Morris De Beer (formerly CSIR), Dr Joseph Anochie-Boateng (CSIR), and Mr Johan O'Connell (CSIR), for many discussions and much encouragement during the study, as well as for creating a conducive work environment that allowed me to complete my PhD research at the CSIR.
- e) Ms Yvette van Rensburg (CSIR), for her assistance with coding the gyratory data analysis software.
- f) Dr Lubinda Walubita (Texas A&M Transportation Institute) and Dr Silipius Mbawala (DIT), for useful discussions and mentorship during the study.
- g) The CSIR's Advanced Material Testing Laboratories (AMTL) staff, particularly Messrs Nnditsheni Mpofo, Ngwako Maake, Kenneth Baloyi, Alan Crawford and Colin Fisher, for their assistance and support during the execution of laboratory tests for this PhD research.
- h) My colleagues at the CSIR, Transport Infrastructure Engineering (TIE) Impact Area, for their support and useful discussion during the study.
- i) AECI Much Asphalt, for supplying materials used for laboratory tests.
- j) My wife Lilian, my family and friends, for their encouragement and support during the study.

TABLE OF CONTENTS

| | | |
|-------|--------------------------------------------------------------|------|
| 1 | INTRODUCTION..... | 1-1 |
| 1.1 | Background..... | 1-1 |
| 1.2 | Problem definition..... | 1-2 |
| 1.3 | Objectives of the study..... | 1-3 |
| 1.4 | Scope of the study..... | 1-3 |
| 1.5 | Methodology..... | 1-4 |
| 1.6 | Contribution to the body of knowledge..... | 1-5 |
| 1.7 | Organisation of the thesis..... | 1-5 |
| 2 | LITERATURE REVIEW..... | 2-1 |
| 2.1 | Introduction..... | 2-1 |
| 2.2 | Overview of HMA and asphalt mix design methods..... | 2-1 |
| 2.2.1 | Marshall asphalt mix design method..... | 2-3 |
| 2.2.2 | Superpave mix design method..... | 2-5 |
| 2.3 | The concept of aggregate packing analysis..... | 2-14 |
| 2.3.1 | Maximum density line concept..... | 2-14 |
| 2.3.2 | Gravel-to-sand ratio..... | 2-16 |
| 2.3.3 | The Bailey method..... | 2-17 |
| 2.3.4 | The dominant aggregate size range..... | 2-20 |
| 2.3.5 | Aggregate packing models..... | 2-23 |
| 2.4 | Compaction of HMA..... | 2-24 |
| 2.4.1 | Laboratory compaction..... | 2-24 |
| 2.4.2 | Field compaction..... | 2-25 |
| 2.4.3 | Measurement of compaction..... | 2-28 |
| 2.5 | Assessing HMA compactability using a gyratory compactor..... | 2-31 |
| 2.5.1 | Locking point concept..... | 2-31 |
| 2.5.2 | The compaction energy index..... | 2-32 |
| 2.5.3 | The compaction and traffic densification indices..... | 2-33 |
| 2.5.4 | Compaction slope..... | 2-34 |
| 2.6 | Factors influencing HMA compaction..... | 2-34 |
| 2.6.1 | Temperature..... | 2-35 |
| 2.6.2 | Binder type..... | 2-36 |
| 2.6.3 | Binder content..... | 2-36 |
| 2.6.4 | Aggregate grading and properties..... | 2-36 |
| 2.7 | Evaluation of rutting resistance of HMA..... | 2-37 |
| 2.7.1 | Wheel-tracking devices..... | 2-38 |
| 2.7.2 | Uniaxial Repeated Load Permanent Deformation Test..... | 2-39 |
| 2.7.3 | Simple Shear Tester (SST)..... | 2-40 |

| | | |
|-------|--------------------------------------------------------------------------------|------|
| 2.7.4 | Uniaxial Shear Tester (UST)..... | 2-42 |
| 2.8 | Summary..... | 2-43 |
| 3 | METHODOLOGY | 3-1 |
| 3.1 | Introduction..... | 3-1 |
| 3.2 | Investigation of the influence of aggregate packing on HMA compactability..... | 3-1 |
| 3.2.1 | Selection of HMA mixes and grading designs | 3-2 |
| 3.2.2 | Aggregate packing analysis..... | 3-6 |
| 3.2.3 | HMA Mixing and compaction..... | 3-6 |
| 3.2.4 | HMA compactability analysis | 3-8 |
| 3.3 | Investigation of the spatial distribution of air voids in compacted HMA..... | 3-13 |
| 3.3.1 | HMA mix design and materials..... | 3-14 |
| 3.3.2 | HMA mixing and compaction | 3-14 |
| 3.3.3 | Asphalt sample preparation and density determination | 3-16 |
| 3.3.4 | Volumetric analysis of compacted HMA specimens | 3-18 |
| 3.4 | Investigation of the influence of compaction on HMA rutting resistance | 3-21 |
| 3.4.1 | HMA mix designs..... | 3-21 |
| 3.4.2 | Mixing and compaction of asphalt samples | 3-23 |
| 3.4.3 | HMA rutting resistance evaluation | 3-27 |
| 3.5 | Summary..... | 3-32 |
| 4 | INFLUENCE OF AGGREGATE PACKING ON HMA COMPACTABILITY | 4-1 |
| 4.1 | Introduction..... | 4-1 |
| 4.2 | Aggregate packing analysis..... | 4-1 |
| 4.2.1 | Shape factor of aggregate gradation curve and the ratio of gravel to sand..... | 4-1 |
| 4.2.2 | Traditional Bailey ratios..... | 4-3 |
| 4.2.3 | Rational Bailey ratios..... | 4-5 |
| 4.2.4 | Correlations of aggregate packing parameters | 4-6 |
| 4.2.5 | Sensitivity of Bailey ratios to change in gradation | 4-8 |
| 4.3 | Determination of HMA compactability parameters | 4-10 |
| 4.3.1 | Locking point..... | 4-11 |
| 4.3.2 | Compaction energy index and traffic densification index..... | 4-14 |
| 4.3.3 | Compaction slope (CS) | 4-17 |
| 4.3.4 | Area under the shear stress curve | 4-19 |
| 4.4 | Parametric correlations | 4-21 |
| 4.5 | Summary..... | 4-25 |
| 5 | SPATIAL DISTRIBUTION OF AIR VOIDS IN COMPACTED HMA SAMPLES | 5-1 |
| 5.1 | Introduction..... | 5-1 |
| 5.2 | Vertical distribution of air voids in laboratory-compacted HMA samples..... | 5-2 |
| 5.2.1 | 170 mm high compacted HMA samples | 5-2 |

| | | |
|-------|------------------------------------------------------------------------------------------------------------|------|
| 5.2.2 | 120 mm high compacted HMA samples | 5-6 |
| 5.2.3 | Influence of sample height on vertical air voids distribution | 5-9 |
| 5.2.4 | Influence of compaction density on vertical air voids distribution..... | 5-11 |
| 5.3 | Radial distribution of air voids in laboratory- laboratory samples | 5-12 |
| 5.3.1 | 170 mm high compacted HMA samples | 5-12 |
| 5.3.2 | 120 mm high compacted HMA samples | 5-14 |
| 5.4 | Vertical distribution of air voids in field extracted cores..... | 5-16 |
| 5.5 | Radial distribution of air voids in field-extracted cores..... | 5-17 |
| 5.6 | Summary..... | 5-19 |
| 6 | INFLUENCE OF COMPACTION METHOD AND DENSITY ON HMA RUTTING RESISTANCE..... | 6-1 |
| 6.1 | Introduction..... | 6-1 |
| 6.2 | Evaluation of rutting tests | 6-2 |
| 6.3 | Influence of the compaction method | 6-10 |
| 6.4 | Influence of compaction density on rutting performance | 6-12 |
| 6.5 | Summary..... | 6-15 |
| 7 | CONCLUSIONS AND RECOMMENDATIONS..... | 7-1 |
| 7.1 | Introduction..... | 7-1 |
| 7.2 | The influence of aggregate packing characteristics on HMA compactability..... | 7-1 |
| 7.3 | The spatial distribution of aggregates in compacted HMA samples | 7-2 |
| 7.4 | The influence of compaction method and density on HMA rutting resistance | 7-3 |
| 7.5 | Recommendations and suggestions for future research..... | 7-3 |
| 8 | REFERENCES..... | 8-1 |
| 9 | APPENDIX A: GYRATORY COMPACTION RESULTS | 9-1 |
| 10 | APPENDIX B: SUMMARY OF BULK DENSITY RESULTS..... | 10-1 |
| 10.1 | Bulk density of laboratory-compacted samples – investigation into vertical air voids distribution | 10-1 |
| 10.2 | Bulk density of laboratory-compacted samples – investigation into radial air voids distribution | 10-3 |
| 11 | APPENDIX C: REPEATED SIMPLE SHEAR TEST AT CONSTANT HEIGHT RESULTS 11-1 | |
| 11.1 | RSST-CH results of slab roller-compacted samples..... | 11-1 |
| 11.2 | RSST-CH results of gyratory-compacted samples | 11-3 |
| 12 | APPENDIX D: UNIAXIAL SHEAR TESTER RESULTS | 12-1 |
| 12.1 | URST results of slab roller-compacted samples | 12-1 |
| 12.2 | URST results of gyratory-compacted samples..... | 12-3 |

LIST OF TABLES

| | |
|--------------------------------------------------------------------------------------------------------------------------|------|
| Table 2.1: Recommended ranges of aggregate ratios for dense-graded asphalt mixes (.Sabita Manual 35/TRH 8, 2020). | 2-19 |
| Table 2.2: Recommended ranges of aggregate ratios for SMA (Sabita Manual 35/TRH 8, 2020). .. | 2-19 |
| Table 2.3: Proposed permeability control criteria for rational Bailey ratios (Horak et al. (2017). .. | 2-20 |
| Table 2.4: Proposed permeability control criteria for DASR descriptors (Horak et al. (2017)..... | 2-23 |
| Table 2.5: Definition of Superpave gyratory compactor locking point using HMA specimen height (Vavrik et al., 1999)..... | 2-31 |
| Table 2.6: Definition of locking point (Alshamsi, 2006)..... | 2-32 |
| Table 3.1: Grading specifications | 3-3 |
| Table 3.2: Physical properties of aggregates | 3-3 |
| Table 3.3: Gradations of 10 mm NMPS mix individual fractions | 3-4 |
| Table 3.4: Gradations of 20 mm NMPS mix individual fractions | 3-5 |
| Table 3.5: Matrix of compacted samples | 3-15 |
| Table 4.1: Summary of locking point results | 4-13 |
| Table 4.2: Summary of CEI results..... | 4-16 |
| Table 4.3: Summary of TDI ₃₀₀ results..... | 4-16 |
| Table 4.4: Summary of compaction slope results..... | 4-19 |
| Table 4.5: Summary of ASS _{max} results..... | 4-20 |
| Table 4.6: Correlation coefficients and coefficients of determination - 10 mm NMPS mixes..... | 4-22 |
| Table 4.7: Correlation coefficients and coefficients of determination - 20 mm NMPS mixes..... | 4-22 |
| Table 5.1: Air voids of 170 mm high samples – vertical distribution..... | 5-2 |
| Table 5.2: Air voids results of the three parts – 4.0% air voids, 170 mm high | 5-3 |
| Table 5.3: Air voids results of the three parts – 7.0% air voids, 170 mm high | 5-3 |
| Table 5.4: Air voids results of the six parts – 4.0% target air voids content | 5-5 |
| Table 5.5: Air voids results of the six parts – 7.0% target air voids content | 5-5 |
| Table 5.6: Air voids of 120 mm high samples – vertical distribution..... | 5-7 |
| Table 5.7: Air voids results of the three parts – 4.0% target air voids content, 120 mm high..... | 5-7 |
| Table 5.8: Air voids results of the three parts – 7.0% target air voids content, 120 mm high..... | 5-8 |
| Table 5.9: Air voids of 170 mm high – radial distribution (4.0% target air voids) | 5-13 |
| Table 5.10: Air voids of 170 mm high – radial distribution (7.0% target air voids) | 5-13 |
| Table 5.11: Air voids of 120 mm high – radial investigation (4.0% target air voids content) | 5-15 |
| Table 5.12: Air voids of 120 mm high – radial investigation (7.0% target air voids content) | 5-15 |
| Table 10.1: Bulk density of 170 mm high samples – vertical distribution..... | 10-1 |
| Table 10.2: Bulk density of the top, middle and bottom – 4.0% target air voids, 170 mm high ... | 10-1 |
| Table 10.3: Bulk density of the top, middle and bottom – 7.0% target air voids, 170 mm high ... | 10-1 |
| Table 10.4: Bulk density results of the six parts – 4.0% target air voids | 10-1 |
| Table 10.5: Bulk density results of the six parts – 7.0% target air voids | 10-2 |
| Table 10.6: Bulk density of 120 mm high samples – vertical distribution..... | 10-2 |
| Table 10.7: Bulk density of the top, middle and bottom – 4.0% target air voids, 120 mm high ... | 10-2 |
| Table 10.8: Bulk density of the top, middle and bottom - 7.0% target air voids, 120 mm high.... | 10-2 |
| Table 10.9: Bulk density of 170 mm high – radial distribution (4.0% target air voids) | 10-3 |
| Table 10.10: Bulk density of 170 mm high – radial distribution (7.0% target air voids) | 10-3 |
| Table 10.11: Bulk density of 120 mm high – radial distribution (4.0% target air voids) | 10-3 |
| Table 10.12: Bulk density of 120 mm high – radial distribution (7.0% target air voids) | 10-3 |

LIST OF FIGURES

| | |
|----------------------------------------------------------------------------------------------------------------------------------|------|
| Figure 1.1: Layout of this thesis | 1-7 |
| Figure 2.1: HMA constituents | 2-2 |
| Figure 2.2: Marshall hammer set-up (SANS 3001-AS1, 2015) | 2-4 |
| Figure 2.3: Marshall stability and flow test set-up (SANS 3001-AS2, 2011)..... | 2-5 |
| Figure 2.4: Process of determining stability and flow (SANS 3001-AS2, 2011)..... | 2-5 |
| Figure 2.5: Illustration of gyratory compaction..... | 2-7 |
| Figure 2.6: Definition of asphalt mix design levels (Sabita Manual 35/TRH 8, 2020) | 2-9 |
| Figure 2.7: Level I mix design process (Sabita Manual 35/TRH 8, 2020)..... | 2-11 |
| Figure 2.8: Levels II & III mix design process (Sabita Manual 35/TRH 8, 2020) | 2-12 |
| Figure 2.9: Illustration of slab roller compaction | 2-13 |
| Figure 2.10: The maximum density line concept | 2-15 |
| Figure 2.11: The 0.45 power gradation curve | 2-16 |
| Figure 2.12: The Bailey ratios illustration (Horak & Cromhout, 2018)..... | 2-18 |
| Figure 2.13: Schematic of DASR and IC concept for three basic grading types..... | 2-21 |
| Figure 2.14: Asphalt mixture components or phases | 2-22 |
| Figure 2.15: Classification of existing particle packing models (Loseby, 2014) | 2-24 |
| Figure 2.16: Compaction train (Sabita, 2008) | 2-27 |
| Figure 2.17: Nuclear density gauge (Pavement Interactive, 2021)..... | 2-27 |
| Figure 2.18: Functioning of Intelligent Compaction roller (FHWA, 2014) | 2-28 |
| Figure 2.19: Compacted HMA phase diagram (Sabita Manual 35/TRH 8, 2020) | 2-29 |
| Figure 2.20: Set-up for vacuum-sealing method | 2-30 |
| Figure 2.21: The compaction energy index (CEI) (Leiva & West, 2008)..... | 2-33 |
| Figure 2.22: CDI and TDI determination (Alshamsi, 2006) | 2-34 |
| Figure 2.23: Typical binder temperature-viscosity chart (ASTM D 2493, 2001) | 2-35 |
| Figure 2.24: Asphalt pavement rutting..... | 2-37 |
| Figure 2.25: Hamburg Wheel-Tracking Device (HWTDD) | 2-38 |
| Figure 2.26: RLPD test set-up at the CSIR | 2-40 |
| Figure 2.27: SST set-up at the CSIR..... | 2-41 |
| Figure 2.28: Photos of (a) UST test set-up, (b) hollow test specimen, and (c) UST placed in UTM chamber (Zak et al., 2016) | 2-42 |
| Figure 3.1: Steps followed in the aggregate packing and compactability investigation | 3-2 |
| Figure 3.2: 10 mm NMPS mixes aggregate grading..... | 3-5 |
| Figure 3.3: 20 mm NMPS mixes aggregate grading..... | 3-6 |
| Figure 3.4: Mechanical HMA mixing..... | 3-7 |
| Figure 3.5: Gyratory compactor and typical compacted HMA sample | 3-7 |
| Figure 3.6: HMA sample height plotted against the number of gyrations | 3-8 |
| Figure 3.7: Shear stress plotted against the number of gyrations | 3-8 |
| Figure 3.8: Estimated and actual bulk density..... | 3-10 |
| Figure 3.9: Degree of compaction versus the number of gyrations | 3-11 |
| Figure 3.10: Air voids content versus the number of gyrations..... | 3-12 |
| Figure 3.11: Main screen of the gyratory data processing software | 3-13 |
| Figure 3.12: 10 mm NMPS mix design gradation | 3-14 |
| Figure 3.13: BTB and HiMA design gradation | 3-16 |
| Figure 3.14: HMA compaction and sample preparation procedures | 3-17 |
| Figure 3.15: SSD test set-up..... | 3-19 |
| Figure 3.16: MVD test set-up..... | 3-20 |
| Figure 3.17: Design gradation for the 10 mm NMPS mix | 3-22 |
| Figure 3.18: Design gradation for the 20 mm NMPS mix | 3-23 |
| Figure 3.19: Gyratory and slab roller compactors | 3-24 |
| Figure 3.20: The gyratory compaction process | 3-25 |
| Figure 3.21: The slab roller compaction process | 3-26 |

| | |
|----------------------------------------------------------------------------------------------------------|------|
| Figure 3.22: Typical HMA samples compacted by the (a) gyratory and (b) slab roller compactors . | 3-26 |
| Figure 3.23: Typical HMA specimens prepared from gyratory-compacted samples | 3-27 |
| Figure 3.24: Typical HMA specimens prepared from slab roller-compacted samples | 3-27 |
| Figure 3.25: SST and UST set-up..... | 3-28 |
| Figure 3.26: Schematic representation of the RSST-CH | 3-29 |
| Figure 3.27: The RSST-CH test set-up | 3-29 |
| Figure 3.28: UST temperature conditioning chamber..... | 3-30 |
| Figure 3.29: Two-dimensional representation of the UST test set-up (Zak et al., 2016)..... | 3-31 |
| Figure 3.30: UST test set-up inside the temperature chamber..... | 3-31 |
| Figure 4.1: Determining the gradation shape factor (n) | 4-2 |
| Figure 4.2: G/S and n parameters of 10 mm NMPS mix | 4-3 |
| Figure 4.3: G/S and n parameters of 20 mm NMPS mix | 4-3 |
| Figure 4.4: Traditional Bailey ratios of the 10 mm NMPS mix | 4-4 |
| Figure 4.5: Traditional Bailey ratios of the 20 mm NMPS mix | 4-5 |
| Figure 4.6: Rational Bailey ratios of the 10 mm NMPS mix | 4-6 |
| Figure 4.7: Rational Bailey ratios of the 20 mm NMPS mix | 4-6 |
| Figure 4.8: n parameter correlated with G/S parameter | 4-7 |
| Figure 4.9: n and G/S parameters correlated with Bailey ratios – 10 mm NMPS mix | 4-8 |
| Figure 4.10: n and G/S parameters correlated with Bailey ratios – 20 mm NMPS mix | 4-8 |
| Figure 4.11: Theoretical gradation curves..... | 4-9 |
| Figure 4.12: Traditional Bailey ratios of the theoretical gradation curves | 4-10 |
| Figure 4.13: Rational Bailey ratios of the theoretical gradation curves | 4-10 |
| Figure 4.14: Rate of change in HMA sample height versus the number of gyrations | 4-12 |
| Figure 4.15: Determination of the locking point | 4-12 |
| Figure 4.16: Average locking point results | 4-14 |
| Figure 4.17: Typical gyratory compaction densification curve..... | 4-15 |
| Figure 4.18: CEI and TDI ₃₀₀ determination..... | 4-15 |
| Figure 4.19: Average CEI results | 4-17 |
| Figure 4.20: Average TDI ₃₀₀ results..... | 4-17 |
| Figure 4.21: Determination of the compaction slope input parameters | 4-18 |
| Figure 4.22: Average compaction slope results..... | 4-19 |
| Figure 4.23: Determining the ASS _{max} | 4-20 |
| Figure 4.24: Average ASS _{max} results | 4-21 |
| Figure 4.25: Correlations between Rational Bailey ratios and compactability parameters – 10 mm NMPS..... | 4-23 |
| Figure 4.26: Correlations between rational Bailey ratios and compactability parameters – 20 mm NMPS..... | 4-24 |
| Figure 5.1: Average air voids – 4.0% target air voids content, 170 mm high samples..... | 5-4 |
| Figure 5.2: Average air voids – 7.0% target air voids content, 170 mm high samples..... | 5-4 |
| Figure 5.3: Vertical distribution of air voids – 4.0% target air voids content, 170 mm high..... | 5-6 |
| Figure 5.4: Vertical distribution of air voids – 7.0% target air voids content, 170 mm high..... | 5-6 |
| Figure 5.5: Average air voids content – 4.0%, 120 mm high samples..... | 5-8 |
| Figure 5.6: Average air voids content – 7.0%, 120 mm high samples..... | 5-9 |
| Figure 5.7: Vertical distribution of air voids – 4.0% air voids content..... | 5-10 |
| Figure 5.8: Vertical distribution of air voids – 7.0% air voids content..... | 5-10 |
| Figure 5.9: Vertical distribution of air voids – 120 mm high samples..... | 5-11 |
| Figure 5.10: Vertical distribution of air voids – 170 mm high samples..... | 5-12 |
| Figure 5.11: Radial distribution of air voids – 4.0% target air voids, 170 mm high..... | 5-13 |
| Figure 5.12: Radial distribution of air voids – 7.0% target air voids, 170 mm high..... | 5-14 |
| Figure 5.13: Radial distribution of air voids – 4.0% target air voids, 120 mm high..... | 5-15 |
| Figure 5.14: Radial distribution of air voids – 7.0% target air voids, 120 mm high..... | 5-16 |
| Figure 5.15: Vertical distribution of air voids in HiMA field cores | 5-17 |

| | |
|------------------------------------------------------------------------------------------------------------------------|------|
| Figure 5.16: Vertical distribution of air voids in BTB field cores | 5-17 |
| Figure 5.17: Radial distribution of air voids for HiMA field cores | 5-18 |
| Figure 5.18: Radial distribution of air voids for BTB field cores..... | 5-18 |
| Figure 6.1: Typical load versus time..... | 6-3 |
| Figure 6.2: Typical displacement versus time..... | 6-3 |
| Figure 6.3: RSST-CH and URST results (10 mm NMPS mix)..... | 6-5 |
| Figure 6.4: RSST-CH and URST results (20 mm NMPS mix)..... | 6-6 |
| Figure 6.5: Comparison of RSST-CH results for the 10 mm and 20 mm NMPS mixes..... | 6-8 |
| Figure 6.6: Comparison of the URST results for the 10 mm and 20 mm NMPS mixes..... | 6-9 |
| Figure 6.7: RSST-CH results – gyratory- and roller-compacted samples (10 mm NMPS mix) ... | 6-10 |
| Figure 6.8: RSST-CH results – gyratory- and roller-compacted samples (20 mm NMPS mix) ... | 6-11 |
| Figure 6.9: URST results – gyratory- and roller-compacted samples (10 mm NMPS mix) | 6-11 |
| Figure 6.10: URST results – gyratory- and roller-compacted samples (20 mm NMPS mix) | 6-12 |
| Figure 6.11: RSST-CH results – gyratory-compacted samples to 4% and 7% target air voids content (10 mm NMPS mix) | 6-14 |
| Figure 6.12: RSST-CH results – gyratory-compacted samples to 4% and 7% target air voids content (20 mm NMPS mix) | 6-14 |
| Figure 6.13: UST results – gyratory-compacted samples with a 4% and 7% target air voids content (10 mm NMPS mix) | 6-15 |
| Figure 6.14: UST results – gyratory-compacted samples with a 4% and 7% target air voids content (20 mm NMPS mix) | 6-15 |
| Figure 9.1: Gyratory compaction results – 10 mm NMPS coarse gradation structure | 9-1 |
| Figure 9.2: Gyratory compaction results – 10 mm NMPS medium gradation structure..... | 9-2 |
| Figure 9.3: Gyratory compaction results – 10 mm NMPS Fine gradation structure | 9-3 |
| Figure 9.4: Gyratory compaction results – 20 mm NMPS coarse gradation structure | 9-4 |
| Figure 9.5: Gyratory compaction results – 20 mm NMPS medium gradation structure..... | 9-5 |
| Figure 9.6: Gyratory compaction results – 20 mm NMPS Fine gradation structure | 9-6 |
| Figure 11.1: RSST-CH results of roller-compacted samples – 10 mm NMPS mix (7% air voids) | 11-1 |
| Figure 11.2: RSST-CH results of roller-compacted samples – 20 mm NMPS mix (7% air voids) | 11-2 |
| Figure 11.3: RSST-CH results of gyratory-compacted samples – 10 mm NMPS mix (4% air voids) | 11-3 |
| Figure 11.4: RSST-CH results of gyratory-compacted samples – 10 mm NMPS mix (7% air voids) | 11-3 |
| Figure 11.5: RSST-CH results of gyratory-compacted samples – 20 mm NMPS mix (4% air voids) | 11-4 |
| Figure 11.6: RSST-CH results of gyratory-compacted samples – 20 mm NMPS mix (7% air voids) | 11-4 |
| Figure 12.1: URST results of slab roller-compacted samples – 10 mm NMPS mix (7% air voids) | 12-1 |
| Figure 12.2: URST results of slab roller-compacted samples – 20 mm NMPS mix (7% air voids) | 12-2 |
| Figure 12.3: URST results of gyratory-compacted samples – 10 mm NMPS mix (4% air voids) | 12-3 |
| Figure 12.4: URST results of gyratory-compacted samples – 10 mm NMPS mix (7% air voids) | 12-3 |
| Figure 12.5: URST results of gyratory-compacted samples – 20 mm NMPS mix (4% air voids) | 12-4 |
| Figure 12.6: URST results of gyratory-compacted samples – 20 mm NMPS mix (7% air voids) | 12-4 |

LIST OF ABBREVIATIONS

| | | |
|---------|---|--------------------------------------------------------------------|
| AASHTO | - | American Association of State Highway and Transportation Officials |
| AI | - | Asphalt Institute |
| AMTL | - | Advanced Material Testing Laboratories |
| ASTM | - | American Society for Testing and Materials |
| BD | - | Bulk Density |
| BTB | - | Bituminous Treated Base |
| CDI | - | Compaction Densification Index |
| CEI | - | Compaction Energy Index |
| COLTO | - | Committee of Land Transportation Officials |
| CS | - | Compaction Slope |
| CSIR | - | Council for Scientific and Industrial Research |
| CSRA | - | Committee of State Road Authorities |
| DASR | - | Dominant Aggregate Size Range |
| DIT | - | Dar Es Salaam Institute of Technology |
| DOT | - | Department of Transport |
| FAA | - | Federal Aviation Administration |
| FHWA | - | Federal Highway Administration |
| HiMA | - | High Modulus Asphalt |
| HMA | - | Hot Mix Asphalt |
| LVDT | - | Linear Variable Displacement Transformer |
| MVD | - | Maximum Void-less Density |
| HS | - | Half Sieve |
| ITS | - | Indirect Tensile Strength |
| NMPS | - | Nominal Maximum Particle Size |
| PCS | - | Primary Control Sieve |
| PG | - | Parliamentary Grant |
| R&D | - | Research and Development |
| RSST-CH | - | Repeated Simple Shear Test at Constant Height |
| SABITA | - | Southern African Bitumen Association |
| SANRAL | - | South African National Roads Agency SOC Ltd |
| SANS | - | South African National Standards |
| SATS | - | South African Technical Specification |
| SCS | - | Secondary Control Sieve |
| SHRP | - | Strategic Highway Research Program |

| | | |
|-----------|---|----------------------------------------|
| SSD | - | Saturated Surface-Dry |
| SUPERPAVE | - | Superior Performing Asphalt Pavements |
| TCS | - | Tertiary Control Sieve |
| TDI | - | Traffic Densification Index |
| TIE | - | Transport Infrastructure Engineering |
| TMH | - | Technical Methods for Highways |
| TRB | - | Transportation Research Board |
| TRH | - | Technical Recommendations for Highways |
| TSR | - | Tensile Strength Ratio |
| URST | - | Uniaxial Repeated Shear Test |
| USA | - | Unites States of America |
| UST | - | Uniaxial Shear Tester |
| VBF | - | Voids Filled with Binder |
| VIM | - | Voids in Mix |
| VMA | - | Voids in Mineral Aggregate |

1 INTRODUCTION

1.1 Background

Hot-Mix Asphalt (HMA) is a visco-elastic material composed of a graded aggregate, bituminous binder and air voids. Several types of HMA mixes may be produced depending on the proportions of constituents (i.e., aggregates, mineral filler and binder) and the desired gradation of aggregate. The South African guideline for the design and use of asphalt in road pavements classifies asphalt mixes into two categories, depending on the aggregate packing (Sabita Manual 35, 2020). The two categories are sand-skeleton and stone-skeleton mixes. In sand-skeleton asphalt mixes, the traffic loads on the HMA layer are mainly carried by the finer aggregate fraction and binder. In contrast, in stone-skeleton asphalt mixes, the traffic loads are carried predominantly by a skeleton of the coarser aggregate fraction. In order to optimise the asphalt mix design, the use of aggregate packing principles is recommended by the latest South African asphalt mix design manuals (Sabita Manual 24, 2020; Sabita Manual 35, 2020).

In HMA pavement layers, the aggregate structure (skeleton) is believed to be responsible for load transfer and resisting pavement distresses. A strong aggregate structure relies on the optimal packing (densification) of aggregates. Several methods that have been developed over the years to assist with the blending of aggregate to obtain optimum packing include the maximum density line concept (Fuller's curve) introduced by Fuller and Thompson (1907), the stone-on-stone contact method developed by Brown and Haddock (1997), and the power-law method suggested by Ruth et al. (2002).

The Bailey method (Vavrik et al., 2002) is another systematic way of optimising aggregate proportions to obtain the desired gradation. The parameters in the Bailey method are related to the asphalt mix volumetric properties (i.e. voids in mineral aggregate, air voids and compaction properties). Although the Bailey method has been used widely, Roque et al. (2006) pointed out that it may not necessarily guarantee aggregate particles to be in contact with each other. They proposed the use of porosity principles in combination with the Dominant Aggregate Size Range (DASR). Recent work by Horak et al. (2017) as well as Horak and Cromhout (2018) proposed some rational Bailey ratios, which incorporate aggregate packing efficiency that includes the concept of binary aggregate packing as described by Olard (2015). The rational Bailey ratios were included in the aggregate packing analysis concepts investigated in this thesis.

Among many other factors, the performance of HMA pavements is also highly dependent on adequate compaction. Inadequate HMA compaction may affect the fundamental properties of the asphalt and result in poor rutting resistance, increased permeability and moisture damage, reduced stiffness, accelerated ageing and reduced fatigue life (Awed et al., 2015; Verhaeghe et al., 2007; Walubita et al., 2016). On the other hand, overcompaction of HMA mixes may result in bleeding and/or crushing of the aggregate particles, which may negatively impact the pavement surface texture and skid resistance properties (Verhaeghe et al., 2007; Walubita et al., 2016).

During compaction, HMA undergoes internal structural changes in response to the compaction effort, whereby the distance between aggregate particles reduces, resulting in decreased air voids (Masad et al., 1999; Walubita et al., 2012). The aggregate packing, binder volume and stiffness, together with the air void distribution, define the internal structure of the HMA, which in turn plays a significant role in the mechanical and volumetric properties of HMA, as well as its ability to resist distresses (Chang & Meegoda, 1997; Masad et al., 1999; Micaelo et al., 2009). The internal structure of compacted HMA also depends on aggregate packing characteristics and the compaction process or method. Hence, there is a need to understand how these characteristics affect HMA compactability and how the compaction process affects the internal structure as well as the volumetric and mechanical properties of the compacted HMA. Such knowledge will ultimately be used to enhance the performance of asphalt pavements.

1.2 Problem definition

Advancements in asphalt mix design methods require the incorporation of aggregate packing principles to enhance the asphalt mix design procedures. This implies developing a framework to incorporate such principles in the existing asphalt mix design procedures. To this end, the study's hypothesis is that the current asphalt mix design procedures could benefit from an understanding of the relationship between aggregate packing characteristics, compaction method, and the volumetric properties and rutting resistance of the compacted HMA.

1.3 Objectives of the study

The main objective of the study was to relate aggregate packing characteristics with the HMA compactability, and the resulting HMA volumetric properties, as well as the ability of the compacted mix to resist rutting. To ensure achievement of this objective, the study was divided into three specific objectives.

The first objective was geared towards understanding how the aggregate packing characteristics influence the compactability of HMA mixes. This included establishing appropriate aggregate packing parameters that better describe the packing of a gradation structure and that relate to the compactability of the HMA mixes.

The second objective was to investigate air voids distribution in laboratory-compacted HMA samples and cores extracted from actual field road sections. Air voids content is an important HMA mix volumetric property that also defines the internal structure of asphalt mixes. As part of this objective, the influence of sample height and compaction density on the air voids distribution was also investigated.

The third objective was to investigate the influence of the compaction method on HMA rutting resistance, including the effect of the compaction density on HMA rutting resistance.

1.4 Scope of the study

The following was included in the scope of the study:

- A review of the literature on the main aspects covered in the study;
- Establishing aggregate packing parameters that better describe the packing characteristics of aggregate structure;
- Establishing appropriate HMA compactability parameters;
- Investigating the relationship between aggregate packing parameters and HMA compactability parameters;
- Examining the air voids distribution in compacted HMA, and the influence of sample size and compaction density, and
- Determining the influence of the laboratory compaction method and compaction density on HMA rutting resistance (which included a comparative evaluation of two rutting tests:

Uniaxial Repeated Shear Test (URST) and Repeated Simple Shear Test at Constant Height (RSST-CH)).

The following were limitations of the study:

- The study focused primarily on laboratory compaction, with limited field-compacted asphalt samples;
- Only commonly used South African dense-graded aggregate structures were used in the study, namely: 10 mm NMPS (sand-skeleton) and 20 mm NMPS (stone-skeleton) grading structures;
- The HMA compactability aspect of the study focused primarily on aggregate packing. Hence the properties of the binder that influences HMA compactability fell outside the scope of the study, and
- With respect to the HMA performance attributes, only the rutting resistance of laboratory-compacted HMA samples was investigated. Rutting is a common distress in asphalt pavements.

1.5 Methodology

To achieve the stated research objectives and cover the scope of the study, the following methodology was adopted:

- A literature review was conducted covering asphalt mix design methods, aggregate packing analysis, HMA compaction and compactability assessment, and the evaluation of HMA rutting resistance;
- Materials and asphalt mix designs were selected;
- Samples of the selected material were prepared for laboratory testing;
- The gradation curves of the selected HMA mixes were analysed to determine aggregate packing parameters;
- Asphalt mixes were prepared;
- Gyratory compaction experiments were performed and the compaction data was analysed to determine HMA compactability parameters and relate to the aggregate packing parameters;
- HMA compaction experiments were conducted to investigate air voids distribution in compacted HMA samples; and

- HMA samples were compacted using gyratory and slab roller compactors. Rutting tests were performed on the asphalt samples and the results were analysed.

1.6 Contribution to the body of knowledge

This study contributes to the state of knowledge in a number of fields:

- Much work has been done in the field of aggregate packing internationally. There is a need to establish aggregate packing parameters that can be incorporated during the asphalt mix design process in a simplified manner. The aggregate gradation curve, which is the basis of most asphalt mix design methods, was used to determine the aggregate packing parameters investigated in this study;
- The parametric correlation that was found between aggregate packing parameters and HMA compactability parameters contributes to technical knowledge. It explains how the aggregate packing affects HMA compactability, which could assist in identifying the potential HMA mix compaction problems;
- Understanding the air voids distribution provides valuable information on the internal structure of compacted HMA and its influence on the HMA volumetric properties and other performance attributes, such as rutting resistance;
- The URST introduced to South Africa as part of this study is a cost-effective test for the evaluation of the asphalt mixes shear properties (rutting resistance) and it could potentially be used as an alternative to the costly RSST-CH, and
- The research done in this study generally contributes to the future revision of existing asphalt mix design procedures in order to develop a framework for incorporating aggregate packing principles.

1.7 Organisation of the thesis

The thesis consists of seven chapters. Figure 1.1 gives a schematic layout of the relationships between the various chapters.

Chapter 1 serves as introduction and provides the background to and context of the study. This is followed by a literature review of the currently available knowledge that is relevant to the aspects covered in this study (Chapter 2). The literature review comprises a description of the composition of HMA, an overview of asphalt mix design methods, aggregates packing analysis, HMA

compaction, assessment of HMA compactability, factors affecting HMA compaction and evaluation of HMA rutting resistance.

Chapter 3 provides a detailed description of the methodology followed during the study. It covers the approach and methodology adopted to investigate each aspect covered in the study, namely the influence of aggregate packing on HMA compactability, the spatial distribution of air voids on compacted HMA, and the effect of the laboratory compaction method and density on HMA rutting resistance. .

Next follow three separate chapters covering data analysis and discussions of the results. Chapter 4 presents an analysis and discussion of the results of the experiments conducted to determine the influence of aggregate packing on HMA compactability. Aggregate packing parameters that best describe the packing of aggregate gradation curves were established and correlated with HMA compactability parameters.

Chapter 5 analyses and discusses the results of investigating the spatial distribution of air voids in compacted HMA. The vertical and radial (diametrical) air voids distributions were investigated using laboratory-compacted asphalt samples and asphalt cores extracted from two road sections. The chapter also reviews the influence of HMA specimen size (height) and compaction densities on the spatial distribution of air void in compacted HMA samples.

The results of the experiments to investigate the effects of the laboratory compaction method and density on HMA rutting resistance are analysed and discussed in Chapter 6. The gyratory and roller slab compactors that are commonly used in South Africa (and in the world at large) were selected for the investigation.

The study conclusions are discussed in the final chapter (Chapter 7). Recommendations for further work are also suggested.

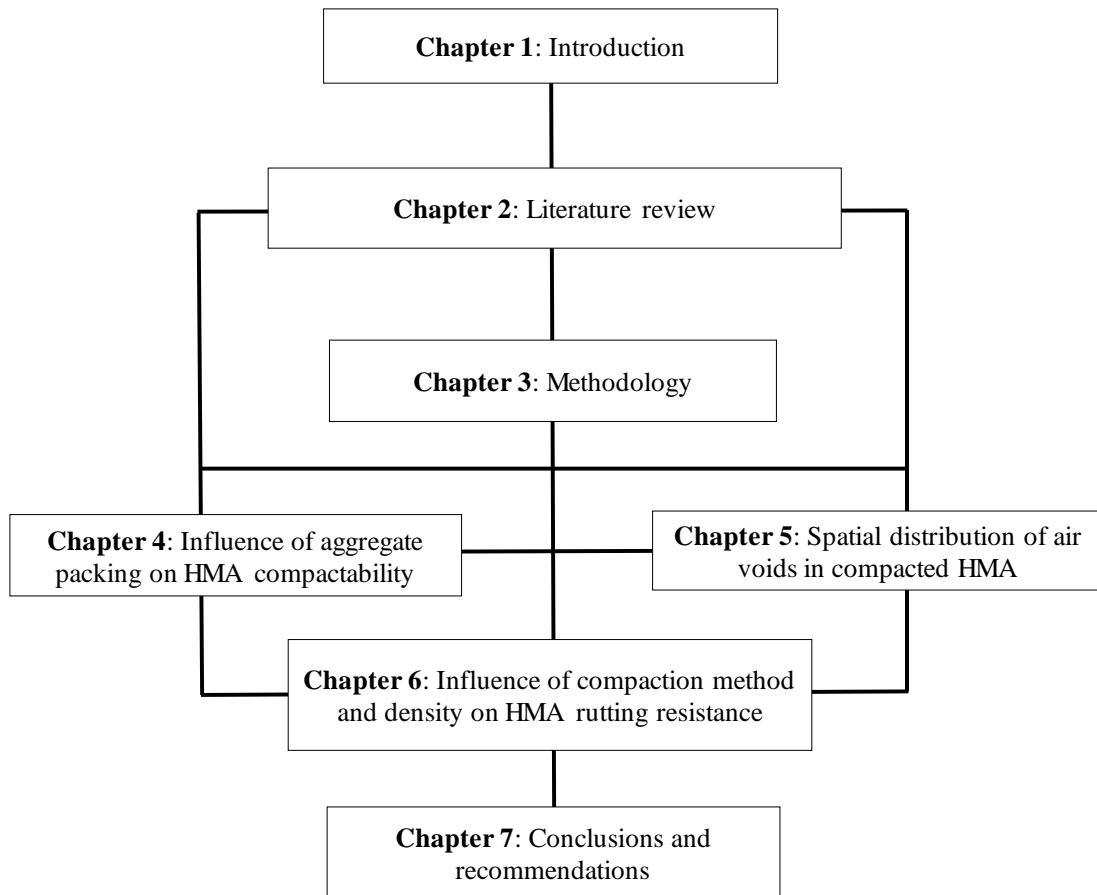


Figure 1.1: Layout of this thesis

2 LITERATURE REVIEW

2.1 Introduction

This chapter gives an overview of the knowledge that is currently available on the aspects covered in the thesis. The literature review covers:

- Overview of HMA and asphalt mix design methods;
- Aggregates packing analysis;
- HMA compaction;
- Assessment of HMA compactability;
- Factors affecting HMA compaction, and
- Evaluation of HMA rutting resistance.

2.2 Overview of HMA and asphalt mix design methods

Hot-Mix Asphalt (HMA) is one of the materials commonly used for the construction of wearing course and base layers of flexible pavements. HMA is visco-elastic material composed of a graded aggregate, mineral filler and bituminous binder (see Figure 2.1). The term “Hot-Mix” derives from the fact that the material is manufactured at elevated temperature, usually varying from 150 to 170°C, depending on the viscosity of the bituminous binder. This is primarily due to the fact that binder viscosity is low at high temperatures, which makes it easier to be mixed with aggregates.

In HMA mixes, bituminous binder acts as a binding agent that glues the other constituent materials into a dense mass, thereby providing a waterproof mixture. On the other hand, aggregates constitute a larger proportion (about 95% by mass) of the HMA, and they form the structure (skeleton) that is responsible for load transfer as well as for resisting pavement distress (Roberts et al., 1996; AI, 2014; Sabita Manual 35/TRH 8, 2020).

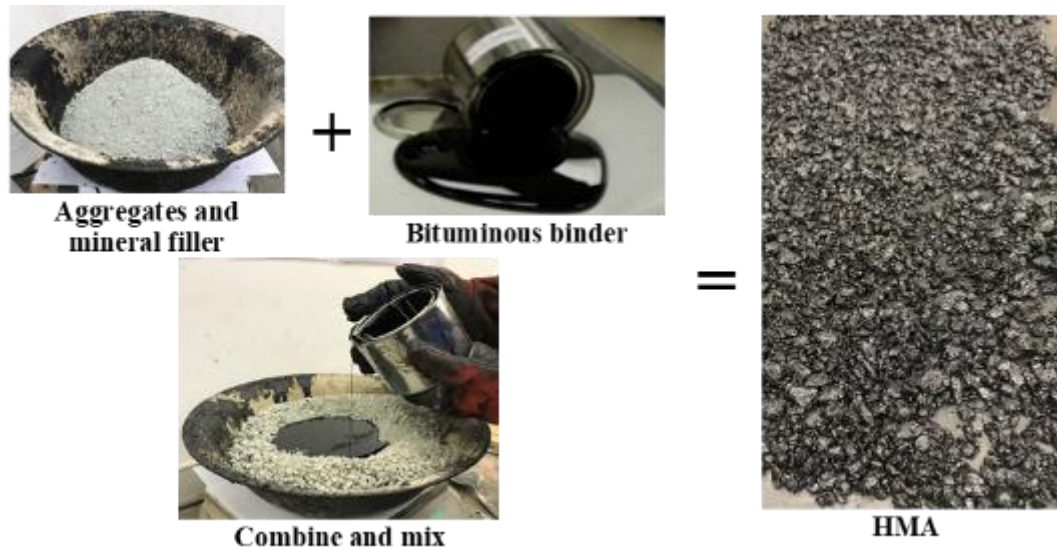


Figure 2.1: HMA constituents

The primary objective of HMA mix design is to determine the combination of constituent materials (binder, aggregates and mineral filler) that will provide a long-lasting performance of the pavement structure. The mix design process involves the selection and blending of aggregate sources (fractions) to produce a proper gradation, as well as the selection of the type and amount of binder that is suitable for that gradation. Ultimately, the desired combination of aggregate grading and binder needs to yield a mix with the following attributes, taking into account other key factors, such as the expected traffic loading and environmental condition (AI, 2014; Sabita Manual 35/TRH 8, 2020):

- Sufficient mix workability (compactability) to allow for efficient placement and compaction during construction;
- An adequate amount of binder to ensure mix durability and resistance to fatigue cracking, without flushing or bleeding;
- Sufficient mix stability that will satisfy the demands of traffic;
- Sufficient mix stiffness for load transfer to underlying pavement layers;
- Sufficient air voids that to allow for minimal additional densification under traffic loading;
- Optimum air voids to limit mix permeability and moisture damage, and
- Sufficient texture to provide skid resistance during undesirable weather conditions.

Laboratory mix design is a critical step that is geared towards ensuring that the above mix attributes are achieved in the field. The laboratory mix design is undertaken using well-established procedures. The design process involves the selection and blending of component materials, the preparation of asphalt mix, the compaction of specimens, and the testing and performance evaluation of the optimum mix. Several HMA mix design methods were developed over the years. The Marshall and Superpave mix design methods, which are both widely used globally, are briefly described in the subsequent sections.

2.2.1 Marshall asphalt mix design method

The basic concepts of the Marshall HMA mix design procedure were developed by Bruce Marshall at the Mississippi Highway Department during the late 1930s. This method was further refined during World War II by the U.S. Army, due to the need for a mix design procedure for proportioning aggregate and binder to sustain heavy wheel load and high tyre pressures of military aircraft (White, 1985). The fundamental principle of the original Marshall method was to select binder content at the desired compaction density that satisfied minimum stability and flow values. The selection of optimum binder content is typically achieved by evaluating the volumetric and strength properties of asphalt specimens compacted at five different binder contents (AI, 2014).

The Marshall method is mostly applicable to the design of dense-graded HMA mixes. A key feature of the method is a Marshall hammer that is used for the compaction of asphalt specimens. The compacted asphalt specimens are then used for mix volumetric analysis, strength evaluation, as well as for the Marshall stability and flow test. Over the years, several road agencies or institutions across the world have standardised the Marshall method to suit their specific needs. In South Africa, the Marshall mix design method has been standardised in SANS 3001-AS1 (2011) and SANS 3001-AS2 (2011) test methods. The basic steps of the Marshall mix design method (SANS 3001-AS2, 2011; AI, 2014; SANS 3001-AS1, 2015) are:

- Aggregate selection (includes evaluation of the physical properties of the aggregate and selection of design gradation);
- Binder selection;
- Asphalt specimens preparation (includes mixing and compaction using Marshall hammer);
- Volumetric analysis of the compacted asphalt samples (density and air voids content);
- Evaluation of the strength of compacted asphalt specimens, and

- Optimum binder content determination.

Figure 2.2 shows the schematic Marshall hammer set-up, whereas Figure 2.3 is an illustration of the Marshall stability and flow test set-up. Figure 2.4 illustrates the process for determining stability and flow values. The stability (S) is the maximum load resistance, whereas the flow value (F) is the total deformation occurring in the specimen to the point of maximum load (SANS 3001-AS2, 2011).

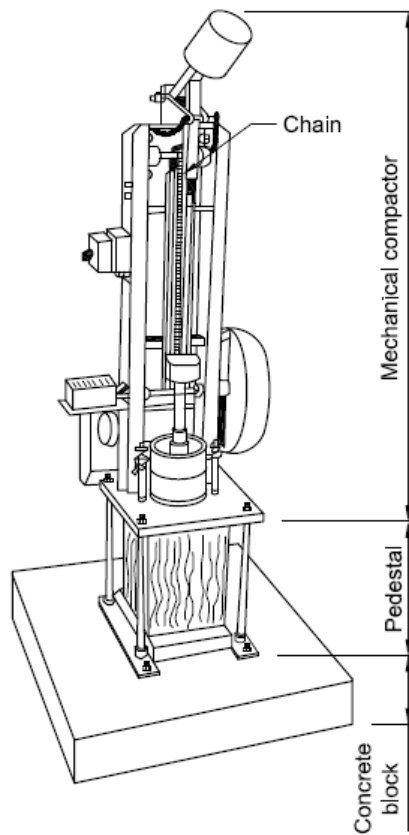
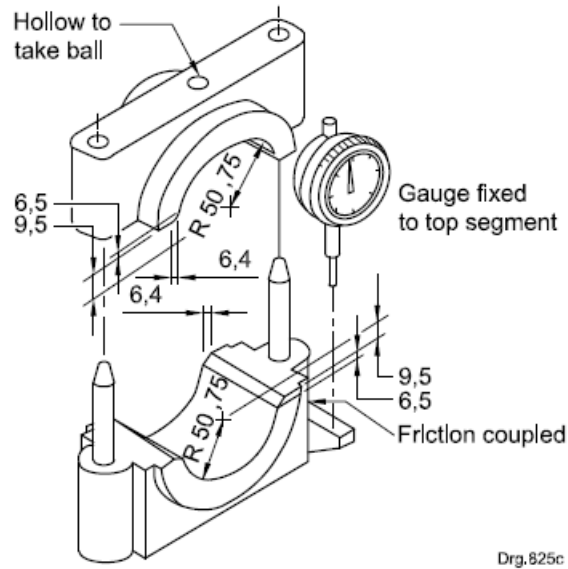


Figure 2.2: Marshall hammer set-up (SANS 3001-AS1, 2015)



R = Radius

Figure 2.3: Marshall stability and flow test set-up (SANS 3001-AS2, 2011)

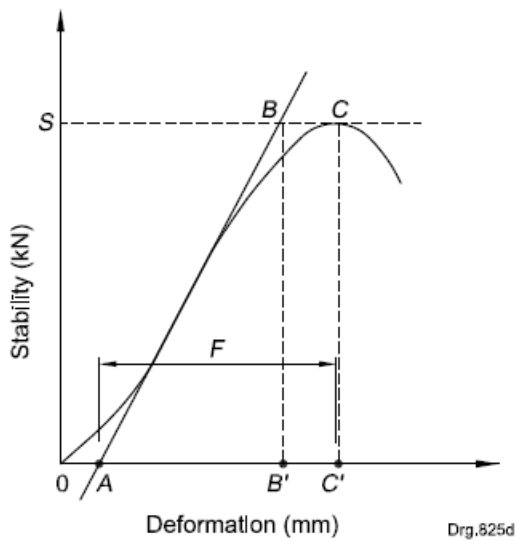


Figure 2.4: Process of determining stability and flow (SANS 3001-AS2, 2011)

2.2.2 Superpave mix design method

The Superpave mix design method is an outcome of the US Strategic Highway Research Program (SHRP) asphalt research (SHRP-A-407, 1994). The Superpave mix design system incorporates the characterisation of performance of materials and considers the performance requirements for a specific the traffic, environment (climate), as well as the structural needs of the particular pavement site (SHRP-A-407, 1994; AI, 2014). The ultimate objective of the Superpave mix

design system is to define a feasible blend of aggregates, mineral filler and binder with the following attributes (SHRP-A-407, 1994):

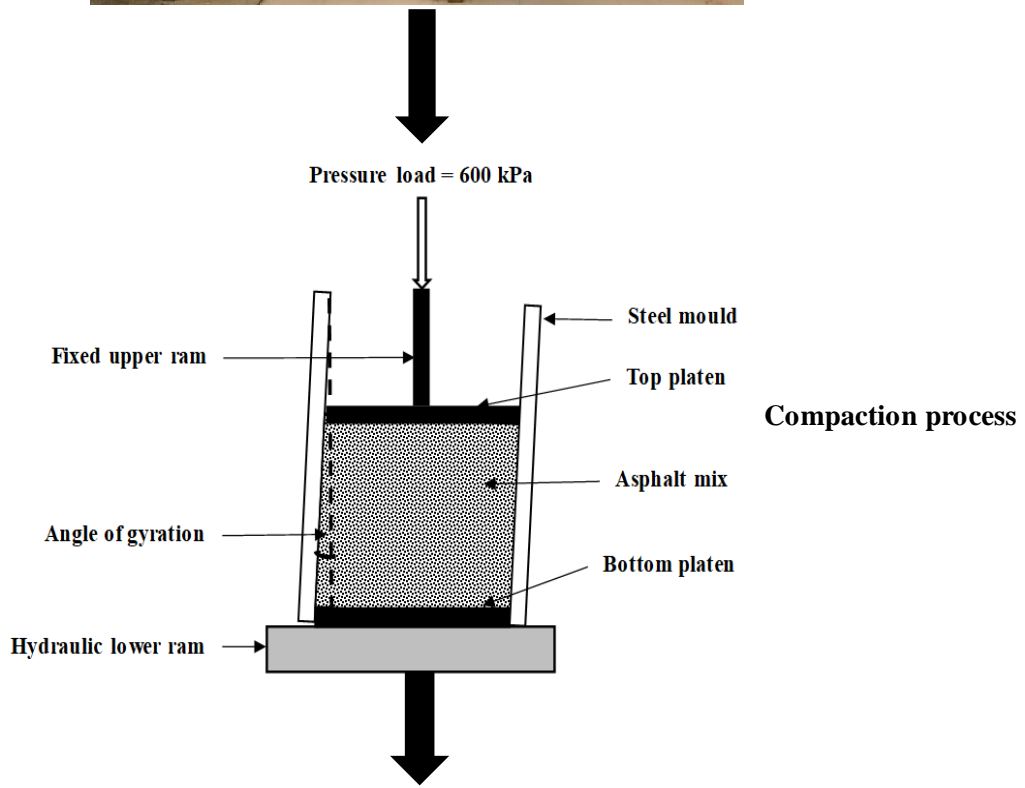
- Sufficient amount of binder that guarantees the durability of the mix;
- Sufficient air voids content and voids in the mineral aggregate;
- Compactable during paving, and
- Satisfactory performance of the asphalt pavement.

The Superpave mix design method is mostly applicable to virgin and recycled aggregate, and to dense-graded HMA mixes produced when unmodified or modified binder is used. The use of the gyratory compactor for the laboratory compaction of the HMA samples is one of the key features of the method. The HMA specimens are used for the evaluation of volumetric and performance properties, which are part of the Superpave mix design process. The Superpave gyratory is believed to improve the ability of laboratory compaction to simulate actual compaction in the field (SHRP-A-407, 1994; Austroads, 2008; FHWA, 2010; Sabita Manual 35/TRH 8, 2020).

Two types of gyratory compactors are commonly used in the asphalt industry, namely Gyropac and Servopac. A study by Oliver et al. (2000) indicated that these compactors yield asphalt samples with different volumetric characteristics, depending on the compaction mould (100 or 150 mm diameter) and mix type. Figure 2.5 shows the Servopac gyratory compactor, an illustration of the compaction process and a typical compacted HMA specimen.



Gyratory compactor



Compaction process



Compacted HMA specimen

Figure 2.5: Illustration of gyratory compaction

The Superpave mix design system represents a paradigm shift from an empirical-based approach to performance-related design and specifications. Several road authorities or institutions across the world have started to implement performance-based mix design approaches similar to the Superpave approach, with some modification to suit their specific needs and local conditions. In Europe, for example, the European standards for bituminous mixtures (EN 12697 and EN 13108) are geared towards the implementing performance-based HMA mix design procedures. In Australia and New Zealand, the Pavement Technology Guide Part 4B: Asphalt, also promotes the performance-based HMA mix design procedures (Austroads, 2014). Similarly, the recently published South African guideline for design of asphalt mixes has also adopted performance-based HMA mix design procedures (Sabita Manual 35/TRH 8, 2020).

The South African asphalt mix design procedure is based on the following key performance requirements, namely: workability (compactability), durability, stiffness, permanent deformation (rutting) resistance, fatigue cracking resistance, and reduced permeability (Sabita Manual 35/TRH 8, 2020).

The asphalt mix design process involves three design levels (I, II, and III), based on factors such as the expected traffic loading, as well as structural damage risks (Sabita Manual 35/TRH 8, 2020). The general recommendations for the application of the three design levels are provided in Figure 2.6.

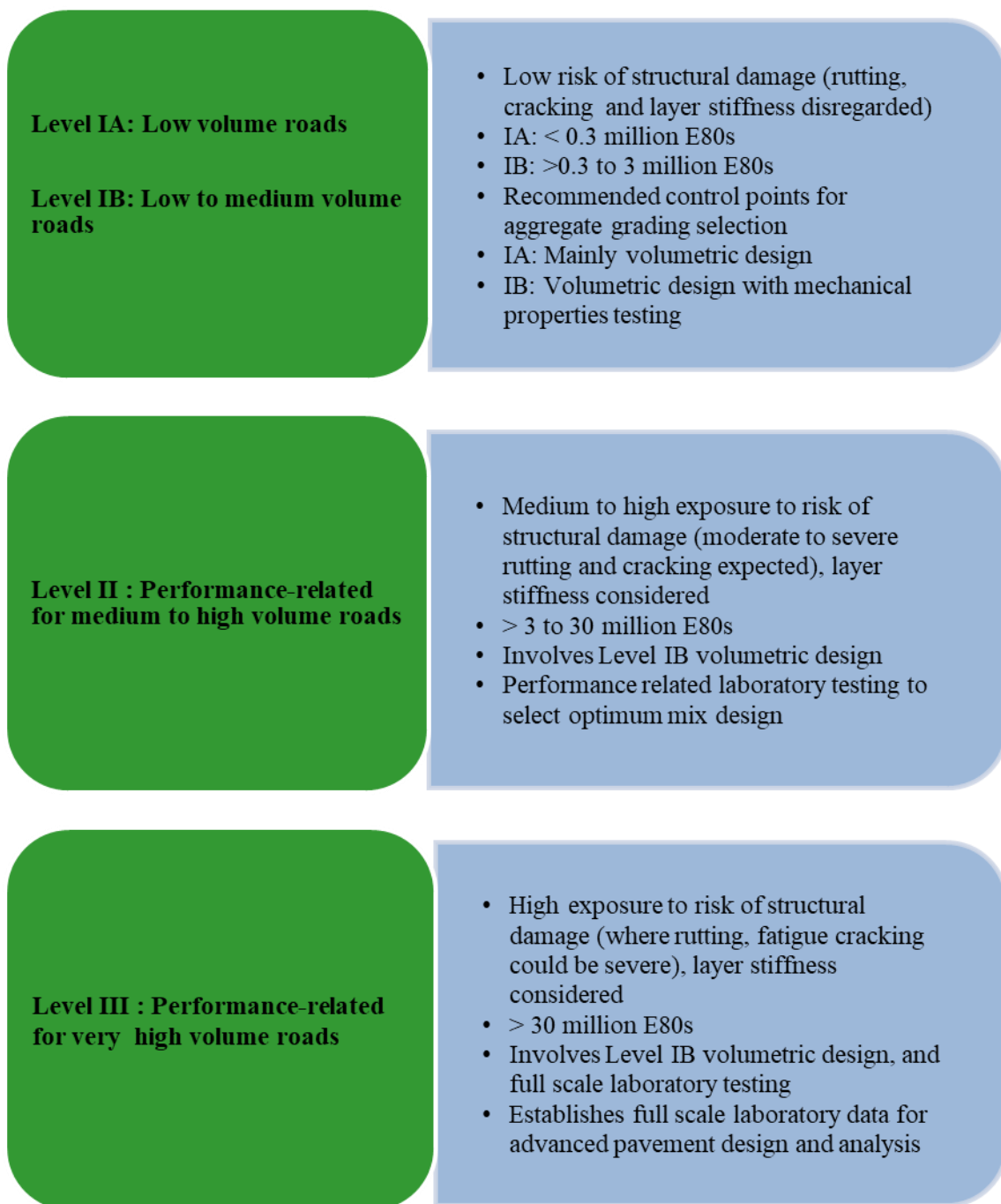


Figure 2.6: Definition of asphalt mix design levels (Sabita Manual 35/TRH 8, 2020)

Regardless of the design level, the South African mix design process involves the following basic steps (Sabita Manual 35/TRH 8, 2020):

- Selection of the type of the asphalt mix;
- Selection of the type of the bituminous binder, taking into account the climate and traffic loading situation;

- Selection of aggregates that meet the specification requirements of the project;
- Development of three trial aggregate grading blends;
- Laboratory asphalt mixing;
- Laboratory compaction of asphalt mix to a density that represents field conditions;
- Measurement of the volumetric properties of the compacted asphalt specimens;
- Mechanical testing of compacted asphalt specimens;
- Determination of the optimum mix;
- Final mix performance evaluation;
- Verification of the performance properties of plant manufactured mix, and
- Selection of job mix.

Figure 2.7 provides an outline the asphalt mix design steps for Level I, whereas the design steps for Level II and Level III are outlined in Figure 2.8. It is important to emphasize that the mix design steps for Levels II and III is essentially similar, except that additional laboratory data needs to be performed at Level III to facilitate the prediction of stiffness, rutting resistance and fatigue cracking resistance. The complete data set allows for the establishment how the mix design is related to asphalt pavement design.

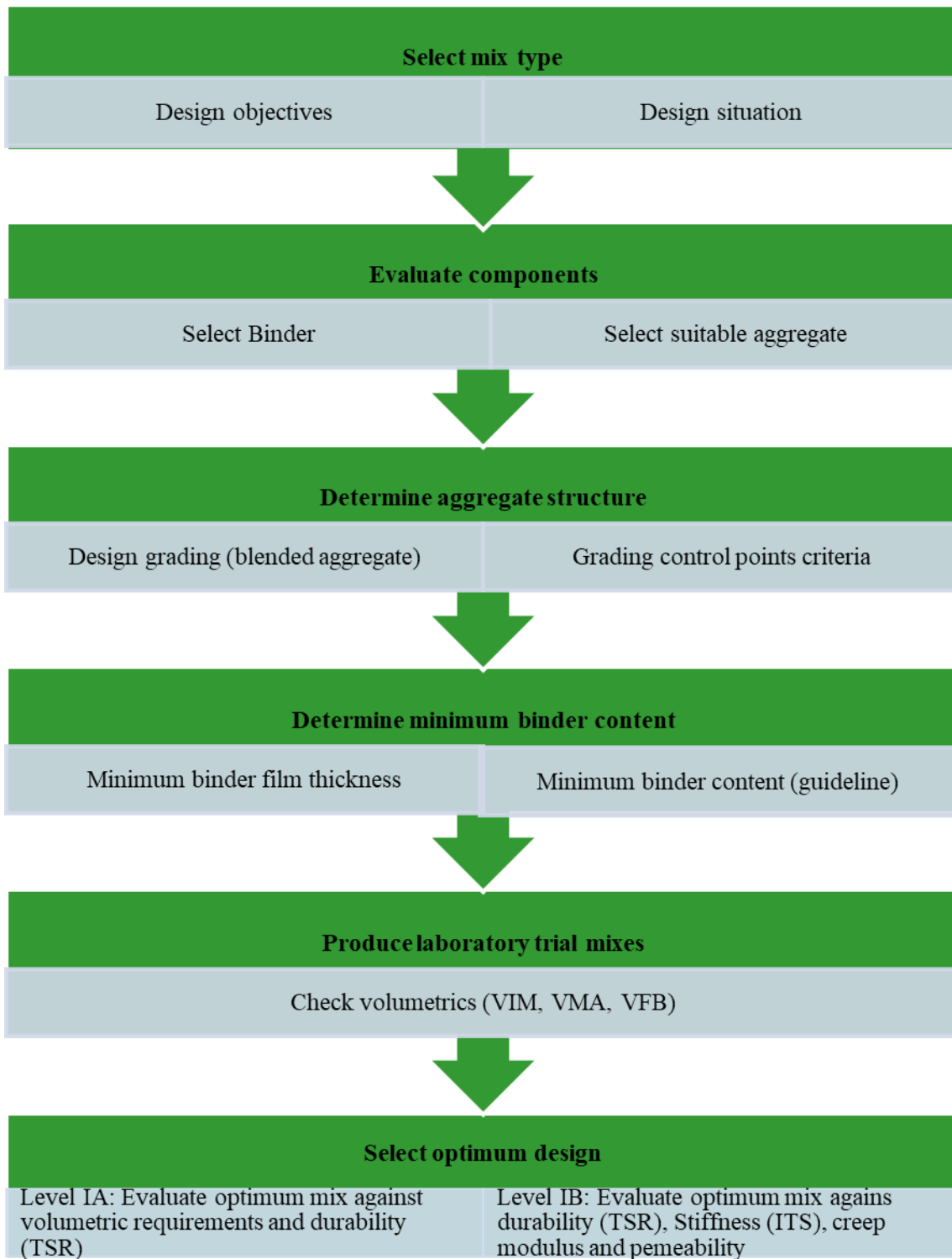


Figure 2.7: Level I mix design process (Sabita Manual 35/TRH 8, 2020)

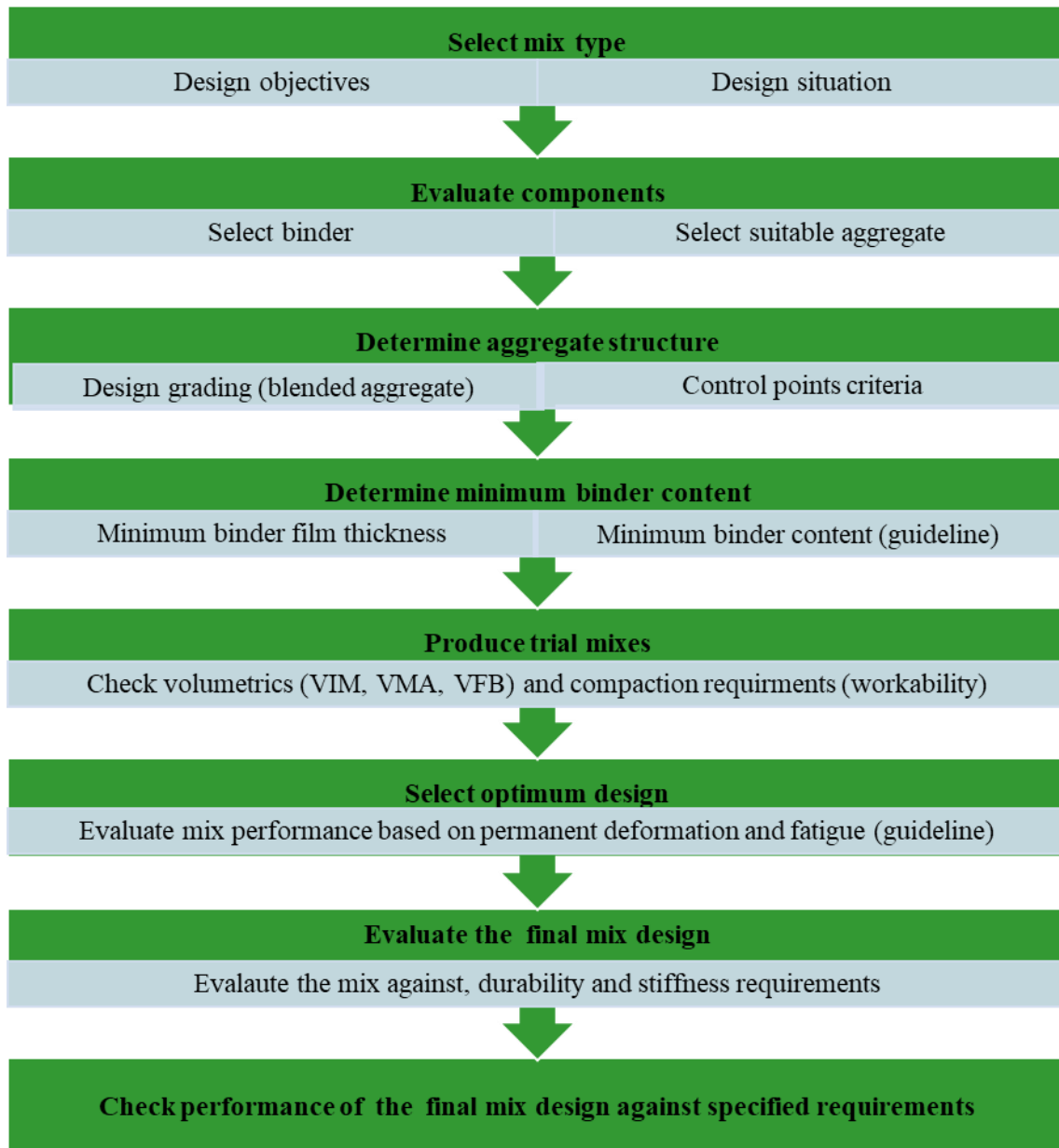


Figure 2.8: Levels II & III mix design process (Sabita Manual 35/TRH 8, 2020)

This thesis focuses primarily on HMA compaction, which is a key component of the asphalt mix design process and asphalt pavement construction. In South Africa, a gyratory compactor (see Figure 2.5) is currently used for compacting most of the cylindrical asphalt specimens required for volumetric and performance evaluation of HMA mixes. However, due to the specimens' geometrical requirements, some tests (i.e., four-point bending) are conducted on beams, which cannot be compacted using a gyratory compactor. To this end, the current South African asphalt mixes design guideline recommends the use of a roller slab compactor as an alternative method for compacting non-cylindrical specimens (Sabita Manual 35/TRH 8, 2020). Figure 2.9 shows a

slab roller compactor, an illustration of the compaction process and a typical compacted slab specimen.

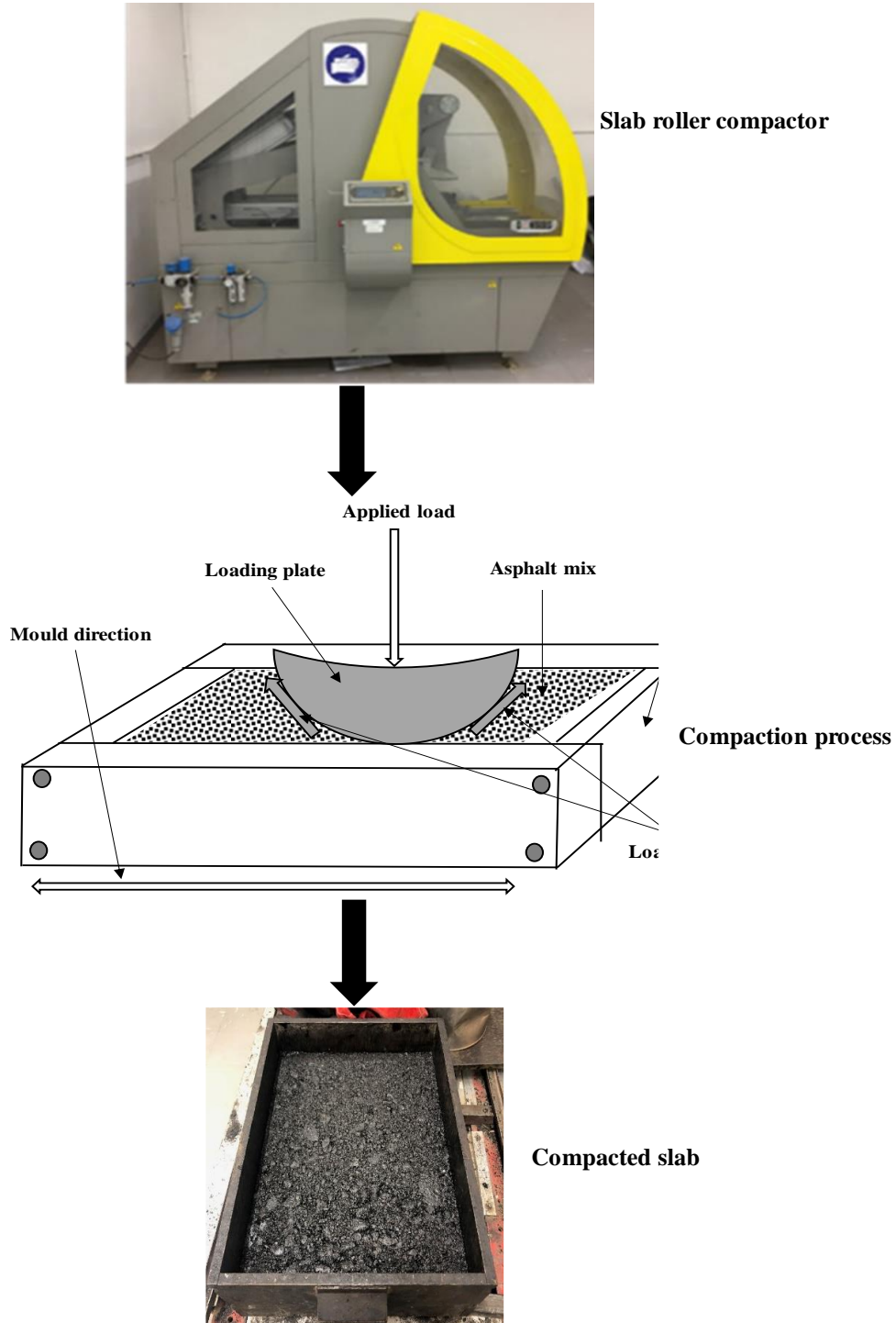


Figure 2.9: Illustration of slab roller compaction

2.3 The concept of aggregate packing analysis

Aggregates constitute a large portion of the materials used for the construction of asphalt pavements layers. As such, the performance of asphalt pavement layers inter alia depends on its aggregate characteristics. To optimise the asphalt mix design, it is essential to understand aggregate packing principles and incorporate them in the asphalt mix design process, as is recommended in the latest asphalt mix design manuals and guideline (Sabita Manual 35/TRH 8, 2020).

Over the years, several concepts and parameters to describe aggregate grading and packing characteristics were developed to facilitate the evaluation of the desired aggregate gradation and the optimum use of the available aggregate fractions. The subsequent sections discuss these aggregate packing concepts and parameters.

2.3.1 Maximum density line concept

Fuller and Thompson (1907) suggested the use of Equation 2.1 (also known as Fuller's curve), to achieve ideal packing of aggregate particles. The n value in Equation 2.1 can provide an indication of the aggregate structure. The higher the n value, the coarser the aggregate gradation, and vice versa, as illustrated in Figure 2.10. In essence, the n value can be used as one of the primary indicators of the packing characteristics of the aggregate skeleton structure.

$$P_i = \left(\frac{d_i}{D_{max}} \right)^n \quad \text{Equation 2.1}$$

Where:

n = aggregate gradation shape factor

D_{max} = the maximum aggregate size

d_i = diameter of the size

P_i = % of aggregate particles

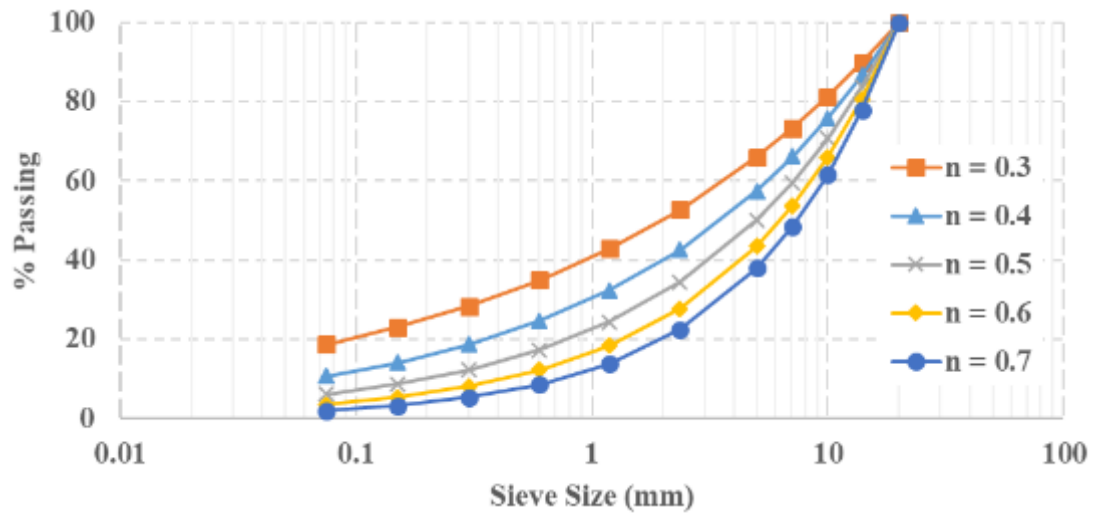


Figure 2.10: The maximum density line concept

Aggregate gradation design charts based on Fuller’s curve principle have become an important element of the evolution of the asphalt mixes design process. Roberts et al. (1996) recommended avoiding HMA mix design with gradation curves following the maximum density line to increase the VMA that allows for adequate bituminous binder that ensures the durability of the asphalt mix. In Figure 2.11, a typical gradation of the South African medium dense-graded asphalt mix with NMPS of 20 mm is plotted with the sieve size to power 0.45. It can be seen that the gradation curve deviates from the maximum density line to create sufficient space for the binder to ensure asphalt mix durability.

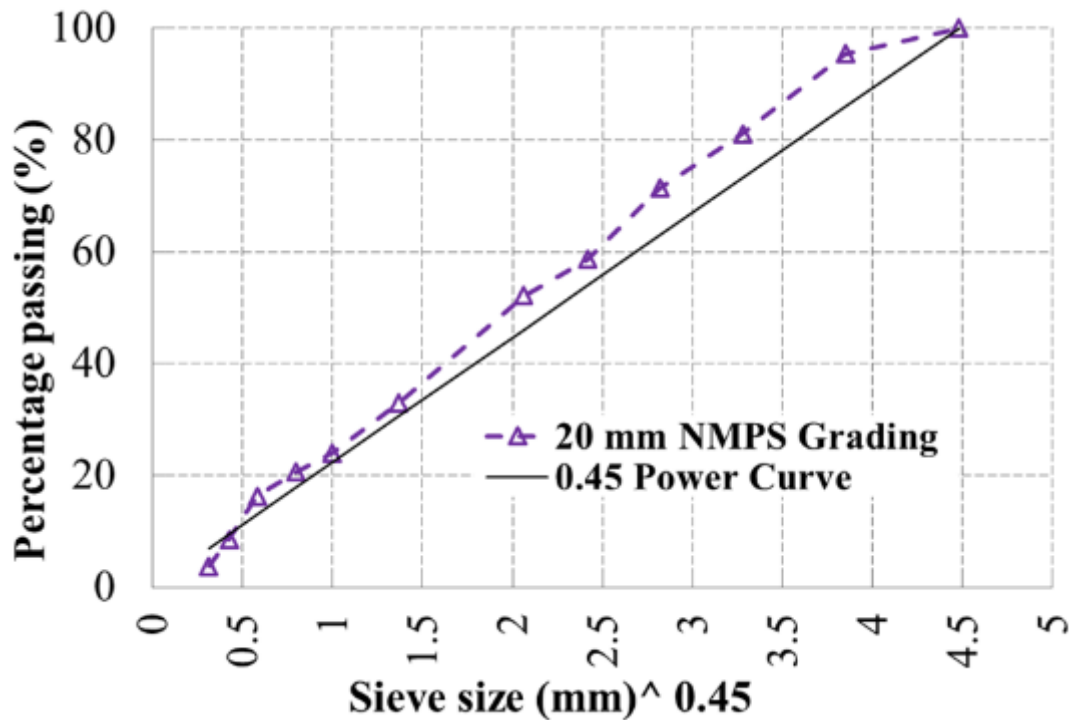


Figure 2.11: The 0.45 power gradation curve

In the past, asphalt mix design guidelines proposed restricted zones based on a 0.45 power chart to prevent the production of poor rutting resistance asphalt mixes (AI, 1996). However, follow-up studies showed that restricted zone is not related to rutting resistance of HMA mixes (Kundhal and Mallick, 2001; Chowdhury et al., 2001). However, aggregate shape and the surface texture was found to play an important role in rutting performance of asphalt mixes.

While maximum density line concept is still widely promoted in many asphalt mix design guidelines across the world, one of its limitations is the inability to relate the role of aggregate shape properties directly to the aggregate packing. The recently published South Africa asphalt mix design manual (Sabita Manual 35/TRH 8, 2020) also acknowledges the importance of aggregate packing and promotes the use of aggregate packing evaluation techniques that are based on sound aggregate packing principles.

2.3.2 Gravel-to-sand ratio

A study by Sanchez-Leal (2007) proposed aggregate grading parameter know as a gravel-to-sand ratio (G/S) that describes the packing characteristics of a specific aggregate grading. The G/S aggregate packing parameter is based on aggregate gradation shape factor (n) and the maximum size of aggregate particles (D_{max}), and is determined using Equation 2.2.

$$\frac{G}{S} = \frac{D_{max}^n - 4.75^n}{4.75^n - 0.075^n} \quad \text{Equation 2.2}$$

The G/S ratio was developed based on Fuller’s concept (Fuller & Thompson, 1907), and can be related to asphalt mix performance attributes such as workability (compactability), reduced permeability and rutting resistance. Sanchez-Leal (2007) reached the following conclusions:

- As the G/S ratio increases, the asphalt mix permeability also increases;
- The larger the G/S ratio, the greater the rutting resistance of the asphalt mix, and
- The workability asphalt mixes diminishes with an increasing G/S ratio.

It is important to point out that the standard sieve sizes as defined by the South African National Standards (SANS) were used in this study, and grading analysis was conducted in accordance with the SANS 3001-AG1 standard test method (SANS 3001-AG1, 2014). Using the SANS 3001-AG1 standard test method, the 5 mm sieve instead of 4.75 mm sieve was used. Consequently, 4.75 mm in Equation 2.2 was replaced with 5 mm for all the analyses conducted in this study.

2.3.3 The Bailey method

Detailed background and the basic principles of the Bailey method can be found in Vavrik et al. (2002). The Bailey method was originally developed as a tool for designing and adjusting aggregate proportions, taking into account the aggregate packing and its influence on the performance of HMA mixes. The method can also be used to evaluate the packing characteristics of the aggregate gradation.

The gradation curve is the basis of the Bailey method, which uses control sieves to determine ratios that provide an indication of the aggregate packing efficiency. The first control sieve is the Nominal Maximum Particle Size (NMPS), which is commonly defined as one sieve larger than the first sieve that retains more than 10% of the overall aggregate blend (AI, 1996). Other key sieve sizes are Half Sieve (HS), Primary Control Sieve (PCS), Secondary Control Sieve (SCS), and Tertiary Control Sieve (TCS) as illustrated in Figure 2.12. Starting with the NMPS, the other sieve sieved are defined in the multiples of 0.22.

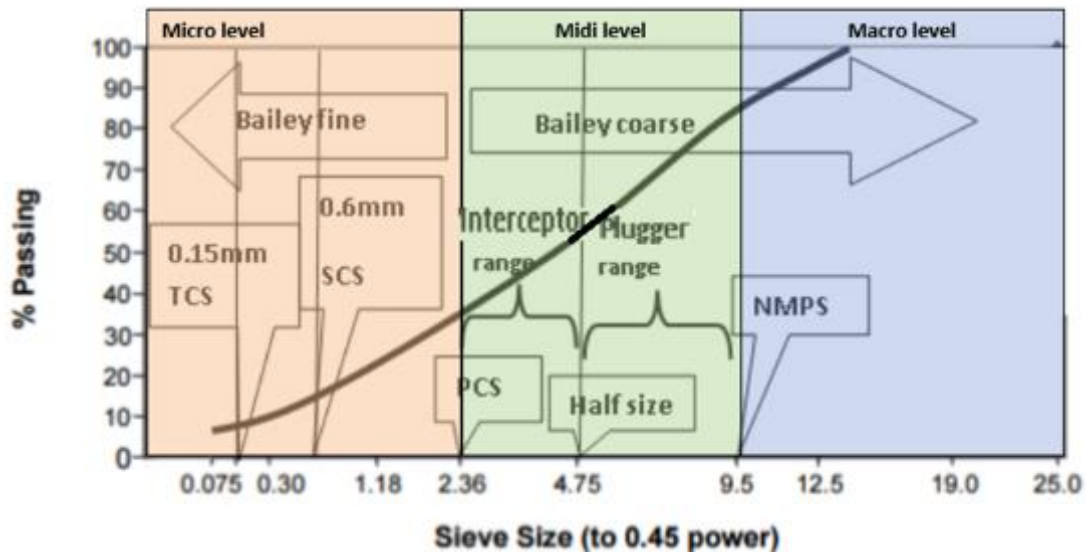


Figure 2.12: The Bailey ratios illustration (Horak & Cromhout, 2018)

Using the Bailey method, coarse and fine aggregate fractions are defined based on the PCS. Coarse aggregates are those with aggregate fractions larger than PCS, whereas fine aggregates are those with aggregate fractions smaller than PCS. The fine component of the aggregate gradation describes the micro-level skeleton of the entire aggregate structure. The coarse component is subdivided into midi and macro-level skeleton (see Figure 2.12). Three ratios determined using Equations 2.3, 2.4 and 2.5 are used to describe the micro, mid and macro-level aggregate gradation structure, respectively.

$$\text{Coarse Aggregate (CA) Ratio} = \frac{(\% \text{ passing HS} - \% \text{ passing PCS})}{100\% - \% \text{ passing HS}} \quad \text{Equation 2.3}$$

$$\text{Fine Aggregate Coarse (FA}_c\text{) Ratio} = \frac{\% \text{ Passing SCS}}{\% \text{ Passing PCS}} \quad \text{Equation 2.4}$$

$$\text{Fine Aggregate Fine (FA}_f\text{) Ratio} = \frac{\% \text{ Passing TCS}}{\% \text{ Passing SCS}} \quad \text{Equation 2.5}$$

The South African guideline document for the design of asphalt mixes (Sabita Manual 35/TRH 8, 2020) recommends a range of aggregate ratios for dense-graded mixes and SMA, which are presented in Table 2.1 and Table 2.2, respectively. It should be emphasised that the recommended range of aggregate ratios provide a starting point where no prior experience exists.

Table 2.1: Recommended ranges of aggregate ratios for dense-graded asphalt mixes (.Sabita Manual 35/TRH 8, 2020).

| NMPS (mm) | CA (coarse-graded) | New CA ratio | Coarse and fine -graded | |
|-----------|--------------------|--------------|-------------------------|-----------------|
| | | | FA _c | FA _f |
| 37.5 | 0.80 – 0.95 | 0.60 – 1.00 | 0.35 – 0.5 | 0.35 – 0.5 |
| 28 | 0.70 – 0.85 | | | |
| 20 | 0.60 – 0.75 | | | |
| 14 | 0.50 – 0.65 | | | |
| 10 | 0.40 – 0.55 | | | |
| 7.1 | 0.35 – 0.50 | | | |
| 5 | 0.30 – 0.45 | | | |

Table 2.2: Recommended ranges of aggregate ratios for SMA (Sabita Manual 35/TRH 8, 2020).

| NMPS (mm) | CA | FA _c | FA _f |
|-----------|-------------|-----------------|-----------------|
| 20 | 0.35 – 0.50 | 0.60 – 0.85 | 0.65 – 0.90 |
| 14 | 0.25 – 0.4 | 0.60 – 0.85 | 0.65 – 0.90 |
| 10 | 0.15 – 0.30 | 0.60 – 0.85 | 0.65 – 0.90 |

A study by Horak et al., (2017) suggested some revision of the traditional Bailey ratios and proposed rational Bailey ratios that incorporate aggregate packing efficiency using binary aggregate packing (BAM) concept as described by Olard (2015). The rational Bailey ratios were been formulated as the inverse of the traditional Bailey ratios (i.e., coarse/fine instead of fine/coarse) in line with the binary aggregate packing (BAP) concept. They are determined using Equations 2.6, 2.7 and 2.8.

$$CA_r = \frac{(\%100 - \%HS)}{(\%HS - \%PCS)} \quad \text{Equation 2.6}$$

$$\frac{C}{F} = \frac{(\%NMPS - \%PCS)}{(\%PCS)} \quad \text{Equation 2.7}$$

$$FA_{rmf} = \frac{(\%SCS - \%TCS)}{(\%TCS - \%Filler)} \quad \text{Equation 2.8}$$

Where:

CA_r = Rational coarse aggregate ratio;

C/F = Coarse to fine aggregate ratio, and

FA_{rmf} = Rational fine aggregate fine ratio;

HS = Half sieve;

PCS = Primary control sieve;

NMPS = Nominal maximum particle size;
 SCS = Secondary control sieve, and
 TCS = Secondary control sieve.

Horak et al. (2017) proposed rational Bailey ratios range presented in Table 2.3 to control the permeability of asphalt mixes. These ranges are believed to correlate with Dominant Aggregate Size Range (DASR) concept discussed in Section 2.3.4.

Table 2.3: Proposed permeability control criteria for rational Bailey ratios (Horak et al. (2017))

| Rational Bailey ratios | Proposed range |
|-------------------------------|-----------------------|
| CA_r | <2 |
| C/F | > 1.11 |
| FA_{rmf} | <2.7 |

2.3.4 The dominant aggregate size range

In the Bailey Method, the ratios sometimes describe two single aggregate contiguous fractions, but often a range of fractions adhering to the contiguous fractions requirement. This may therefore not adhere to the Binary Aggregate Packing (BAP) requirement of two single fraction combination. It is often a whole aggregate fraction range in combination that forms a skeleton or framework. Roque et al.'s (2006) hypothesis on the primary aggregate skeleton suggests the existence of an interactive range of particle sizes that contributes to the interlocking of aggregates. These larger stone particles interact with each other and tend to form the primary structure of the asphalt mixture that resists deformation and fracture.

The Dominant Aggregate Size Range (DASR) is defined as the interactive range of particle sizes that constitutes the dominant structural network of aggregate (primary stone skeleton). Particle sizes larger than the DASR will simply float in the DASR matrix and will not play a major role in the aggregate structure. This has clear similarities with the oversized aggregate fraction description given before for the Bailey Method.

The DASR volumetric composition for three basic aggregate grading types is illustrated conceptually in two dimensions as shown in Figure 2.13. Particles smaller than the DASR fill the voids known as the Interstitial Volume (IV) between DASR particles. The IV includes the

bitumen binder, aggregate and air voids, described as the Interstitial Components (ICs) that are found within the interstices of the DASR structure. The IC aggregates, combined with binder, form a secondary structure in the mixture to help resist deformation and fracture, and they are the primary source of adhesion and resistance to tension.

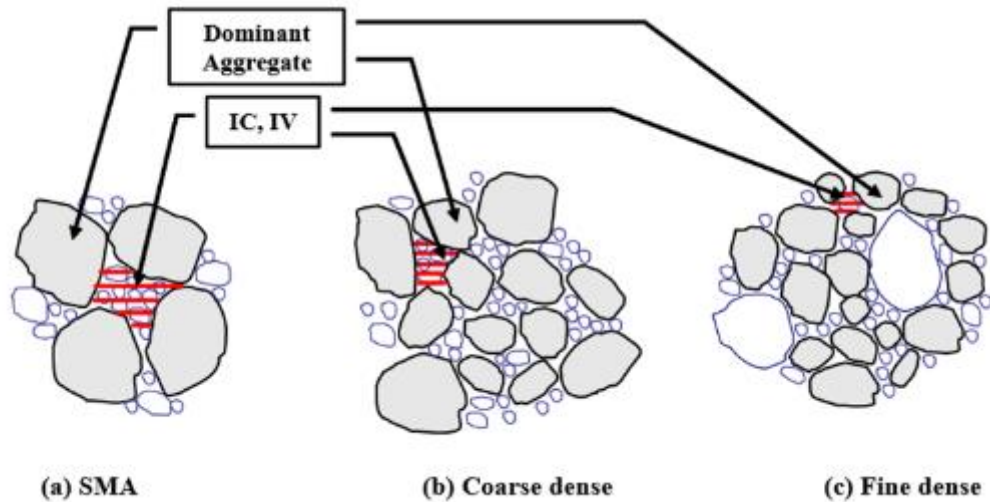


Figure 2.13: Schematic of DASR and IC concept for three basic grading types

Research by Kim et al. (2006) indicates that porosity can be used as a criterion to ensure contact between DASR particles within the asphalt mixture and to provide adequate interlocking and resistance to deformation and fracture. The actual volumetric relationships are illustrated in Figure 2.14. The Voids in the Mineral Aggregate (VMA) (see Equation 2.10) of asphalt mixtures is a well-known concept used in asphalt technology. VMA indicates the volume of available space between aggregates in a compacted mixture. In the case of asphalt, the VMA also includes the bitumen binder volume. Porosity can be calculated for any DASR by assuming that a mixture has a certain effective bitumen content and air voids (i.e. VMA) for a given gradation, and can be determined using Equation 2.11.

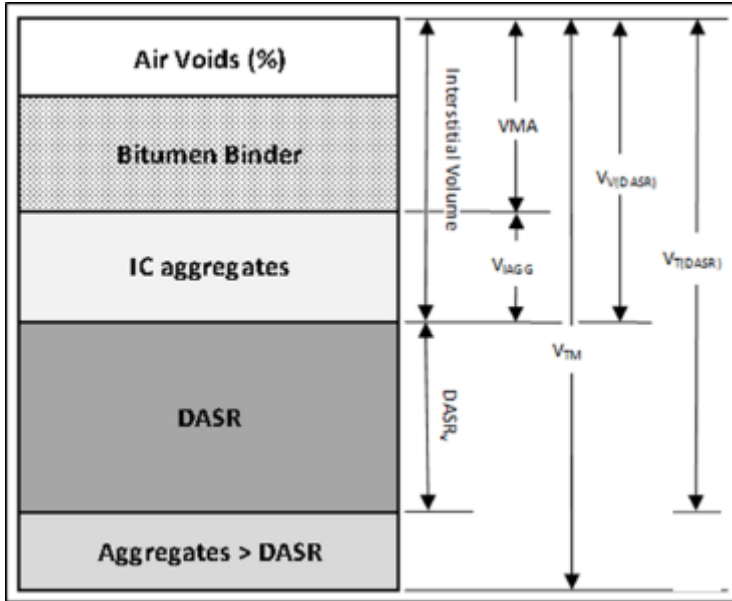


Figure 2.14: Asphalt mixture components or phases

$$VMA = V_{TM} - V_{AGG} \quad \text{Equation 2.9}$$

$$\eta_{DASR} = \frac{V_{V(DASR)}}{V_{T(DASR)}} = \frac{V_{ICAGG} + VMA}{V_{TM} - V_{AGG} > DASR} \quad \text{Equation 2.10}$$

Where:

η_{DASR} = DASR porosity

$V_{Interstitial\ volume}$ = volume of IC aggregate particles, including VMA

$V_{AGG > DASR}$ = volume of aggregate particles larger than DASR

V_{TM} = total volume of asphalt mixture

$V_{T(DASR)}$ = total volume of DASR aggregate particles

$v_{V(DASR)}$ = air voids volume

V_{ICAGG} = volume of IC aggregate particles

Denneman et al. (2007) simplified the DASR porosity determination for one or two fractions using Equation 2.12.

$$\eta_{(4.75-2.36)} = \frac{\left[\left(\frac{PP_{2.36}}{100} \right) (V_{TM} - VMA) + VMA \right]}{\left[\left(\frac{PP_{4.75}}{100} \right) (V_{TM} - VMA) + VMA \right]} \quad \text{Equation 2.11}$$

Where:

$\eta_{(4.75-2.36)}$ = aggregate fraction porosity (passing 4.75 mm sieve, but retained on 2.36 mm sieve)

$PP_{2.36}$ = % aggregate particles passing 2.36 mm sieve

$PP_{4.75}$ = % aggregate particles passing 4.75 mm sieve

Similar to the rational Bailey ratios discussed in Section 2.3.3, Horak et al. (2017) proposed a range of DASR descriptors presented in Table 2.4 to control the permeability of asphalt mixes.

Table 2.4: Proposed permeability control criteria for DASR descriptors (Horak et al. (2017))

| Skeleton level | DASR descriptor | Proposed range |
|-----------------------|------------------------|-----------------------|
| Macro | Large Aggregate | >0.65 |
| Midi | Coarse of fines | < 0.65 |
| Micro | Fine to filler | <0.60 |

2.3.5 Aggregate packing models

Researchers in the field of concrete and asphalt mix design agree that near-maximum packing density is usually optimum for strength and durability. There is a strong link between optimised grading and packing density, and in the case of concrete mixes, workability is clearly influenced (Loseby, 2014). This optimum packing objective is the same for asphalt mixtures, but differs in the sense that the cement paste is replaced with the thermoplastic influence of the bitumen binder mastic component.

Various particle packing models are available and can be used as a tool to either estimate packing density or determine the required volume fractions of different particle sizes to achieve a particular packing density. A classification of the packing models developed by a variety of researchers is summarised in Figure 2.15 and distinguishes between the two main groups – discrete and continuous models. Discrete models describe a particle size distribution consisting of particles of specific different size classes, resulting in a gap between consecutive particle sizes. Continuous models are based on a particle size distribution that contains particles of all possible sizes within the given range.

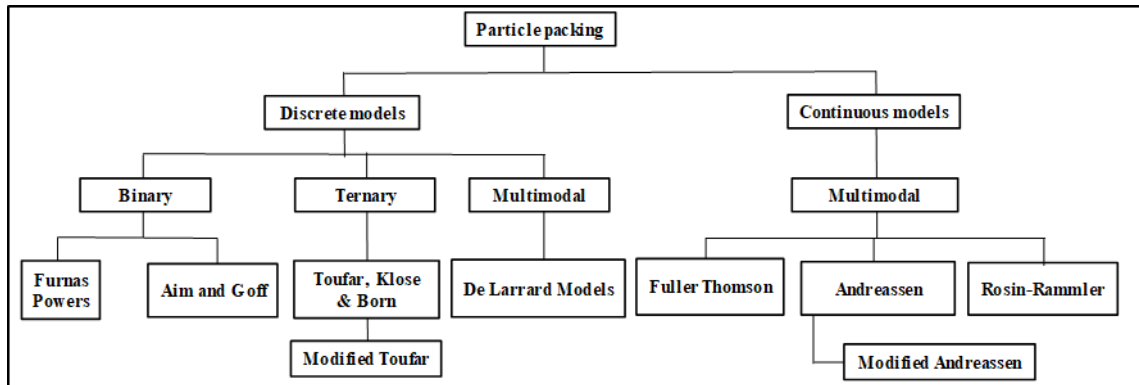


Figure 2.15: Classification of existing particle packing models (Loseby, 2014)

Optimisation of aggregate packing is an essential part of ensuring the performance of asphalt mixes. Packing density (d), which is defined by using Equation 2.12, is one of the key concepts in the analysis of aggregate packing. Aggregate packing density is affected by several parameters, including particle size distribution (grading) and aggregate shape properties (i.e. form, angularity and surface texture).

$$d = \frac{V_s}{V_T} \quad \text{Equation 2.12}$$

Where:

V_s = the volume of aggregate content in a container of known volume

V_T = the total volume of the content of the container

2.4 Compaction of HMA

2.4.1 Laboratory compaction

The primary goal of laboratory HMA compaction is to fabricate asphalt specimens for the characterisation of HMA volumetric and mechanical properties. Several types of devices that are available for use in the laboratory compaction of asphalt specimens include the Marshall Impact Compactor (hammer), California Kneading Compactor, Gyrotory Compactor, Roller Compactor and Vibratory Compactor (Roberts et al., 1996; Austroads, 2014; AI, 2014; Sabita Manual 35/TRH 8, 2020). These devices often differ in terms of how the compaction load is applied (impact, kneading, vibration load, or a combination of all three) and the geometry of the compacted specimens (cylindrical or rectangular).

During the asphalt mix design, the choice of the compaction device is often guided by the mix design method employed. For instance, the Marshall asphalt mix design methods make use of the Marshall Impact Compactor, whereas the Gyratory Compactor is used in the Superpave asphalt mix design method (AI, 2014; Austroads, 2014; Sabita Manual 35/TRH 8, 2020). The choice of a compaction device also depends on the geometry (cylindrical, trapezoidal or rectangular) of the specimen required for a specific test. In South Africa, for example, mix volumetric properties and mechanical properties such as stiffness and permanent deformation are evaluated by making use of cylindrical specimens fabricated with a gyratory compactor. On the other hand, the four-point beam fatigue test makes use of rectangular beam specimens fabricated using a roller slab compactor (Sabita Manual 35/TRH 8, 2020).

Ideally, the laboratory compaction method should reflect the field compaction. Unfortunately, most of the available laboratory compaction devices have some limitation in terms of simulating the field compaction. This is primarily because asphalt compaction is a complicated process, in which the reorientation and interlock of aggregates take place. To this end, it is important to recognise that different compaction devices may produce asphalt specimens with different engineering properties.

A study by Khan et al. (1998) compared different laboratory and field compaction methods. The selected laboratory compaction methods were Marshall Automatic Compactor, Marshall Manual Compactor, California Kneading Compactor and Gyratory Shear Compactor. It was concluded that the Gyratory Shear Compactor most closely represented the engineering properties of the field cores. Several other studies also demonstrated that most of the available laboratory compaction methods are not capable of producing asphalt specimens with a homogenous internal structure, particularly concerning air voids distribution and the arrangement of aggregate particles (Masad et al., 1999; Partl et al., 2007; Walubita et al., 2012; Komba et al., 2019a). This may influence the engineering properties of the compacted asphalt specimens.

2.4.2 Field compaction

Field compaction is a process of compressing HMA to achieve good interlock of aggregate particles and reduce air voids to an acceptable level. Compaction enables the HMA layer to achieve the following (Kennedy et al., 1984; Kandhal & Koehler, 1984; Sabita, 2008; FAA, 2013):

- Develop strength and achieve stability of the HMA layer;
- Provide resistance against rutting and fatigue cracking;
- Reduce the permeability of the asphalt layer;
- Reduce moisture damage, and
- Prevent HMA from oxidative hardening (ageing).

Thus, achieving adequate field compaction is an essential aspect of the construction of HMA to ensure satisfactory performance of pavement. Dense-graded asphalt mixes should ideally be compacted to 6 to 7% of air voids content, and should not fall below 3% (Linden et al., 1989; Roberts et al., 1996). The work by Linden et al. (1989) suggests that for dense-graded HMA mixes, a 1% air voids content increase above the 6 to 7% range – due to poor compaction – could shorten the service life of the HMA pavement layer by approximately 10%.

Field HMA compaction is commonly undertaken using steel wheel rollers (static or vibratory) and pneumatic tyre rollers. The compaction is usually accomplished in a three-stage rolling sequence to ensure that the designed compaction density is achieved. A specific roller type is usually preferred for each compaction stage, as described below (Sabita, 2008; FAA, 2013).

- **Breakdown rolling:** Takes place immediately behind the paver where the mat temperature is highest. Most of the compaction is achieved in this phase, resulting in a density increase up to approximately 91% of Maximum Void-less Density (MVD). Steel wheel vibratory rollers are generally preferred for the breakdown rolling compaction stage.
- **Intermediate rolling:** This stage follows directly after breakdown rolling, and should continue until the required density (typically 93% of MVD) is achieved. Due to their kneading action, pneumatic tyre rollers are most preferred for the intermediate compaction stage.
- **Finish rolling:** This is the final stage in which the irregularities in the surface are smoothed over to remove roller marks. Steel wheel static rollers are generally preferred for the finishing rolling compaction stage, because they produce a smooth surface.

Figure 2.16 shows a typical HMA compaction sequence, also referred to as a compaction train.

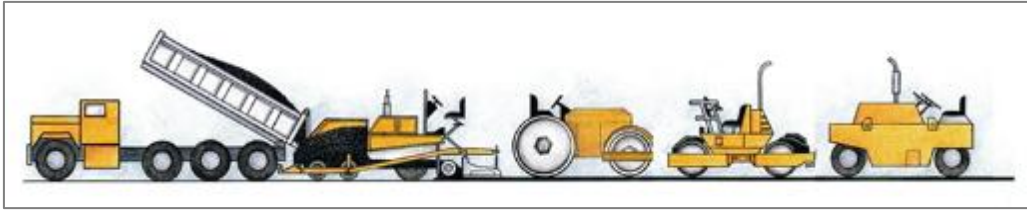


Figure 2.16: Compaction train (Sabita, 2008)

Compaction quality control is an important aspect of HMA compaction. During field HMA compaction, the achieved compaction density after a specific number of roller passes is constantly monitored by using portable devices such as a nuclear density gauge (see Figure 2.17). Temperature is another parameter to be monitored during HMA compaction, as it significantly influences the compactability of the HMA. As the HMA temperature decreases, the more effort required to compact the asphalt mix.

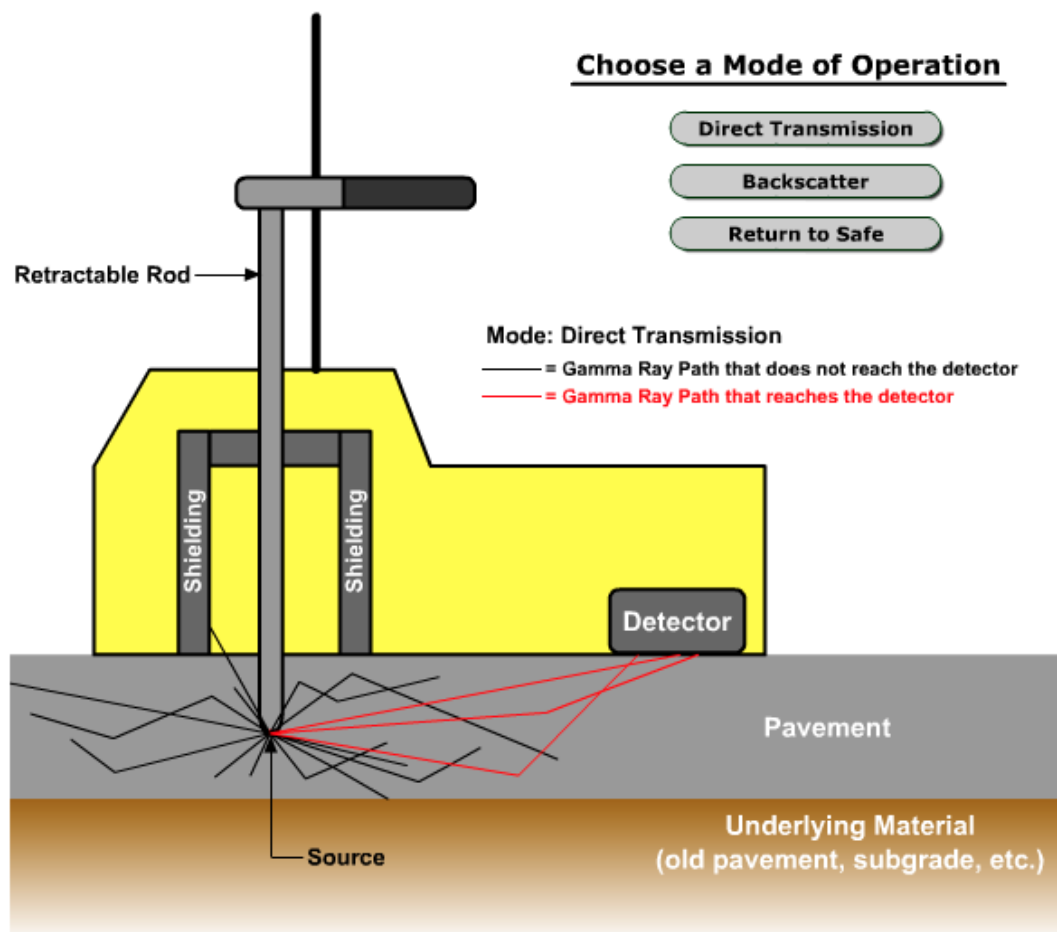


Figure 2.17: Nuclear density gauge (Pavement Interactive, 2021)

A limitation of the conventional roller compactors is that roller operators do not receive feedback on what is happening to the HMA material during compaction. To achieve the desired compaction levels, the roller operators often rely on pre-established roller patterns and using density measured at spot locations. To address this challenge, Intelligent Compaction (IC) technology that equips the conventional rollers with instruments to monitor asphalt mix compaction in real-time is increasingly being deployed (Gallivan et al., 2011; Xu & Chang, 2013; FHWA, 2014). Figure 2.18 presents a schematic illustration of the Intelligent Compaction roller.

While the use of the IC roller is promising to be useful for achieving the target level of asphalt compaction, some studies report that the final intelligent compaction measurement values do not correlate well with the densities of HMA field cores (Leyland, 2014; FHWA, 2014).



Figure 2.18: Functioning of Intelligent Compaction roller (FHWA, 2014)

2.4.3 Measurement of compaction

Laboratory determination of volumetric properties of asphalt samples is a fundamental component of asphalt mix design and construction. The quality of compacted HMA is often evaluated in terms of volumetric properties, which are determined by measuring the mass and volume of the HMA mix and its constituent components (i.e., aggregate, binder and air).

To facilitate determination of the volumetric properties, it is helpful to represent the compacted HMA in terms of a so-called phase diagram (AI, 2014; Sabita Manual 35/TRH 8, 2020). The phase diagram breaks down the compacted HMA into its key components (air, effective binder, absorbed binder and aggregate) as illustrated in Figure 2.19.

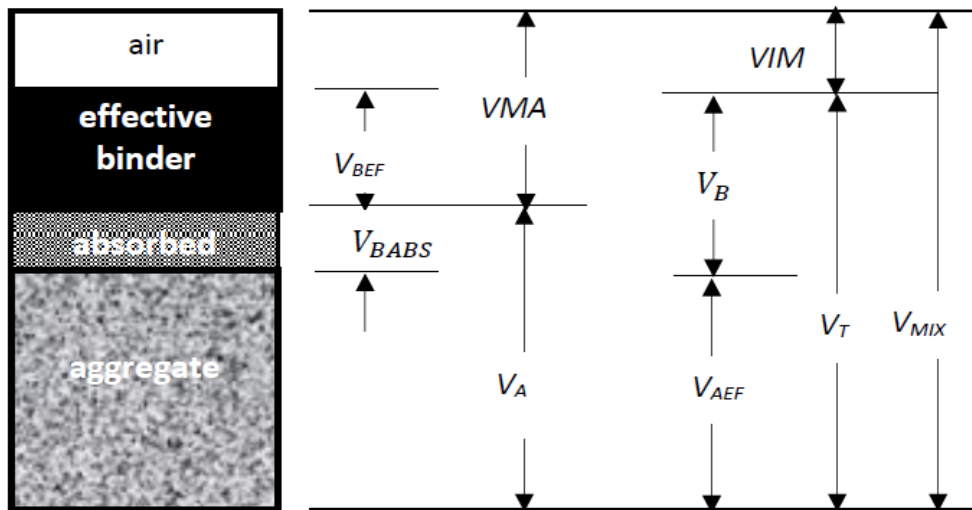


Figure 2.19: Compacted HMA phase diagram (Sabita Manual 35/TRH 8, 2020)

Where:

V_{IM} = volume of air voids

V_{MA} = volume of voids in mineral aggregate

V_B = total volume of binder within the asphalt mixture

V_{BABS} = the volume of the binder absorbed by the aggregate particles pores

V_{BEF} = the effective volume of the binder

V_A = the volume of aggregate particles

V_{AEF} = the effective volume of aggregate particles

V_T = the total binder and aggregate volume

V_{MIX} = volume of compacted asphalt sample

During the HMA compaction process the volume of air is reduced. Hence, air voids content is an asphalt mix property of interest that is usually expressed as the percentage of voids to the total volume. In order to calculate the air voids content of the compacted asphalt specimen, both the Bulk Density (BD) and Maximum Void-less Density (MVD) of the asphalt need to be measured.

The saturated-surface-dry (SSD) method (SANS 3001-AS10, 2011) is one of the widely used approaches for determining the bulk density of compacted asphalt samples. It is most suited for the determination of density of impermeable dense-graded asphalt mixes. To calculate the air voids content of the compacted HMA, the MVD also needs to be determined. The South African standard procedure for determining the MVD is described in SANS 3001-AS11. Both, the bulk density and MVD are required for determination of the air voids content of compacted asphalt samples.

One of the limitations of the SSD method is its inability to accurately determine the density of permeable HMA specimens with interconnected voids. To this end, the vacuum-sealing approach (see Figure 2.20) is preferred to determine the bulk density of permeable asphalt specimens such as porous asphalt mixes (Crouch et al., 2002; Williams et al., 2007). The detailed procedure is described in ASTM D 6752 (2004).



Figure 2.20: Set-up for vacuum-sealing method

Another approach of determining the air voids content of the compacted asphalt samples is using advanced technologies such as X-ray Computed Tomography (X-ray CT) scanning (Masad et al., 1999; Masad, 2004; Walubita et al., 2012). This approach can also be used to determine the size and of the air voids distribution (Partl et al., 2007). However, the approach is not a practical routed application and is thus limited currently to research studies.

2.5 Assessing HMA compactability using a gyratory compactor

One of the critical aspects of HMA mix design is to ensure that the mix can easily be compacted in the field. The energy needed to achieve a specific density or percentage of air voids contents is commonly referred to as the compactability of the HMA mix. HMA compactability is believed to be related to the characteristics of the gyratory compaction densification curve.

Previous research studies proposed several approaches towards the analysis of gyratory compaction data to determine parameters that describe the compactability of HMA mixes (Bahia et al., 1998; Awed et al., 2015; Komba et al., 2019a). The next sections provide a brief description of the HMA compactability parameters that can be computed from gyratory compaction basic output data.

2.5.1 Locking point concept

During gyratory compaction, the aggregate particles are squeezed together. Subsequently, these particles start to develop an interlocked structure and resist further compaction. The locking point is defined as the number of gyrations at which aggregate particles start to resist compaction.

Previous research proposed different ways of defining the locking point. Vavrik et al. (1999) defined the locking point as the first of three consecutive gyrations that yield the same HMA specimen height, where these gyrations follow two sets of gyrations that have the same height (see Table 2.5).

Table 2.5: Definition of Superpave gyratory compactor locking point using HMA specimen height (Vavrik et al., 1999)

| | 1 | 2 | 3 | 4 | 5 | 6 | 7 | 8 | 9 | 10 |
|-----|--------------|--------------|-------|-------|----------------------------------|--------------|--------------|-------|-------|-------|
| 80 | 111.9 | 111.9 | 111.8 | 111.8 | 111.7 | 111.7 | 111.6 | 111.6 | 111.5 | 111.5 |
| 90 | 111.4 | 111.4 | 111.3 | 111.3 | <i>111.2^{LP}</i> | 111.2 | 111.2 | 111.1 | 111.1 | 111.0 |
| 100 | 111.0 | 110.9 | 110.9 | 110.8 | 110.8 | 110.8 | 110.7 | 110.7 | 110.7 | 110.6 |

Alshamsi (2006) defined the gyratory compaction locking point as the number of gyrations at which three consecutive gyrations do not change the HMA specimen height by more than 0.05 mm (see Table 2.6).

Table 2.6: Definition of locking point (Alshamsi, 2006)

| Number of Gyration | Rate of Change | |
|--------------------|----------------|---------------|
| 61 | 0.07 | |
| 62 | 0.06 | |
| 63 | 0.08 | |
| 64 | 0.07 | |
| 65 | 0.06 | |
| 66 | 0.07 | |
| 67 | 0.07 | |
| 68 | 0.06 | |
| 69 | 0.06 | |
| 70 | 0.05 | Locking Point |
| 71 | 0.05 | |
| 72 | 0.05 | |
| 73 | 0.05 | |
| 74 | 0.05 | |

Leiva and West (2008) defined the locking point in three different ways:

- **Locking point 2-1:** defined as the first occurrence of two consecutive gyrations yielding the same height of the sample;
- **Locking point 2-2:** defined as the second occurrence of two consecutive gyrations yielding the same height of the sample, and
- **Locking point 2-3:** defined as the third occurrence of two consecutive gyrations giving the same height of sample.

Generally, a higher locking point is an indication that the mixture requires more effort to compact. The locking point concept can help asphalt mix designers preclude overcompaction of HMA mixtures and minimise the possibility of breaking aggregate particles during compaction.

2.5.2 The compaction energy index

The compaction energy index (CEI) is defined as the area under the gyratory compaction densification curve from the 8th gyration to 92% compaction (Bahia et al., 1998) (see Figure 2.21). The CEI indicates the ease of laying of the mixture during construction. HMA mixes with lower CEI values are desirably less difficult to compact (Awed et al., 2015). HMA mixes with CEI closer to zero are classified as tender mixes.

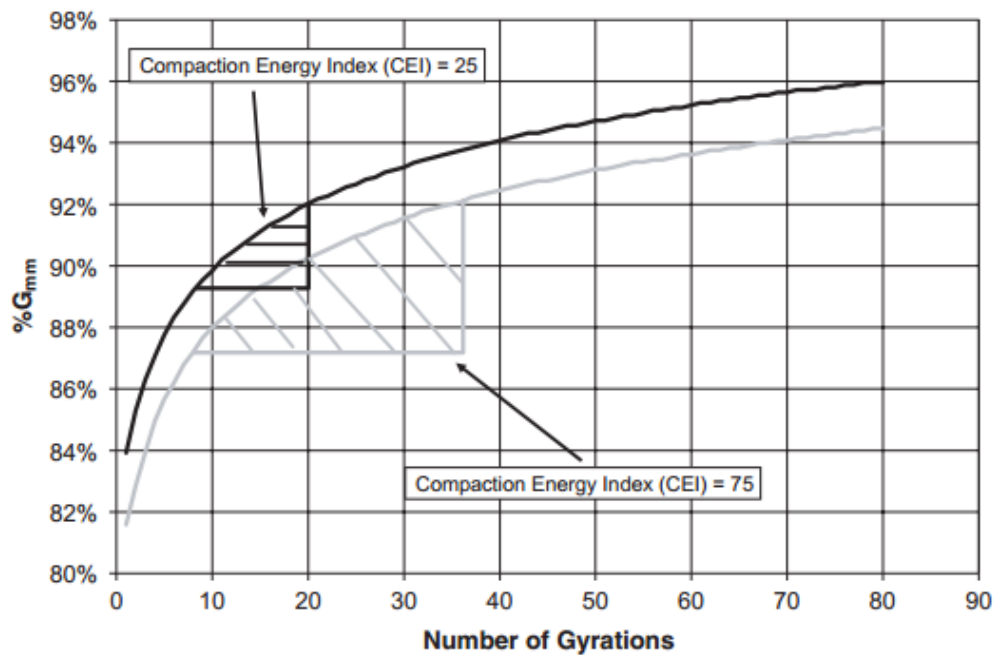


Figure 2.21: The compaction energy index (CEI) (Leiva & West, 2008)

2.5.3 The compaction and traffic densification indices

The compaction densification index (CDI) is defined as the area under the gyratory compaction densification curve from the first gyration to the Superpave Gyratory Compactor (SGC) locking point (Alshamsi, 2006) (see Figure 2.22). Generally, the higher the CDI, the more difficult the mix is to compact during construction.

The traffic densification index (TDI) is defined as the area under the gyratory compaction densification curve from 92% to 98% compaction (Awed et al., 2015) (see also Figure 2.22). High TDI values suggest more resistance to densification under traffic loads and better mixture stability. It should be pointed out that in practice, certain mixes cannot easily be compacted to 98%. Therefore, a new traffic densification index (TDI₃₀₀) was proposed by Komba et al. (2019a), and is defined as the area under the densification curve from 92% to 300 gradations.

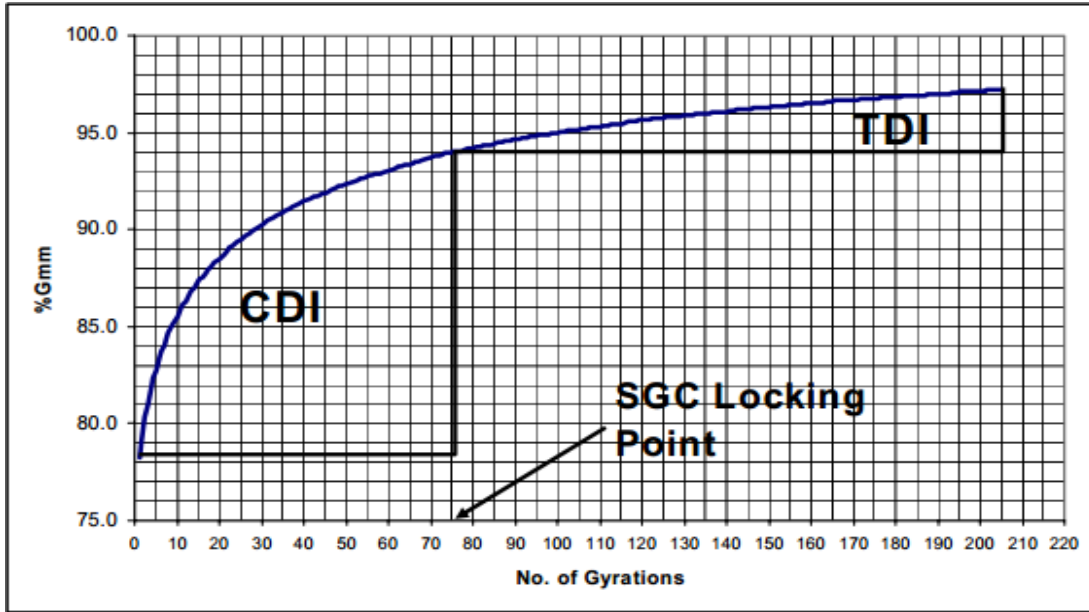


Figure 2.22: CDI and TDI determination (Alshamsi, 2006)

2.5.4 Compaction slope

The gyratory compaction slope (CS) is calculated using Equation 2.13 (Wang et al., 2000). Thus, CS is essentially used to determine the rate at which the asphalt compaction is changing.

$$CS = \frac{\% \text{ compaction at } N_{max} - \% \text{ compaction at } N_{initial}}{\log(N_{max}) - \log(N_{initial})} \quad \text{Equation 2.13}$$

Where:

$N_{initial}$ = the number of gyrations at initial of the compaction

N_{max} = the number of gyrations at the end of the asphalt compaction

2.6 Factors influencing HMA compaction

HMA compaction is affected by several factors ranging from environmental factors (i.e., temperature and wind speed) to mix specific parameters such as grading, aggregate size, aggregate shape properties, binder type and binder content. Construction-related factors such as lift thickness, foundation support, roller type and operation (i.e., speed and number of passes) also affect the field compactability of HMA. The most critical factors affecting HMA compactability in the laboratory environment are briefly discussed in the sections that follow.

2.6.1 Temperature

HMA temperature has a direct effect on binder viscosity, which in turn influences compaction. At elevated temperatures, HMA mixes exhibit high compactability due to low binder viscosity. On the other hand, as the temperature of the HMA decreases, its binder becomes more viscous and resistant to deformation, which results in a smaller reduction in air voids at a given compaction load or effort and causes difficulty in achieving the required compaction density (FAA, 2013).

For unmodified binders, the temperature-viscosity relationship (see Figure 2.23) is often used to guide the selection of HMA mixing and compaction temperatures. Typically, the mixing and compaction temperatures should correspond with binder viscosities of approximately 0.17 ± 0.02 Pa.s and 0.28 ± 0.03 Pa.s respectively (ASTM D 2493, 2001). It should however be pointed out that modified binders are sensitive to shear rate; hence the standard ASTM D 2493 method often yields unreasonably high mixing and compaction temperatures (Bahia et al., 1998; TRB, 2006). To address this challenge, several researchers proposed alternative approaches for determining mixing and compaction temperatures of HMA produced by using modified binders (Yildirim et al., 2000; TRB, 2006; Mturi et al., 2013; Qasim et al., 2019).

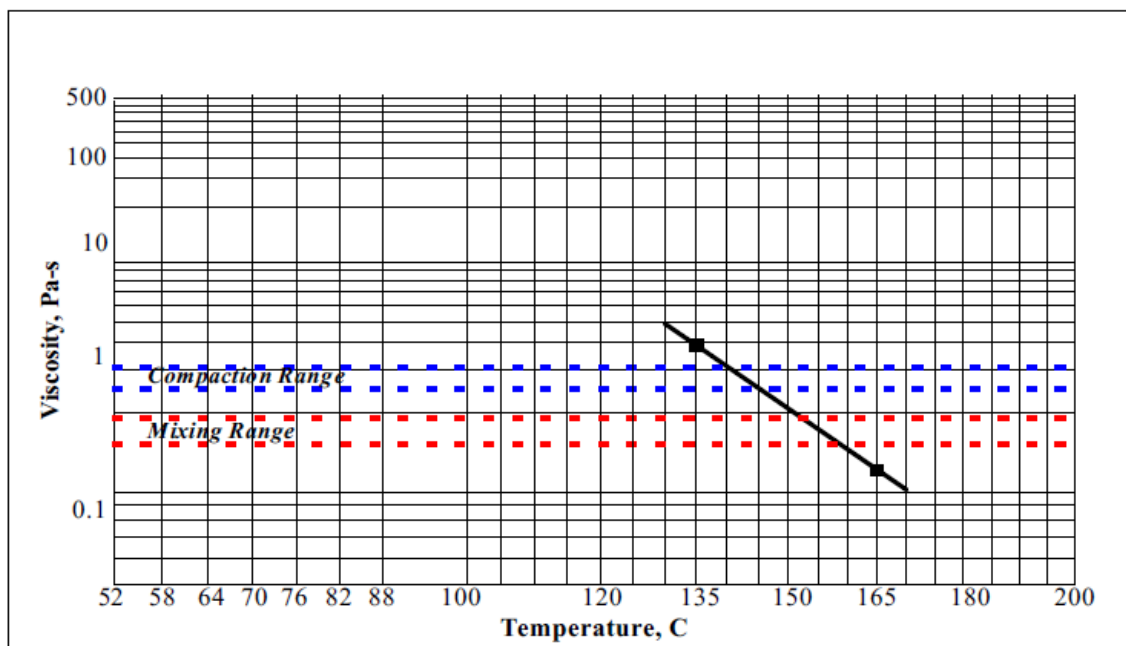


Figure 2.23: Typical binder temperature-viscosity chart (ASTM D 2493, 2001)

2.6.2 Binder type

Binder type or grade influences the compactability of HMA, primarily through its viscosity property. A binder that has higher viscosity will generally yield a stiff HMA mix at a given temperature, which in turn will require a greater compaction effort to achieve the required density. Binder hardening or ageing that occurs during the manufacture and transportation of HMA will also affect the compactability of the mix (FAA, 2013).

2.6.3 Binder content

Binder acts as a lubricant of aggregate; hence, a mix with too little binder may be stiff and require more compaction effort, whereas a mix with too much binder will be less stiff and compact easily (FAA, 2013). However, HMA should be manufactured with optimum binder content. Too much binder may increase the possibility of defects, such as bleeding and reducing mix stability. On the other hand, too little binder will yield HMA with inadequate durability.

2.6.4 Aggregate grading and properties

Aggregate grading influences HMA compactability. It furthermore affects the packing characteristics and the way the aggregate interlocks, which in turn influence the ease with which aggregate will rearrange under compaction (Roberts et al., 1996; FAA, 2013). In general, for continuously graded dense aggregate, a coarse-graded structure is often easier to compact than a fine-graded structure (FAA, 2013).

HMA compactability is also influenced by aggregate properties including shape or form; angularity (i.e., number of fractured faces); surface texture; hardness; and nominal aggregate size. While an increase in aggregate attributes such as angularity and surface texture improves the mechanical properties of HMA, more compaction effort is needed to achieve the required density (Button et al., 1990; Chen et al., 2005; Pan et al., 2005; Arasan et al., 2011; FAA, 2013; Komba, 2013; Komba et al., 2013; AI, 2014).

In general, rough-textured aggregate particles are more difficult to compact than smooth-textured ones. Cubical aggregate particles require more compaction effort than rounded particles, while flat and elongated particles tend to resist re-orientation and may break during compaction, leading to change in the gradation and resulting in difficulties in achieving the required density. HMA

mix design guidelines therefore recommend minimum use of flat and elongated particles to reduce the possibility of particles breaking down during compaction or under traffic loading (AI, 2014; Sabita Manual 35/TRH 8, 2020).

2.7 Evaluation of rutting resistance of HMA

Rutting (also known as permanent deformation) is one of the common asphalt pavement distresses. As illustrated in Figure 2.24, the rutting of road pavements manifests itself in the form of surface depressions along the wheel-path (ruts). When pavement ruts are filled with water, they can cause the phenomenon of vehicle hydroplaning (i.e. pulling a vehicle towards rut paths), which may pose a significant safety risk (Pavement Interactive, 2020).



Figure 2.24: Asphalt pavement rutting

Asphalt pavement rutting is primarily caused by two different mechanisms: vertical consolidation due to traffic loading, and lateral distortion (also known as shoving), mostly due to an asphalt mix design problem (Komba et al, 2018, Komba et al., 2019c, Pavement Interactive, 2020). As such, the resistance of HMA against permanent deformation or rutting is one of the important criteria in the design of asphalt mixes. Among other factors, the resistance of HMA mixes against permanent deformation depends on the aggregate packing characteristics and adequate compaction (Verhaeghe et al., 2007, Sabita Manual 35/TRH 8, 2020).

Over the years, several test methods have been developed to evaluate the resistance of HMA mixes against permanent deformation. The Marshall Stability and Hveem Stabilometer tests are

among those originally developed to indirectly evaluate the resistance of HMA mixes against permanent deformation. Since then, technological advancements resulted in the development of devices specifically designed to assess the resistance of HMA mixes against permanent deformation. The next section briefly discusses the devices and associated tests that are commonly used to evaluate the resistance of HMA mixes against permanent deformation.

2.7.1 Wheel-tracking devices

Over the years, several laboratory wheel-tracking devices were developed to assess the asphalt mixes' susceptibility to rutting, moisture damage and stripping. The available wheel-tracking devices are grouped in two categories: small-scale and large-scale wheel-tracking devices. The small-scale devices include the Hamburg Wheel-Tracking Device (HWTD) and Nottingham Wheel Tracking Machine, whereas the French Rutting Tester (FRT) is an example of the large-scale wheel-tracking devices.

The Hamburg Wheel-Tracking Device (HWTD) was developed in Hamburg, Germany, in the 1970s to assess the rutting and stripping potential of asphalt mixes. It is one of the most widely used devices in South Africa and worldwide (Pavement Interactive, 2020; Sabita Manual 35/TRH 8, 2020). The HWTD can also indicate insufficient binder stiffness, weak aggregate structure and poor aggregate-binder adhesion (Sabita Manual 35/TRH 8, 2020). Figure 2.25 shows a photo of the HWTD available at the CSIR's pavement material testing laboratory in South Africa.



Figure 2.25: Hamburg Wheel-Tracking Device (HWTD)

The detailed wheel-tracking test procedure has been standardised in test methods such as the American AASHTO T 324, the European EN 12697-22 and the Australian AGPT-T231. The test

can be conducted on slab asphalt samples and core samples extracted from slab roller compactor or gyratory-compacted asphalt.

It is important to recognise that the available wheel-tracking devices differ in aspects such as wheel type (steel wheel versus pneumatic tyre), wheel diameter, the magnitude of wheel load, and how the wheel load is applied. Consequently, the different wheel-tracking devices could yield different results, which should be taken into account when evaluating the test results. A study by Bodin et al. (2009) compared small- and large-scale wheel-tracking devices, and concluded that the results are sensitive to material type, with small wheel-tracking devices generally yielding high rut depth values. In essence, this means that the rutting specification developed using a specific device should ideally not be used to assess the results obtained when a different device was used.

2.7.2 Uniaxial Repeated Load Permanent Deformation Test

The Repeated Load Permanent Deformation (RLPD) test measures the permanent deformation properties of the asphalt sample. The results of the RLPD test have been used to provide key parameters for model rutting potential in the American Mechanistic-Empirical Pavement Design Guide (MEPDG) pursued by the American Association of State Transportation Officials (AASHTO), as documented in NCHRP 1-37A (2002). Furthermore, the permanent deformation properties obtained from this test can also be used to rank asphalt mixes (Anochie-Boateng et al., 2010).

As part of the revision of the South African Pavement Design Method (SAPDM), now known as South African Road Design Systems (SARDS), a standard protocol for undertaking the RLPD tests was developed (Anochie-Boateng et al., 2010) following the NCHRP 9-29 protocol (NCHRP 9-29, 1999). In South Africa, the RLPD tests are conducted using gyratory-compacted samples at varying temperatures and deviator stress. The gyratory asphalt samples are usually compacted to 170 mm high and 150 mm diameter, following which a 100 mm high specimen is cored from the centre, and the top and bottom 10 mm are trimmed to obtain a 150 mm high by 100 mm diameter specimen.

At the CSIR pavement materials testing laboratory in South Africa, the RLPD tests are conducted using a Universal Testing Machine 25 (UTM-25) device. Figure 2.26 contains a photo of the RLPD test set-up. During the test, permanent deformation of the sample is recorded at each load

application, and the corresponding plastic and elastic strains are computed. By applying Equation 2.14, the resilience modulus can be determined by using the computed plastic strain together with the deviator stress (Anochie-Boateng et al., 2010).

$$M_R = \frac{\delta_P}{\epsilon_r} \quad \text{Equation 2.14}$$

Where:

M_R = resilient modulus

δ_d = dynamic deviate stress

ϵ_r = resilience (recoverable) axial strain



Figure 2.26: RLPD test set-up at the CSIR

2.7.3 Simple Shear Tester (SST)

The Simple Shear Tester (SST), also known as the Superpave shear tester, is used to determine permanent shear strain and complex shear modulus (G^*) of asphalt mixes. The SST measures the asphalt mix resistance against permanent deformation using the Repeated Simple Shear Test at

Constant Height (RSST-CH). On the other hand, the shear modulus of the sample is measured using the Shear Frequency Sweep Test at Constant Height (SFST-CH).

The SST was introduced in South Africa more than a decade ago. As part of the revision of the South African Pavement Design Method (SAPDM), a standard protocol for undertaking the RSST-CH tests was developed (Anochie-Boateng et al., 2010). Figure 2.27 shows a photo of the SST set-up at the CSIR pavement materials testing laboratory in South Africa. The RSST-CH test procedure was standardised as the AASHTO 320 (2007) standard test method. In South Africa, the RSST-CH tests are conducted using 150 mm diameter by 60 mm high asphalt specimens cored from slabs. The RSST-CH can also be conducted using core samples produced from gyratory-compacted samples.

During the RSST-CH tests, a horizontal shear force of 69 kPa is applied to the cylindrical asphalt sample for 0.1 seconds, followed by a 0.6 second rest period. The sample's response in terms of shear displacement is measured using a Linear Variable Displacement Transformer (LVDT) mounted horizontally and used to determine the shear strain.



Figure 2.27: SST set-up at the CSIR

2.7.4 Uniaxial Shear Tester (UST)

The Uniaxial Shear Tester (UST) was developed as part of a research project to address the lack of equipment for measuring asphalt mixture shear properties in Europe and to simplify the SST described in Section 2.8.3 (Zak et al., 2016). The UST device can be used as an insert in common laboratory equipment such as the Universal Testing Machines (UTM). Figure 3.28 shows a typical UST test set-up and specimen.

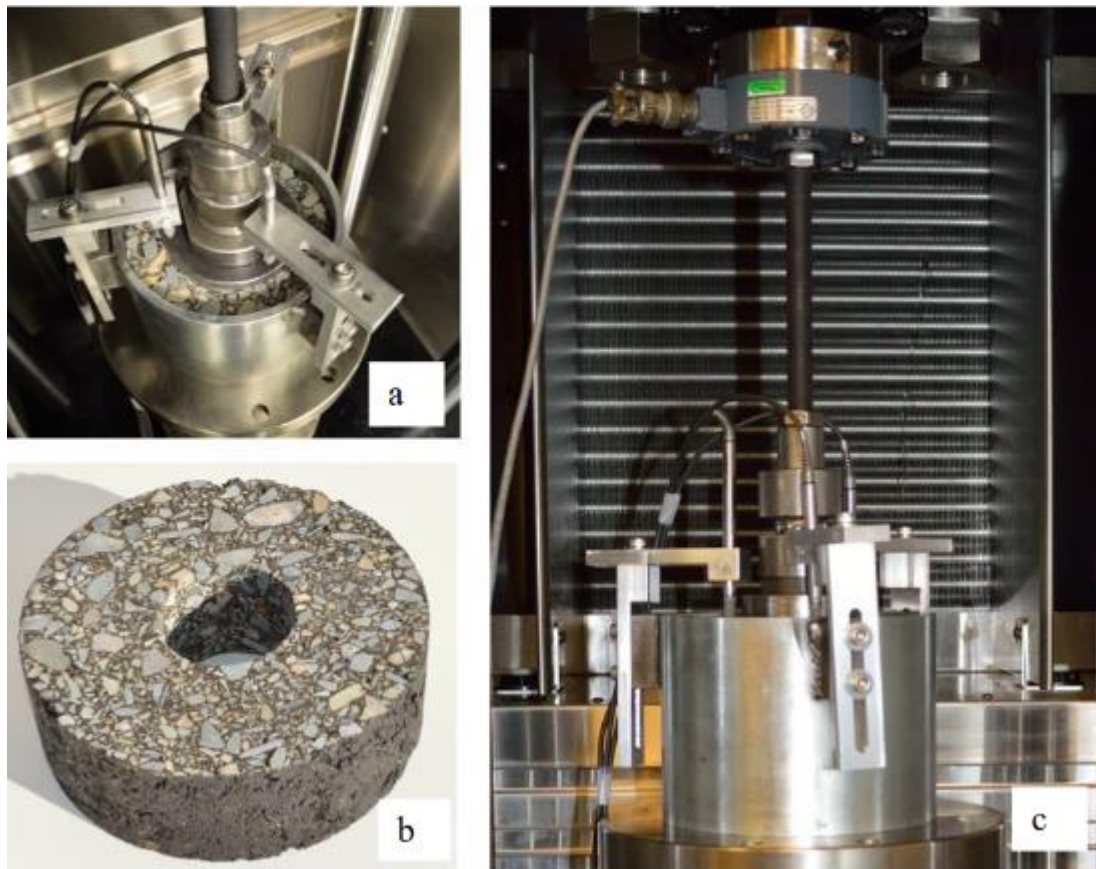


Figure 2.28: Photos of (a) UST test set-up, (b) hollow test specimen, and (c) UST placed in UTM chamber (Zak et al., 2016)

Similar to the SST device, the UST device can be used to determine the resistance of asphalt mixes against permanent deformation and the shear modulus. Using the UST, the asphalt mix resistance against permanent deformation is measured using the Uniaxial Repeated Shear Test (URST), whereas the shear modulus is measured using the Uniaxial Shear Frequency Sweep Test (USFST).

The URST test is conducted using the AASHTO 320 (2007) standard test method. Unlike the RSST-CH, a 69 kPa cyclic shear load (0.1 seconds loading, followed by a 0.6 second rest period) is applied vertically. The resulting vertical displacement response is measured using three LVDT mounted at 120° intervals along the specimen's circumference. The measured replacement data is processed to determine the accumulated permanent shear strain.

2.8 Summary

This chapter provided an overview of the available knowledge on the aspects covered in the study. This information formed the basis for developing the methodology used in our study. It also informed the analysis and discussion of results of experiments that were carried out to investigate various aspects of this study.

An overview of HMA and asphalt mix design methods was presented in Section 2.2. HMA consists of a graded aggregate, bituminous binder, and mineral filler. The proportion of each component is established using a structured design process and takes into account other key factors, such as the expected traffic loading and environmental conditions. The asphalt mix design process is geared towards selecting a combination of the component materials to ensure that the resulting mixture can be compacted and possess the desired performance attributes. It also involves selecting a suitable aggregate structure with space between particles to accommodate the bituminous binder and preventing bleeding rutting.

Over the years, several methods for designing asphalt mixes were developed to ensure that the asphalt mix design process yields the desired performance attributes. These asphalt mix design methods include the Marshall and Superpave asphalt mix design methods. The Superpave mix design system, which was initially developed in the USA, is increasingly adopted by several road authorities or institutions worldwide, with some modifications to fit their specific local conditions.

Section 2.3 discussed aggregate packing concepts, which are increasingly incorporated into the asphalt mix design process to optimise the selection of aggregate. The aggregate packing concepts discussed include the maximum density line, gravel-to-sand ratio, Bailey ratios, the dominant aggregate size range concept and theoretical aggregate packing models. The aggregate gradation curve can be used as the basis for determining most of the aggregate packing parameters. While these aggregate packing parameters have been in existence for over decades, it is not clearly understood which of them are most appropriate for characterising aggregate packing

characteristics. Understanding how aggregate packing characteristics are related to asphalt mix performance attributes such as workability or compactability could assist in identifying potential asphalt mix compaction problems during the mix design stage.

Section 2.4 discussed HMA compaction, which is an essential aspect of HMA mix design and construction. The primary goal of laboratory asphalt compaction is to fabricate laboratory specimens to characterise asphalt volumetric and mechanical properties. Over the years, several laboratory asphalt compaction devices were developed. However, such devices often differ in terms of the geometry of the compacted specimens (cylindrical or rectangular) and how the compaction load is applied. Furthermore, the literature indicated that the properties of asphalt samples compacted using different laboratory compactors might differ, particularly in respect of air voids distribution and the arrangement of aggregate particles. As such, the mechanical properties of asphalt samples produced by different compaction devices may not necessarily be similar.

For the field compaction, asphalt compaction enables the asphalt layer to develop strength and achieve stability, to reduce permeability, to provide resistance against rutting and fatigue cracking, to reduce moisture damage, and to prevent oxidative hardening. Field asphalt compaction is commonly undertaken using conventional steel wheel rollers and pneumatic tyre rollers. One of the limitations of the conventional roller compactors is that they do not receive feedback on what is happening on the asphalt material during compaction. Intelligent Compaction (IC) can monitor and control the compaction process in real time and is increasingly deployed in the asphalt construction industry for exactly this purpose.

Section 2.4 also discussed the determination of compacted asphalt samples' volumetric properties (density) to evaluate the compaction quality, which is a fundamental component of asphalt mix design and construction. It discussed two commonly used methods: the SSD and vacuum-sealing methods. The SSD method is most suited for determining the density of impermeable dense-graded asphalt specimens. In contrast, the vacuum-sealing approach is preferred to determine the density of permeable asphalt specimens such as porous asphalt mixes. The current study used the SSD method because all the asphalt mixes investigated were dense graded.

Section 2.5 discussed the assessment of asphalt mix compactability by analysing the basic compaction gyratory compaction data. Asphalt mix compactability parameters such as locking point, the compaction energy index, compaction and traffic densification indices and compaction

slope, can be easily determined by analysing the gyratory compaction process densification curve. These asphalt mix compactability parameters form the basis of the correlation with aggregate packing parameters carried out in this study.

Section 2.6 was devoted to a discussion of the factors that influence HMA compaction, such as temperature, binder type, binder content, aggregate gradation and physical properties of aggregates. This study focused primarily on the influence of aggregate gradation, based on which we determined several parameters that define the characteristics of aggregate packing. We subsequently related them to the HMA mix compactability.

The literature review ended with a discussion on the evaluation of HMA rutting resistance presented in Section 2.7. Several available HMA rutting evaluation devices and their associated tests were discussed, including the HWTD, UTM, SST and UST. Different road agencies and authorities nowadays recommend a specific rutting evaluation test or device, depending on factors such as availability and cost.

3 METHODOLOGY

3.1 Introduction

This chapter describes the methodology followed in the study. The methodology was developed while taking into account the currently available knowledge on the aspects investigated, as presented in Chapter 2. The study's three specific objectives included investigating:

- the influence of aggregate packing on HMA compactability;
- the spatial distribution of air voids in compacted HMA, and
- the influence of laboratory compaction method and compaction density on HMA rutting resistance.

This methodology chapter consists of three separate sections addressing each of the above three specific objectives. Section 3.2 covers the methodology followed to investigate the influence of the aggregate packing characteristics on HMA compactability. It includes a description of the experimental plan, selection of HMA mixes and grading designs, aggregate packing analysis, HMA compaction and the determination of HMA compatibility parameters. Section 3.3 discusses the methodology followed to investigate the spatial distribution of air voids in compacted HMA samples under different compaction density and sample height. It describes the HMA mix design, HMA sample compaction, specimen preparation and density determination. The methodology used to investigate the effect of the laboratory compaction method and compaction density on HMA rutting resistance is discussed in Section 3.4. The section covers the selection of HMA mix designs, the compaction of HMA specimens, and the undertaking of rutting resistance tests and associate data processing. A summary of the methodology chapter is provided in Section 3.5.

3.2 Investigation of the influence of aggregate packing on HMA compactability

As stated previously, the specific objective of this study was to investigate the influence of the aggregate packing characteristics on the compactability of HMA. The study used three sand skeleton and three stone skeleton HMA mixes. For each HMA mix, parameters that describe aggregate packing characteristics, including the gravel-to-sand ratio, gradation shape factor, as well as three traditional Bailey ratios and three rational Bailey ratios, were determined. This process was followed by compacting HMA samples of each mix using a gyratory compactor. The gyratory compaction data was analysed to determine five parameters that describe HMA

compactability, and subsequently related to aggregate packing. Figure 3.1 provides a schematic illustration of the investigation carried out for the sand and stone skeleton mixes.

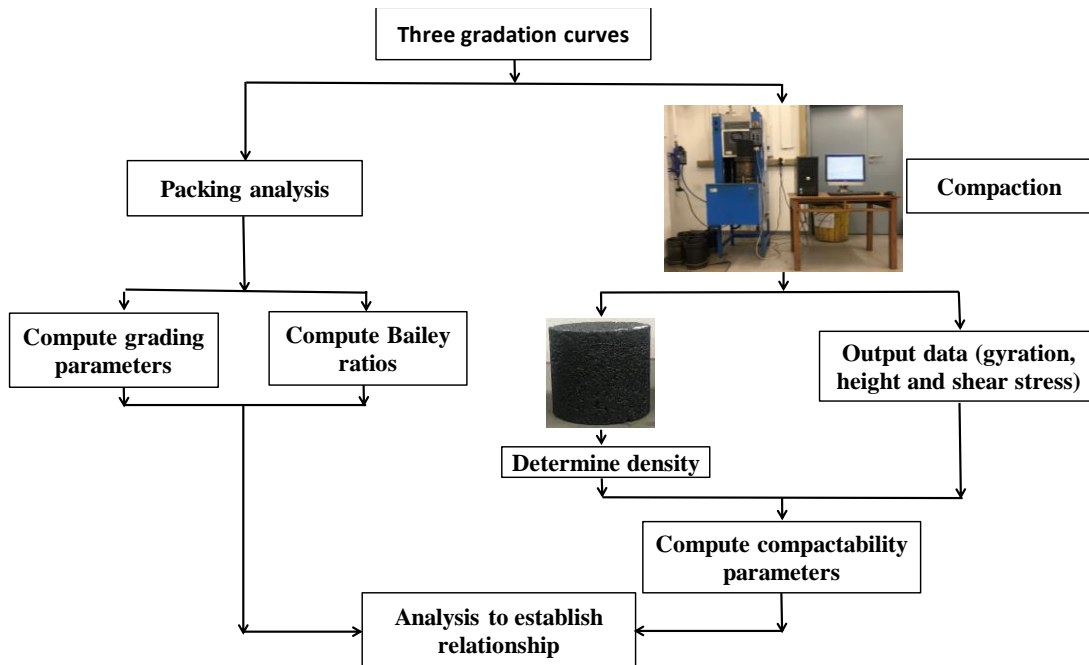


Figure 3.1: Steps followed in the aggregate packing and compactability investigation

3.2.1 Selection of HMA mixes and grading designs

Two types of grading structures of the commonly used South African wearing course HMA mixes were used in the study:

- 10 mm NMPS dense-graded mix (sand skeleton) - also known as medium continuously graded asphalt mix, and
- 20 mm NMPS dense-graded mix (stone skeleton) - also known as coarse continuously graded asphalt mix.

The mix designs, aggregate and bituminous binder materials were sourced from the same commercial asphalt plant in the Gauteng province of South Africa. Table 3.1 shows the grading specifications of the two HMA mixes (COLTO, 1998). The basic properties of the aggregates are presented in Table 3.2, alongside the specifications stipulated in the South African asphalt mix design guideline (Sabita Manual 35/TRH 8, 2020). Overall, the physical properties of all the aggregates complied with the specifications.

Table 3.1: Grading specifications

| Sieve size (mm) | Percentage passing sieve size (%) | | | |
|--------------------|-----------------------------------|---------|-----------------------------|---------|
| | 10 mm NMPS dense-graded mix | | 20 mm NMPS dense-graded mix | |
| | Minimum | Maximum | Minimum | Maximum |
| 28 | - | - | 100 | - |
| 20 | - | - | 85 | 100 |
| 14 | 100 | - | 71 | 84 |
| 10 | 82 | 100 | 62 | 76 |
| 7.1 | 68 | 87 | 52 | 69 |
| 5 | 54 | 75 | 42 | 60 |
| 2 | 35 | 50 | 30 | 48 |
| 1 | 27 | 42 | 22 | 38 |
| 0.6 | 18 | 32 | 16 | 28 |
| 0.3 | 11 | 23 | 12 | 20 |
| 0.15 | 7 | 16 | 8 | 15 |
| 0.075 | 4 | 10 | 5 | 10 |

Table 3.2: Physical properties of aggregates

| Property | Test method | Result | | Specification |
|-----------------------------------------------------|----------------|---------------|---------------|---------------|
| | | 10 mm NMPS | 20 mm NMPS | |
| Coarse aggregates bulk density (kg/m ³) | SANS 3001-AG20 | 2900 | 2960 | - |
| Fine aggregates bulk density (kg/m ³) | SANS 3001-AG21 | 2732 | 2924 | - |
| Coarse aggregates water absorption (%) | SANS 3001-AG20 | 0.40 | 0.39 | ≤ 1.0 |
| Fine aggregates water absorption (%) | SANS 3001-AG21 | 0.74 | 0.55 | ≤ 1.5 |
| Flakiness index (%) | SANS 3001-AG4 | 20.09 | 12.40 | ≤ 25 |
| Polishing stone value | SANS 3001-AG11 | 46 | 50 | ≥ 45 |
| 10% Fine aggregates crushing test | SANS 3001-AG10 | 504 | 344 | ≥ 160 |
| Aggregate crushing value (%) | SANS 3001-AG10 | 5.9 | 12.0 | ≤ 25 |

The 10 mm NMPS mixes consisted of Andesite aggregates and a 50/70 penetration grade binder (PG 58-22). The aggregates comprised of six fractions with individual gradations are presented in Table 3.3. On the other hand, the 20 mm NMPS mixes consisted of Dolerite aggregates and 35/50 penetration grade binder (PG 64-16). The aggregates comprised of eight fractions with

gradations individual gradations are presented in Table 3.4. The binders used in the study conform to penetration-grade bitumen specifications (SANS 4001-BT1, 2016), as well as to the South African Performance Grade (PG) bitumen specification (SATS 3208, 2019).

Table 3.3: Gradations of 10 mm NMPS mix individual fractions

| Fraction/ Sieve size (mm) | 9.5 mm | 6.7 mm | Crusher dust | Crusher sand | Mine sand | Filler |
|--------------------------------------|---------------|---------------|-------------------------|---------------------|------------------|---------------|
| 37.5 | 100 | 100 | 100 | 100 | 100 | 100 |
| 28 | 100 | 100 | 100 | 100 | 100 | 100 |
| 20 | 100 | 100 | 100 | 100 | 100 | 100 |
| 14 | 100 | 100 | 100 | 100 | 100 | 100 |
| 10 | 96 | 100 | 100 | 100 | 100 | 100 |
| 7.1 | 41 | 95 | 100 | 97 | 100 | 100 |
| 5 | 11 | 30 | 96 | 84 | 100 | 100 |
| 2 | 3 | 5 | 56 | 52 | 100 | 100 |
| 1 | 3 | 3 | 36 | 33 | 100 | 100 |
| 0.6 | 2 | 3 | 27 | 23 | 100 | 100 |
| 0.3 | 2 | 3 | 19 | 14 | 87 | 100 |
| 0.15 | 2 | 2 | 14 | 7 | 38 | 100 |
| 0.075 | 1.6 | 2.0 | 10.1 | 4.2 | 11.0 | 99.0 |

Table 3.4: Gradations of 20 mm NMPS mix individual fractions

| Fraction/ Sieve size (mm) | 22.4 mm | 13.2 mm | 9.5 mm | 6.7 mm | Crusher dust | Crusher sand | Mine sand | Filler |
|------------------------------|---------|---------|--------|--------|-----------------|-----------------|--------------|--------|
| 37.5 | 100 | 100 | 100 | 100 | 100 | 100 | 100 | 100 |
| 28 | 100 | 100 | 100 | 100 | 100 | 100 | 100 | 100 |
| 20 | 79 | 100 | 100 | 100 | 100 | 100 | 100 | 100 |
| 14 | 15 | 97 | 100 | 100 | 100 | 100 | 100 | 100 |
| 10 | 1 | 42 | 88 | 100 | 100 | 100 | 100 | 100 |
| 7.1 | 0 | 2 | 9 | 82 | 100 | 100 | 100 | 100 |
| 5 | 0 | 1 | 1 | 17 | 100 | 98 | 100 | 100 |
| 2 | 0 | 1 | 0.4 | 0.3 | 59 | 42 | 100 | 100 |
| 1 | 0 | 1 | 0.4 | 0.3 | 35 | 19 | 100 | 100 |
| 0.6 | 0 | 1 | 0.3 | 0.2 | 25 | 12 | 100 | 100 |
| 0.3 | 0 | 1 | 0.3 | 0.2 | 16 | 7 | 87 | 100 |
| 0.15 | 0 | 1 | 0.3 | 0.2 | 10 | 4 | 37 | 100 |
| 0.075 | 0.1 | 0.6 | 0.3 | 0.2 | 4.2 | 2.4 | 9.3 | 97.0 |

To investigate the influence of the aggregate packing characteristics on the compactability of HMA mixes, three grading structures were designed for each of the 10 mm and 20 mm NMPS mixes. The gradation curves of the HMA mixes were designed to fall within the required specifications (COLTO, 1998), and resulted in three distinct gradation curves – fine, medium and coarse. Figure 3.2 and Figure 3.3 plot the gradation curves for the 10 mm and 20 mm NMPS HMA mixes respectively. All the gradation curves fell within the specified envelopes.

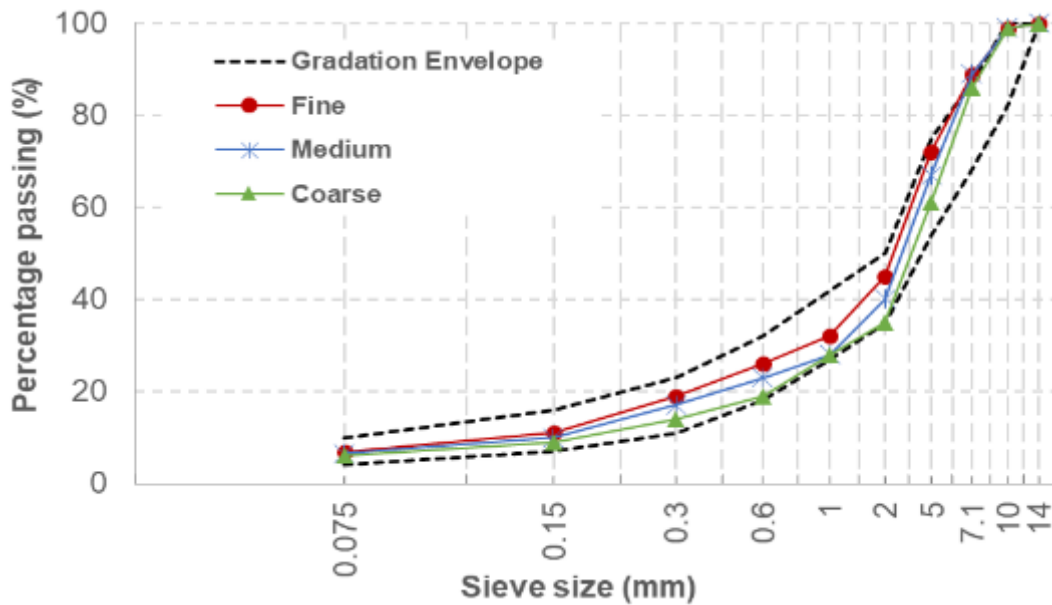


Figure 3.2: 10 mm NMPS mixes aggregate grading

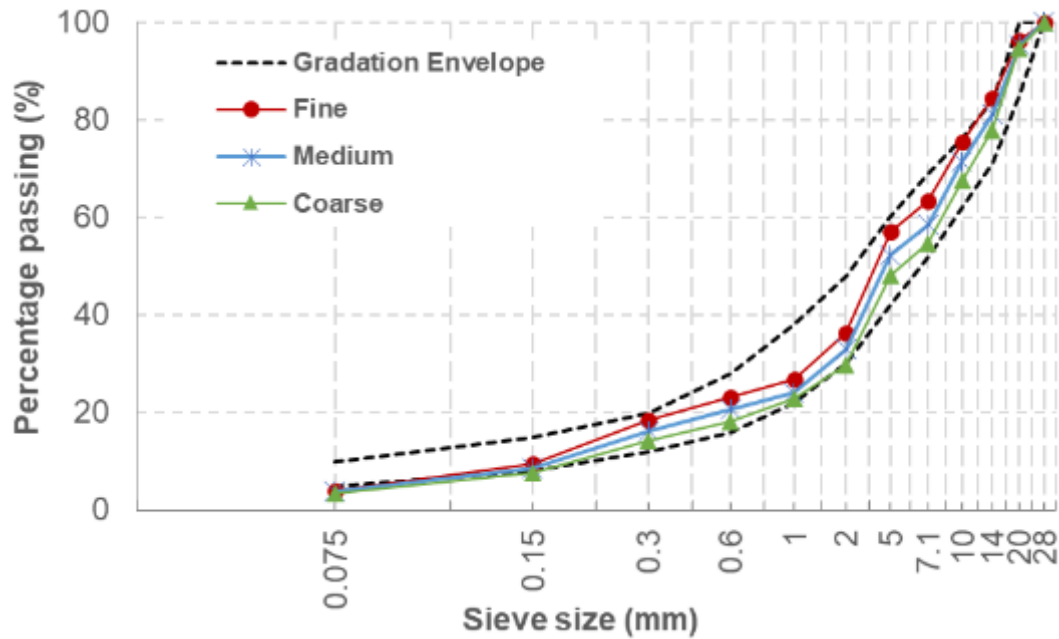


Figure 3.3: 20 mm NMPS mixes aggregate grading

3.2.2 Aggregate packing analysis

The gradation curves of each of the HMA mixes formed the basis of the aggregate packing analysis. The gradation curves of each HMA mix were analysed to determine the following parameters, which describe the aggregate packing characteristics: two aggregate gradation parameters (G/S and n), three traditional Bailey ratios (CA , FAC , and FA_f), and three traditional Bailey ratios (CA_r , C/F , and $FARM_f$).

The above rational Bailey ratios were selected to represent macro, midi (or meso) and micro skeleton matrix levels' packing of gradation structure. The results of the aggregate packing parameters are analysed and discussed in Chapter 4.

3.2.3 HMA Mixing and compaction

The mixing and compaction of the HMA samples were done according procedures described by Anochie-Boateng et al. (2010). The calculated masses of individual aggregate fractions were blended in accordance with the design grading and pre-heated to the required mixing temperatures. The mixing temperatures were 150°C and 160°C for 10 mm and 20 mm NMPS mixes respectively. A mechanical mixer (Figure 3.4) was used to mix the pre-heated aggregate and binder until a uniform mixture was obtained (approximately 15 minutes). After mixing, the loose HMA material was placed into an oven set at compaction temperature for four hours to

simulate short-term ageing (Anochie-Boateng et al., 2010). The compaction temperatures were 135°C, and 145°C for 10 mm and 20 mm NMPS mixes respectively.



Figure 3.4: Mechanical HMA mixing

After simulating short-term ageing, HMA specimens were compacted using a gyratory compactor. Figure 3.5 shows (a) the gyratory compactor used in this study, alongside (b) a typical compacted HMA sample. The mould diameter was 150 mm, and all the HMA specimens were compacted to 300 gyrations. For each aggregate gradation, three replicates of HMA specimens were compacted.



(a) Gyratory compactor



(b) Compacted HMA sample

Figure 3.5: Gyratory compactor and typical compacted HMA sample

3.2.4 HMA compactability analysis

The basic output data obtained during the gyratory compaction included the HMA sample height and the shear stress corresponding to each gyration. Typical HMA sample height versus the number of gyrations is plotted in Figure 3.6, while Figure 3.7 plots the shear stress versus the number of gyrations.

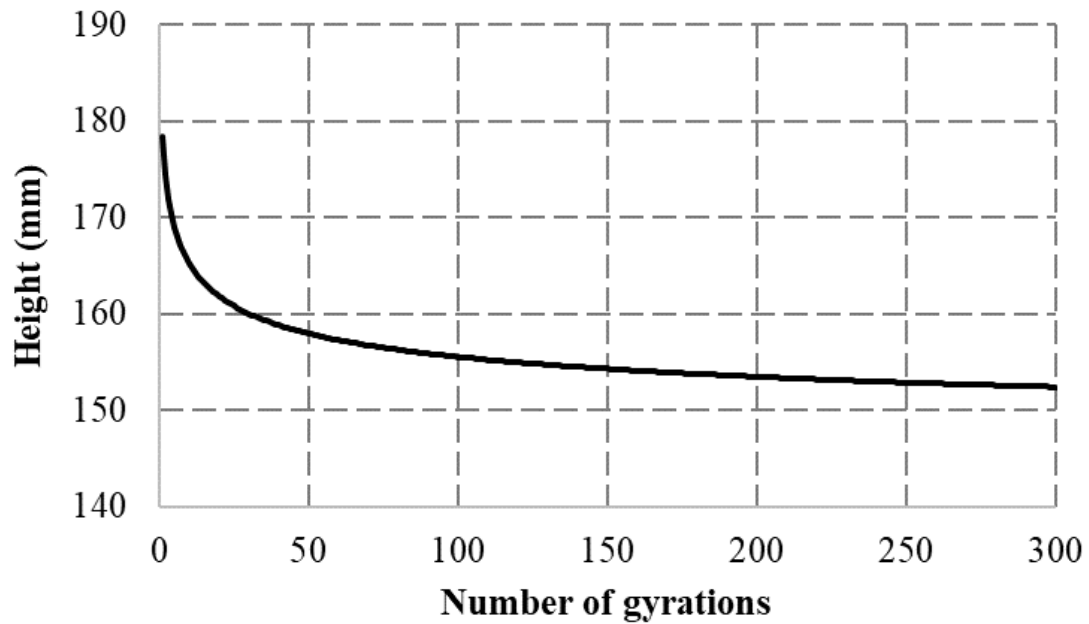


Figure 3.6: HMA sample height plotted against the number of gyrations

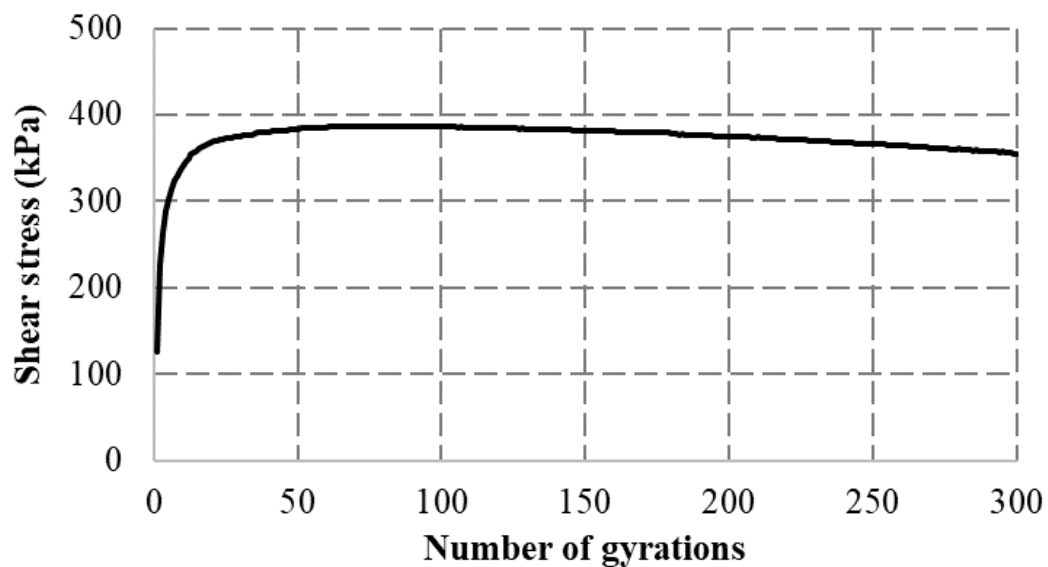


Figure 3.7: Shear stress plotted against the number of gyrations

Using the gyratory mould diameter and the sample height after each gyration, Equation 3.1 was used to compute volume.

$$EV_n = H_n \times \pi r^2 \quad \text{Equation 3.1}$$

Where:

EV_n = the estimated volume at each gyration in m^3

H_n = sample height at each gyration in m

r = the radius of the gyratory compaction mould in m

The volume at each gyration was subsequently used to compute estimate bulk density using Equation 3.2.

$$EBD_n = \frac{M}{EV_n} \quad \text{Equation 3.2}$$

Where:

EBD_n = the estimated bulk density at each gyration in kg/m^3

M = mass of HMA specimen in kg

EV_n = the estimated volume at each gyration in m^3

Once the compaction of the HMA sample was completed, the actual density of the HMA sample was determined using the SSD method (SANS 3001-AS10, 2011). At the end of each gyration, the actual bulk density was used together with the estimated bulk density to calculate the bulk density, using Equation 3.3.

$$BD_n = EBD_n \times \frac{BD_N}{EBD_N} \quad \text{Equation 3.3}$$

Where:

BD_n = the bulk density at each gyration

EBD_n = the estimated bulk density at each gyration

BD_N = the bulk density corresponding to the final gyration

EBD_N = the estimated bulk density at the end of compaction

Figure 3.8 shows typical plots of actual and estimated density during the gyratory compaction process. The actual density is generally higher than the estimated density, which is the expected trend.

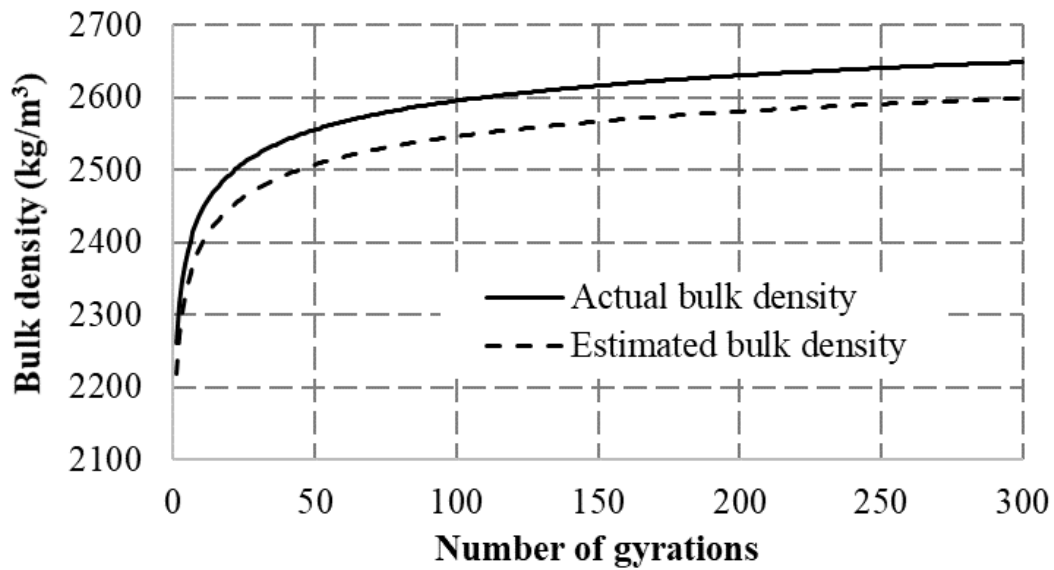


Figure 3.8: Estimated and actual bulk density

After determining the density of the HMA specimens at each gyration, the degree of compaction at each gyration was calculated using Equation 3.4. The degree of compaction is essentially the bulk density expressed as a percentage of MVD.

$$DC_n = \frac{BD_n}{MVD} \times 100 \quad \text{Equation 3.4}$$

Where:

DC_n = the percentage degree of compaction at any gyration n

BD_n = the bulk density at any gyration n

MVD = the maximum void-less density of the HMA mix

Figure 3.9 shows a typical plot of the degree of compaction versus the number of gyrations. At the initial stage of the compaction process, the HMA material is still in a loose state. Hence, the degree of compaction increases rapidly with an increase in the number of gyrations. As the HMA specimen densifies, the increase in the number of gyrations results in a relatively small increase in the degree of compaction.

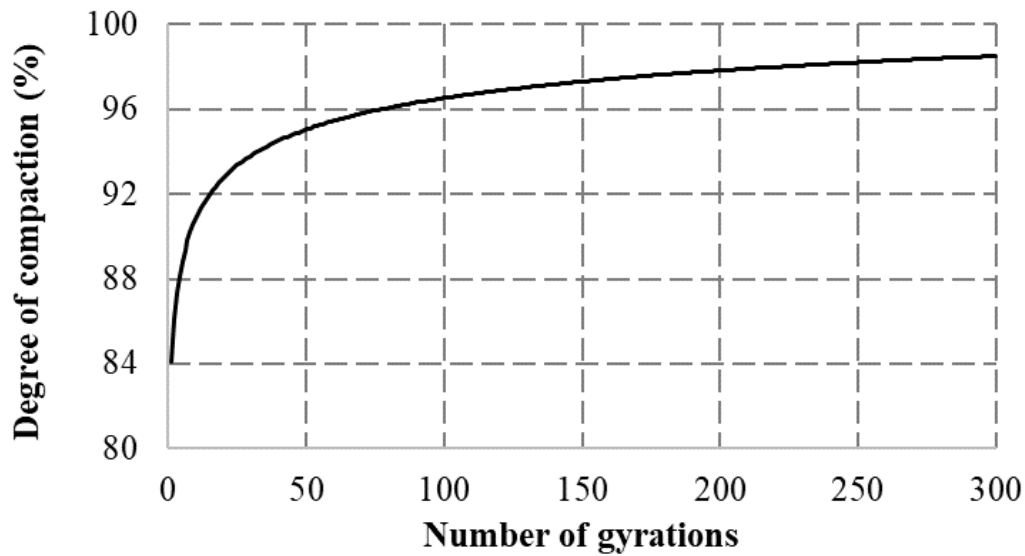


Figure 3.9: Degree of compaction versus the number of gyrations

The HMA compaction process results in a reduction of the volume of air in the mix. Hence, the air voids content is a key characteristics of interest. The bulk density of the compacted HMA specimen and the MVD of the HMA mix were used to determine air voids content for each gyrations. Equation 3.5 was used for this purpose.

$$AV_n = \frac{MVD - BD_n}{MVD} \times 100 \quad \text{Equation 3.5}$$

Where:

AV_n = the percentage air voids content at any gyration n

BD_n = the bulk density at any gyration n

MVD = the maximum void-less density of the HMA mix

Figure 3.10 shows a typical plot of the air voids content versus the number of gyrations. As expected, at the early stage of the compaction process, the air voids content decreases rapidly when the number of gyrations increases. As the HMA specimen densifies, the increase in the gyrations results in a relatively small decrease in the amount of voids.

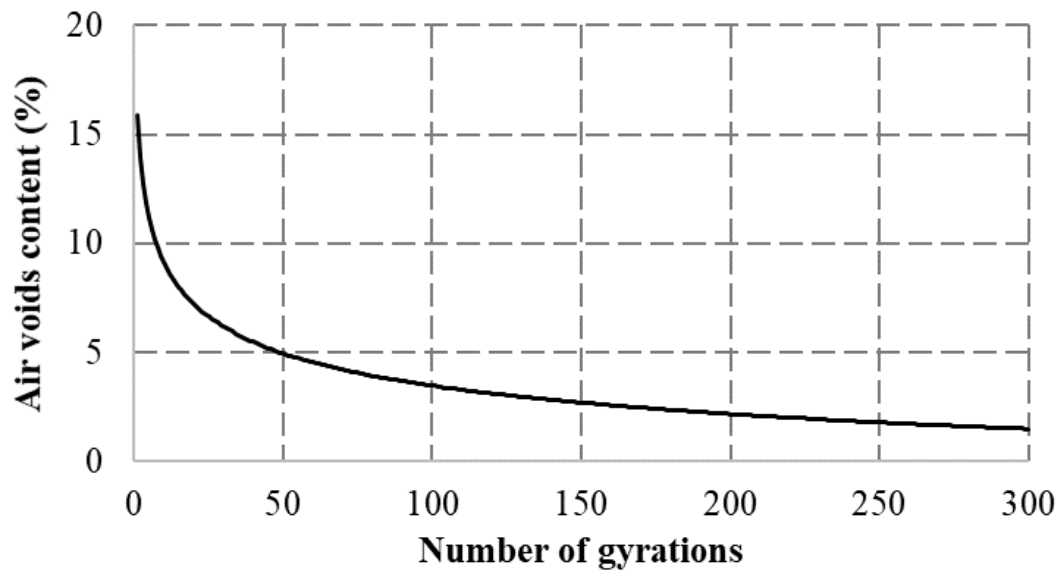


Figure 3.10: Air voids content versus the number of gyrations

As part of this research project, a software program known as “IPAC Reader” was developed to facilitate the computations described above. The software data inputs were the following:

- IPAC file (ASCII format) from the gyratory compaction process containing sample height and shear stress data
- Bulk density of the sample at the end of compaction
- Mass of HMA material added in the gyratory compaction mould
- MVD of the mix

Figure 3.11 shows a screenshot of the developed software. The software was coded to allow analysis using the following pre-selected options (also illustrated in Figure 3.11 shows):

- A single IPAC file – analysis results exported to a single to Excel file
- A batch of IPAC files (two or more files) – analysis results exported to separate files
- A set of three IPAC files for three replicate samples – analysis results exported to a single Excel file containing three different worksheets

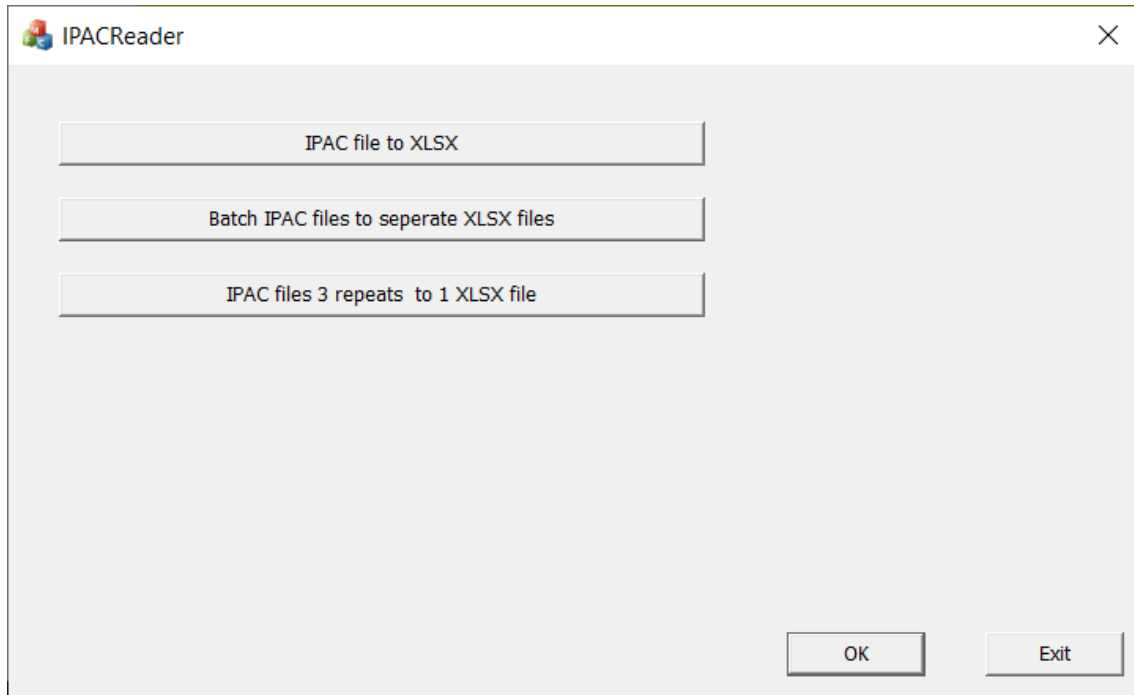


Figure 3.11: Main screen of the gyratory data processing software

The results of the gyratory compaction data described above constitute the basis for analysis presented in Chapter 4 to determine the HMA compactability parameters. The following HMA compactability parameters were determined:

- Locking point (LP);
- Compaction energy index (CEI);
- Traffic densification index (TDI_{300});
- Compaction slope (CS), and
- Area under shear stress (ASS_{max}).

3.3 Investigation of the spatial distribution of air voids in compacted HMA

This specific objective of the study aimed to investigate air voids distribution in laboratory-compacted HMA samples and cores extracted from actual field road sections. Gyratory-compacted HMA samples were used to investigate the vertical and radial (diametrical) distribution of air voids. The HMA samples were compacted at two different target air voids contents (4.0% and 7.0%) and two sample heights (120 mm and 170 mm). The study also investigated the spatial distribution of air voids in asphalt cores extracted from two road sections near Pretoria, South Africa.

3.3.1 HMA mix design and materials

A 10 mm NMPS mix consisting of Andesite aggregates and penetration grade (50/70) asphalt binder was selected to investigate the special distribution of air voids in compacted HMA. The asphalt binder conforms to the South African specification for penetration bitumen (SANS 4001-BT1, 2016) and is equivalent to PG 58-22 – as per the South African Performance Grade (PG) bitumen specification (SATS 3208, 2019). Figure 3.12 plots the HMA mix design gradation curve, which falls within the specified envelopes according to the South African standard specifications for road and bridge works (COLTO, 1998). Among other factors, the 10 mm NMPS was selected to limit the segregation of the mix during placement into the compaction mould, which is more prone to coarse gradation, such as the 20 mm NMPS (Sabita Manual 35/TRH 8, 2020).

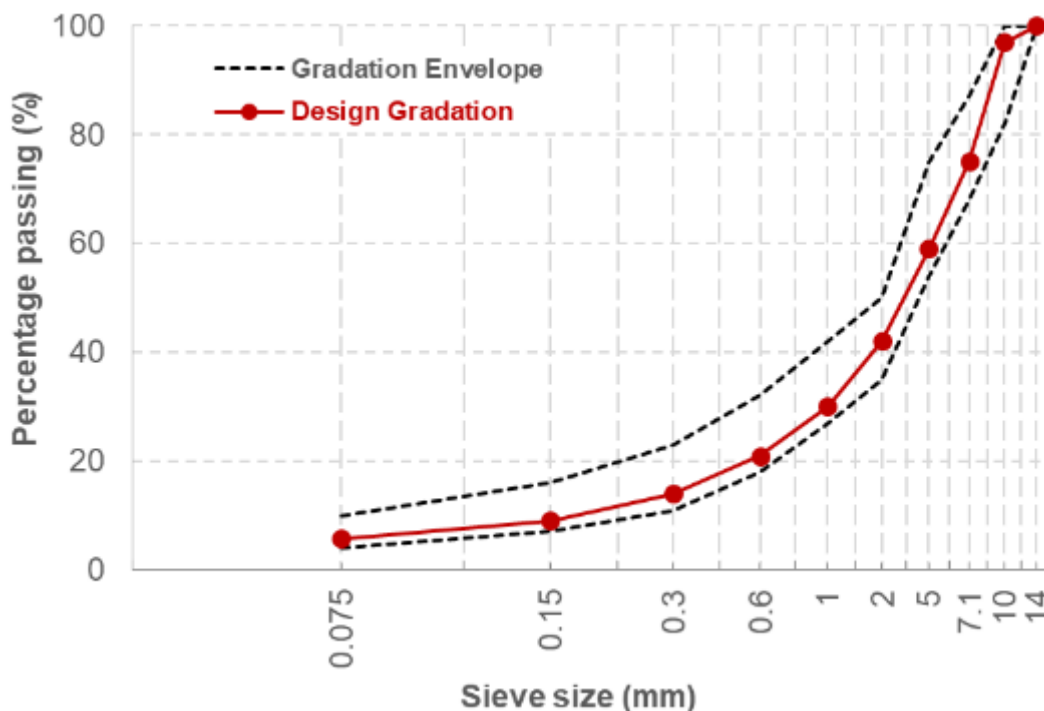


Figure 3.12: 10 mm NMPS mix design gradation

3.3.2 HMA mixing and compaction

The mixing and compaction of the HMA specimens were done according to protocols for testing asphalt mixes in South Africa (Anochie-Boateng et al., 2010), as described in Section 3.2.4. A gyratory compactor was used to compact HMA samples to a typical design and a field construction air voids content of approximately 4.0% and 7.0% respectively. A 150 mm diameter mould was used, and HMA samples were compacted to 170 mm and 120 mm target heights. The 170 mm was selected as the typical height for compacting samples for HMA performance tests such as the dynamic modulus and repeated axial load permanent deformation tests.

On the other hand, 120 mm high samples were used during HMA design to evaluate the mix volumetric properties as described in the South African HMA design manual (Sabita Manual 35/TRH 8, 2020). For each combination of target air voids and sample height, three replicate HMA samples were compacted as summarised in Table 3.5. The matrix presented in Table 3.5 allowed investigation of the influence of both the target air voids and the sample height on the spatial distribution of air voids.

Table 3.5: Matrix of compacted samples

| Target air voids content (%) | Height (mm) | Number of samples | Representation |
|------------------------------|-------------|-------------------|--------------------------|
| 4.0 | 170 mm | 3 | Design air voids content |
| | 120 mm | 3 | |
| 7.0 | 170 mm | 3 | Field air voids content |
| | 120 mm | 3 | |

As mentioned earlier, the laboratory study was supplemented with limited field asphalt cores that were extracted from the South African National Roads Agency SOC Ltd (SANRAL) experimental section on R104 road near Pretoria, South Africa. Most of the flexible pavement designed and constructed in South Africa, the asphalt surfacing layer has a maximum thickness of 50 mm, making it unsuitable for the vertical air voids distribution aspect of the study. Hence, the asphalt base layer mixes had selected for this aspect of the study. The asphalt cores used in this study were extracted from the sections constructed with Bituminous Treated Base (BTB) and High Modulus Asphalt (HiMA) mixes. Among other factors, the selection of the two field asphalt mixes was primarily informed by their layer thicknesses (i.e., greater than 120 mm), which allowed for the investigation of both vertical and radial distribution of air voids as described in Section 3.3.3.. Figure 3.13 plot the design gradations of the BTB and HiMA mixes, respectively. The NMPSs of the HiMA and the BTB mixes were 14 and 20 mm, respectively. It should be emphasised that the study primarily focused on the laboratory compacted HMA samples. The

limited field samples were used to complement the laboratory study, considering that the laboratory and field conditions are not necessarily similar.

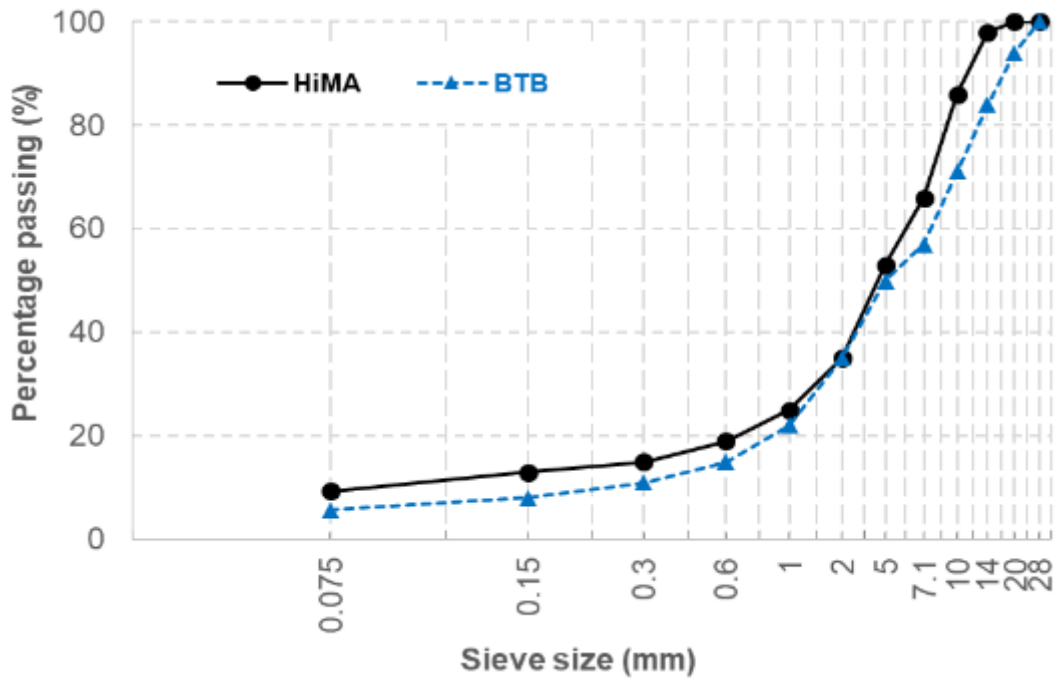


Figure 3.13: BTB and HiMA design gradation

3.3.3 Asphalt sample preparation and density determination

Specimens of 100 mm diameter were cored from the centre of the 170 mm high HMA samples, and the top and bottom 10 mm edges were trimmed to produce 150 mm high specimens. The purpose of coring and trimming was to remove surface roughness, which influences the density uniformity of laboratory-compacted HMA samples (Anochie-Boateng et al., 2010 and 2011). The experimental procedures for HMA compaction and preparation of samples for investigation of the spatial distribution of air voids in compacted HMA samples are depicted in Figure 3.14.

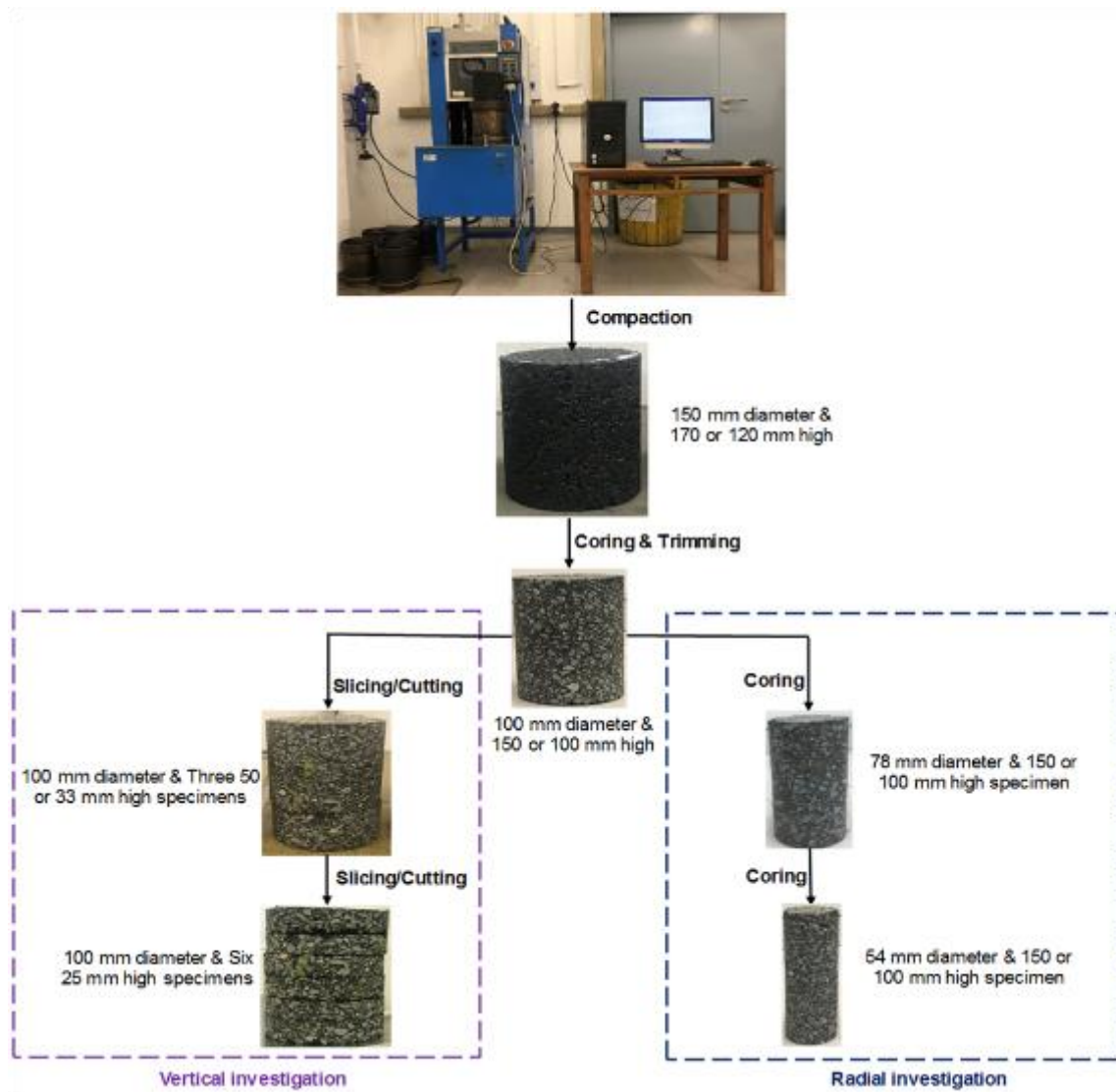


Figure 3.14: HMA compaction and sample preparation procedures

To investigate the vertical distribution of air voids, the bulk density of the 150 mm high specimens was determined according to SANS 3001-AS10 (2011). Next, the specimens were sliced/cut into three specimens of 50 mm height (top, middle and bottom) and the bulk density of each specimen was determined. The 50 mm high specimens were subsequently sliced into two 25 mm high specimens (resulting in six parts), and their bulk densities were determined again.

The preparation of the 120 mm high samples followed a similar approach. 100 mm diameter specimens were cored from the centre, and the tops and bottoms were trimmed to produce 100 mm high specimens before the bulk density was determined. The 100 mm high specimens were sliced/cut into three specimens of approximately 33.3 mm height (top, middle and bottom) and the bulk density of each specimen was determined.

To investigate the radial distribution of air voids, the density of the 100 mm diameter samples was determined. The samples were cored to 78 mm diameter, and the bulk density was determined. Afterwards, the 78 mm diameter specimens were cored to 54 mm, and their bulk density was determined again. The 100, 78, and 54 diameters were selected because of the standard coring bits that are commercially available in South Africa.

The field-extracted core sample preparation procedure was as described above for the laboratory-prepared samples, except that the field cores were sliced to a maximum of four (rather than six) specimens due to insufficient sample thickness.

3.3.4 Volumetric analysis of compacted HMA specimens

In this study, the bulk density of the compacted asphalt specimens was determined by using the Saturated Surface-Dry (SSD) method (SANS 3001-AS10, 2011). This is because the HMA mixes that were investigated were dense-graded. The procedure can be summarised as follows (SANS 3001-AS10, 2011):

- Determining the dry mass of specimen (M1);
- Determining mass of fully immersed specimen (M2) in water (see Figure 3.15), and
- Determining the saturated surface-dry mass of the specimen (M3).

The determined masses (M1 to M3) are used to calculate the bulk density of the compacted HMA specimen. Equation 3.6 is used for a situation where the expected water absorption is less than 0.85%, which was the case for the HMA specimens used in this study (SANS 3001-AS10, 2011).

$$BD = \frac{(M_1)}{M_3 - M_2} \times \rho_w \quad \text{Equation 3.6}$$

Where:

BD = specimen bulk density (kg/m³)

M₁ = specimen dry mass (g)

M₂ = specimen mass water (g)

M₃ = mass of saturated surface-dry specimen (g)

ρ_w = water density (kg/m³)



Figure 3.15: SSD test set-up

SANS 3001-AS11 (2011) method was used to determine the Maximum void-less density (MVD) of the HMA mixes. Figure 3.16 shows a typical MVD test set-up, and the test procedure for dense-graded HMA mixes can be summarised as follows (SANS 3001-AS11, 2011):

- The process started with cleaning, drying and weighing a flask and glass plate and recording their mass (M1);
- The flask is filled with loose HMA specimen up to approximately one-third full, followed by weighing and recording the mass (M2);
- Water is poured into the flask until the specimen is fully submerged. A vacuum pump (pressure reduced to 30 mm mercury) is attached to the flask for a period of approximately 15 minutes. The flask is agitated by tapping the sides at intervals of approximately 2 minutes;
- The flask is restored to atmospheric pressure and stirred with a glass rod to remove visible bubbles. The flask is filled with water and conditioned into a water bath for 10 minutes.
- The mass of the content with a dry glass plate is recorded (M3), and
- The flask is emptied, cleaned, and refilled with water at room temperature. Its mouth is sealed with a dry glass plate, and the mass of the assembly is recorded (M4).

Using the four masses (M1 to M4) and applying Equation 3.7, the MVD of the HMA mix is calculated in a situation where no water is absorbed by the aggregate.

$$MVD = \frac{(M_2 - M_1)}{\frac{((M_4 - M_1) - (M_3 - M_1))}{\rho_w}} \quad \text{Equation 3.7}$$

Where:

MVD = maximum void-less density (kg/m³)

M₁ = mass of the flask assembly (g)

M₂ = mass of the flask assembly and the sample (g)

M₃ = mass of the flask assembly and the HMA specimen filled with water (g)

M₄ = mass of the flask and water (g)

ρ_w = water density (kg/m³)



Figure 3.16: MVD test set-up

After determining the bulk density (BD) and MVD, Equation 3.8 was used to calculate the air voids content (VA) of compacted HMA specimens (SANS 3001-AS11, 2011). The air voids contents of the samples form the basis of the analysis provided in Chapter 5.

$$VA = \frac{(MVD - BD)}{MVD} \times 100 \quad \text{Equation 3.8}$$

3.4 Investigation of the influence of compaction on HMA rutting resistance

The primary goal of laboratory HMA compaction is to fabricate asphalt specimens to characterise HMA volumetric properties and mechanical properties. Among other considerations, choosing a compaction device depends on the HMA specimen's geometrical requirements for a specific test. Most HMA performance tests make use of cylindrical-, rectangular- or trapezoidal-shaped specimens of varying sizes. Due to the test specimens' geometrical requirements, different types of compaction devices are often employed in the laboratory to compact HMA samples. In South Africa, a gyratory compactor is recommended for the compaction of cylindrical HMA samples to evaluate mix volumetric properties (Sabita Manual 35/TRH 8, 2020). The gyratory compactor is also used to compact samples for the characterisation of HMA mix properties, including workability, stiffness, strength, and rutting resistance. On the other hand, rectangular beam specimens prepared from slab roller-compacted samples are used to characterise the cracking resistance of HMA using the four-point beam fatigue test. It should be pointed out that other mix properties such as strength and rutting resistance can also be evaluated by using slab roller-compacted samples.

Ideally, the laboratory compaction method should reflect the field compaction. Unfortunately, most of the available laboratory compaction devices have some limitation in terms of simulating the field compaction. This is primarily because asphalt compaction is a complicated process in which the reorientation and interlock of aggregates occur. To this end, it is important to recognise that different compaction devices may produce asphalt specimens with different engineering properties. Thus, this specific objective of the study investigated the rutting resistance of HMA samples compacted using a gyratory compactor and slab roller compactor – the compactor types that are used most often in South Africa and worldwide. Two HMA rutting tests were used during the investigations: the Repeated Simple Shear Test at Constant Height (RSST-CH) and the Uniaxial Repeated Shear Test (URST). The test results that were obtained form the basis of the analysis provided in Chapter 6.

3.4.1 HMA mix designs

Two typical South African wearing course HMA mixes were selected to investigate the influence of the compaction method and compaction density on rutting performance. The gradation structures of the two HMA mixes were 10 mm NMPS (sand skeleton) and 20 mm NMPS (stone skeleton) respectively. The 10 mm NMPS mix comprised Andesite aggregate and 50/70

penetration grade bitumen (PG 58-22), with optimum binder content of 5.0%. The 20 mm NMPS mix comprised Dolerite aggregate and 35/50 penetration grade binder (PG 64-16), with optimum binder content of 4.3%. Figure 3.17 and Figure 3.18 plot the HMA mix design gradation curves for the 10 mm and 20 mm NMPS mixes respectively. The design gradations of both mixes fall within the envelopes specified in the South African standard specifications for road and bridge works (COTO, 1998).

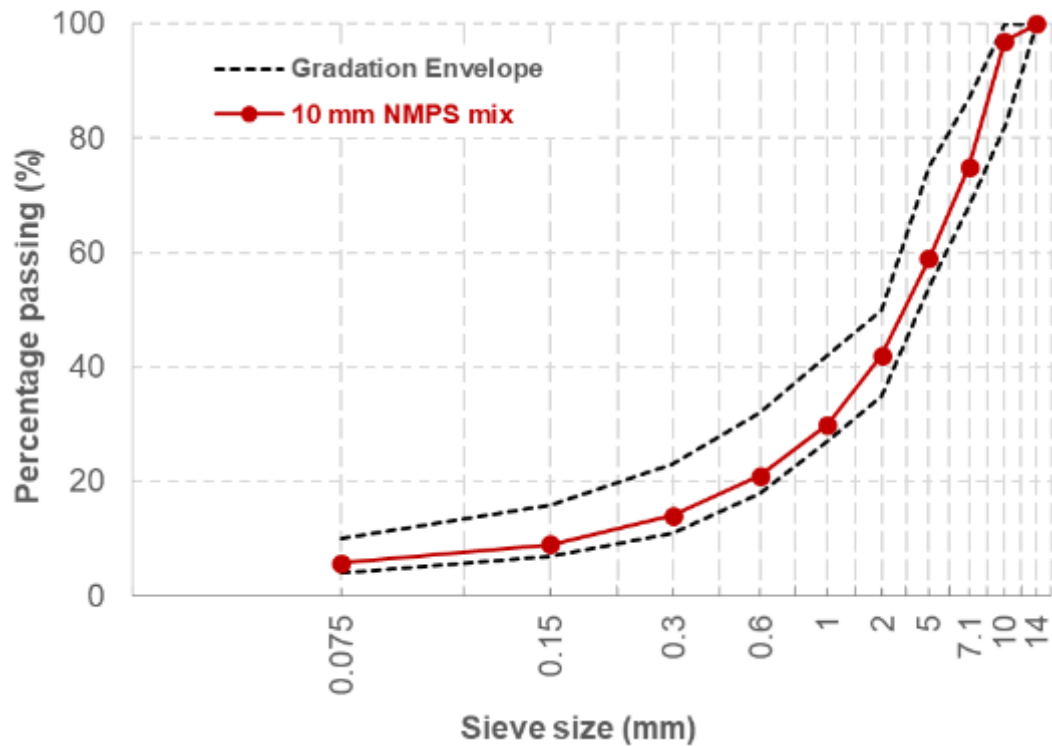


Figure 3.17: Design gradation for the 10 mm NMPS mix

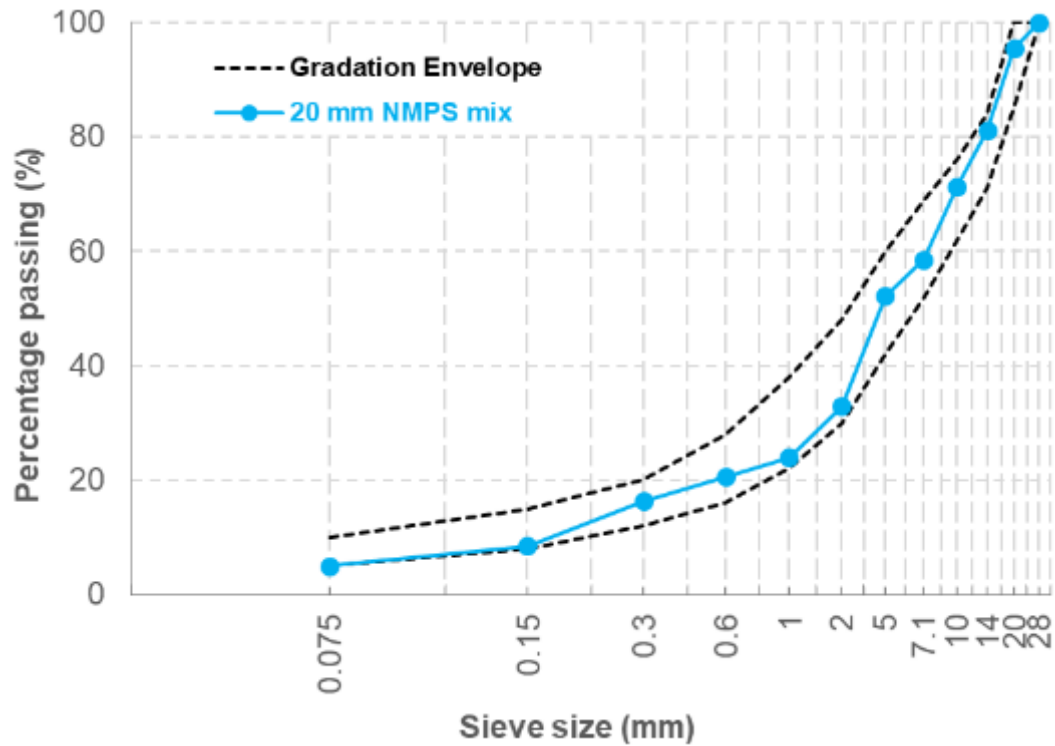


Figure 3.18: Design gradation for the 20 mm NMPS mix

3.4.2 Mixing and compaction of asphalt samples

The mixing of HMA samples was done using a mechanical mixer as described in Section 3.2.4. Following simulation of short-term ageing, the HMA samples were compacted using two different methods: the gyratory compactor and slab roller compactor. Figure 3.19 shows photos of the (a) gyratory compactor and (b) slab roller compactor used in the study. For each compaction method, two sets of samples were compacted to a target of 4.0% and 7.0% air voids content. The main reason for compacting the HMA samples to two different target air voids contents was to investigate the effect of compaction density on the HMA rutting resistance.



(a) Gyratory compactor



(b) Slab Roller compactor

Figure 3.19: Gyratory and slab roller compactors

The gyratory compaction process is illustrated in Figure 3.20. The following fundamental parameters controlled the compaction process:

- Vertical pressure: usually 600 kPa
- Angle of gyration: 1.25° external angle recommended in South Africa
- Gyration frequency: 30 gyrations per minute recommended in South Africa

The above control parameters are often established and specified in gyratory compaction procedures and protocols applicable in a specific country. Other operating parameters that influence compaction density include the number of gyrations and the mould diameter. A 150 mm diameter mould was used in this study.

Using a gyratory compactor, the compaction is achieved by applying static compression pressure and shearing of the HMA sample. Static compression pressure is applied to the HMA sample placed in a cylindrical mould through a fixed upper ram. A gyratory motion is implemented using three actuators attached to the hydraulic lower ram that is placed at an interval of 120°, resulting in shearing action.

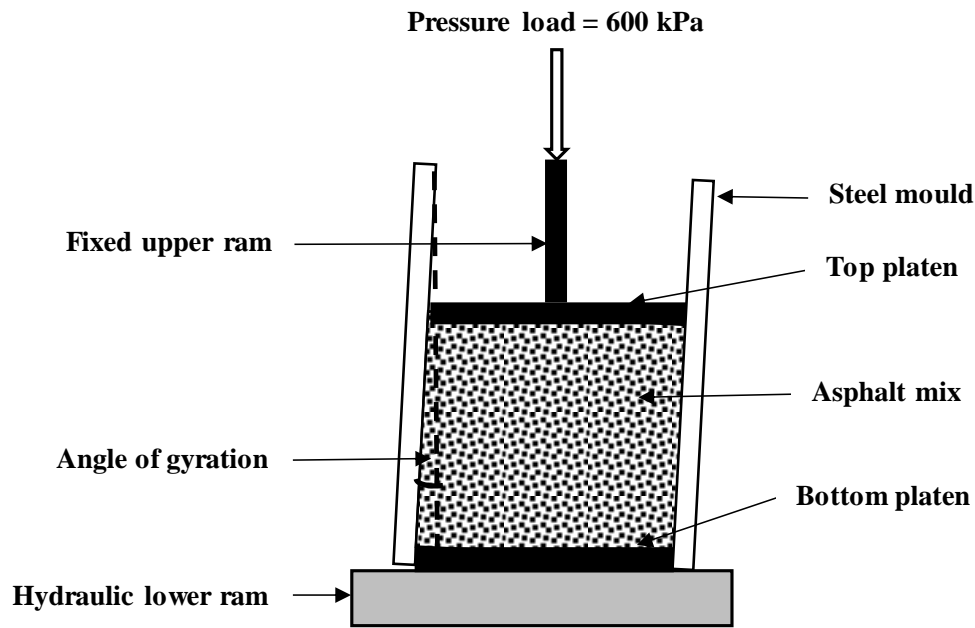


Figure 3.20: The gyratory compaction process

Figure 3.21 provides a schematic illustration of the HMA compaction process performed by a roller slab compactor. The following fundamental parameters control this compaction process:

- Static vertical load
- Pendulum motion of the loading plate
- The horizontal movement of the slab mould

During the slab roller compaction process, a static load is applied to the sample through a semi oval-shaped contact plate that exhibits a pendulum-like motion. At the same time, the rectangular mould moves horizontally. The roller compactor used in this study has a maximum loading capacity of 30 kN. A maximum load was used in this study, translating to a static pressure of approximately 275 kPa. Other operating parameters that influence compaction density include the cycles applied to the HMA sample and the size of the rectangular mould. In this study, a standard 400 mm x 300 mm mould was used.

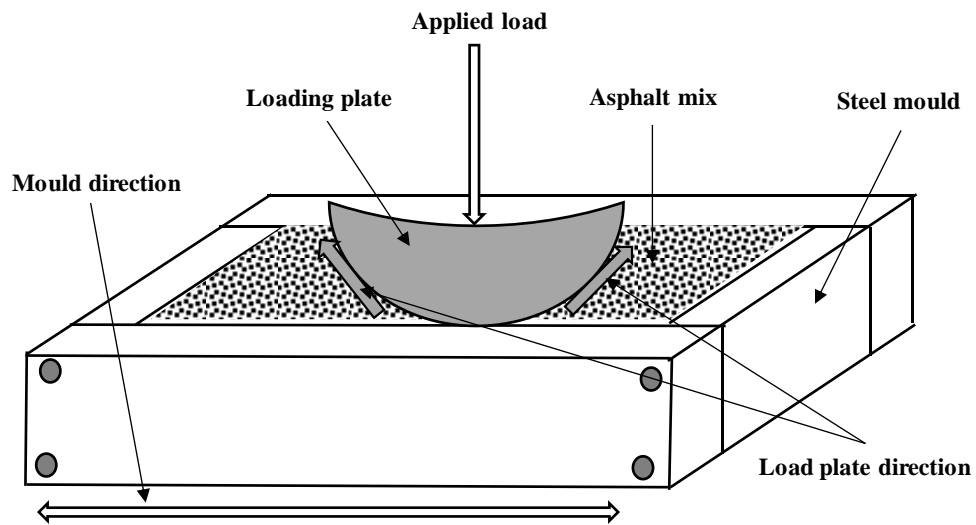


Figure 3.21: The slab roller compaction process

Essentially, the gyratory compactor yields cylindrical asphalt samples, whereas the roller compactor produces rectangular-shaped asphalt samples. Figure 3.22 shows photos of the typical samples produced by the gyratory and slab roller compactors. These HMA samples were used to prepare the rutting test specimens shown in Figure 3.23 and Figure 3.24 respectively.



a) Gyratory compacted sample



b) Slab roller compacted sample

Figure 3.22: Typical HMA samples compacted by the (a) gyratory and (b) slab roller compactors



a) RSST-CH test specimens



b) URST test specimens

Figure 3.23: Typical HMA specimens prepared from gyratory-compacted samples



a) RSST-CH test specimens



b) URST test specimens

Figure 3.24: Typical HMA specimens prepared from slab roller-compacted samples

3.4.3 HMA rutting resistance evaluation

As stated earlier, the rutting resistance of HMA specimens was evaluated in this study using two different test methods: the Repeated Simple Shear Test at Constant Height (RSST-CH), and the recently introduced Uniaxial Repeated Shear Test (URST). The fundamental differences between the two tests include the following:

- In the URST, the shear load is applied vertically (same as the compaction direction), whereas in the RSST-CH, the shear load is applied horizontally (perpendicular to compaction direction), and
- The URST is a confined test, with the specimen in a ring, while the RSST-CH test is an unconfined test with the top and bottom plates glued to the specimen.

The URST and RSST-CH tests are best suited to evaluate the rutting performance of HMA as a result of vertical consolidation and lateral distortion respectively. Figure 3.25 shows photos of the Simple Shear Tester (SST) and Uniaxial Shear Tester (UST) set-up used for conducting the RSST-CH and URST tests respectively.

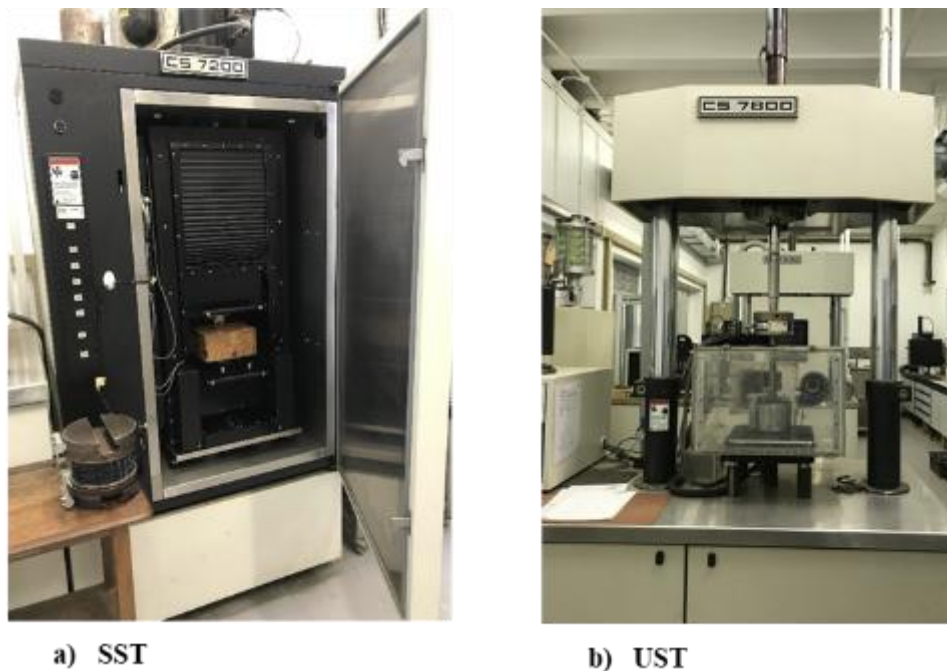


Figure 3.25: SST and UST set-up

The RSST-CH test determines the permanent shear strain of asphalt samples. Figure 3.26 illustrates simple shear acting on asphalt specimens during the RSST-CH test. During the application of the shear load, the vertical (L) movement of the sample is kept constant, and Equation 3.9 is used to calculate the resulting shear strain.

$$\text{Shear strain} = \frac{\Delta L}{L} \quad \text{Equation 3.9}$$

Where:

ΔL = horizontal deformation

L = original length

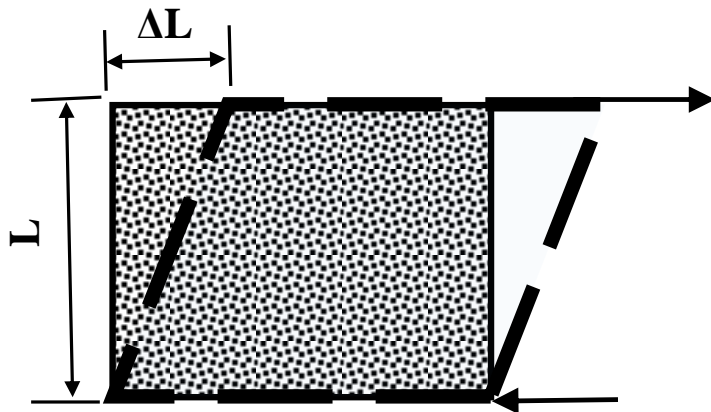


Figure 3.26: Schematic representation of the RSST-CH

In order to create the situation presented in Figure 3.26, the asphalt sample is glued to plate on the top and bottom (see Figure 3.27). In this study, the RSST-CH tests were carried out according to procedures stipulated in the AASHTO T 320 standard test method. A 69 kPa cyclic load was applied to the asphalt specimen horizontally by moving the bottom plate. Each cycle comprised the load being applied for 0.1 seconds followed by a 0.6 seconds rest period. Linear Variable Displacement Transformers (LVDTs) were used to measure the horizontal displacement of the asphalt specimen. A vertical actuator maintained the height of the specimen.



Figure 3.27: The RSST-CH test set-up

The UST test device is cheaper and more simple, as it can be used in combination with any laboratory machine capable of applying a controlled vertical load – such as the commonly

available Universal Testing Machine (UTM) or the CS 7800 used in this study. The CS 7800 machine was modified to include a temperature conditioning chamber (see Figure 3.28). Furthermore, the URST set-up does not require the asphalt specimen to be glued to the top and bottom plates, as is the case for the RSST-CH.



Figure 3.28: UST temperature conditioning chamber

The URST tests were conducted on the 150 mm asphalt specimens with a 50 mm hole drilled in the middle. Figure 3.29 provides a two-dimensional representation of the UST test set-up. The asphalt specimen is placed into a cylinder, which restricts horizontal strain. A knee joint is used to apply a cyclic vertical load to the sample through a steel insert in the hollow of the sample.

Like the RSST-CH, the URST tests were carried out according to procedures stipulated in the AASHTO T 320 standard test method. A vertical cyclic load of 69 kPa (i.e., approximately 1.2 kN shear load) was applied to the asphalt test specimen. Each loading cycle lasted for 0.1 seconds of load and 0.6 seconds of rest respectively. The resulting vertical displacement was recorded using three LVDTs mounted at 120° intervals along the specimen's circumference, as illustrated in Figure 3.30.

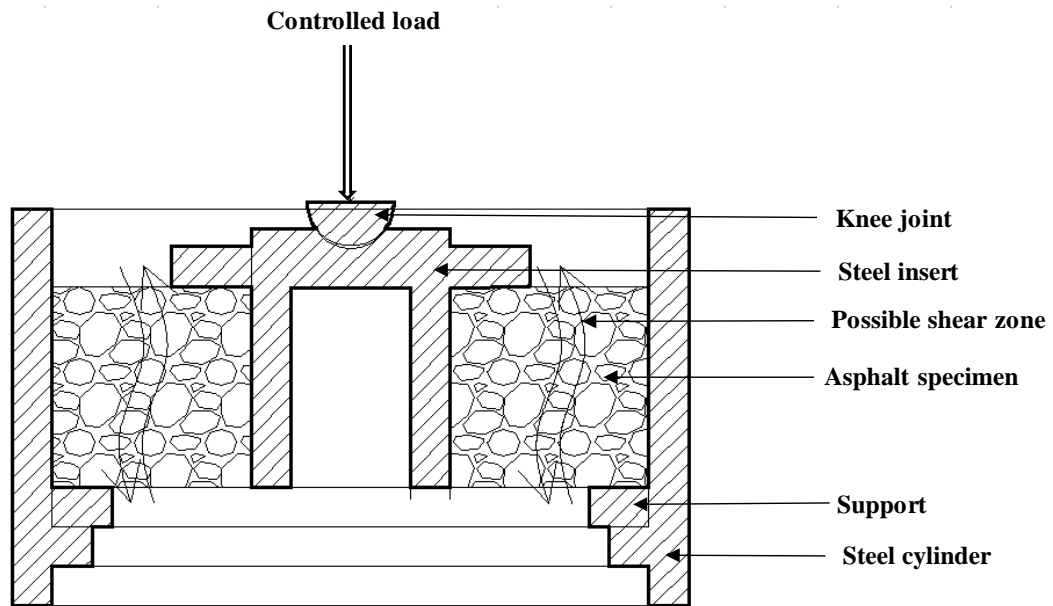


Figure 3.29: Two-dimensional representation of the UST test set-up (Zak et al., 2016)

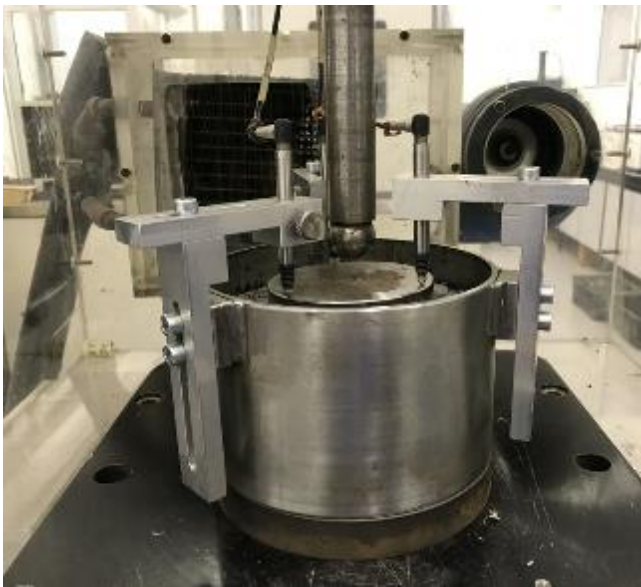


Figure 3.30: UST test set-up inside the temperature chamber

RSST-CH and URST tests were undertaken in the two different phases of this study. The first phase focused on a comparative evaluation of the two rutting tests. During this phase, rutting tests were conducted on roller slab-compacted samples at three temperatures (40, 50, and 60°C). For each temperature, three replicate specimens were tested and used to calculate the average result. Based on the analysis of the results of the first phase of testing, a temperature of 50°C was found to be most appropriate for the second testing phase, which investigated the influence of the compaction method and compaction density on HMA rutting resistance. The 50°C allowed for

the collection of sufficient data set for the comparison of the rutting resistance of the asphalt mixes evaluated. It is also recommended in the South African guidelines for designing asphalt mixes (Sabita manual 35, 2020). Hence, all the HMA rutting tests in the second phase were carried out at a temperature of 50°C.

3.5 Summary

This chapter presented the methodology followed during the study. It offered detailed descriptions of the approaches followed to investigate the influence of aggregate packing on HMA compactability, the influence of the spatial distribution of air voids on compacted HMA, and the influence of the compaction method on HMA rutting resistance. Overall, the study methodology included the following key tasks: material sourcing (i.e., aggregates, bitumen, etc.), materials preparation, asphalt mix design, mixing and sample compaction, and specimen preparation, limited field coring; density measurements, volumetric analysis, specimen conditioning; laboratory testing (RSSTCH, URST), and the associated data analysis.

4 INFLUENCE OF AGGREGATE PACKING ON HMA COMPACTABILITY

4.1 Introduction

Chapter 4 presents the analysis and discussion of the results of the experimental work described in Section 3.2, namely to investigate the influence of aggregate packing characteristics on HMA compactability. The gradations of three 10 mm NMPS grading structures and three 20 mm NMPS wearing course HMA mixes commonly used in South Africa were analysed to determine aggregate packing parameters. For each of the gradation structures, HMA samples were compacted using a gyratory compactor, after which the compaction data was analysed to determine five parameters of HMA compactability. The HMA compactability parameters were subsequently correlated with the aggregate packing parameters.

Chapter 4 is structured as follows: Section 4.2 presents an analysis of aggregate gradation curves to determine aggregate packing parameters. The analysis of gyratory compaction data to determine parameters that describe the HMA compactability is presented in Section 4.3. A parametric correlation of the aggregate packing parameters and HMA compactability parameter is presented in Section 4.4, followed by a summary of the key findings in Section 4.5.

4.2 Aggregate packing analysis

A total of six aggregate gradation curves (three 10 mm NMPS and three 20 mm NMPS) were used for this aspect of the study. The gradation curves were analysed to determine eight aggregate packing parameters – shape factor (n); gravel-to-sand ratio (G/S); three traditional Bailey ratios; and three rational Bailey ratios. The results of the aggregate packing parameters are presented and discussed in the sections that follow. Finally, a theoretical evaluation of the gradation parameters was undertaken to establish the most appropriate gradation parameters that can be recommended for use by asphalt mix designers.

4.2.1 Shape factor of aggregate gradation curve and the ratio of gravel to sand

Over the years, the shape factor (n) of the aggregate gradation curve has been used to describe aggregate packing. The gradation curves of the aggregate used in this study were analysed to determine their shape factor (n) through a non-linear optimisation procedure (see Equation 2.2 introduced earlier in Chapter 2). The optimization procedure involved using the actual grading analysis results to fit a non-linear model to determine each grading curve's shape factor (n). Figure

4.1 presents a typical plot of actual gradation and of the gradation determined using the n parameter through the optimisation procedure. The two gradations are similar, indicating that the n parameter can be used to describe the aggregate gradation curve. Following the determination of the shape factor (n) of each aggregate gradation curve, it was subsequently used to determine the gravel-to-sand ratio (G/S) parameter using Equation 2.3 introduced earlier in Chapter 2.

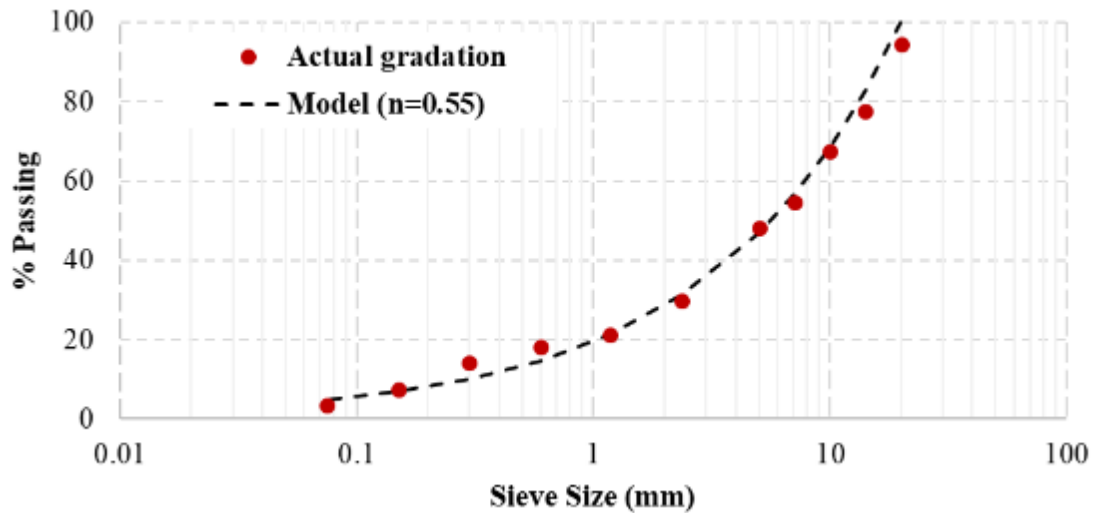


Figure 4.1: Determining the gradation shape factor (n)

Figure 4.2 and Figure 4.3 present the aggregate gradation parameters (n and G/S) of 10 mm NMPS and 20 mm NMPS mixes respectively. For each 10 mm and 20 mm NMPS, the three gradation curves included coarse, medium and fine-graded. The aggregate packing parameters suggest that the finer the gradation structure, the lower the G/S and n values. Overall, the observed trend is consistent with the original concept formulated by Fuller and Thompson (1907), which widely accepts that the lower the n value, the finer the gradation, and the opposite is true.

For the gradation curves analysed in this study, the n values appear to be relatively less sensitive to the change in gradation structure than the G/S values. For instance, the n parameters of the 10 mm NMPS gradation were 0.40, 0.43 and 0.47 for fine, medium and coarse gradation structures respectively. On the other hand, the G/S values of the 10 mm NMPS were 0.72, 0.66 and 0.62 for fine, medium and coarse gradation structures respectively. A similar trend can be observed in Figure 4.3 for the 20 mm NMPS grading structures, except that the values are generally higher than those for 10 mm NMPS. Overall, the observed trends suggest that for the gradations analysed in this study, the G/S parameter appears to differentiate the gradation structure better than the n parameter.

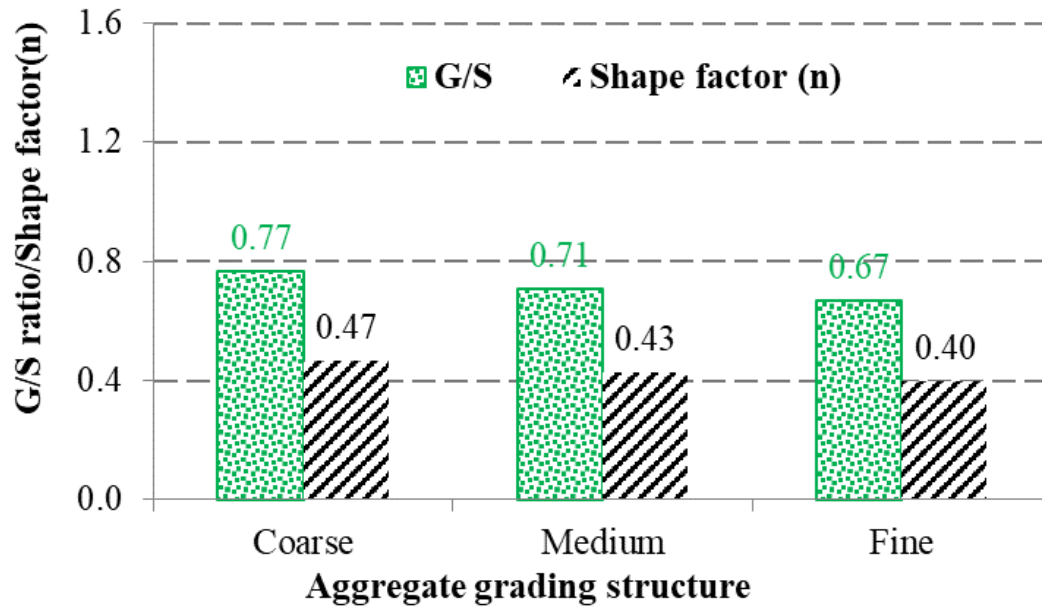


Figure 4.2: G/S and n parameters of 10 mm NMPS mix

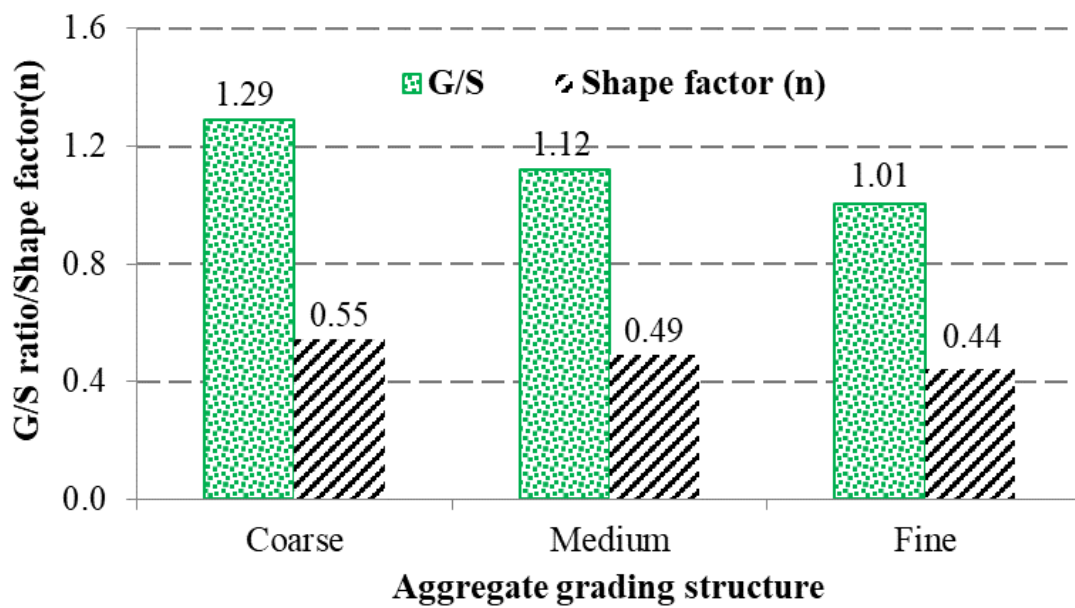


Figure 4.3: G/S and n parameters of 20 mm NMPS mix

4.2.2 Traditional Bailey ratios

The same gradations used for the determination of n and G/S gradation parameters (Section 4.2.1) were analysed to determine the three traditional Bailey ratios (CA, FAc, and FAf). Equations 2.4

to 2.6, as introduced in Chapter 2, were used respectively. The CA, FA_c and FA_f describe the packing characteristics of the macro, midi and micro aggregate skeleton matrix levels respectively.

Figure 4.4 and Figure 4.5 present the traditional Bailey ratios of 10 mm NMPS and 20 mm NMPS mixes respectively. Overall, the results show that all three traditional Bailey ratios increase as the gradation structure becomes finer. However, the CA ratio appears to be more sensitive than the FA_c and FA_f ratios to changes in the aggregate grading structure. This means that out of the three traditional Bailey ratios, the CA ratio appears to be a better descriptor of the gradation structure. Furthermore, the CA ratio values of the 10 mm NMPS gradation structures are generally higher than those of the 20 mm NMPS gradation structures, indicating the magnitude of the CA ratio depends on the NMPS.

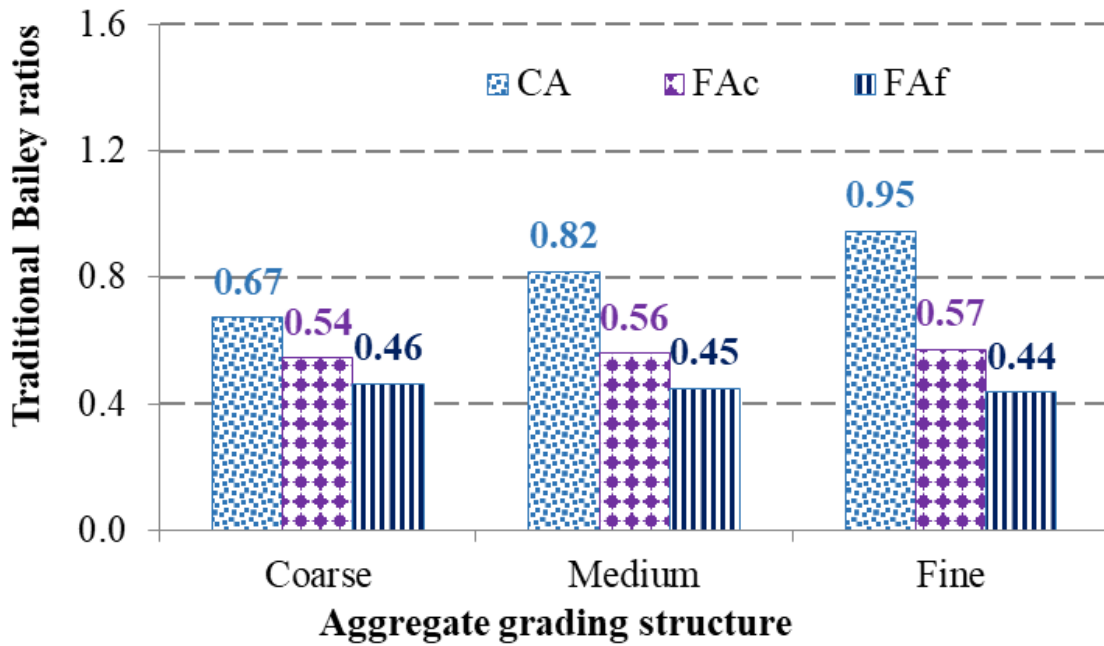


Figure 4.4: Traditional Bailey ratios of the 10 mm NMPS mix

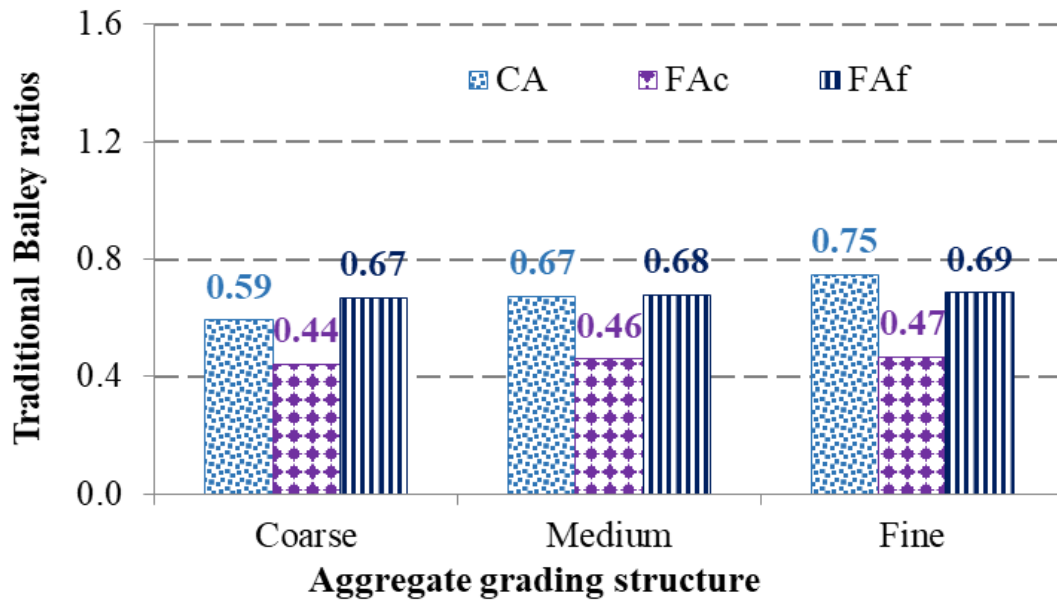


Figure 4.5: Traditional Bailey ratios of the 20 mm NMPS mix

4.2.3 Rational Bailey ratios

Three rational Bailey ratios – Rational Coarse Aggregate ratio (CA_r); Rational Coarse/Fine ratio (C/F); and Rational Fine Aggregate Fine ratio (FA_rmf) – were determined using Equations 2.7 to 2.9 respectively. Similar to the traditional Bailey ratios, the CA_r, C/F and FA_rmf describe the packing characteristics of the macro, midi and micro aggregate skeleton matrix levels respectively.

Figure 4.6 and Figure 4.7 present the rational Bailey ratios of the 10 mm NMPS and 20 mm NMPS mixes respectively. Contrary to the traditional Bailey ratios, the rational Bailey ratios decrease as the aggregate gradation structure becomes finer (with the exception of the FA_rmf for the 10 mm NMPS mix). This trend was expected and is consistent with the available literature. The rational Bailey ratios were formulated in an inverse format (i.e., coarse/fine), in line with the binary aggregate fraction packing principles (Olard, 2015; Horak et al., 2017; Horak & Cromhout, 2018; Komba et al., 2019a).

Furthermore, unlike the traditional Bailey ratios, the three rational Bailey ratios (CA_r, C/F and FA_rmf) are more sensitive to the aggregate grading structure. This means that the rational Bailey ratios appear to provide a better description than the traditional Bailey ratios of the packing characteristics of the macro, midi and micro skeleton matrix levels.

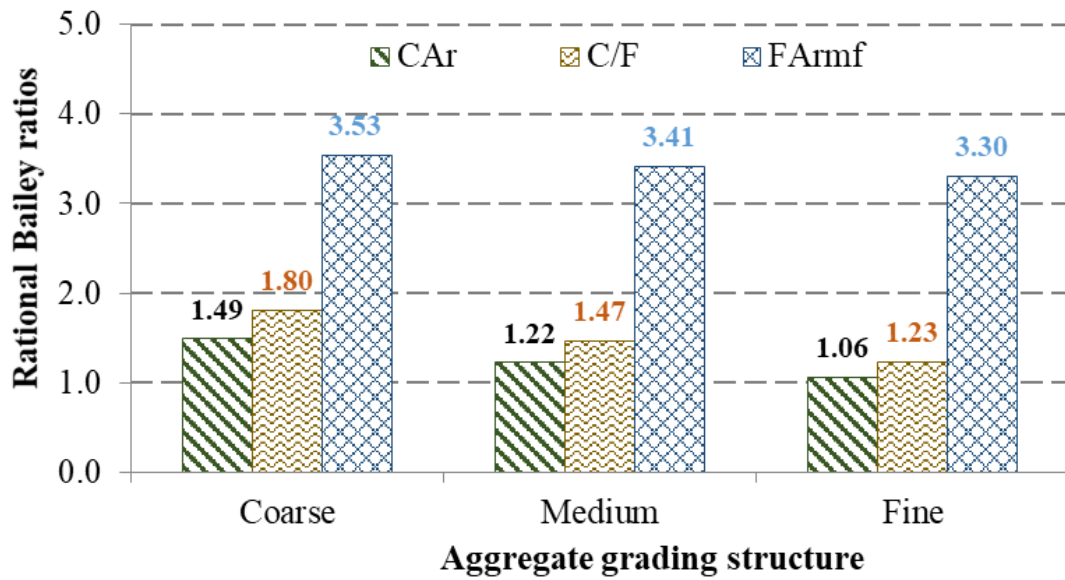


Figure 4.6: Rational Bailey ratios of the 10 mm NMPS mix

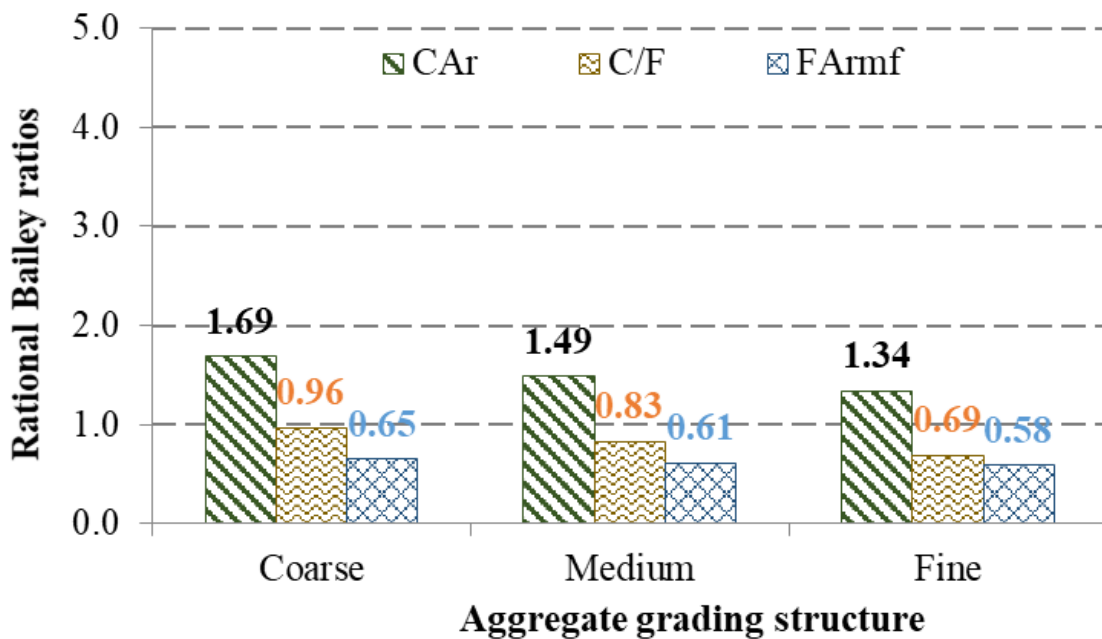


Figure 4.7: Rational Bailey ratios of the 20 mm NMPS mix

4.2.4 Correlations of aggregate packing parameters

To better understand their relationships, this section provides a correlation of the aggregate packing parameters determined in Sections 4.2.1 to 4.2.3. The following correlations were drawn:

- Shape factor correlated with gravel-to-sand ratio;

- Shape factor and gravel-to-sand ratio correlated with traditional Bailey ratios;
- Shape parameter and gravel-to-sand ratio correlated with rational Bailey ratios, and
- Correlation between the traditional Bailey ratios and the rational Bailey ratios.

Figure 4.8 to Figure 4.10 shows plots of the correlation trends and display the coefficients of determination (R^2) in each figure. The three points plotted in the figures represent aggregate packing determined for each of the fine, medium and coarse gradation structures for the 10 mm and 20 mm NMPS mixes.

Overall, the shape factor (n) exhibits an excellent positive correlation with the gravel-to-sand ratio (G/S), as demonstrated in Figure 4.8. This was expected because the n grading parameter is one of the inputs for determining the G/S parameter (Equation 2.3). The gradation parameters (n and G/S) exhibited negative correlations with traditional CA and the FAC ratios but positive correlations with the $F Af$ (Figure 4.9 and Figure 4.10). Similar trends were observed for the correlations between the G/S and, and the rational Bailey ratios (CA_r , C/F and $F Arm_f$), but the trend lines were in the opposite direction. As expected, this is due to the rational Bailey ratios are in an inverse format (i.e., coarse/fine), as was explained earlier.

The slope of the correlations between the G/S and n , and the traditional Bailey ratios (CA , FAC and $F Af$) is steeper than that of the correlations with the rational Bailey ratios (CA_r , C/F and $F Arm_f$). This is in line with the findings reported in Section 4.2.3, according to which the rational Bailey ratios are more sensitive to change in the gradation structure than the traditional Bailey ratios.

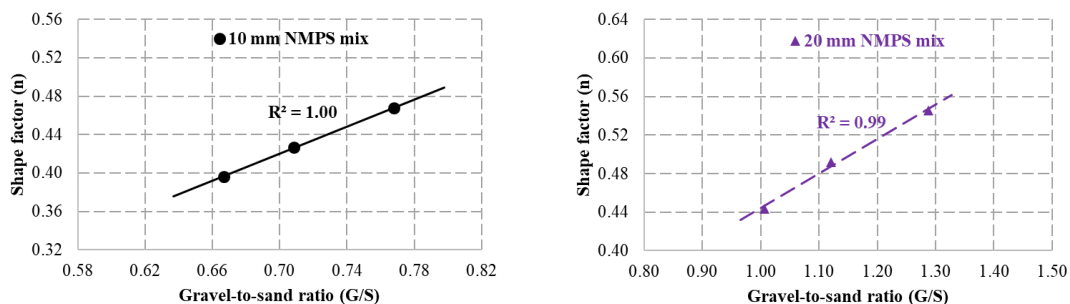


Figure 4.8: n parameter correlated with G/S parameter

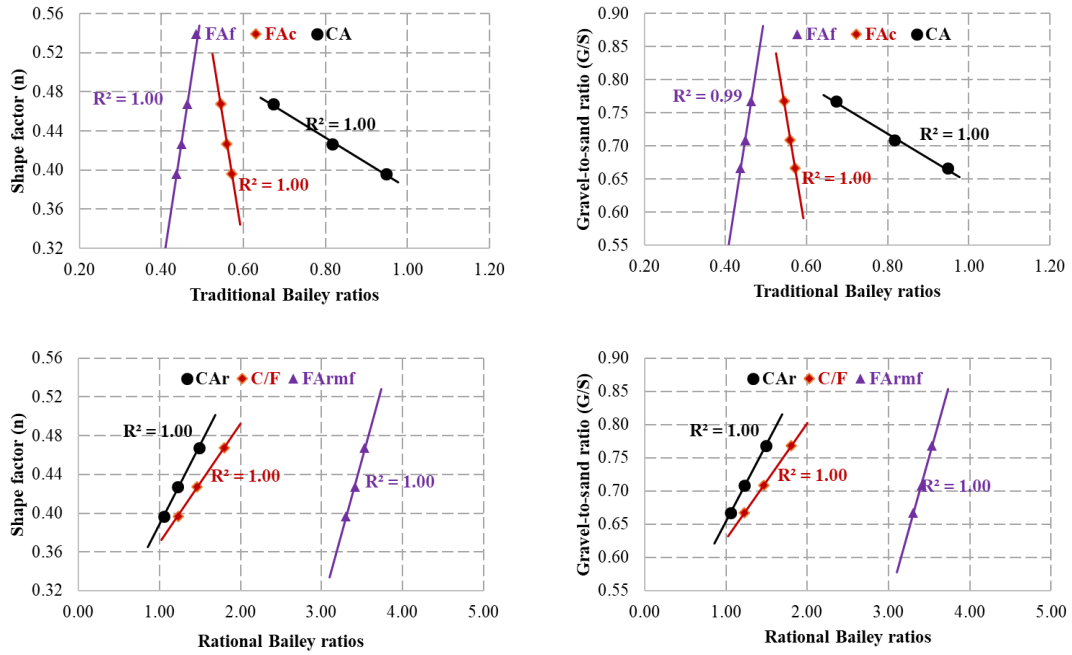


Figure 4.9: n and G/S parameters correlated with Bailey ratios – 10 mm NMPS mix

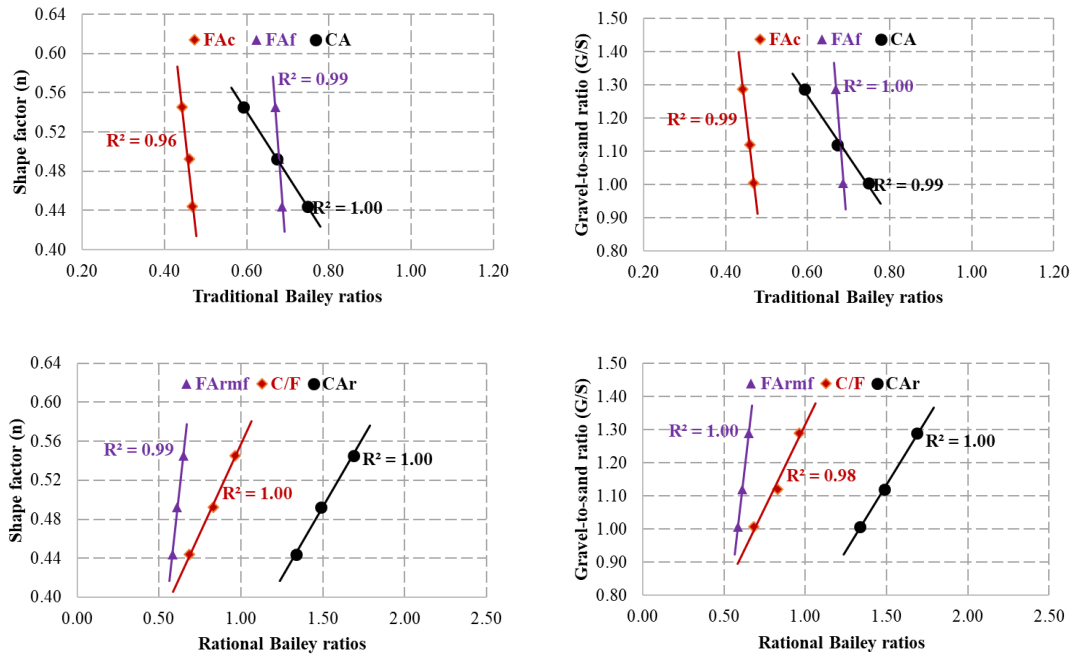


Figure 4.10: n and G/S parameters correlated with Bailey ratios – 20 mm NMPS mix

4.2.5 Sensitivity of Bailey ratios to change in gradation

Five different theoretical gradation curves with 20 mm NMPS were created to verify the sensitivity of the Bailey ratios to change in gradation. The theoretical gradation curves were

created such that the shape factor (n) ranged from 0.3 to 0.7 at an increment of 0.1. The gradation curves as presented in Figure 4.11 show that the higher the shape factor (n) value, the coarser the gradation – which was the expected trend.

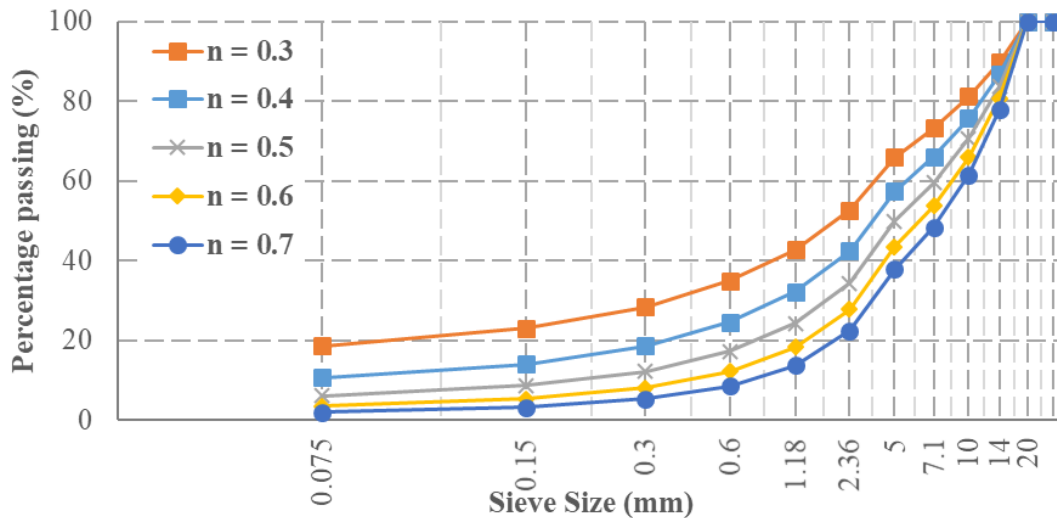


Figure 4.11: Theoretical gradation curves

The theoretical gradation curves were analysed to determine their traditional and rational Bailey ratios. Figure 4.12 and Figure 4.13 show the traditional and rational ratios respectively. As expected, the traditional Bailey ratios decreased as the aggregate gradation structure became coarser. In contrast, the rational Bailey ratios exhibited an inverse trend (i.e., ratios increased as the gradation structure became coarser). This is because the rational Bailey ratios have been formulated in inverse format.

The macro-level packing parameter (i.e., CA) of the traditional Bailey ratio ranges from 0.81 to 0.38 (a difference of 0.43), and corresponds to a change in gradation factor (n) from 0.3 to 0.7 (Figure 4.12). On the other hand, the equivalent macro-level parameter (i.e., CA_r) for the rational Bailey ratio ranges from 1.23 to 2.59 (a difference of 1.36) and corresponds to a change in gradation factor (n) from 0.3 to 0.7 (Figure 4.13). Similar trends can be observed for the mid-level and micro-level packing parameters (i.e., F_{Ac} and F_{Af} for the traditional Bailey ratios and C/F and F_{Arm} for the rational Bailey ratios). The results confirm that the rational Bailey ratios are more sensitive to the changes in the gradation curve and they provide a better description of the packing characteristics of the gradation structure on the macro, midi (or meso) and micro skeleton matrix levels.

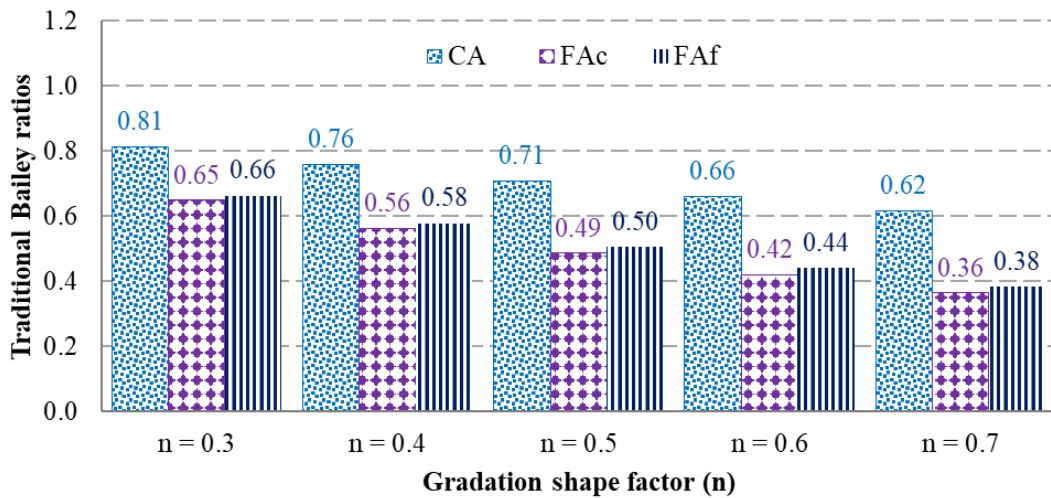


Figure 4.12: Traditional Bailey ratios of the theoretical gradation curves

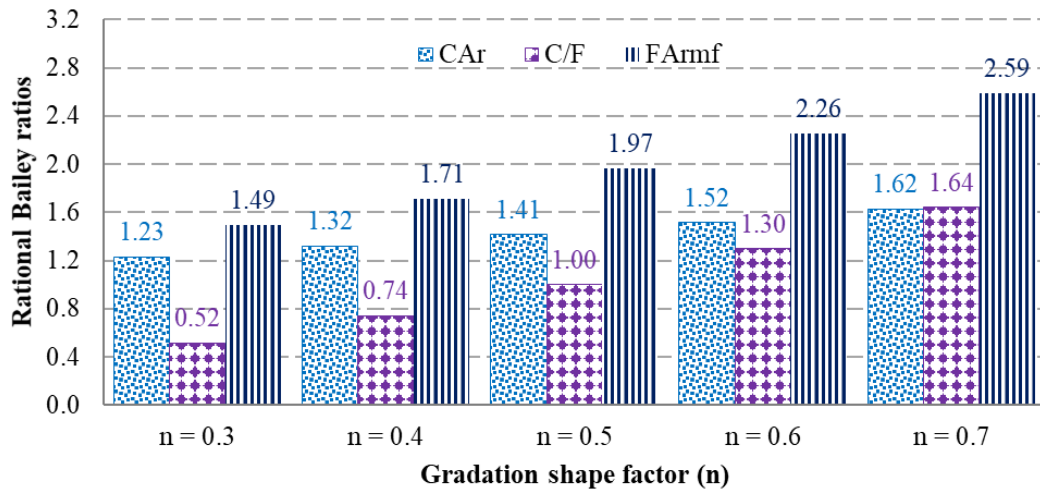


Figure 4.13: Rational Bailey ratios of the theoretical gradation curves

4.3 Determination of HMA compactability parameters

HMA mixes were manufactured based on each of the six aggregate gradation curves (three 10 mm NMPS and three 20 mm NMPS) used for packing analysis (see Section 4.2). The HMA mixes were compacted using a gyratory compactor. The compactability of each HMA mix was evaluated by analysing the gyratory compaction data to determine compactability parameters. These parameters indicate the mix's resistance to the compaction energy and they included locking point (LP), compaction energy index (CEI), traffic densification index (TDI300), compaction slope (CS), and the area under shear stress (ASS_{max}).

The next sections present the results of the analysis of each of the HMA mix compactability parameters. These compactability parameters were further correlated with aggregate packing parameters in Section 4.4.

4.3.1 Locking point

During the gyratory compaction process, a rapid change in the HMA sample height occurs at the initial stage of the compaction process, as demonstrated in Figure 4.14. This is because during the initial stage of HMA compaction, the material is in a loose state, which makes it easier to compact. As the compaction proceeds (i.e., compaction efforts or the number of gyrations are increasing), the aggregate particles are forced together. As they lock up to form a packed structure, the process is accompanied by the reduction of air voids. Once aggregate particle interlocking starts to take place, it becomes difficult to compact the HMA specimen, and this results in a lower rate of change of the HMA sample height.

The number of gyrations at which the HMA mix resists further compaction is referred to as the locking point (LP) and is related to the compactability or workability of the HMA mix. The locking point is defined in this study as the first of three consecutive gyrations that yield the same HMA specimen height, where this gyration follows the two sets of gyrations that have the same height (Vavrik et al., 1999). Figure 4.15 illustrates how the locking point is determined for typical gyratory compaction data. The locking point concept can also be successfully used to prevent overcompaction of HMA mixes (Vavrik et al., 1999).

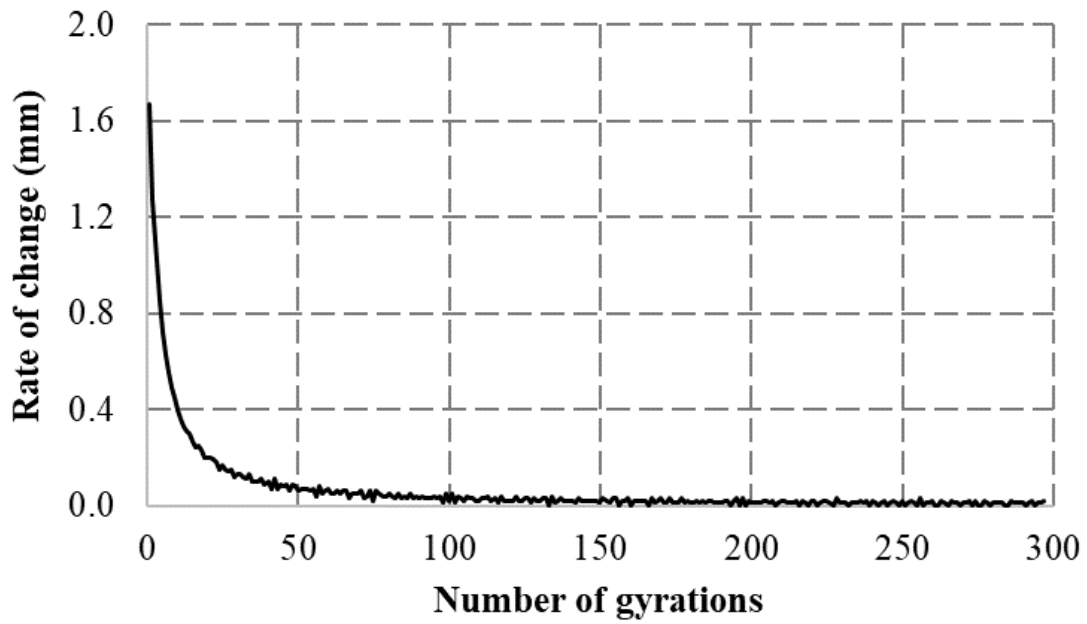


Figure 4.14: Rate of change in HMA sample height versus the number of gyrations

| Number of gyrations | Specimen height (mm) |
|---------------------|----------------------|
| 75 | 156.5 |
| 76 | 156.5 |
| 77 | 156.4 |
| 78 | 156.4 |
| 79 | 156.3 |
| 80 | 156.3 |
| 81 | 156.2 |
| 82 | 156.2 |
| 83 | 156.2 |
| 84 | 156.1 |
| 85 | 156.1 |
| 86 | 156.0 |
| 87 | 156.0 |
| 88 | 156.0 |
| 89 | 155.9 |
| 90 | 155.9 |

Locking point →

Figure 4.15: Determination of the locking point

As previously indicated, a total of six HMA mixes were used in the study (three 10 mm NMPS and three 20 mm NMPS). For each of the 10 mm and 20 mm NMPS mixes, the three mixes included coarse, medium and fine-graded structures. For each gradation structure, three repeat

samples were compacted, and the compaction data was analysed to obtain locking points. Table 4.1 presents a summary of the statistical parameters of the results. The coefficient of variation (CoV) values were generally low (ranging from 1.9 to 10.6%), which indicated that the locking point was repeatable and had low variability. The standard deviation (STD) values are also generally low.

Table 4.1: Summary of locking point results

| Mix | Statistical parameter | Gradation structure | | |
|-------------------|-----------------------|---------------------|--------|-------|
| | | Coarse | Medium | Fine |
| 10 mm NMPS | Mean | 121.0 | 109.0 | 108.3 |
| | STD | 4.6 | 11.5 | 3.2 |
| | CoV (%) | 3.8 | 10.6 | 3.0 |
| 20 mm NMPS | Mean | 78.3 | 80.3 | 89.7 |
| | STD | 3.8 | 1.5 | 4.7 |
| | CoV (%) | 4.8 | 1.9 | 5.3 |

The mean locking point results are graphically presented in Figure 4.16. The locking points of the 20 mm NMPS mixes were generally lower than those of the 10 mm NMPS mixes. This indicates that the higher the NMPS, the more workable was the mix. For 10 mm NMPS mixes, the locking points decreased as the grading structure changed from coarser to fine, whereas the locking points of the 20 mm NMPS mixes increased as the grading structure changed from coarse to fine.

Overall, the locking point was influenced by the NMPS and the gradation structure. This indicates that the widely used concept of compacted HMA mixes to a predefined number of gyrations (i.e., N design) or targeted air voids content should be used in combination with the understanding locking point of the mix. This could help to prevent the possibility of breaking the aggregates and changing the gradation structure if excessive compaction is undertaken past the locking point.

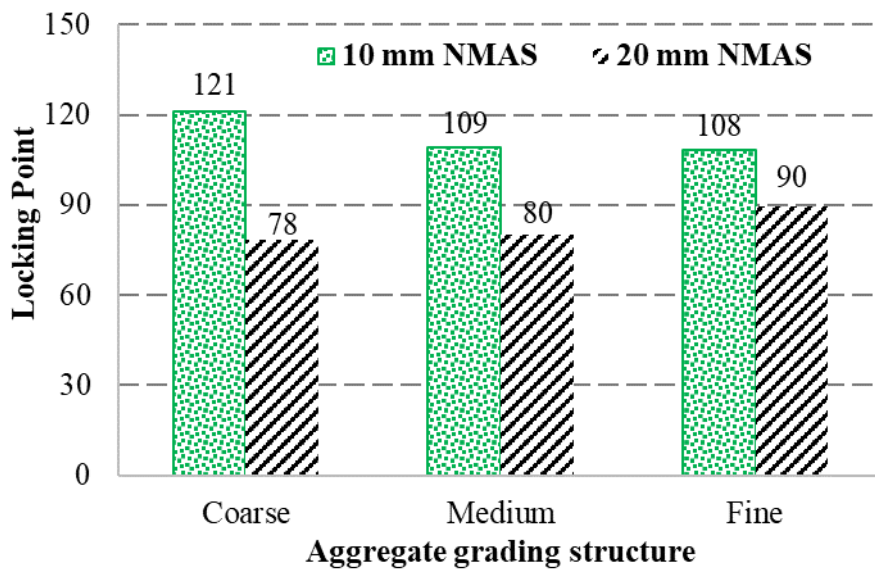


Figure 4.16: Average locking point results

4.3.2 Compaction energy index and traffic densification index

One of the fundamental outputs obtained after analysis of the basic gyratory compaction data is the degree of compaction at each gyration. Figure 4.17 shows a typical plot of the degree of compaction versus the number of gyrations, which is commonly referred to as the densification curve. The densification curves of all the asphalt samples tested in this study are included in Appendix A. The key characteristic of the densification curve, as depicted in Figure 4.17, is that at the initial stage of the compaction process, the HMA material is still in a loose state. Hence, the degree of compaction increases rapidly with an increase in the number of gyrations. Once the HMA sample has achieved a certain level of densification, further escalation in the number of gyrations results in a relatively small increase in the degree of compaction.

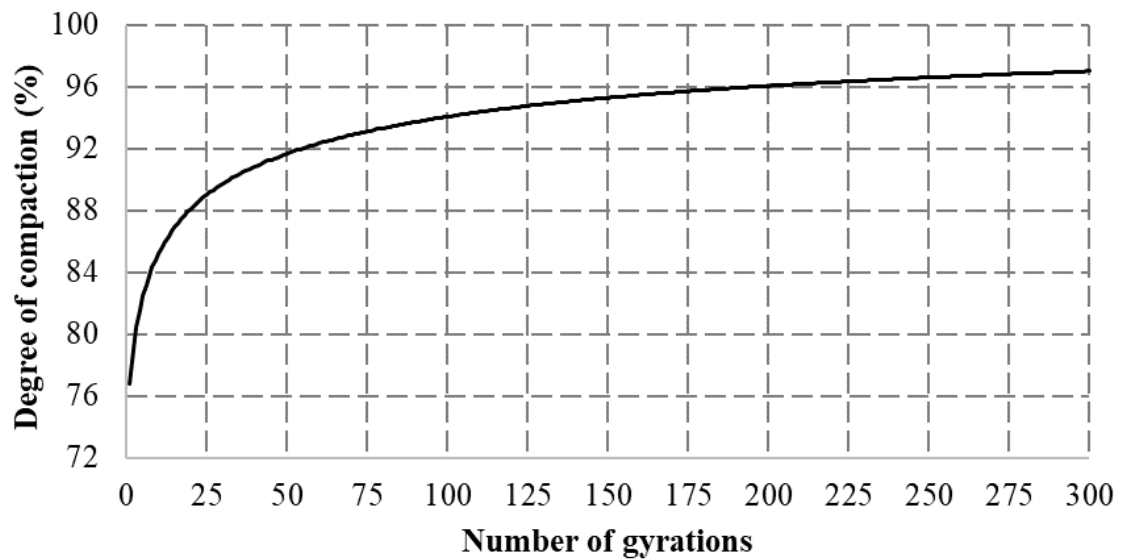


Figure 4.17: Typical gyratory compaction densification curve

The densification curve can be used to determine two parameters (see Figure 4.18.) that indicate the compactability of HMA mixes. The two parameters were the compaction energy index (CEI) (Bahia et al., 1998) and traffic densification index (TDI_{300}) (Komba et al., 2019a).

Generally, the HMA mixes with higher CEI values are more difficult to compact. On the other hand, the higher the TDI_{300} , the less difficult it is to compact the mix. It should however be emphasised that CEI values closer to zero are indicate tender HMA mixes and should be avoided, as they may fail prematurely (Awed et al., 2015).

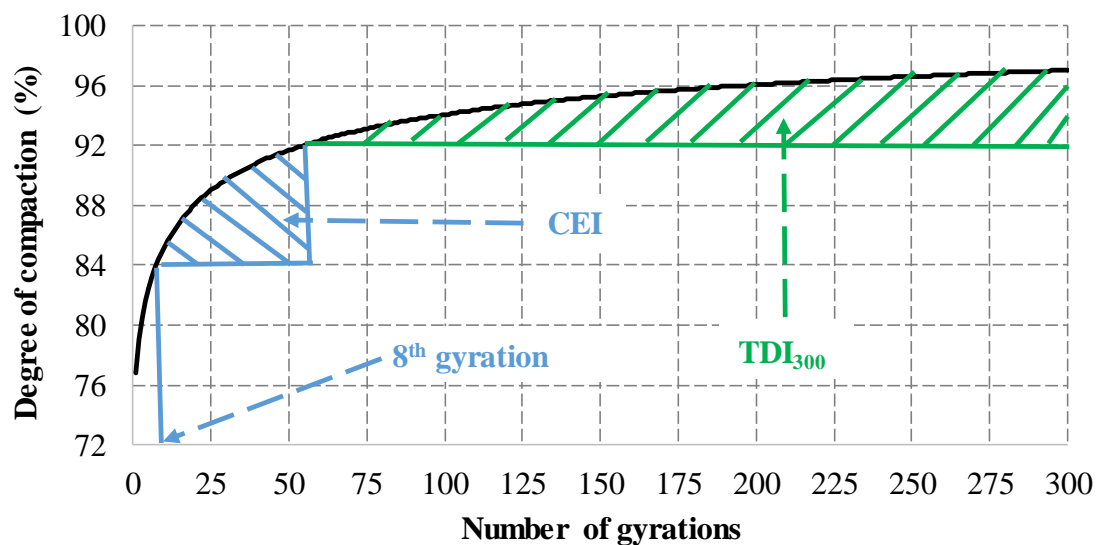


Figure 4.18: CEI and TDI_{300} determination

Table 4.2 and Table 4.3 present a summary of CEI and TDI₃₀₀ results respectively, while the mean CEI and TDI₃₀₀ parameters are graphically presented in Figure 4.19 and Figure 4.20 respectively. The average TDI₃₀₀ values of the 20 mm NMPS mixes are higher than those of the 10 mm NMPS mixes, indicating that coarser-graded mixes are easier to compact than fine-graded mixes. For the same NMPS, the TDI₃₀₀ values increase as the gradation structures change from coarser to fine graded, indicating that less compaction effort is required. Similarly, the CEI values decrease as the gradation structures change from coarser to fine graded. Lower CEI values are associated with the easy compactability of the HMA mix, which agrees with the findings in respect of the TDI₃₀₀ values. Furthermore, the CoV values of the TDI₃₀₀ are generally lower than those of the CEI, which indicates that the TDI₃₀₀ parameter is more repeatable and reliable than the CEI parameter.

Table 4.2: Summary of CEI results

| Mix | Statistical parameter | Gradation structure | | |
|------------|-----------------------|---------------------|--------|------|
| | | Coarse | Medium | Fine |
| 10 mm NMPS | Mean | 538 | 190 | 196 |
| | STD | 230 | 35 | 23 |
| | CoV (%) | 42.7 | 18.6 | 11.7 |
| 20 mm NMPS | Mean | 114 | 115 | 110 |
| | STD | 13 | 14 | 4 |
| | CoV (%) | 11.4 | 11.8 | 3.2 |

Table 4.3: Summary of TDI₃₀₀ results

| Mix | Statistical parameter | Gradation structure | | |
|------------|-----------------------|---------------------|--------|------|
| | | Coarse | Medium | Fine |
| 10 mm NMPS | Mean | 914 | 1264 | 1349 |
| | STD | 18 | 100 | 84 |
| | CoV (%) | 2.0 | 7.9 | 6.2 |
| 20 mm NMPS | Mean | 1210 | 1271 | 1575 |
| | STD | 252.9 | 297.8 | 66.6 |
| | CoV (%) | 20.9 | 23.4 | 4.2 |

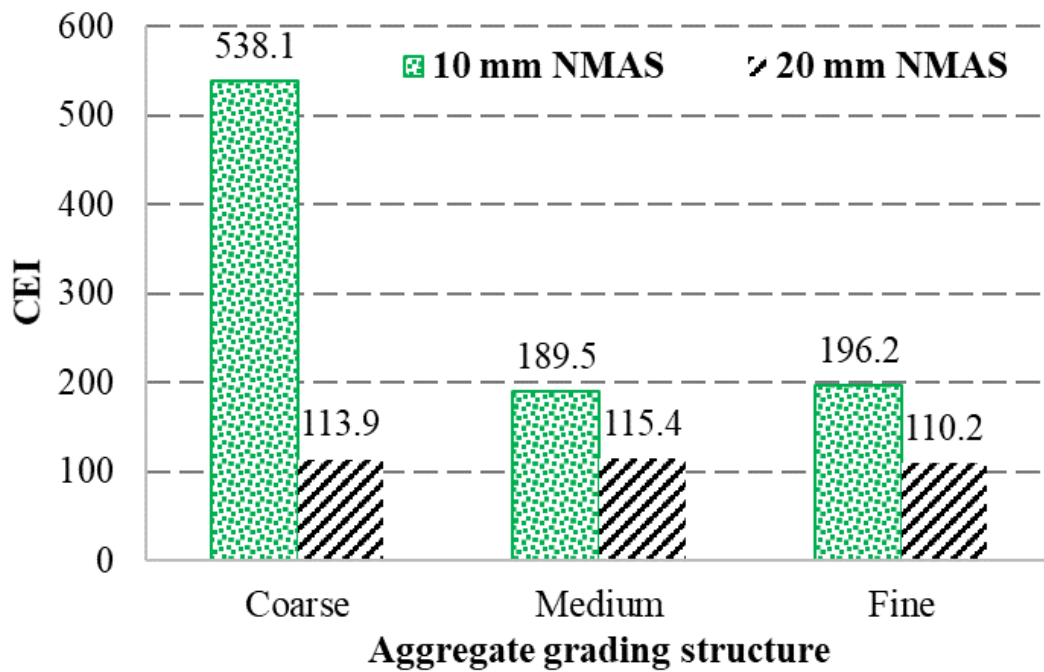


Figure 4.19: Average CEI results

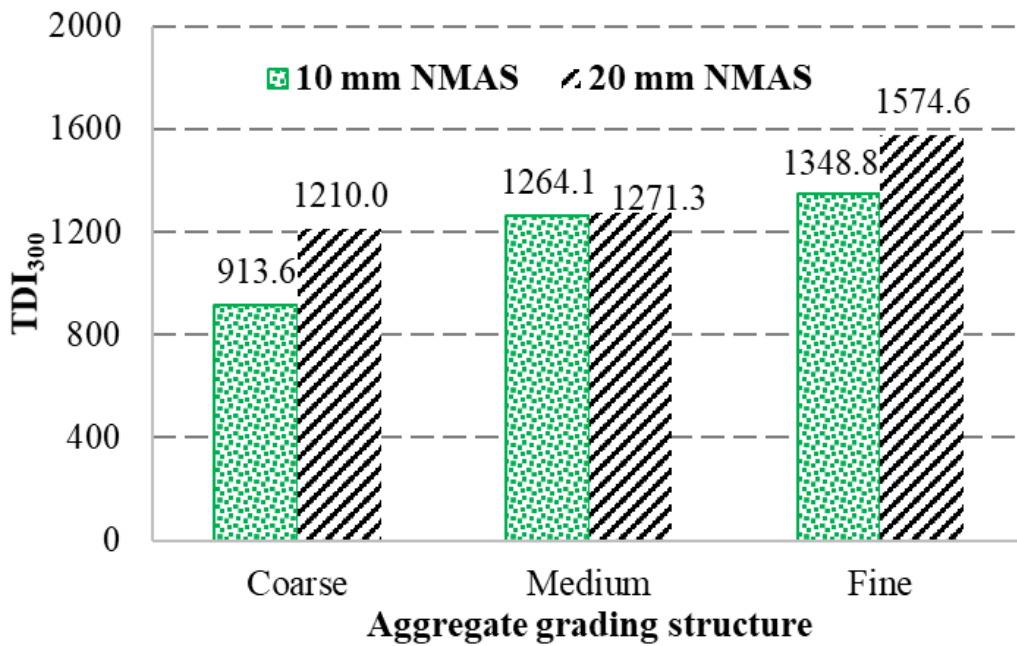


Figure 4.20: Average TDI₃₀₀ results

4.3.3 Compaction slope (CS)

The gyratory compaction densification curve of each HMA sample was analysed to determine the compaction slope (CS). Equation 4.1 (proposed by Wang et al., 2000) was used for this

purpose. Figure 4.21 illustrates how the parameters required for the computation of the compaction slope were determined.

$$CS = \frac{\% \text{ compaction at } N_{max} - \% \text{ compaction at } N_{initial}}{\log(N_{max}) - \log(N_{initial})} \quad \text{Equation 4.1}$$

Where:

$N_{initial}$ = number of gyrations at initial compaction

N_{max} = number of gyrations at maximum compaction.

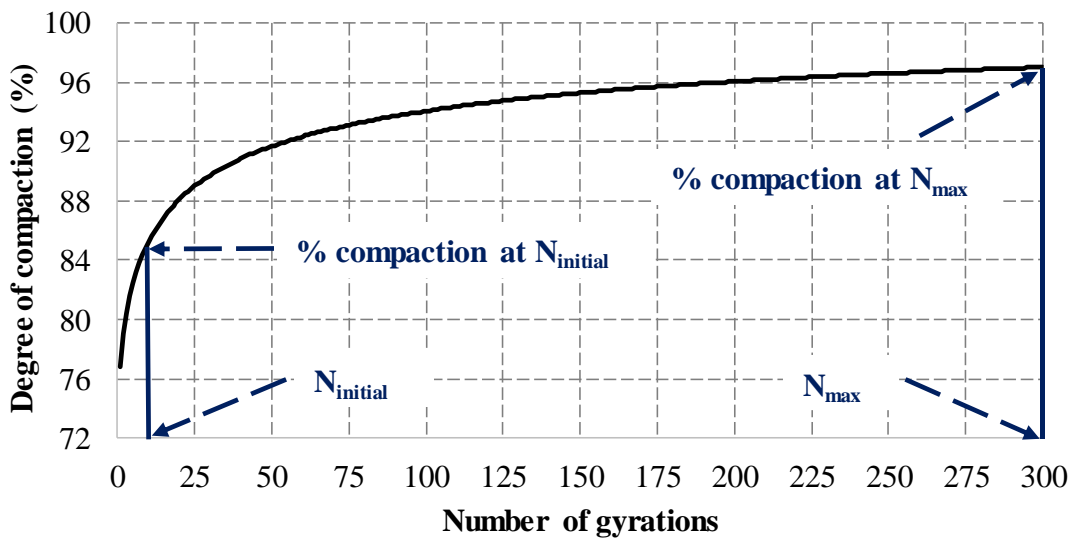


Figure 4.21: Determination of the compaction slope input parameters

A summary of statistical parameters of the compaction slope (CS) results is presented in Table 4.4. Figure 4.22 is a graphic representation of the mean CS parameters. The average CS values of the 10 mm HMA mixes are generally lower than those of the 20 mm HMA mixes. For 10 mm NMPS mixes, the CS values decrease as the gradation structure changes from coarse to fine, and the opposite is true for the 20 mm NMPS. The CoV values are low, indicating that the CS parameters are repeatable.

Table 4.4: Summary of compaction slope results

| Mix | Statistical parameter | Gradation structure | | |
|------------|-----------------------|---------------------|--------|------|
| | | Coarse | Medium | Fine |
| 10 mm NMPS | Mean | 5.2 | 4.8 | 4.7 |
| | STD | 0.1 | 0.3 | 0.3 |
| | CoV (%) | 1.1 | 5.4 | 5.9 |
| 20 mm NMPS | Mean | 3.2 | 3.4 | 4.0 |
| | STD | 0.1 | 0.3 | 0.3 |
| | CoV (%) | 3.8 | 8.0 | 6.8 |

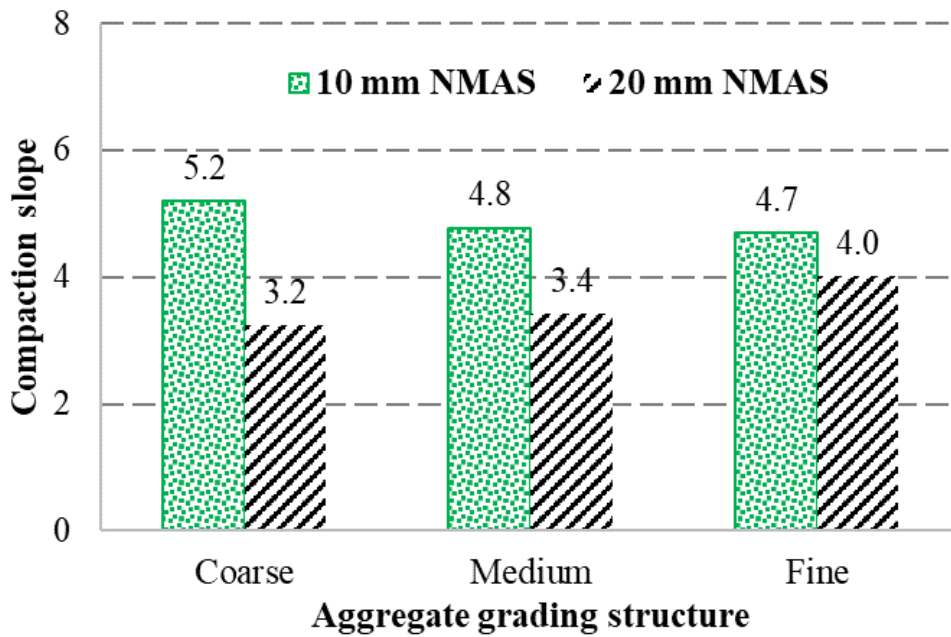


Figure 4.22: Average compaction slope results

4.3.4 Area under the shear stress curve

The area under shear stress (ASS_{max}) from the 8th gyration to the maximum shear stress was determined for each HMA sample, as illustrated in Figure 4.23. This is a new parameter proposed in this study. Generally, the higher the ASS_{max} , the more difficult it is to compact the HMA mix.

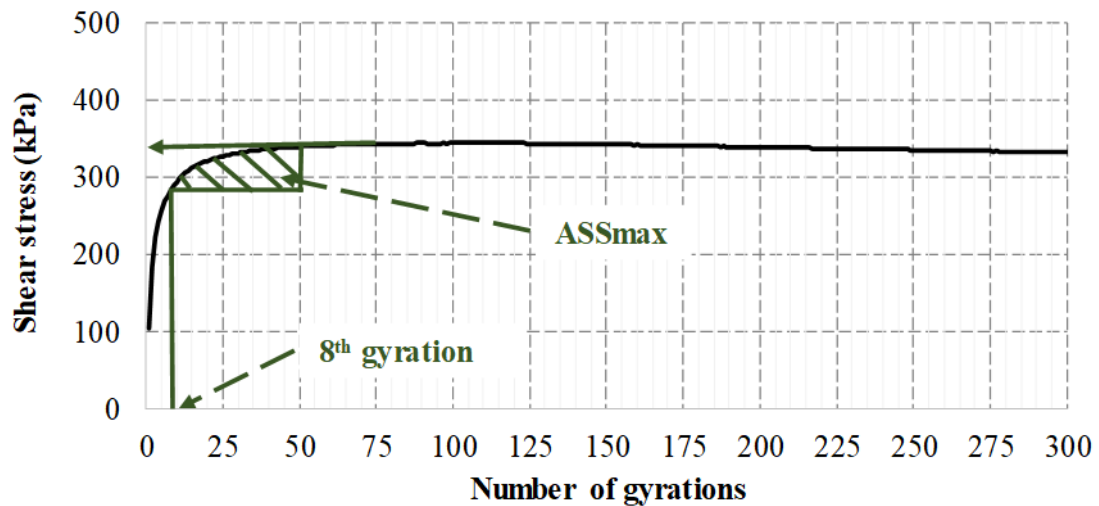


Figure 4.23: Determining the ASS_{max}

Table 4.5 presents a summary of ASS_{max} results and the mean ASS_{max} values are graphically presented in Figure 4.24. The average ASS_{max} values of the 20 mm NMPS mixes are higher than those of the 10 mm NMPS mixes, indicating that coarser-graded mixes are easier to compact than fine-graded mixes. For the same NMPS, the ASS_{max} values decrease as the grading structure changes from coarser to fine graded, indicating that less compaction energy is required to achieve the desired density. The CoV values are generally high, which indicates that the ASS_{max} parameters are not repeatable.

Table 4.5: Summary of ASS_{max} results

| Mix | Statistical parameter | Gradation structure | | |
|------------|-----------------------|---------------------|--------|------|
| | | Coarse | Medium | Fine |
| 10 mm NMPS | Mean | 4229 | 3424 | 3511 |
| | STD | 738 | 887 | 691 |
| | CoV (%) | 17.4 | 25.9 | 19.7 |
| 20 mm NMPS | Mean | 4063 | 3092 | 2655 |
| | STD | 1230 | 1176 | 2133 |
| | CoV (%) | 30.3 | 38.0 | 80.3 |

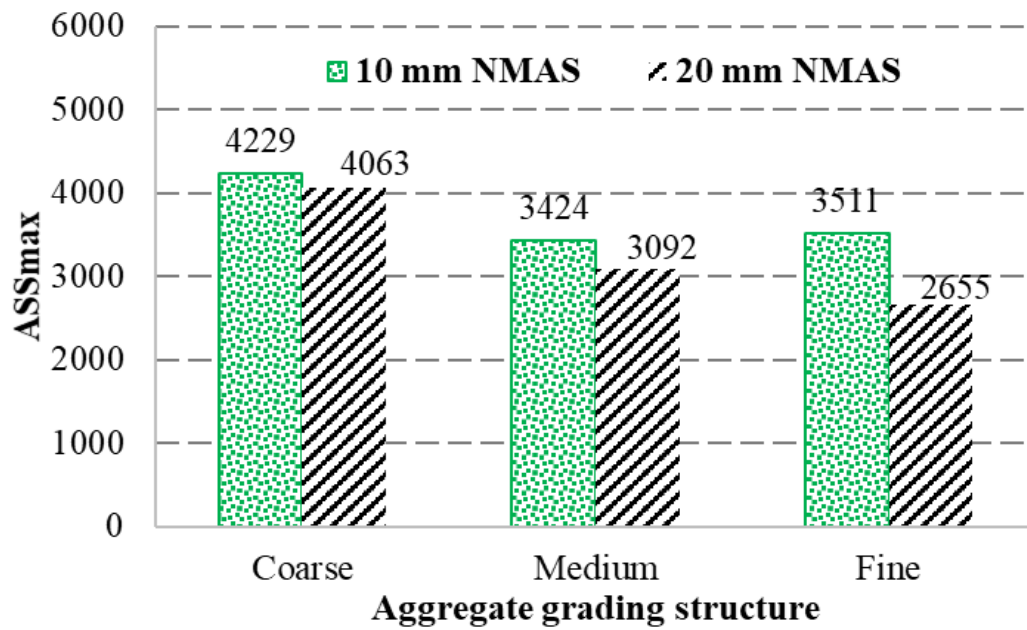


Figure 4.24: Average ASS_{max} results

4.4 Parametric correlations

The results presented in Section 4.3 showed that the rational Bailey ratios are more sensitive to changes in the gradation structure and they provide a better description of the packing characteristics of the macro, midi and micro skeleton matrix levels. Hence, it was decided to use the rational Bailey ratios for parametric correlations with the HMA compactability parameters. To this end, the average HMA compactability parameters (LP, CEI, TDI_{300} , CS and ASS_{max}) of each of the HMA mixes (coarse, medium and fine-graded) were correlated to their respective rational Bailey ratios (CA_r , C/F and F_{Arm_f}).

Table 4.6 and Table 4.7 summarise the correlation coefficient (r) and the coefficients of determination (R^2) for the 10 mm NMPS and 20 mm NMPS mixes respectively. The positive r values indicate a positive linear correlation or relationship, whereas negative r values indicate a negative linear correlation. Overall, the LP, TDI_{300} , CS, and ASS_{max} parameters show stronger correlations with the rational Bailey ratios ($r > |0.84|$). The correlations for CEI, in contrast, were found to be relatively weaker to medium, especially for the 20 mm NMPS mixes (r ranging from $|0.61|$ to $|0.71|$).

Table 4.6: Correlation coefficients and coefficients of determination - 10 mm NMPS mixes

| <i>Parameter</i> | <i>LP</i> | | <i>CEI</i> | | <i>TDI₃₀₀</i> | | <i>CS</i> | | <i>ASS_{max}</i> | |
|-------------------|-----------|----------------------|------------|----------------------|--------------------------|----------------------|-----------|----------------------|--------------------------|----------------------|
| | <i>r</i> | <i>R²</i> | <i>r</i> | <i>R²</i> | <i>r</i> | <i>R²</i> | <i>r</i> | <i>R²</i> | <i>r</i> | <i>R²</i> |
| CAr | 0.94 | 0.88 | 0.92 | 0.84 | -0.98 | 0.96 | 0.97 | 0.94 | 0.88 | 0.77 |
| C/F | 0.93 | 0.86 | 0.90 | 0.82 | -0.97 | 0.94 | 0.96 | 0.93 | 0.87 | 0.75 |
| FArm _f | 0.90 | 0.82 | 0.87 | 0.76 | -0.95 | 0.91 | 0.94 | 0.89 | 0.84 | 0.69 |

Table 4.7: Correlation coefficients and coefficients of determination - 20 mm NMPS mixes

| <i>Parameter</i> | <i>LP</i> | | <i>CEI</i> | | <i>TDI₃₀₀</i> | | <i>CS</i> | | <i>ASS_{max}</i> | |
|-------------------|-----------|----------------------|------------|----------------------|--------------------------|----------------------|-----------|----------------------|--------------------------|----------------------|
| | <i>r</i> | <i>R²</i> | <i>r</i> | <i>R²</i> | <i>r</i> | <i>R²</i> | <i>r</i> | <i>R²</i> | <i>r</i> | <i>R²</i> |
| CAr | -0.90 | 0.82 | 0.63 | 0.40 | -0.90 | 0.81 | -0.93 | 0.86 | 0.99 | 0.98 |
| C/F | -0.94 | 0.89 | 0.71 | 0.51 | -0.94 | 0.89 | -0.96 | 0.93 | 0.97 | 0.95 |
| FArm _f | -0.89 | 0.79 | 0.61 | 0.37 | -0.89 | 0.79 | -0.92 | 0.84 | 1.00 | 0.99 |

Figure 4.25 graphically presents the correlation trends between the compactability parameters and the rational Bailey ratios for the 10 mm NMPS mixes. Each data point in the figure represents a combination of the average compactability parameters of the coarse, medium and fine-graded HMA mixes for the particular NMPS and their respective Bailey ratios. For the 10 mm NMPS mixes, the LP, CEI, CS, and ASS_{max} compactability parameters positively correlate with the Bailey ratios, while the TDI_{300} values show a negative correlation. (Recall that the analysis in Section 4.2.4 indicated that for 10 mm NMPS, the Bailey ratios decrease as the aggregate gradation becomes coarse. Hence, the correlation trends suggest that the finer the gradation structure, the more difficult it is to compact.)

Similarly, the correlation trends for the 20 mm NMPS mixes are graphical illustrated in Figure 4.26. The CEI and ASS_{max} compactability parameters positively correlate with the Bailey ratios, while the TDI_{300} , LP, and CS show a negative correlation with the Bailey ratios. Recall from Section 4.2.4 that for 20 mm NMPS grading structures, the Bailey ratios are for coarse gradation structure. Hence, the correlation trends suggest that the fine 20 mm NMPS mix is less difficult to compact.

In general, a weaker correlation was observed between the CEI and the Bailey ratios (especially for the 20 mm NMPS mixes). It should be emphasized that the CEI compactability parameter is determined from the 8th gyration to 92% degree of compaction. This is an early HMA compaction stage. Hence the HMA mix is more likely to be loose, and the influence of aggregate packing is minimal. For the 10 mm NMPS mixes, the ASS_{max} parameter also exhibits a relatively weaker correlation with the rational Bailey ratios.

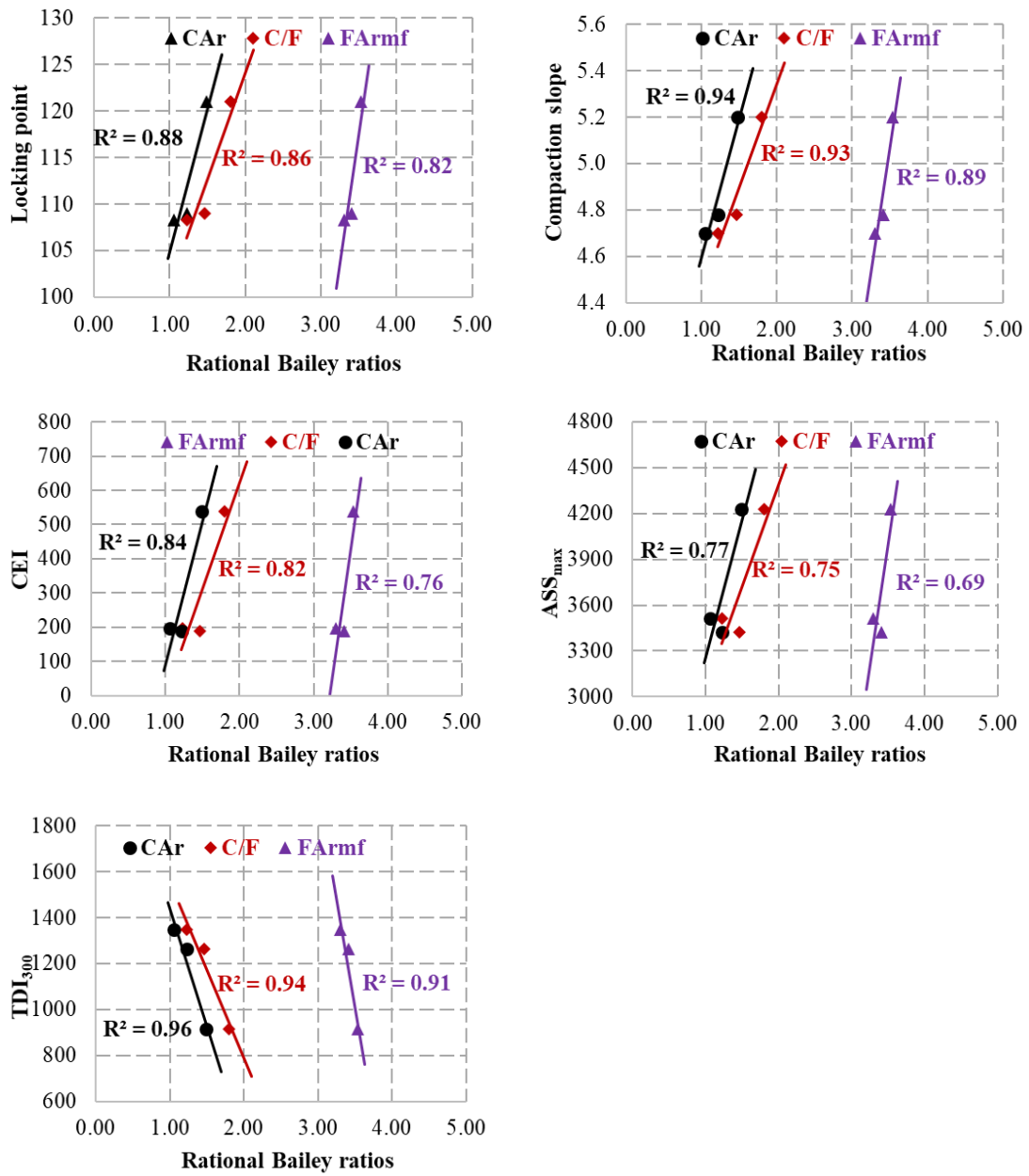


Figure 4.25: Correlations between Rational Bailey ratios and compactability parameters – 10 mm NMPS

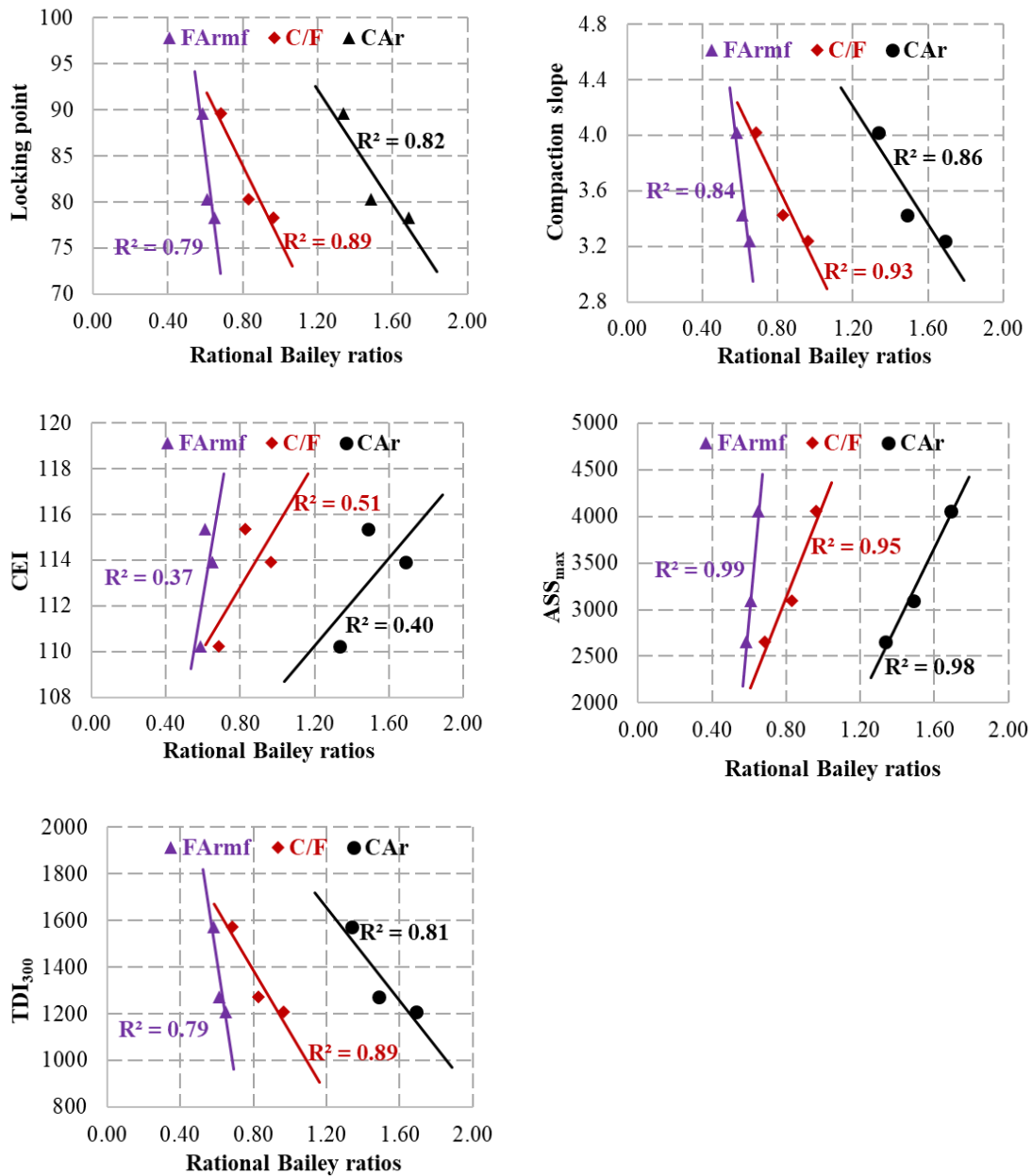


Figure 4.26: Correlations between rational Bailey ratios and compactability parameters – 20 mm NMPS

4.5 Summary

The overall objective of this chapter was to investigate the influence of aggregate packing characteristics on HMA compactability. The experiment and analysis performed had three main aims. The first was to establish parameters that best describe packing characteristics of aggregate gradation structure (Section 4.2). The second aim was to determine parameters that can be used to describe the compactability of HMA (Section 4.3). The final aim was to perform a parametric correlation to establish the relationship between HMA compactability parameters and aggregate packing parameters (Section 4.4).

In Section 4.2, six aggregate gradation curves were analysed to determine eight packing parameters: gradation parameters (n and G/S); three traditional Bailey ratios (CA , F_{Ac} and F_{Af}); and three rational Bailey ratios (CA_r , C/F and F_{Armf}). The results showed that all these aggregate packing parameters were able to distinguish the gradation structures investigated. However, the rational Bailey ratios were found to be more sensitive to changes in the gradation structure and they provided a better description of the packing characteristics of macro, midi/meso and micro skeleton matrix levels.

Section 4.3 presented the analysis and discussion of the results of five HMA compactability parameters: the locking point (LP); compaction energy index (CEI); traffic densification index (TDI_{300}); compaction slope (CS); and the area under shear stress (ASS_{max}). The compactability parameters exhibited different but logical relationships with the NMPS and gradation structure or curve. The compactability of the HMA mixes was found to be influenced by the NMPS and the packing of the gradation structure. For the gradation structures of the sand skeleton (such as the 10 mm NMPS used in this study), the study found that more compaction energy is required to compact the mix to the design density as the gradation becomes finer. In contrast, in the case of sand skeleton mixes (20 mm NMPS) – the finer the mix, the easier it was to compact.

The analysis and discussion of the results of the parametric correlation between aggregate packing parameters and HMA compactability parameters were presented in Section 4.4. The results show that most of the HMA compactability parameters exhibited a strong correlation with the rational Bailey ratios, whereas a relatively weaker correlation was found with the CEI and ASS_{max} compactability parameters. Overall, the results of the parametric correlation suggested that the TDI_{300} , LP , and CS compactability parameters relate more logically to the NMPS and aggregate gradation structure.

Although the study was limited to six aggregate gradation structures, it has been demonstrated that aggregate gradation parameters can easily be computed from the basic gradation curve. The aggregate packing parameters may be very useful in predicting the compactability of HMA mixes and may avoid the need for additional laboratory or field testing. The findings may need to be validated by collating and analysing a database of existing asphalt mixes that consist of good and poor performing asphalt mixes so as to derive typical correlations and ranges of parameters to guide adjustments to the gradation curve of a specific mix. This will also allow for the setting of specifications for each of the aggregate packing parameters and HMA compactability parameters.

5 SPATIAL DISTRIBUTION OF AIR VOIDS IN COMPACTED HMA SAMPLES

5.1 Introduction

This chapter presents analysis and discussion of the results of the experimental work described in Section 3.3, namely to investigate the spatial distribution of air voids in compacted HMA samples. In the laboratory study, a 10 mm NMPS HMA mix was used to investigate the vertical and radial distribution of air voids of gyratory-compacted samples. The HMA samples were compacted at two target air voids contents (4.0% and 7.0%) and two sample heights (120 mm and 170 mm). The 7.0% and 4.0% air voids contents were chosen to represent the air voids of the HMA mix during the stable condition of its design life and the phase immediately after construction (Sabita Manual 35/TRH 8, 2020).

The South African guideline document for the use and design of asphalt mix for road pavements recommends a 4.0% target air voids content for the compaction of HMA samples in order to evaluate their volumetric properties and workability during the asphalt mix design stage (Sabita Manual 35/TRH 8, 2020). On the other hand, the 7.0% target is used for compaction samples to evaluate mix properties such as the dynamic modulus (stiffness) and resistance against permanent deformation (rutting). For sample height, a 170 mm high was chosen for dynamic modulus and repeated axial load permanent deformation tests, while the 120 mm high samples were recommended to evaluate the workability and volumetric properties of HMA during mix design (Sabita Manual 35/TRH 8, 2020).

The study furthermore investigated the spatial distribution of air voids in asphalt cores extracted from two road sections that had been constructed using the standard South African Bituminous Treated Base (BTB) and High Modulus Asphalt (HiMA) mixes. The field core samples were extracted from SANRAL's experimental section on R104 road near Pretoria, South Africa. The field cores were extracted from the lane of the experimental section that has been closed to normal traffic to eliminate the effect of long-term densification of the asphalt layers.

Sections 5.2 and 5.3 contain an analysis and discussion of the results of the vertical and radial distribution of air voids in laboratory-compacted HMA samples respectively. Sections 5.4 and 5.5 subsequently analyse and discuss the results of the vertical and radial distribution of air voids in field asphalt cores respectively. The chapter ends with a summary and discussion of the key findings in Section 5.6.

5.2 Vertical distribution of air voids in laboratory-compacted HMA samples

5.2.1 170 mm high compacted HMA samples

As explained in the experimental plan described in Section 3.2, two sets of 170 mm high HMA samples were compacted at two target air voids contents (7.0% and 4.0%). For each combination of sample height and target air voids, three replicate samples were compacted, which allowed for the identification of any possible outliers. The samples were prepared using a procedure described in Section 3.3.3. A 100 mm diameter specimens were cored from the centre of 170 mm high HMA samples, and the top and bottom 10 mm were trimmed to produce 150 mm high specimens. Next, the bulk density (BD) of each specimen was determined using the SSD method as described in Section 3.3.4. The bulk density results were used together with the MVD of the mix to compute the air voids of the HMA sample using Equation 3.8 (see Chapter 3). The MVD of the mix was determined to be 2622 kg/m³. The bulk density results are presented in Appendix B.

Table 5.1 presents a summary of the air voids content results. Sample statistics including mean, standard deviation (STD), coefficient of variation (CoV) and standard error (SE) are included in the results presented in the table. Overall, the air voids content of all the samples falls within the target compaction density (i.e., 4.0±0.5% and 7.0±0.5%). Furthermore, the CoV values are generally low, indicating that the air voids content of the three repeat samples does not differ significantly.

Table 5.1: Air voids of 170 mm high samples – vertical distribution

| Repeat | 4.0% target air voids content (%) | 7.0% air voids content (%) |
|----------------|------------------------------------------|-----------------------------------|
| 1 | 4.3 | 6.9 |
| 2 | 4.3 | 7.1 |
| 3 | 4.4 | 6.8 |
| Mean | 4.4 | 6.9 |
| STD | 0.0 | 0.2 |
| CoV (%) | 0.9 | 2.2 |
| SE | 0.0 | 0.1 |

After determination of the bulk density and voids of the compacted HMA samples, each sample was cut into three equal parts of approximately 50 mm high (a top, middle and bottom layer). The samples were thoroughly dried overnight, following which the bulk density of each part was determined and used to compute the air voids content of the samples. Table 5.2 and Table 5.3

present the air voids results of the three parts of the laboratory HMA samples that were compacted to a height of 170 mm and a target air voids content of 4.0% and 7.0% respectively.

For each repeat sample, the statistical parameters were calculated using the results of the parts (i.e., top, middle and bottom) the sample. It was interesting to note that each repeat sample's mean air voids content did not differ significantly from the results for the full sample before cutting (Table 5.1). Overall, the CoV values of the 4.0% target voids content samples were high, indicating that the vertical variation in the voids was higher than that of the 7.0%.

Table 5.2: Air voids results of the three parts – 4.0% air voids, 170 mm high

| Repeat | Air voids content (%) | | | Mean (%) | STD (%) | CoV (%) | SE |
|--------|-----------------------|--------|--------|----------|---------|---------|-----|
| | Top | Middle | Bottom | | | | |
| 1 | 4.3 | 4.2 | 4.5 | 4.3 | 0.2 | 3.5 | 0.1 |
| 2 | 4.9 | 3.6 | 4.6 | 4.4 | 0.7 | 15.2 | 0.4 |
| 3 | 5.2 | 3.9 | 4.3 | 4.5 | 0.7 | 15.4 | 0.4 |

Table 5.3: Air voids results of the three parts – 7.0% air voids, 170 mm high

| Repeat | Air voids content (%) | | | Mean (%) | STD (%) | CoV (%) | SE |
|--------|-----------------------|--------|--------|----------|---------|---------|-----|
| | Top | Middle | Bottom | | | | |
| 1 | 6.8 | 6.4 | 6.5 | 6.6 | 0.2 | 3.3 | 0.1 |
| 2 | 7.0 | 6.5 | 7.1 | 6.9 | 0.3 | 5.0 | 0.2 |
| 3 | 6.4 | 6.0 | 7.3 | 6.6 | 0.6 | 9.6 | 0.4 |

Figure 5.1 and Figure 5.2 plot the average of the air voids results of the three separate parts (i.e., top, middle and bottom) of samples compacted to 170 mm high and a target air voids content of 4.0% and 7.0% respectively. The air voids content values of the middle parts were generally low, indicating that the achieved compaction density was higher than for the top and for the bottom. Furthermore, the vertical variation in the air voids content was more pronounced for the samples compacted to a 4.0% target air voids content.

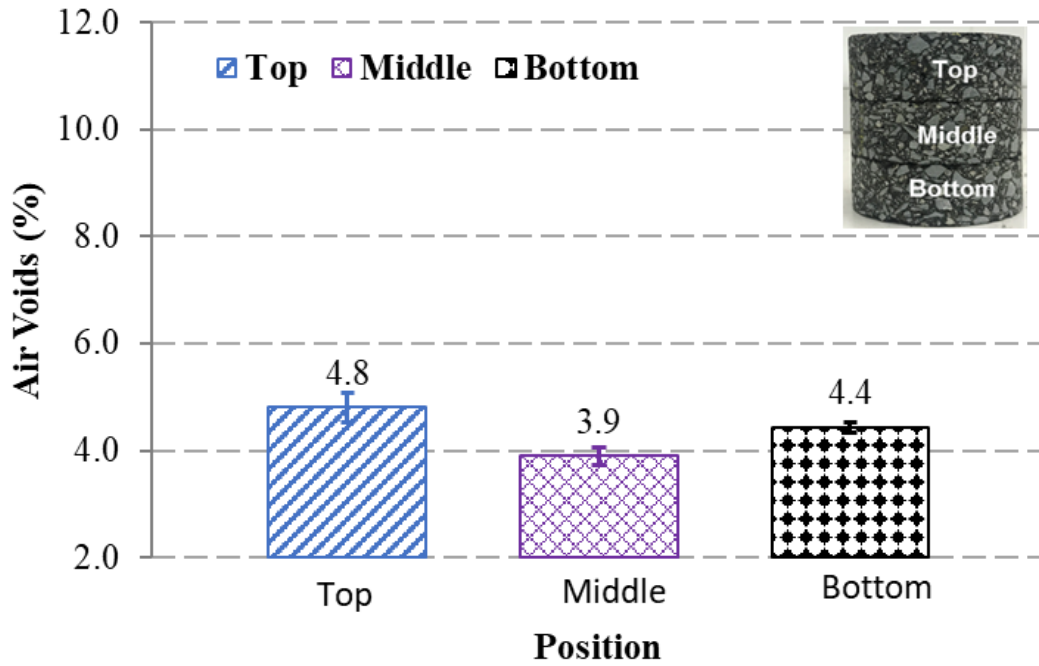


Figure 5.1: Average air voids – 4.0% target air voids content, 170 mm high samples

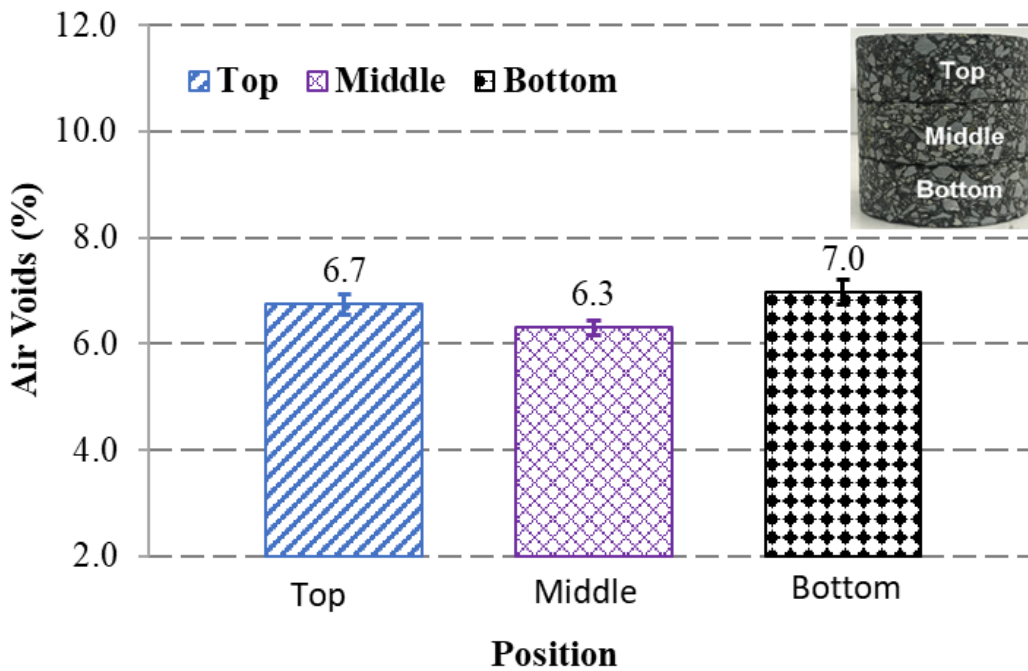


Figure 5.2: Average air voids – 7.0% target air voids content, 170 mm high samples

The top, middle and bottom parts of the asphalt samples were each further subdivided into two parts (approximately 25 mm high each), making a total of six parts per sample. Each part was thoroughly dried overnight, after which its bulk density was determined, and the bulk density result was used to compute the air voids content.

Table 5.4 and Table 5.5 present the air voids results of the eventual six parts (1 is the top, and 6 is the bottom) for target air voids content of 4.0% and 7.0% respectively. While the mean air voids content does not differ significantly from that of the full sample (Table 5.1), the air voids content of the six parts differs significantly, indicating a higher variation of the air voids content (CoV greater than 22%). In general, the CoV values of the 4.0% air voids content samples (greater than 22%) are higher than those of the 7.0% (greater than 32%).

Table 5.4: Air voids results of the six parts – 4.0% target air voids content

| Repeat | Air voids content (%) | | | | | | Mean (%) | STD (%) | CoV (%) | SE |
|--------|-----------------------|-----|-----|-----|-----|-----|----------|---------|---------|-----|
| | 1 | 2 | 3 | 4 | 5 | 6 | | | | |
| 1 | 5.7 | 3.3 | 4.0 | 4.2 | 3.1 | 6.3 | 4.1 | 1.3 | 32.1 | 0.5 |
| 2 | 6.4 | 3.5 | 3.8 | 3.5 | 2.7 | 6.9 | 4.0 | 1.7 | 42.7 | 0.7 |
| 3 | 6.9 | 3.7 | 4.0 | 3.9 | 3.0 | 5.8 | 4.3 | 1.5 | 35.5 | 0.6 |

Table 5.5: Air voids results of the six parts – 7.0% target air voids content

| Repeat | Air voids content (%) | | | | | | Mean (%) | STD (%) | CoV (%) | SE |
|--------|-----------------------|-----|-----|-----|-----|-----|----------|---------|---------|-----|
| | 1 | 2 | 3 | 4 | 5 | 6 | | | | |
| 1 | 9.5 | 5.1 | 6.2 | 6.4 | 5.6 | 7.7 | 6.6 | 1.6 | 24.5 | 0.7 |
| 2 | 8.5 | 5.6 | 6.8 | 6.2 | 5.2 | 9.5 | 6.5 | 1.7 | 26.1 | 0.7 |
| 3 | 8.4 | 5.0 | 5.8 | 6.6 | 6.4 | 8.7 | 6.4 | 1.5 | 22.9 | 0.6 |

Figure 5.6 and Figure 5.5 plot the air voids content results as a function of the HMA sample height for 4.0% and 7.0% air voids content. For each figure, each data point represents the average of three repeat specimens. The figures also plot the average air voids content of the entire HMA samples determined before cutting it into three separate parts. Overall, the middle part of the HMA samples had low air voids content than the top and the bottom parts.

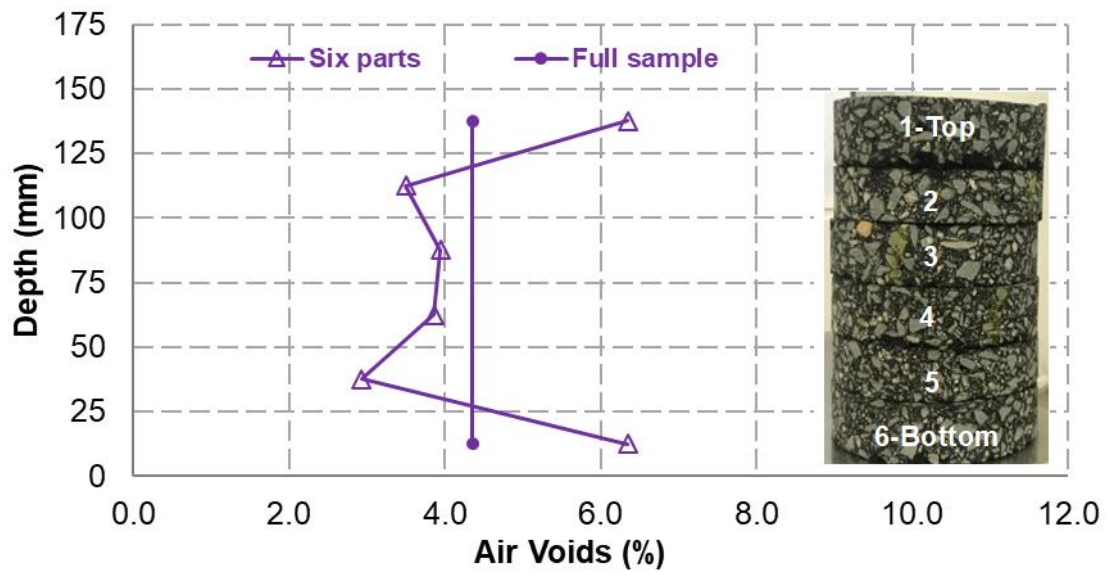


Figure 5.3: Vertical distribution of air voids – 4.0% target air voids content, 170 mm high

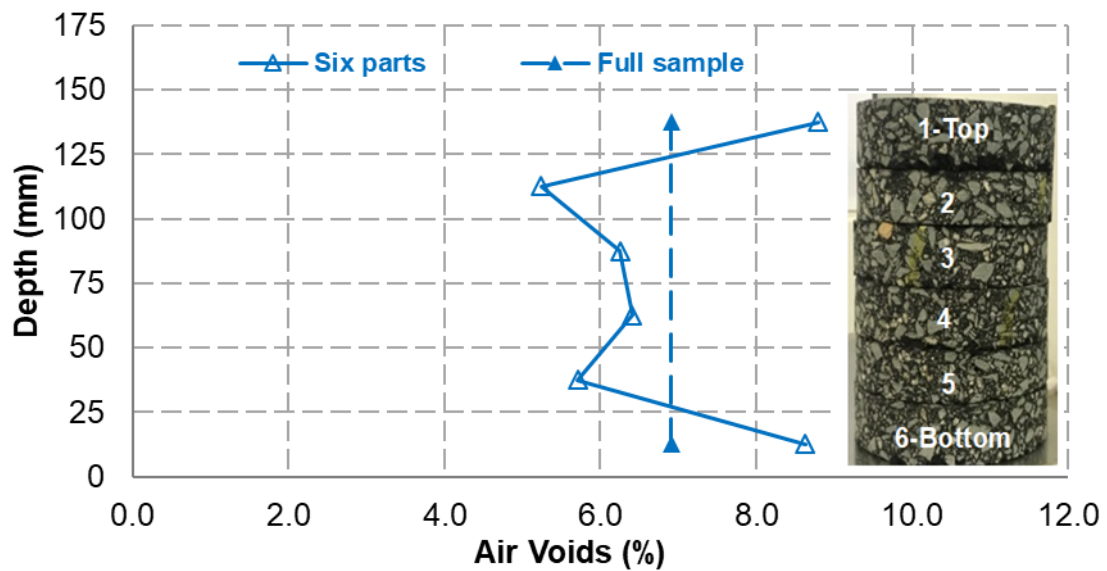


Figure 5.4: Vertical distribution of air voids – 7.0% target air voids content, 170 mm high

5.2.2 120 mm high compacted HMA samples

Two sets of 120 mm high HMA samples were compacted at two target air voids contents (4.0% and 7.0%). As in the case of the HMA samples that were compacted to 170 mm high, the bulk density of each of the samples was determined using the SSD method. The bulk density results were subsequently used together with the MVD of the asphalt mix to calculate the air voids content.

Table 5.6 summarises the results of the air voids content. Overall, the content of all the samples fell within the target compaction density (i.e., $4.0\pm 0.5\%$ and $7.0\pm 0.5\%$). CoV values were generally low, indicating that the air voids content of the three repeat samples did not differ significantly. However, the CoV of the $4.0\pm 0.5\%$ target air voids content is slightly higher than that of the 7.0%. This is due to the air voids content of the first sample being lower than the other two but still falling within the target of $4.0\pm 0.5\%$.

Table 5.6: Air voids of 120 mm high samples – vertical distribution

| Repeat | 4.0% target air voids (%) | 7.0% target air voids (%) |
|----------------|----------------------------------|----------------------------------|
| 1 | 3.6 | 6.5 |
| 2 | 4.7 | 7.2 |
| 3 | 4.8 | 7.0 |
| Mean | 4.4 | 6.9 |
| STD | 0.7 | 0.4 |
| CoV (%) | 15.2 | 5.4 |
| SE | 0.4 | 0.2 |

Once the bulk density and voids of the compacted HMA samples were determined, each of the 120 mm high samples was cut into three equal parts (a top, middle and bottom layer). The samples were thoroughly dried overnight, following which the bulk density of each part was determined and the air voids content was computed.

Table 5.7 and Table 5.8 present the air voids results of the three parts of the laboratory HMA samples that were compacted to 120 mm high and had target air voids contents of 4.0% and 7.0% respectively. Similar to the samples compacted to 170 mm, each sample's mean air voids content did not differ significantly from that determined on the full sample (Table 5.6). However, there was a significant difference between the air voids of each of the top, middle and bottom parts, as reflected by the higher CoV. Again, the CoV values of the 4.0% target voids content samples were generally high, indicating that the vertical variation of the air voids was higher than that of the 7.0%.

Table 5.7: Air voids results of the three parts – 4.0% target air voids content, 120 mm high

| Repeat | Air voids content (%) | | | Mean (%) | STD (%) | CoV (%) | SE |
|---------------|------------------------------|---------------|---------------|-----------------|----------------|----------------|-----------|
| | Top | Middle | Bottom | | | | |
| 1 | 4.9 | 2.3 | 4.2 | 3.8 | 1.4 | 35.6 | 0.8 |
| 2 | 6.4 | 3.1 | 5.5 | 5.0 | 1.7 | 34.7 | 1.0 |
| 3 | 5.9 | 2.9 | 6.1 | 5.0 | 1.8 | 35.6 | 1.0 |

Table 5.8: Air voids results of the three parts – 7.0% target air voids content, 120 mm high

| Repeat | Air voids content (%) | | | Mean (%) | STD (%) | CoV (%) | SE |
|--------|-----------------------|--------|--------|----------|---------|---------|-----|
| | Top | Middle | Bottom | | | | |
| 1 | 7.1 | 5.0 | 7.8 | 6.6 | 1.4 | 21.7 | 0.8 |
| 2 | 8.6 | 5.7 | 7.7 | 7.3 | 1.5 | 20.6 | 0.9 |
| 3 | 8.2 | 5.4 | 7.2 | 6.9 | 1.4 | 20.1 | 0.8 |

Figure 5.5 and Figure 5.6 plot the average of the air voids results of the three separate parts (i.e., top, middle and bottom) of samples compacted to 120 mm high and with a target air voids content of 4.0% and 7.0% respectively. The air voids of the middle parts were significantly low, indicating that the achieved compaction density was higher than in the top and bottom parts. Similar to the 170 mm high sample, the variation in compaction became more pronounced at the 4.0% voids content.

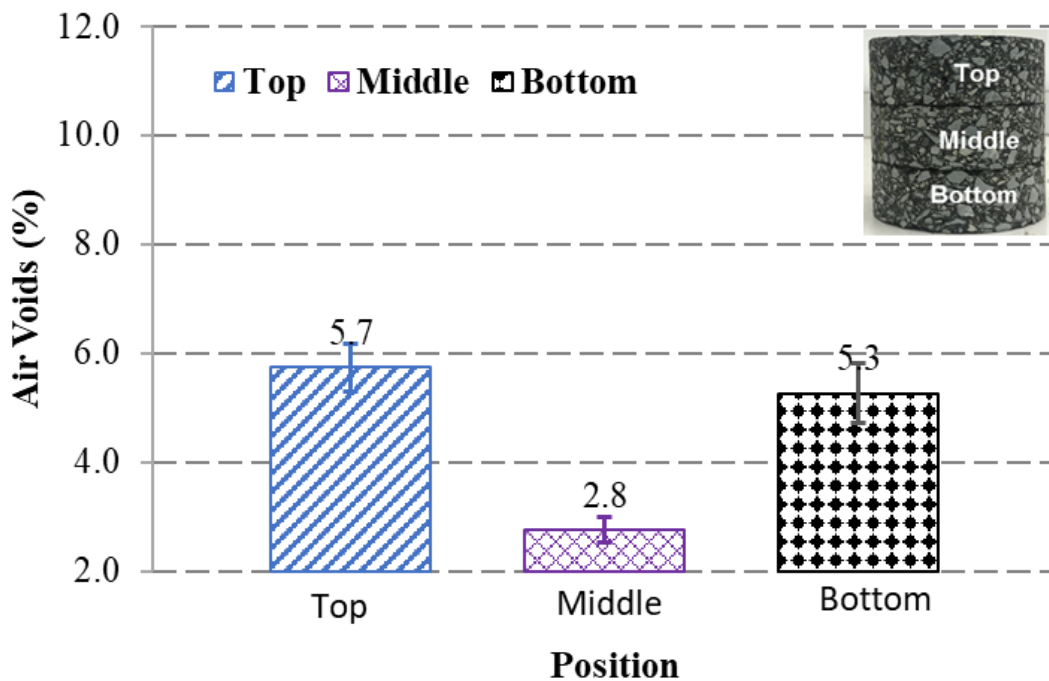


Figure 5.5: Average air voids content – 4.0%, 120 mm high samples

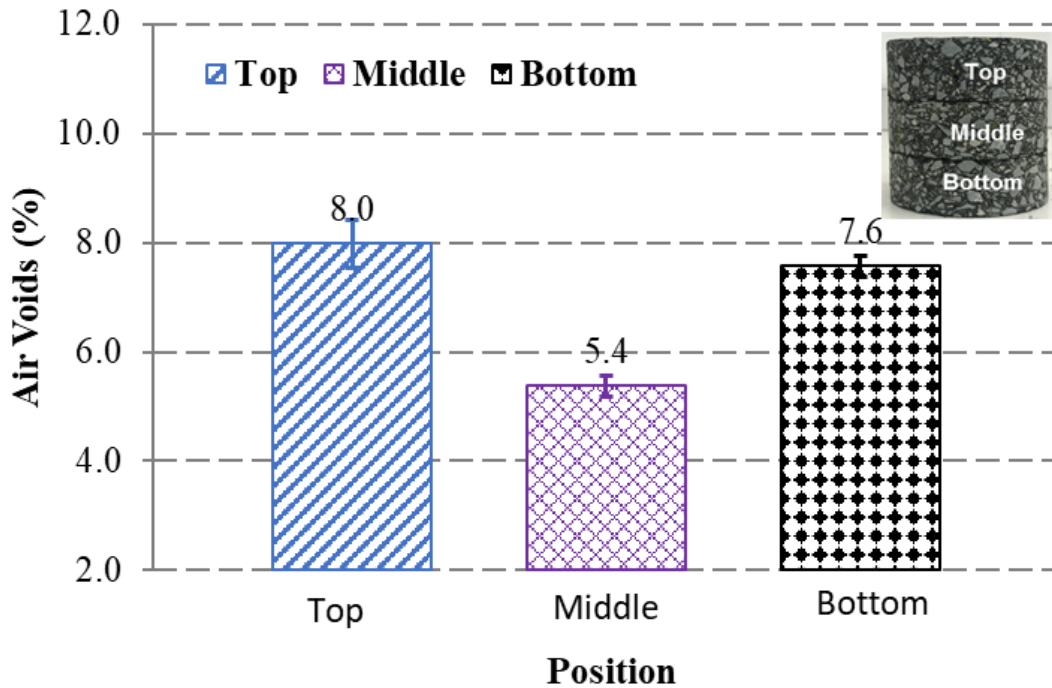


Figure 5.6: Average air voids content – 7.0%, 120 mm high samples

5.2.3 Influence of sample height on vertical air voids distribution

To assess the variation of the vertical air voids distribution with sample height under the gyratory compaction, the average results of the samples compacted to 120 mm and 170 mm heights were plotted on one graph. Figure 5.7 and Figure 5.8 plot the average air voids of the top, middle and bottom parts for the samples compacted to an air voids content of 4.0% and 7.0% respectively.

For both sample heights (120 mm and 170 mm), the air voids content of the middle part was lower than that of the top and the bottom, indicating that the compaction density of the middle part was higher than that of the top and bottom. However, the vertical variation in the air voids content was more pronounced for the HMA samples compacted to 120 mm. The middle part had significantly low air voids contents, while the top and bottom both had higher air voids content.

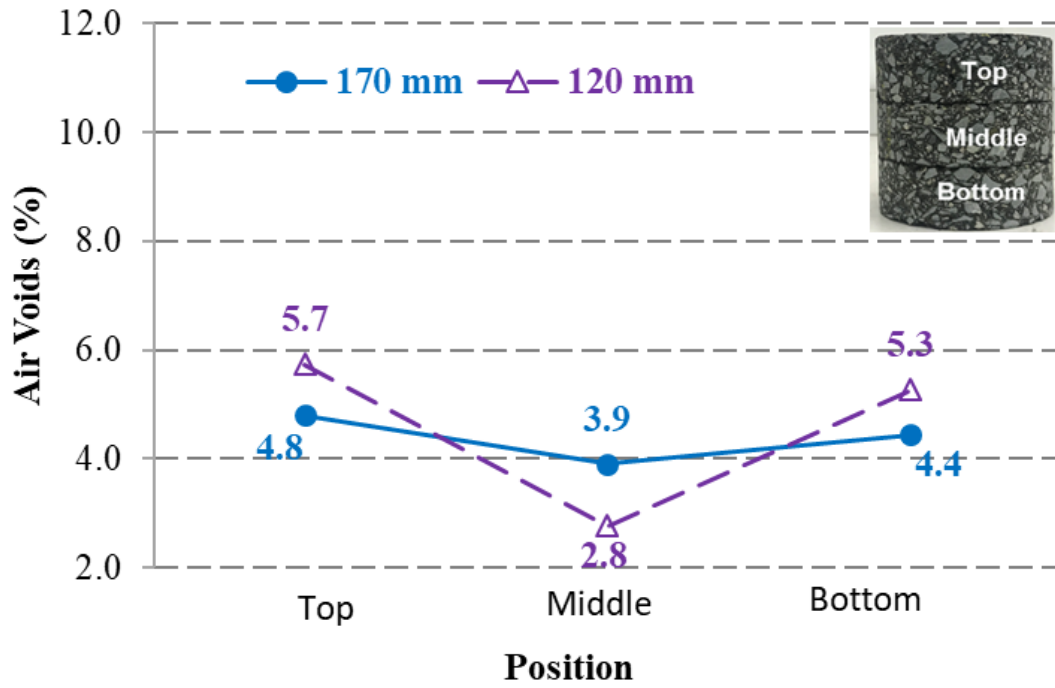


Figure 5.7: Vertical distribution of air voids – 4.0% air voids content

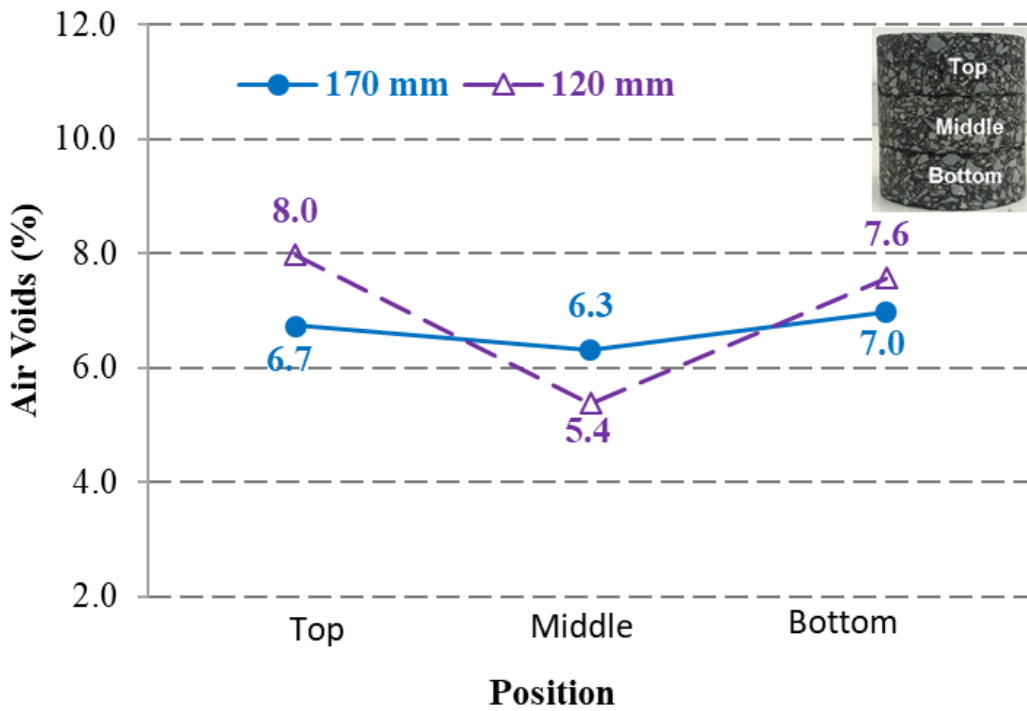


Figure 5.8: Vertical distribution of air voids – 7.0% air voids content

5.2.4 Influence of compaction density on vertical air voids distribution

The influence of the compaction density on the vertical air voids distribution was assessed by plotting together the air voids of the samples compacted to 4.0% and 7.0% target air voids content. In Figure 5.9 and Figure 5.10, the average air voids of the top, middle and bottom parts are plotted for the samples compacted to a target height of 120 mm and 170 mm respectively.

For both target compaction density (4.0% and 7.0%), the air voids content of the middle part was lower than in the top and the bottom, indicating that the compaction density of the middle part was high than that of the top and bottom. Furthermore, the vertical variation of the voids was more pronounced for the samples compacted to the 4.0% (i.e., the slope of the 4.0% target air voids lines is steeper than that of the 7.0%).

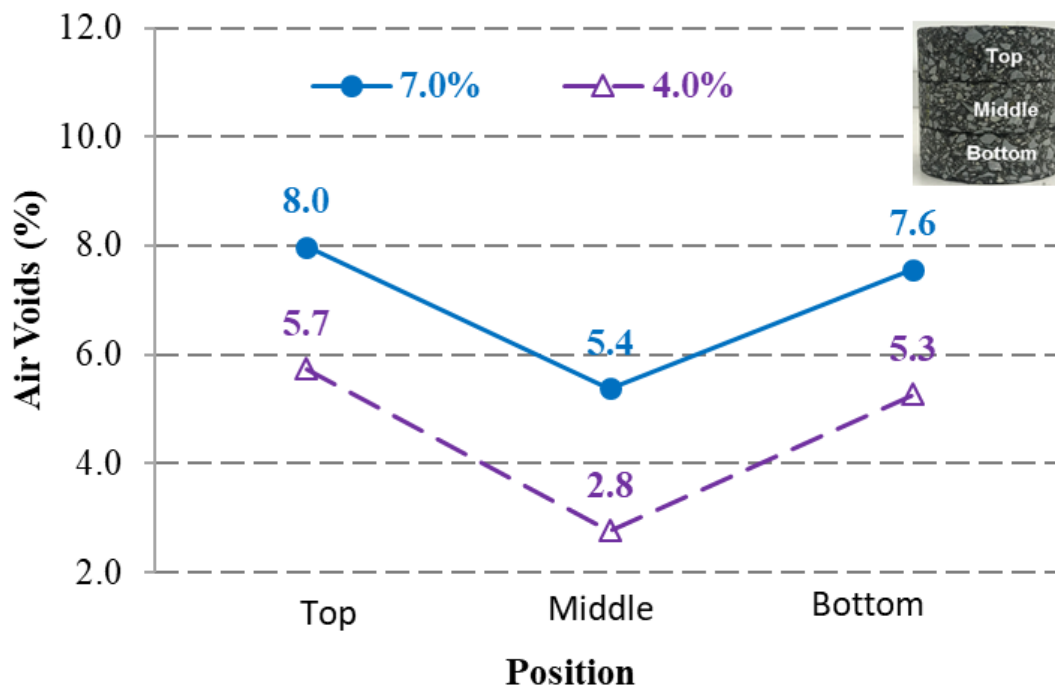


Figure 5.9: Vertical distribution of air voids – 120 mm high samples

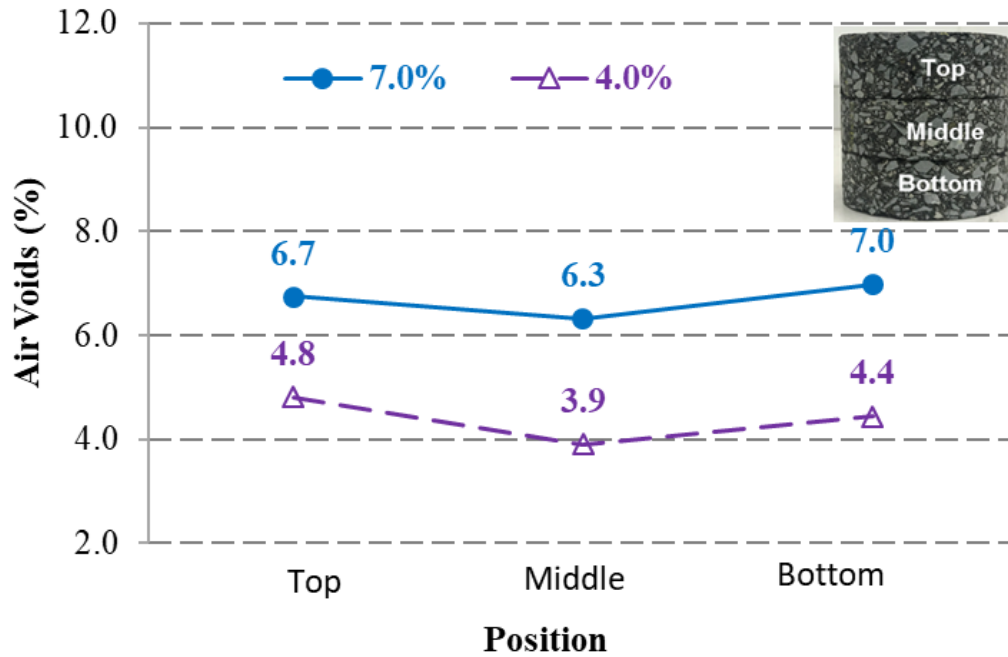


Figure 5.10: Vertical distribution of air voids – 170 mm high samples

5.3 Radial distribution of air voids in laboratory- laboratory samples

5.3.1 170 mm high compacted HMA samples

Similar to the investigations into the vertical air voids distribution, the 170 mm high samples were compacted to two target air voids contents (4.0% and 7.0%). The diameter of the mould used during gyratory compaction was 150 mm. From the 170 mm (high) by 150 mm (diameter) samples, 100 mm diameter specimens were cored from the centre. Next, the top and bottom 10 mm were trimmed to produce 150 mm high specimens, and then the bulk density (BD) of each sample was determined. Afterwards, a 78 mm diameter sample was cored from the centre of each sample, dried overnight (to remove water introduced from the previous bulk density determination), and the bulk density was determined again. Lastly, a 54 mm diameter sample was again cored from the centre, dried overnight, and the BD was determined (see the results in Appendix B).

The bulk density of each sample was used together with the MVD of the HMA mix to determine the air voids content of that sample. Table 5.9 and Table 5.10 provide a summary of the air voids of the 100, 78 and 54 mm diameter samples for the 4.0% and 7.0% target air voids contents, respectively. Overall, the air voids content of all the samples fell within the target compaction density (i.e., $4.0 \pm 0.5\%$ and $7.0 \pm 0.5\%$). Furthermore, as the diameter of the samples was reduced from 100 mm to 54 mm, there was a relatively small change in the air voids content, regardless of

the differences in compaction density. The CoV values were generally low, indicating that the air voids content of the 100, 78 and 54 mm diameter samples did not differ significantly.

The mean air voids content of the 4.0% and 7.0% target air voids content are plotted in Figure 5.11 and Figure 5.12, respectively. For each set of results, the standard error bars are comparable, indicating that, statistically, the air voids of the 100, 78 and 54 mm samples do not differ significantly.

Table 5.9: Air voids of 170 mm high – radial distribution (4.0% target air voids)

| Repeat | Diameter | | | Mean (%) | STD (%) | CoV (%) | SE |
|--------|----------|-------|-------|----------|---------|---------|-----|
| | 100 mm | 78 mm | 54 mm | | | | |
| 1 | 4.3 | 4.0 | 3.7 | 4.0 | 0.3 | 7.1 | 0.2 |
| 2 | 4.3 | 4.2 | 4.1 | 4.2 | 0.1 | 3.2 | 0.1 |
| 3 | 4.6 | 4.5 | 4.4 | 4.5 | 0.1 | 2.4 | 0.1 |

Table 5.10: Air voids of 170 mm high – radial distribution (7.0% target air voids)

| Repeat | Diameter | | | Mean (%) | STD (%) | CoV (%) | SE |
|--------|----------|-------|-------|----------|---------|---------|-----|
| | 100 mm | 78 mm | 54 mm | | | | |
| 1 | 6.7 | 6.4 | 6.6 | 6.6 | 0.1 | 2.0 | 0.1 |
| 2 | 7.0 | 6.7 | 6.5 | 6.7 | 0.3 | 3.8 | 0.1 |
| 3 | 6.8 | 6.6 | 6.6 | 6.7 | 0.1 | 2.0 | 0.1 |

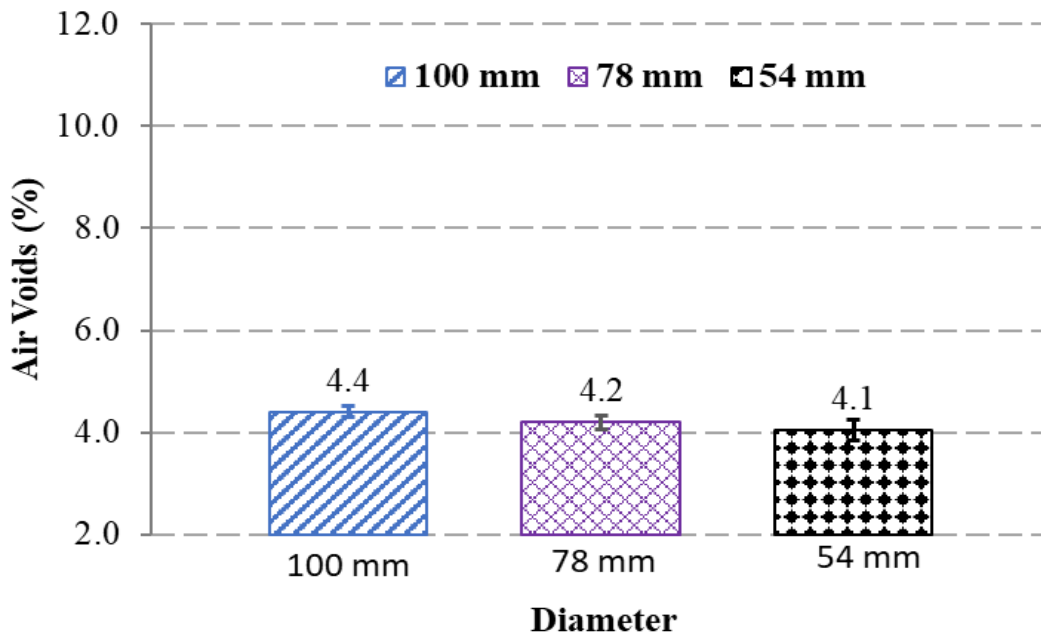


Figure 5.11: Radial distribution of air voids – 4.0% target air voids, 170 mm high

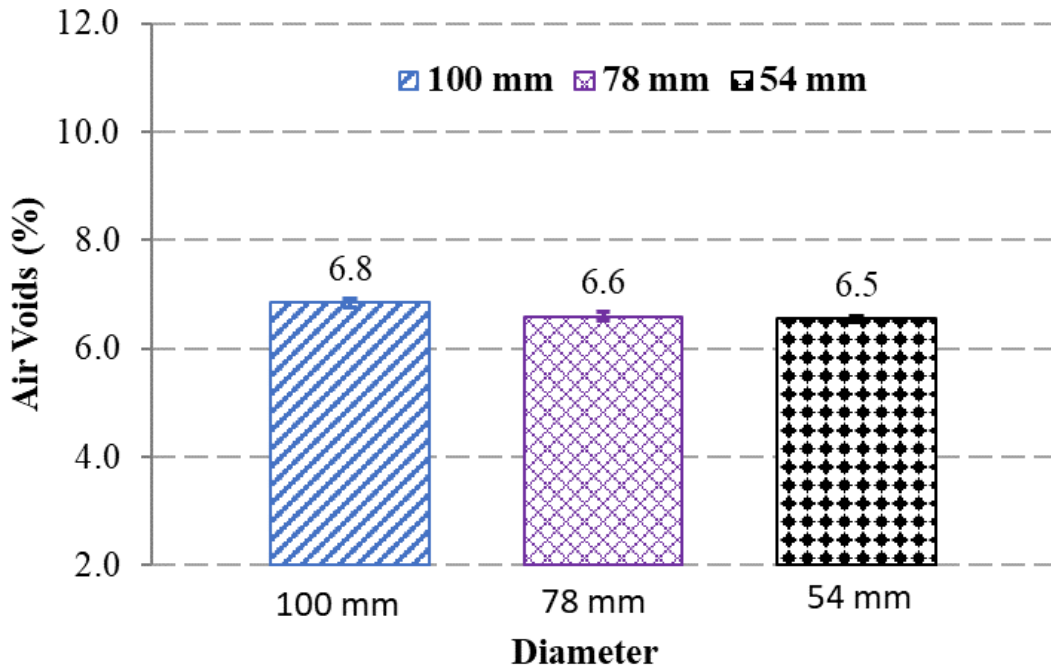


Figure 5.12: Radial distribution of air voids – 7.0% target air voids, 170 mm high

5.3.2 120 mm high compacted HMA samples

The procedure used for the preparation of the 120 mm samples was similar to that used for the 170 mm samples. From the 120 mm (high) by 150 mm (diameter) samples, 100 mm diameter samples were cored from the centre, and the top and bottom 10 mm were trimmed to produce 100 mm high specimens, following which the bulk density was determined. The samples were dried, a 78 mm sample was cored from the centre, and the bulk density was determined. A fourth sample of diameter 54 mm was lastly cored, followed by a final determination of bulk density. The bulk density of each sample was used to compute its air voids content.

Table 5.11 and Table 5.12 summarise the air voids determined on the 100, 78 and 54 mm diameter samples for 4.0% and 7.0% target air voids content respectively. Similar to the 170 mm high samples, the 4.0% target of air voids content samples fell within the target compaction density (i.e., $4.0 \pm 0.5\%$ and $7.0 \pm 0.5\%$). Two samples with a 7.0% target air voids content fell outside the target compaction level. However, the CoV values were generally low, indicating that the air voids content of the 100, 78 and 54 mm diameter samples did not differ significantly.

The mean air voids content of the 4.0% and 7.0% target air voids content are plotted in Figure 5.18 and Figure 5.17 respectively. The mean values and the standard error bars were comparable,

indicating that, statistically, the air voids of the 100, 78 and 54 mm samples did not differ significantly.

Table 5.11: Air voids of 120 mm high – radial investigation (4.0% target air voids content)

| Repeat | Diameter | | | Mean (%) | STD (%) | CoV (%) | SE |
|--------|----------|-------|-------|----------|---------|---------|-----|
| | 100 mm | 78 mm | 54 mm | | | | |
| 1 | 3.6 | 3.5 | 3.8 | 3.6 | 0.1 | 3.7 | 0.1 |
| 2 | 4.2 | 4.1 | 4.5 | 4.3 | 0.2 | 5.0 | 0.1 |
| 3 | 4.0 | 4.0 | 4.2 | 4.1 | 0.1 | 3.2 | 0.1 |

Table 5.12: Air voids of 120 mm high – radial investigation (7.0% target air voids content)

| Repeat | Diameter | | | Mean (%) | STD (%) | CoV (%) | SE |
|--------|----------|-------|-------|----------|---------|---------|-----|
| | 100 mm | 78 mm | 54 mm | | | | |
| 1 | 6.6 | 6.3 | 6.4 | 6.4 | 0.1 | 2.2 | 0.1 |
| 2 | 8.0 | 7.9 | 7.9 | 8.0 | 0.1 | 0.8 | 0.0 |
| 3 | 5.9 | 5.8 | 5.6 | 5.8 | 0.1 | 2.4 | 0.1 |

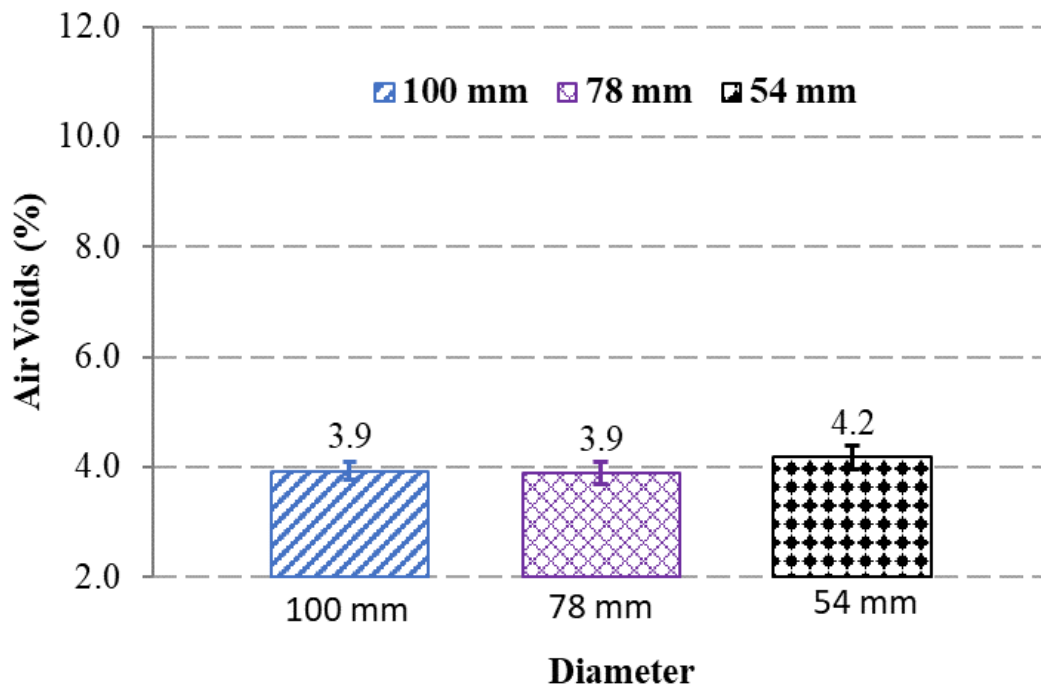


Figure 5.13: Radial distribution of air voids – 4.0% target air voids, 120 mm high

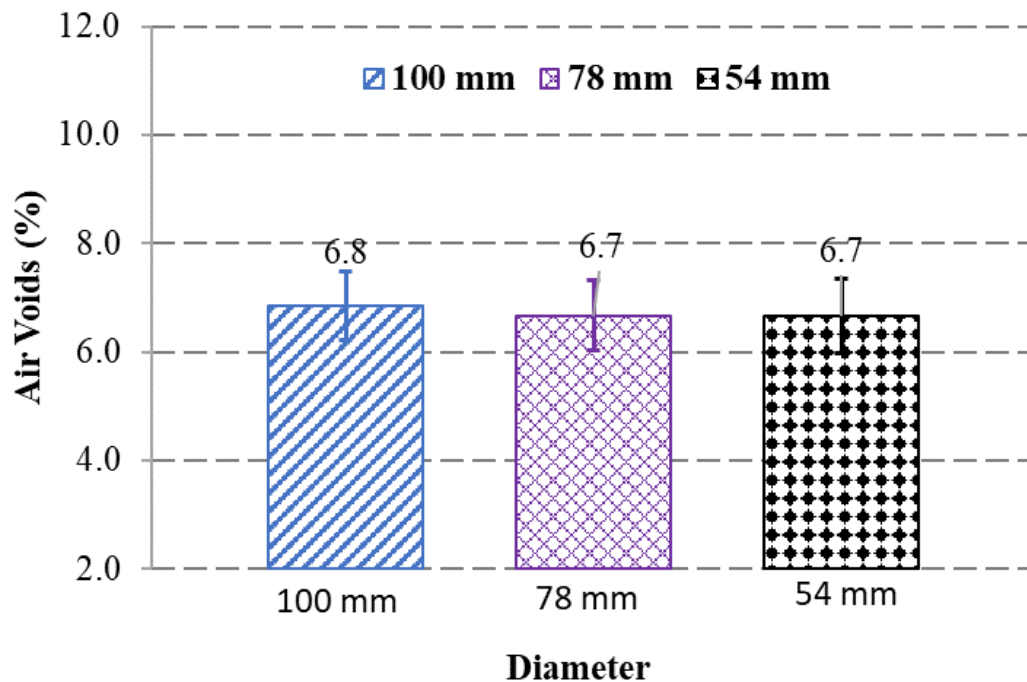


Figure 5.14: Radial distribution of air voids – 7.0% target air voids, 120 mm high

5.4 Vertical distribution of air voids in field extracted cores

As described in the methodology chapter (Section 3.2.3), two sets of field cores were obtained from SANRAL’s experimental section on R104 road near Pretoria, South Africa. The two sets of asphalt core samples were obtained from sections that had been constructed using standard South African BTB and HiMA mixes respectively. Due to insufficient specimen height, the field cores were sliced into four specimens only, as opposed to the six specimens that could be obtained from the laboratory-compacted samples.

The vertical distribution of the air voids for the HiMA and BTB field cores are presented in Figure 5.15 and Figure 5.16 respectively. The average air voids content that was determined using the entire HMA sample before slicing is also included in the figures. Overall, for the HiMA cores, the result follows the same trend as for the laboratory-compacted samples, whereby the top and bottom ends exhibit high air voids. However, for the BTB cores, only the bottom part exhibits higher air voids and the difference in compaction levels is significantly higher than for the HiMA cores.

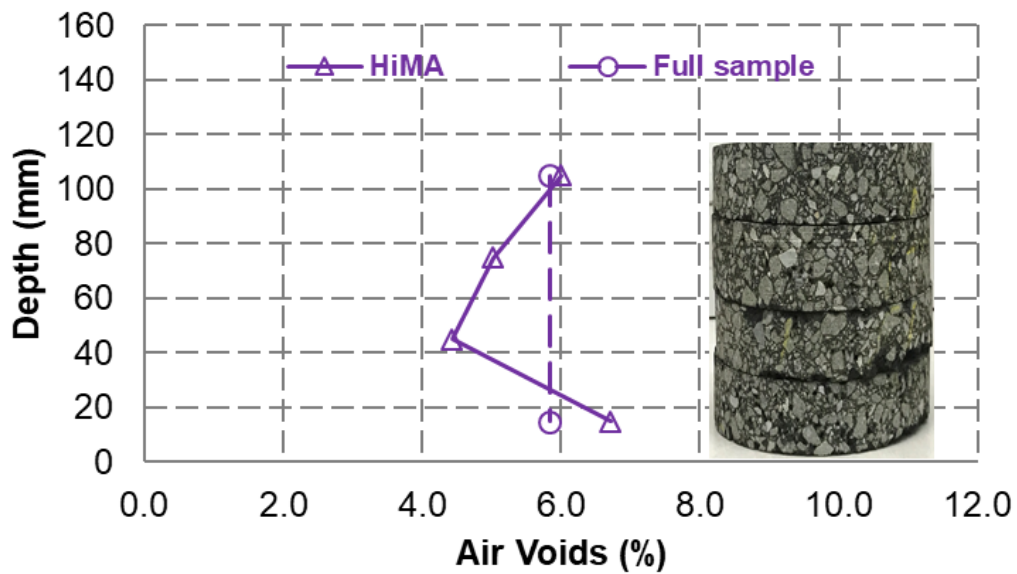


Figure 5.15: Vertical distribution of air voids in HiMA field cores

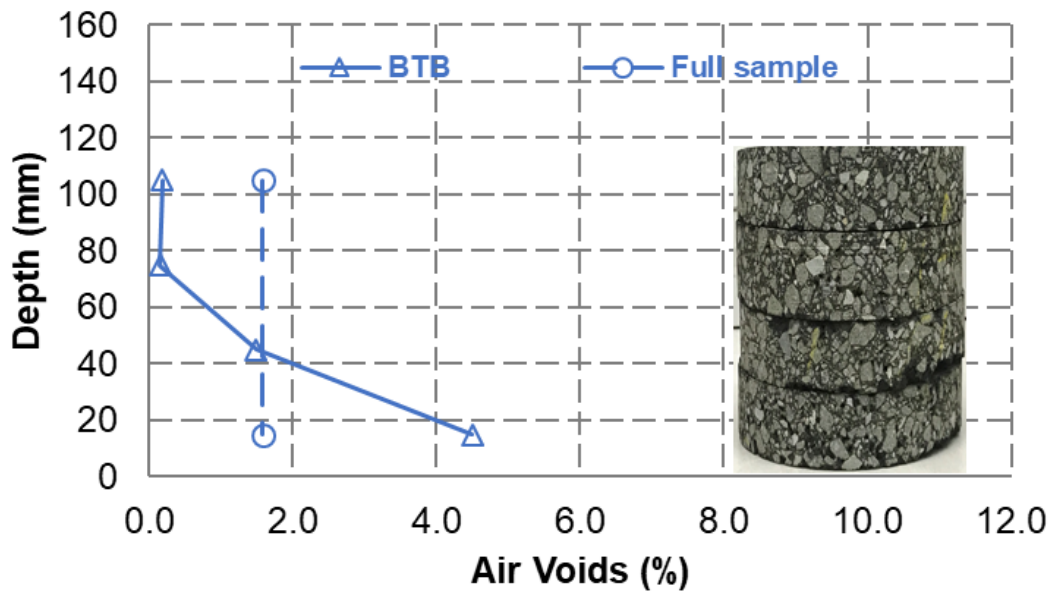


Figure 5.16: Vertical distribution of air voids in BTB field cores

5.5 Radial distribution of air voids in field-extracted cores

As for the laboratory-compacted samples, the investigation of the vertical distribution of the field core samples was carried out on 100, 78, and 54 mm diameter samples. Figure 5.17 and Figure 5.18 present the radial air voids distribution results of the field core specimens for HiMA and BTB mixes respectively. The results of the field core samples also show insignificant differences in the

air voids for the 100, 78 and 54 mm diameter specimens, despite the air voids content values of the HiMA cores being higher than those of the BTB.

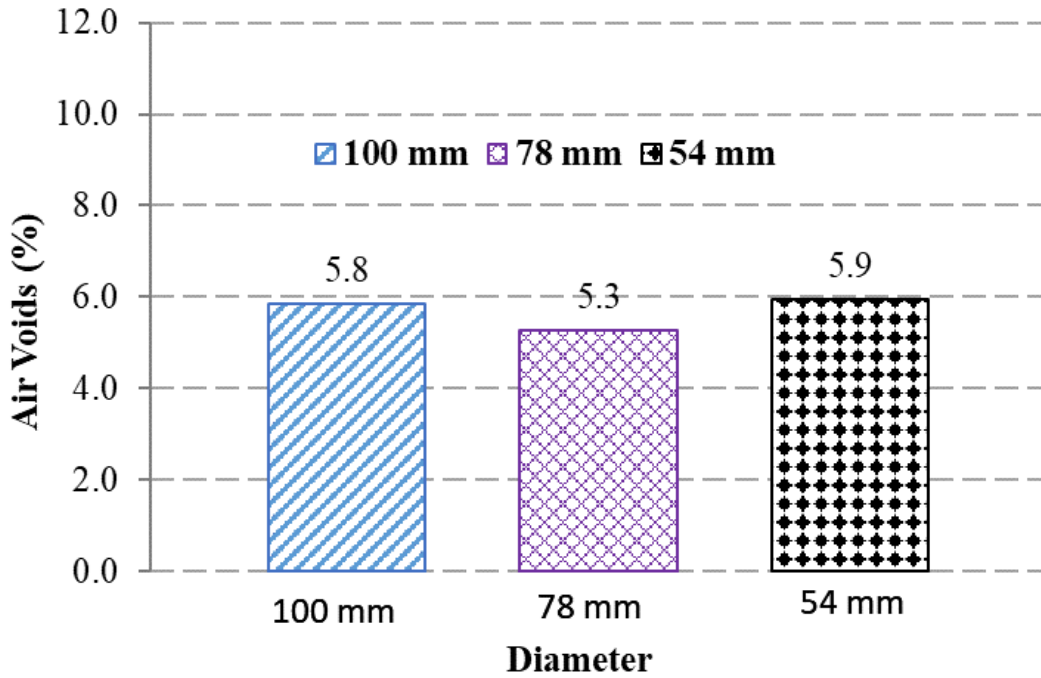


Figure 5.17: Radial distribution of air voids for HiMA field cores

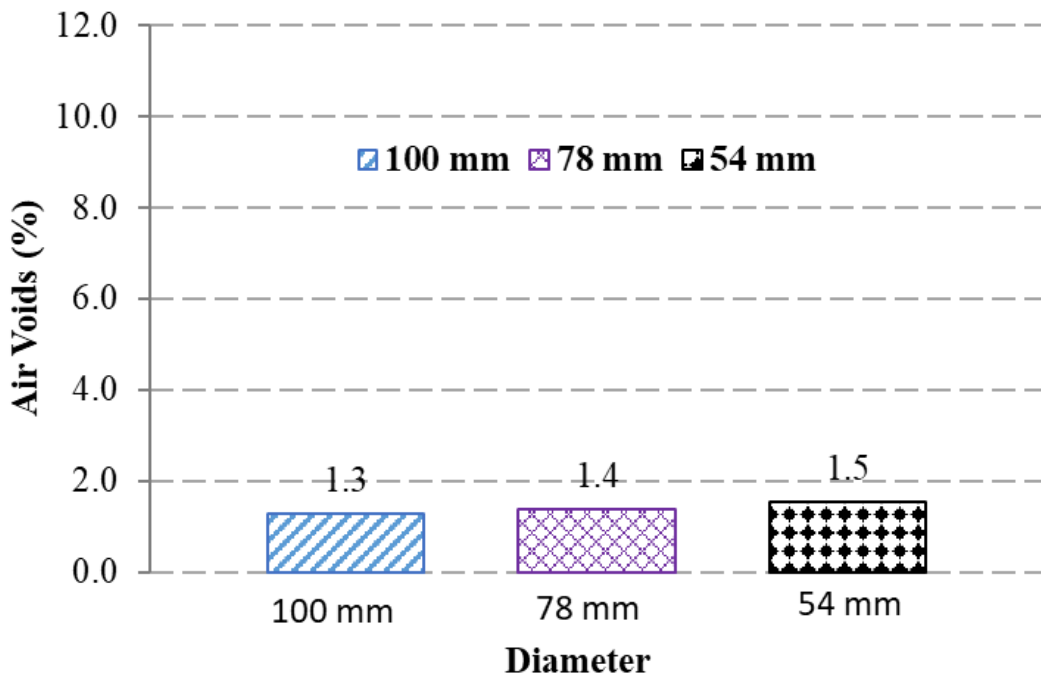


Figure 5.18: Radial distribution of air voids for BTB field cores

5.6 Summary

This chapter investigated the spatial distribution of air voids in laboratory HMA samples that had been compacted using a gyratory compactor. The HMA samples were compacted at two different compaction densities and two sample heights. The study also investigated the distribution of air voids in asphalt cores obtained from actual field road sections.

Section 5.2 presented the results of the investigation of the vertical distribution of air voids content in the gyratory-compacted samples. The analysis results showed that the vertical distribution of the air voids in the gyratory-compacted samples differed. The top and bottom parts exhibited a relatively high air voids content (i.e., low compaction density).

The vertical air voids distribution was found to be influenced by both the height of the sample and the compaction density. For both 120 mm and 170 mm high samples, the air voids content of the middle part was lower than the top and the bottom, indicating that the compaction density of the middle part was higher than that of the top and bottom ends. The possible reason for the observed trend could be due to the set-up of the gyratory compactor and how the compaction load is applied. The compaction load is applied through the top platen. The bottom platen provides a reactive force, thereby squeezing together the aggregates in the middle portion of the HMA sample, possibly resulting in more compaction energy. Furthermore, the gyratory motion of the mould during the compaction process could result in more compaction energy being exerted in the middle of the HMA sample.

One of the key implications of the findings is that the current practice of trimming 10 mm from the top and bottom ends of the HMA samples before density measurement and performance testing may not necessarily ensure uniform air voids in the different specimens (Sabita Manual 35/TRH 8, 2020). Furthermore, the trimming of the specimens results in a decrease in the overall average voids of the sample. This has implications for sample preparation to specific target voids.

With respect to the influence of the sample height, the results indicated that the vertical variation of the air voids content was more pronounced on the HMA samples compacted to 120 mm, with the middle part having significantly low air voids contents. This indicates that thin asphalt pavement layers, which are mainly used in South Africa (typically 50 mm thick), could be more prone to the vertical variation air voids content. Therefore, appropriate quality control and assurance need to be exercised during field compaction.

The samples compacted to a higher compaction density (4.0% air voids content) exhibited a higher variation of vertical air voids content than the samples compacted at a lower density (7.0% air voids content). This indicates that the internal structure of the samples compacted to 4.0% differs from those compacted to 7.0%, which in turn may influence their mechanical properties. The influence of the compaction density on HMA rutting resistance will be investigated in Chapter 6.

The results of the investigation into the radial distribution of air voids in the gyratory-compacted samples were presented in Section 5.3. The radial distributions of air voids were found to be uniform, regardless of the sample height (120 mm or 170 mm) and the compaction density (4.0% or 7.0%). Furthermore, compaction density and sample heights were found not to influence the radial air voids distribution.

Section 5.4 presented the results of the investigation into the vertical air voids distribution in field asphalt core samples of the HiMA and BTB asphalt mix pavement layers. For the HiMA field cores, the vertical air voids distribution was found to be similar to that of the laboratory-compacted samples (i.e., the middle part was more compacted than the top and bottom parts). In contrast, only the bottom parts of the BTB cores had higher air voids, with the difference in compaction levels being significantly higher than those of the HiMA cores.

It should be pointed out that the observed trend of the vertical air voids distribution on the field asphalt cores could also be influenced by the supporting layer into which the asphalt layer was compacted. During the field compaction process, a vertical load is applied on the top of the layer, and the underlying layer provides a reactive force, squeezing together the aggregate particles. This means that a more flexible underlying supporting layer could result in less compaction at the bottom of the HMA layer. Furthermore, the gradation of the mix may also influence the vertical air void distribution. For the field HMA mixes investigated in this study, the BTB mix (20 mm NMPS) was coarser than the HiMA mix (14 mm NMPS). A previous study by Walubita et al. (2012) suggested that coarse-graded HMA mixes do not receive sufficient compactive energy at the bottom of the layer. This phenomenon results in less aggregate reorientation and consequently contributing to less compaction and poor air voids distribution structure at the bottom of the layer, which is in line with the findings of this study.

The results of the radial distributions of the air voids in field core samples were presented in Section 5.5. As in the case of the laboratory-compacted samples, the results of the field asphalt core samples showed insignificant differences in radial air voids distribution.

One of the key implications of the findings is that, as the distribution of the air voids defines the internal structure of the HMA, the observed trends point to the conclusion that the top, middle and bottom parts of the HMA specimens are likely to possess different internal structures. Consequently, the HMA properties such as permeability, resistance to permanent deformation, fatigue cracking and moisture damage may also differ for the top, middle and bottom parts. Therefore, asphalt mix designers should consider the possible influence of aspects such as target compaction density and sample height on the volumetric and mechanical properties.

6 INFLUENCE OF COMPACTION METHOD AND DENSITY ON HMA RUTTING RESISTANCE

6.1 Introduction

This chapter presents the analysis and discusses the results of the experimental work described in Section 3.4 aimed at investigating the influence of the laboratory compaction method and compaction density on the rutting resistance of compacted HMA samples. Generally, it is widely accepted that better HMA compaction enhances HMA performance attributes. However, previous studies have shown that different laboratory compaction methods or devices may yield HMA samples that differ in terms of aspects such as aggregate orientation and internal structure, particularly with respect to the air voids distribution (Partl et al., 2007; Walubita et al., 2012). Therefore, it is essential to understand better how the compaction method or device affect the internal structure of the compacted HMA samples and the HMA performance attributes such as rutting resistance.

In this study, the HMA samples investigated were compacted using two different compactors, namely the gyratory compactor and the slab roller compactor. These two compaction methods are recommended for the compacting of samples for the evaluation of asphalt mix volumetric properties and mechanical performance in South Africa and worldwide (AI, 2014; Austroads, 2014; Sabita Manual 35/TRH 8, 2020).

The laboratory study used two different HMA mixes, a 10 mm NMPS (sand skeleton) mix and a 20 mm NMPS (stone skeleton) mix. Two HMA rutting tests, namely the Repeated Simple Shear Test at Constant Height (RSST-CH) and the Uniaxial Repeated Shear Test (URST), were used to evaluate the rutting resistance of the compacted HMA samples. The set-up of the URST and RSST-CH best represented the vertical consolidation and lateral distortion respectively, which are the two main mechanisms of HMA rutting. The samples were compacted at two different target compaction densities (4.0% and 7.0%), which represent the air voids of the HMA mix during the stable condition of its design life and during the phase immediately after construction respectively (Sabita Manual 35/TRH 8, 2020).

The chapter is structured as follows: Section 6.2 presents a comparative evaluation of the two rutting tests used in the study. The results of the experiments conducted to investigate the influence of the compaction method on the HMA rutting resistance are analysed and discussed in Section 6.3. This is followed by Section 6.4, which focuses on the experiments carried out to

investigate the influence of the compaction density on HMA rutting resistance. The chapter ends with a summary and discussion of the key findings that are presented in Section 6.5.

6.2 Evaluation of rutting tests

The RSST-CH and the URST tests were used in this study to evaluate the rutting resistance of the compacted HMA sample. The tests were performed using the Simple Shear Tester (SST) and the Uniaxial Shear Tester (UST) equipment, respectively. The SST equipment has been used in South Africa for over a decade to evaluate the shear properties (rutting resistance) of asphalt mixes. However, only one SST is available in South Africa due to (among other factors) the high cost of the equipment.

The UST, in contrast, was purposely developed as a cost-effective tool for testing the shear properties of asphalt mixes (Zak et al., 2016). It is simpler and cheaper than the SST and can be used as an alternative to the SST. As part of this project, a UST equipment was procured from Czech Technical University in Europe in order to investigate the shear properties of compacted asphalt samples. Since the UST equipment is new in South Africa, it was necessary to undertake a comparative evaluation with the SST. Slab roller-compacted samples were chosen for the comparative evaluation. Two HMA mixes of 10 mm NMPS and 20 mm NMPS were used in the comparative study. For each HMA mix, three slab samples were compacted with a roller compactor to approximately 7.0% air voids content. Three core specimens (150 mm diameter each) were extracted for URST and RSST-CH tests from each slab.

For the RSST-CH tests, a 69 kPa cyclic load was applied horizontally to the asphalt specimen by moving the bottom plate (AASHTO 320, 2007). Each cycle consisted of the load being applied for 0.1 seconds, followed by 0.6 seconds rest period. A Linear Variable Displacement Transformer (LVDT) was used to measure the horizontal displacement of the asphalt specimen. A vertical actuator maintained the height of the specimen to ensure that it remains constant during the test. For each specimen was subjected to 5000 load cycles, or the number of cycles up to where the sample failed – whichever came first.

Like the RSST-CH, the URST tests were carried out according to procedures stipulated in the AASHTO T 320 standard test method. A vertical cyclic load of 69 kPa (i.e., approximately 1.2 kN shear load) was applied to the asphalt test specimen. Similar to the RSST-CH, each loading cycle consisted of 0.1 seconds and 0.6 seconds of loading and rest periods respectively. The resulting vertical displacement was measured using three LVDTs mounted at 120° intervals along

the specimen's circumference. Figure 6.1 and Figure 6.2 respectively plot the typical load and corresponding displacement for a 7-second load application period for the URST test.

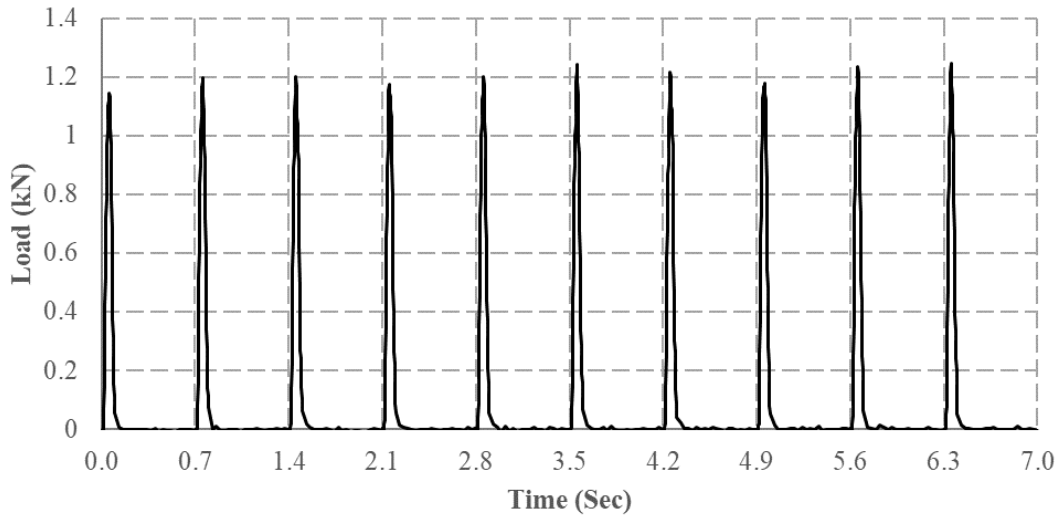


Figure 6.1: Typical load versus time

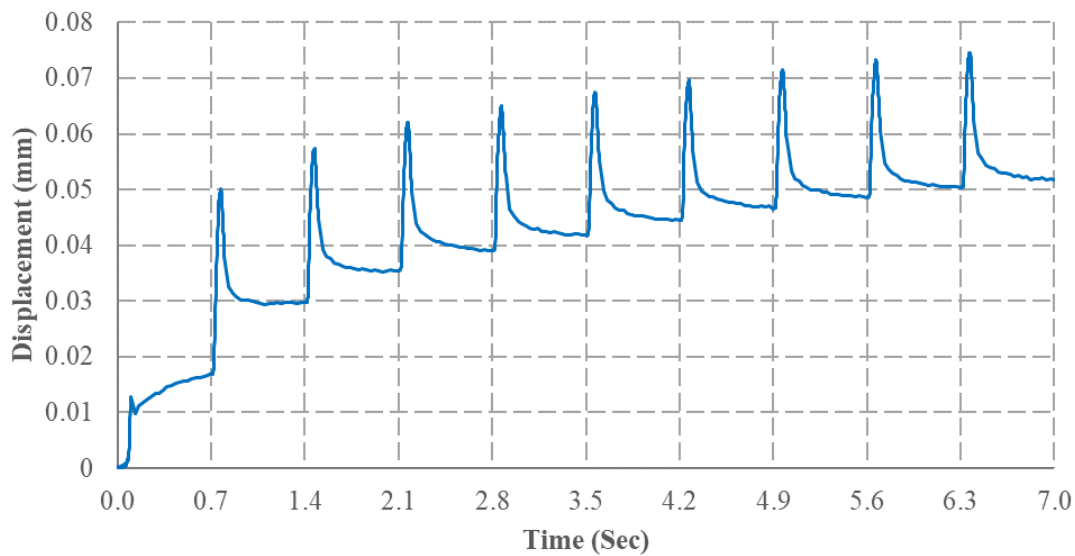


Figure 6.2: Typical displacement versus time

For each of the two HMA mixes, the RSST-CH and URST tests were performed at three different temperatures (40, 50 and 60 °C). The use of three specimens allowed for the identification of any possible outlier result. For each equipment and temperature combination, three replicate specimens were tested and used to calculate an average result. The LVDT displacement

measurements were processed to determine permanent shear strain according to the procedures stipulated in the AASHTO 320 (2007) standard test method. The permanent shear strain results of individual RSST-CH and URST tests specimens are presented in Appendices C and D respectively.

Figure 6.3 and Figure 6.4 plot the average permanent shear strain for the 10 mm and 20 NMPS mixes respectively. For both tests, the permanent shear strain increased as the number of load cycles increased. The higher the temperature, the higher the permanent shear strain values, which was the expected trend for viscoelastic materials such as HMA. At lower temperature (40 °C), the permanent shear strain values of the URST and RSST-CH tests did not differ significantly. However, at elevated temperatures (50 and 60 °C), the RSST-CH had higher permanent shear strain values.

The differences in the permanent shear strain values could be attributed to the differences in the set-up and how the shear load was applied in the URST and the RSST-CH:

- In the URST, the shear force was applied vertically (same as the compaction direction), whereas in the RSST-CH the shear force was applied horizontally (perpendicular to compaction direction);
- The URST is a confined test, with the specimen in a ring to restrict horizontal deformation, while the RSST-CH test is an unconfined test with the top and bottom plates glued to the specimen, and
- During the URST test, the material was forced to compress as it was horizontally confined, and the material was forced to stay within the ring. On the other hand, in the case of the RSST-CH test, the sample was free to move horizontally as the sample deformed, which possibly resulted in higher permanent strain values.

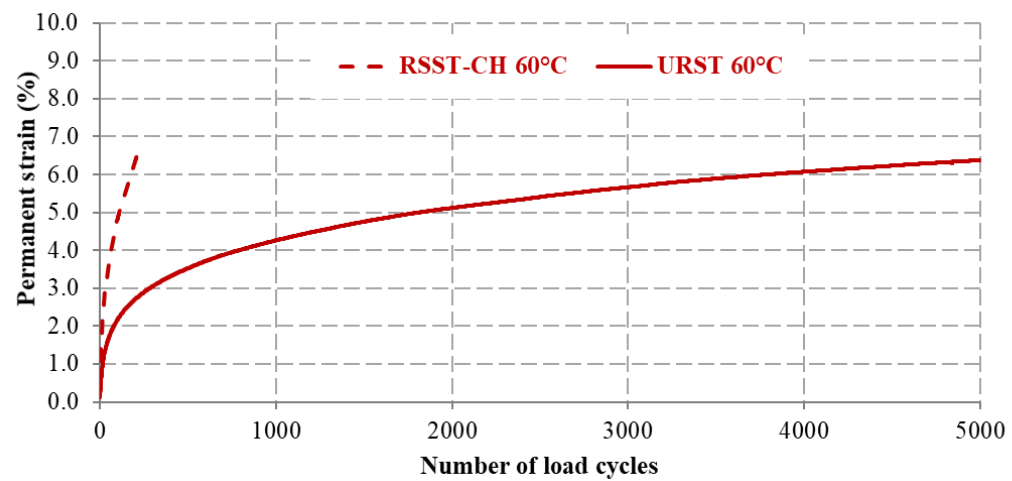
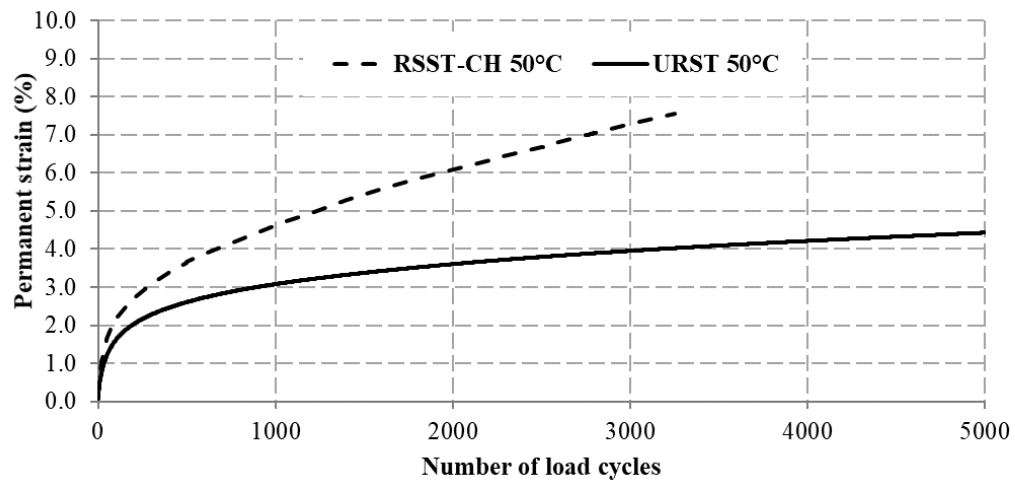
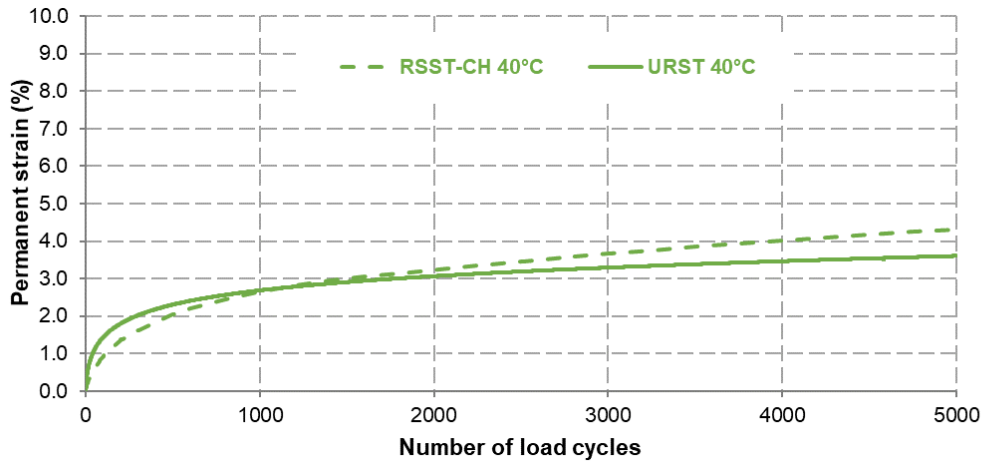


Figure 6.3: RSST-CH and URST results (10 mm NMPS mix)

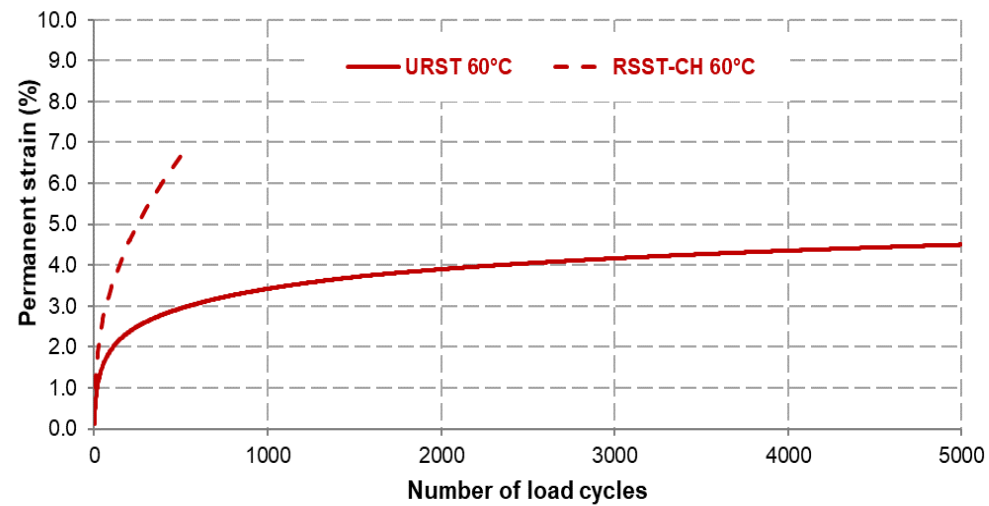
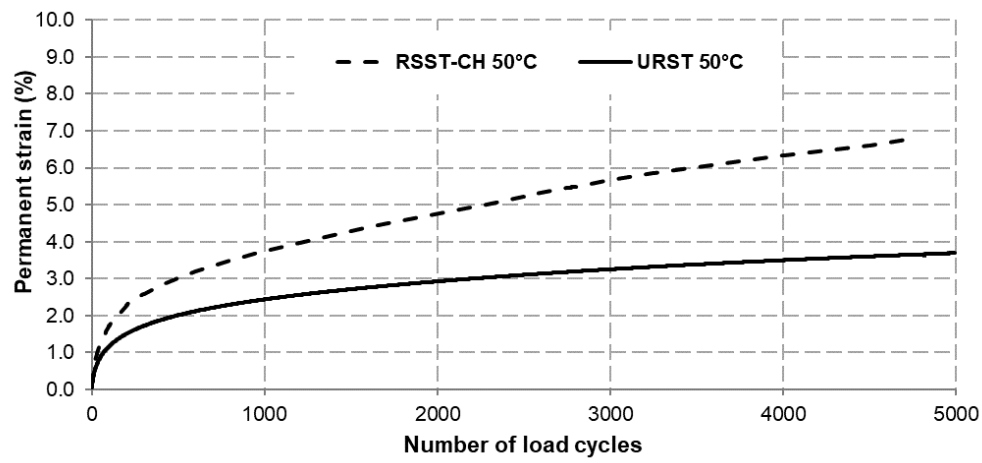
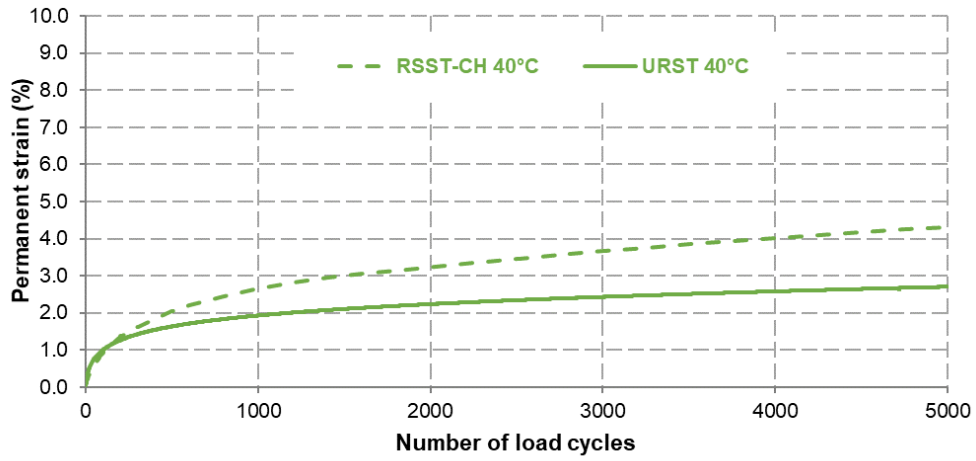


Figure 6.4: RSST-CH and URST results (20 mm NMPS mix)

Figure 6.5 and Figure 6.6 compare the permanent shear strain results of the RSST-CH and the URST tests respectively for the two mixes used in the study (i.e., 10 mm and 20 mm NMPS). At

a temperature of 40 °C, the RSST-CH test results (see Figure 6.5) show that the 10 NMPS mm mix had relatively lower permanent shear strain values than the 20 mm mix. Both mixes reached the 5 000 load cycles without shear failure. At 50 °C and 60 °C, the RSST-CH results indicate that the 20 NMPS mix had lower shear strain values than the 10 mm NMPS mix. However, both mixes failed before reaching 5 000 load cycles.

The URST test results (see Figure 6.6) indicate that 20 mm NMPS had lower permanent shear strain values than the 10 mm NMPS mix. The differences in the permanent shear strain values were more pronounced at the high temperature (i.e., 60 °C). Unlike the RSST-CH test results, it was possible to apply 5 000 load cycles to all the mixes and at the three test temperatures without excessive deformation of the specimens. [Recall from the methodology chapter (Section 3.4.1) that the 10 mm and 20 mm NMPS mixes were produced using 50/70 penetration grade bitumen (PG 58-22) and 35/50 penetration grade binder (PG 64-16) respectively. Hence, among other factors, the permanent shear strain values at elevated temperature could be influenced by the binder properties (i.e., PG 64-16 binder is stiffer than PG 58-22 binder).

Overall, a 60 °C temperature appeared to be too high for the RSST-CH tests, as the HMA specimens failed after the application of less than 210 and 500 load cycles for the 10 mm and 20 mm NMPS mixes respectively. On the other hand, a temperature of 40 °C was on the lower side, as it could not differentiate between the rutting performances of the mixes investigated. A 50 °C temperature was found to be more appropriate, as it allowed for the application of a sufficient number of load cycles while also clearly differentiating between the rutting performances of HMA mixes. Based on the findings of the comparative evaluation, a temperature of 50 °C was chosen for the rest of the study. The chosen temperature of 50 °C is also in line with recommendations in the South African guidelines (Sabita Manual 35/TRH 8, 2020).

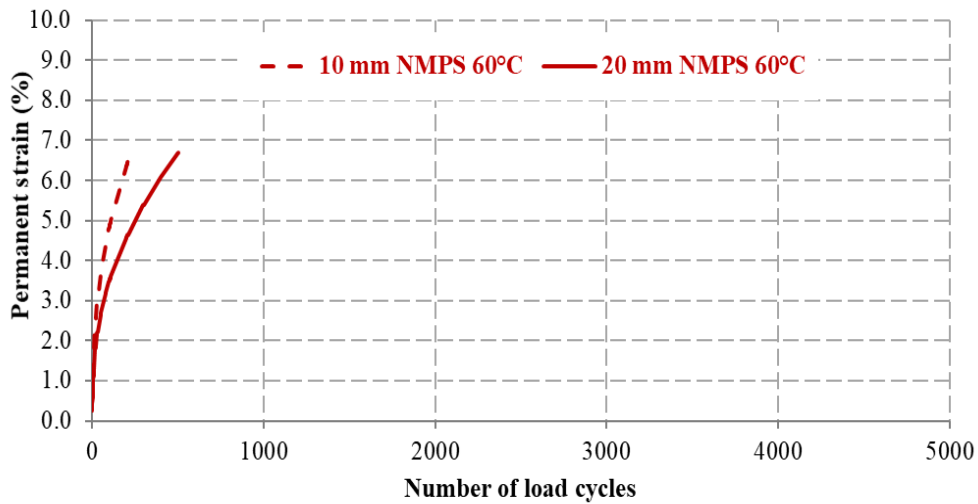
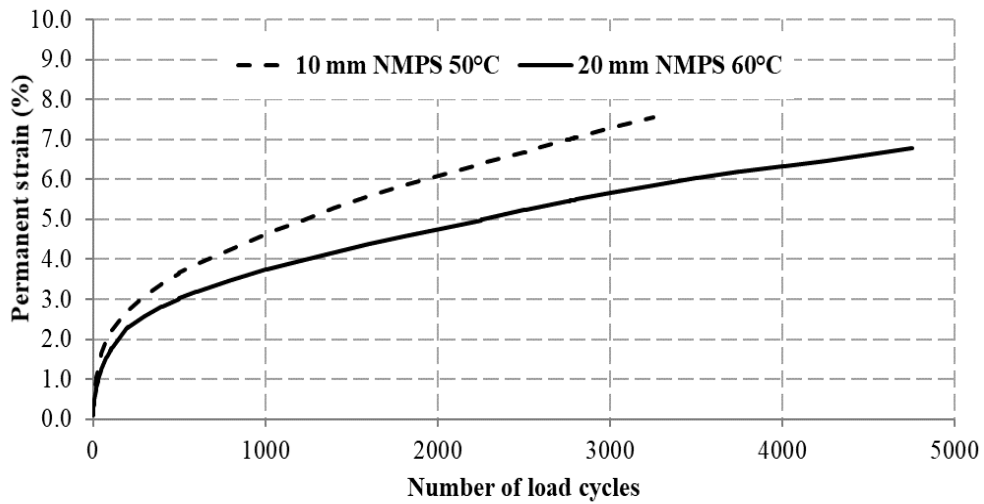
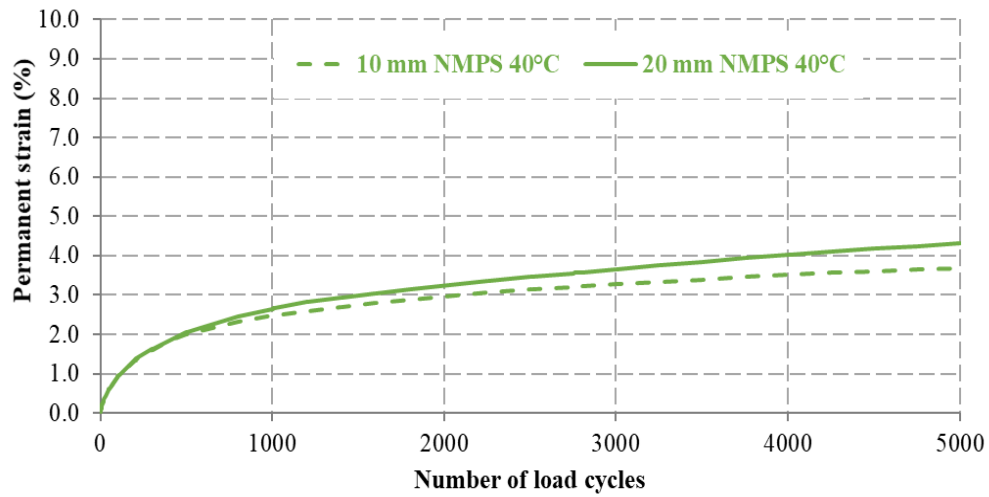


Figure 6.5: Comparison of RSST-CH results for the 10 mm and 20 mm NMPS mixes

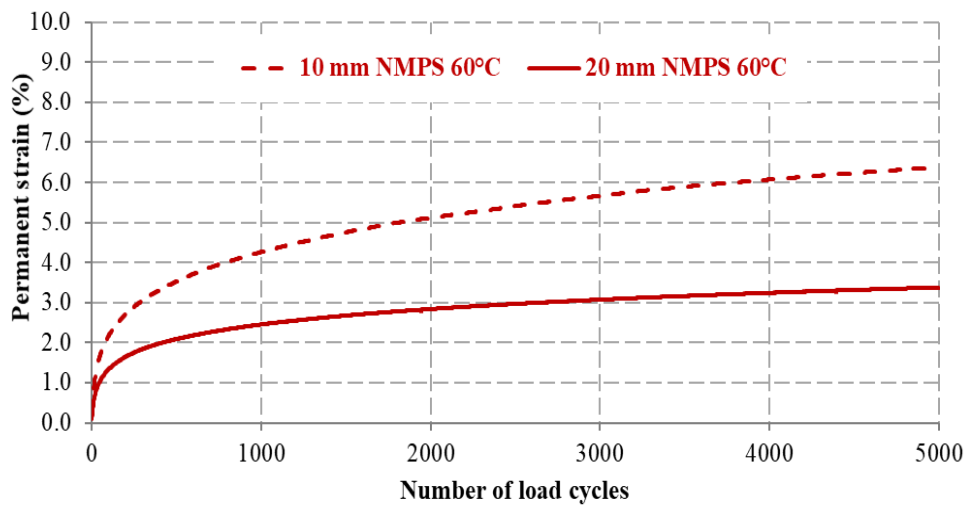
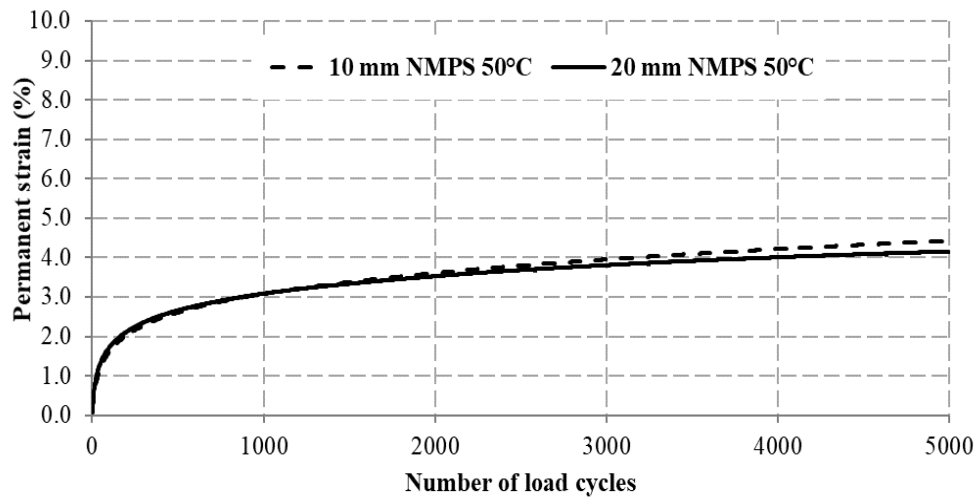
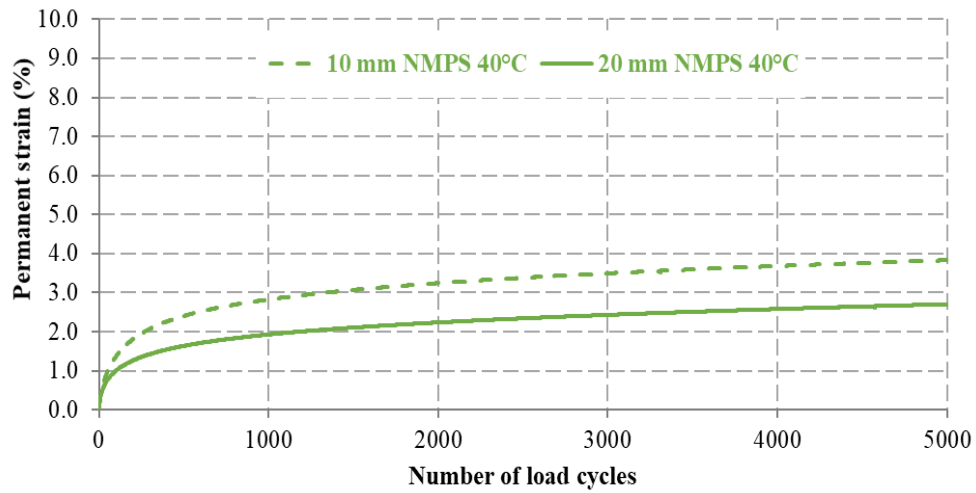


Figure 6.6: Comparison of the URST results for the 10 mm and 20 mm NMPS mixes

6.3 Influence of the compaction method

Following the comparative evaluation of the RSST-CH and URST tests (Section 6.2), the two methods were used for testing HMA samples compacted with the gyratory compactor and the slab roller compactor. The aim was to investigate the influence of the compaction method on the rutting resistance of compacted HMA samples. The HMA samples were compacted to a target of approximately 7.0% air voids content, which represents air voids content at a phase immediately after asphalt paving.

Two HMA mixes – a 10 mm NMPS (sand skeleton) mix and a 20 mm NMPS (stone skeleton) mix – were used in the study to compare compaction methods. For each HMA mix, six replicate specimens were prepared. A set of three specimens was used for RSST-CH tests, and the remaining three specimens were used for the URST tests, after which the average results were calculated. The RSST-CH and URST tests were carried out at a temperature of 50°C, and the processed results of the individual RSST-CH and URST samples are presented in Appendices C and D respectively.

Figure 6.7 and Figure 6.8 plot the average RSST-CH results of the 10 mm and 20 mm NMPS mixes respectively. The results show that the permanent shear strain values of the slab roller-compacted samples are higher than those of the gyratory-compacted samples, regardless of the HMA mix type (i.e., 10 mm versus 20 mm NMPS mixes). The difference in the permanent shear strain values is more pronounced for the 10 mm NMPS mix. The figures also show that the roller-compacted specimens of both mixes failed before reaching 5 000 load cycles. This implies that their rutting resistance is poorer than that of the gyratory-compacted specimens.

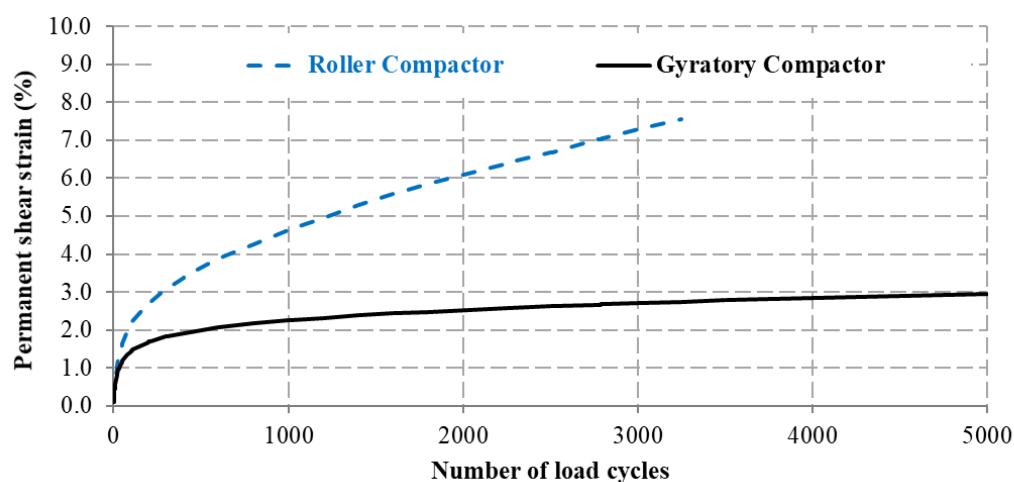


Figure 6.7: RSST-CH results – gyratory- and roller-compacted samples (10 mm NMPS mix)

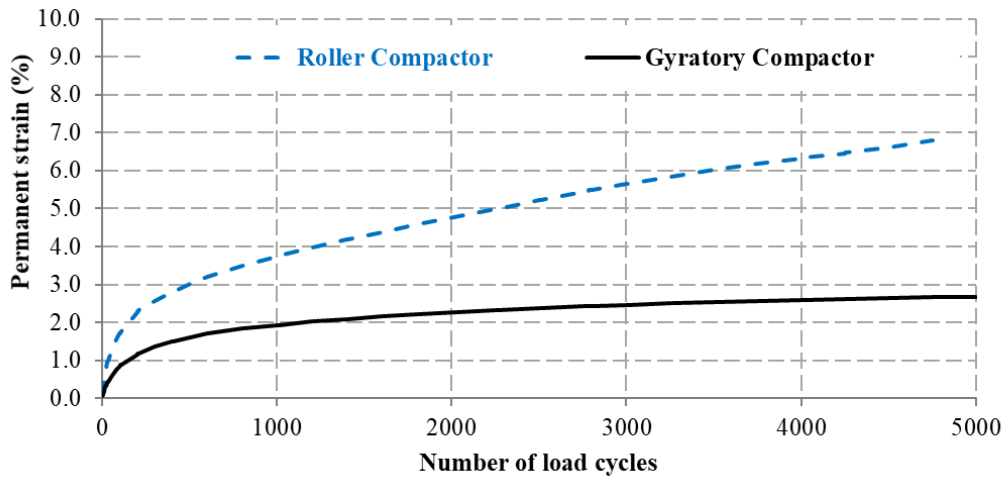


Figure 6.8: RSST-CH results – gyrotory- and roller-compacted samples (20 mm NMPS mix)

The average URST results of the 10 mm and 20 mm NMPS mixes are presented in Figure 6.9 and Figure 6.10 respectively. Like the RSST-CH results, the permanent shear strain values of the slab roller-compacted samples are higher than those of the gyrotory compactor. This also means that the gyrotory-compacted samples have better rutting resistance. As in the case of the RSST-CH results, the difference in the permanent shear strain values is more pronounced for the 10 mm NMPS mix. Unlike the RSST-CH results, both mixes sustained 5 000 load cycles.

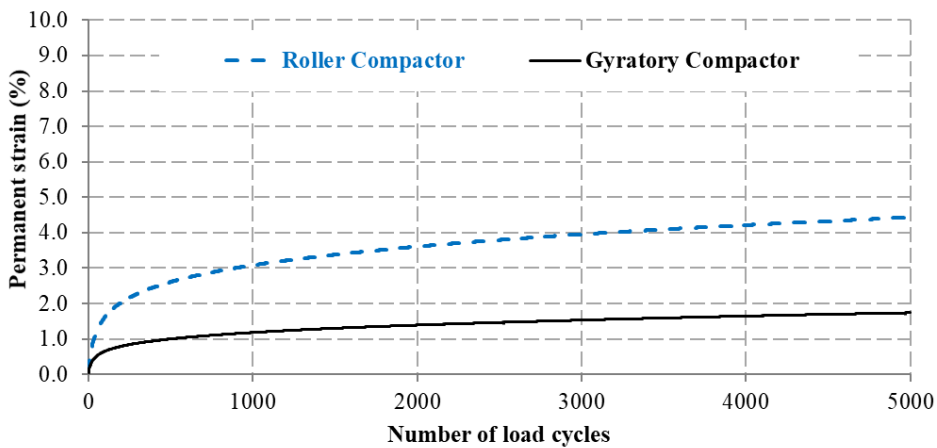


Figure 6.9: URST results – gyrotory- and roller-compacted samples (10 mm NMPS mix)

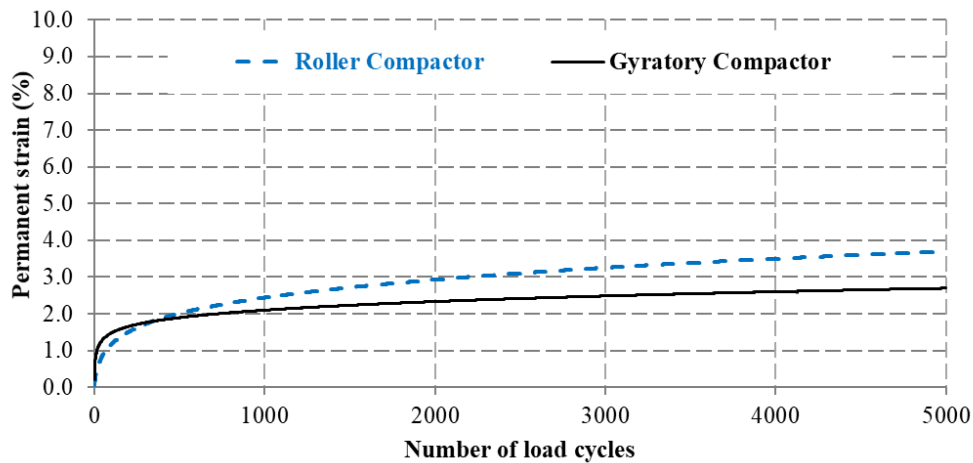


Figure 6.10: URST results – gyratory- and roller-compacted samples (20 mm NMPS mix)

Overall, the findings reported in this section suggest that the gyratory-compacted samples exhibited better rutting resistance, regardless of the rutting evaluation test (i.e., RSST-CH or UST). Since the HMA samples tested were compacted to a similar density (approximately 7.0% air voids content), the RSST-CH and URST test results suggest that achieving a similar density does not necessarily guarantee that the HMA samples will have a similar rutting resistance. The compaction method influences the internal structure of the HMA, and consequently, the rutting resistance.

Furthermore, the methodology chapter (Section 3.4.2) shows that the gyratory compactor and the slab roller compactor differ in terms of the magnitude and compaction load applied to the sample. The gyratory compactor achieves compaction by simultaneous application of static compression pressure (600 kPa) and shearing action that results from the gyratory motion (1.25° used in this study). On the other hand, the slab roller compactor achieves compaction by applying a static load of a maximum of 30 kN (approximately 275 kPa) through a semi oval-shaped contact plate that performs a pendulum-like motion. The observed differences in the rutting resistance of HMA samples compacted by means of these two methods suggest that the magnitude and how the compaction load is applied to the sample influence the internal structure of the HMA samples, which in turn affects their rutting resistance.

6.4 Influence of compaction density on rutting performance

In Section 6.3 it was established that the rutting resistance of HMA mixes is influenced by the compaction method, and that HMA samples compacted with the gyratory compactor have a better rutting resistance than samples compacted with the slab roller compactor. This section now

investigates the rutting resistance of HMA samples compacted at two different target compaction densities. In order to eliminate the influence of the compaction method, one compaction method (a gyratory compactor) was selected to compact the HMA samples. The use of a single compaction method ensured that only the influence of compaction density is evaluated (i.e., same compaction method, but different target compaction densities). Furthermore, since it is relatively easier to obtain the target compaction density when using a gyratory compactor, this method is recommended for compacting most of the samples for HMA mix performance evaluation in South Africa (Sabita Manual 35/TRH 8, 2020).

The rutting resistance of two HMA mixes (10 mm NMPS and 20 mm NMPS mix) was investigated. For each mix, two sets of HMA samples were compacted to approximately 4.0% and 7.0%, representing asphalt design density and field density, respectively. Six replicate specimens were prepared for a combination of mix type and target compaction density (three for RSST-CH tests and three for URST tests). Both the RSST-CH and URST tests were carried out at a temperature of 50°C. The processed results of the individual RSST-CH and URST test specimens are presented in Appendices C and D respectively.

Figure 6.11 and Figure 6.12 compare the average RSST-CH results of the 10 mm and 20 mm NMPS mixes respectively. The results show that the permanent shear strain values of the 7.0% target air voids content samples are higher than those of the 4.0%, regardless of the HMA mix type (whether 10 mm or 20 mm NMPS). The difference in the permanent shear strain values is more pronounced for the 10 mm NMPS mix. This means that the rutting resistance of samples compacted to a 4.0% target air void content is better than the rutting resistance of those compacted to 7.0% target air voids content.

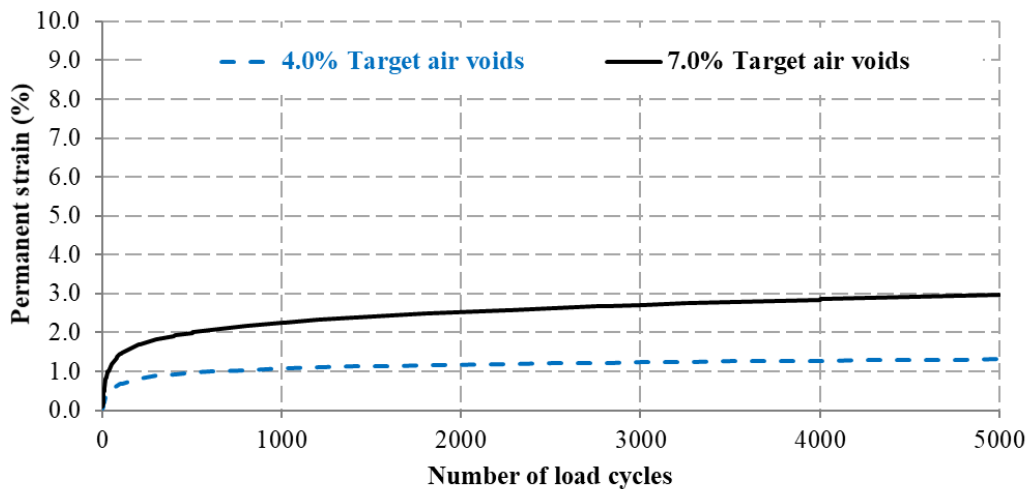


Figure 6.11: RSST-CH results – gyratory-compacted samples to 4% and 7% target air voids content (10 mm NMPS mix)

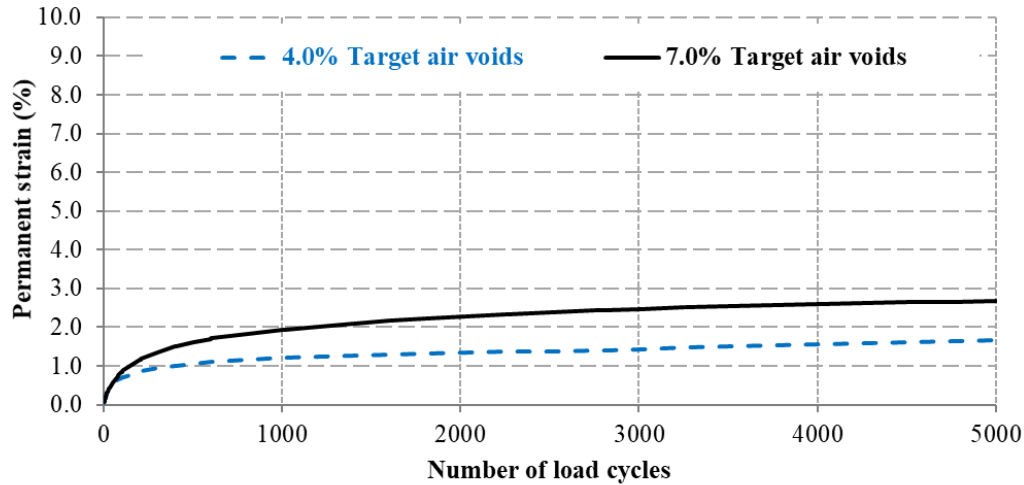


Figure 6.12: RSST-CH results – gyratory-compacted samples to 4% and 7% target air voids content (20 mm NMPS mix)

The average URST results of the 10 mm and 20 mm NMPS mixes are presented in Figure 6.13 and Figure 6.14, respectively. As in the case of the RSST-CH results, the permanent shear strain values of the samples with a 7.0% target air voids content are higher than those with 4.0%. Again, this means that the rutting resistance of samples compacted to 4.0% air voids content is better than the resistance of those compacted to 7.0% air voids content. The permanent shear strain values obtained using URST are generally lower than those of the RSST-CH tests, which could be due to the difference in the set-up of the two tests (see the explanation in Section 6.2).

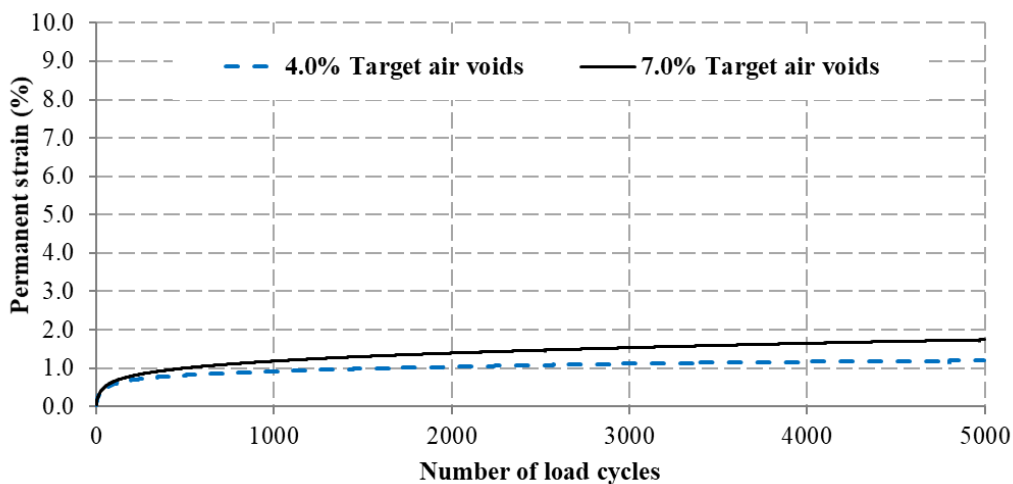


Figure 6.13: UST results – gyratory-compacted samples with a 4% and 7% target air voids content (10 mm NMPS mix)

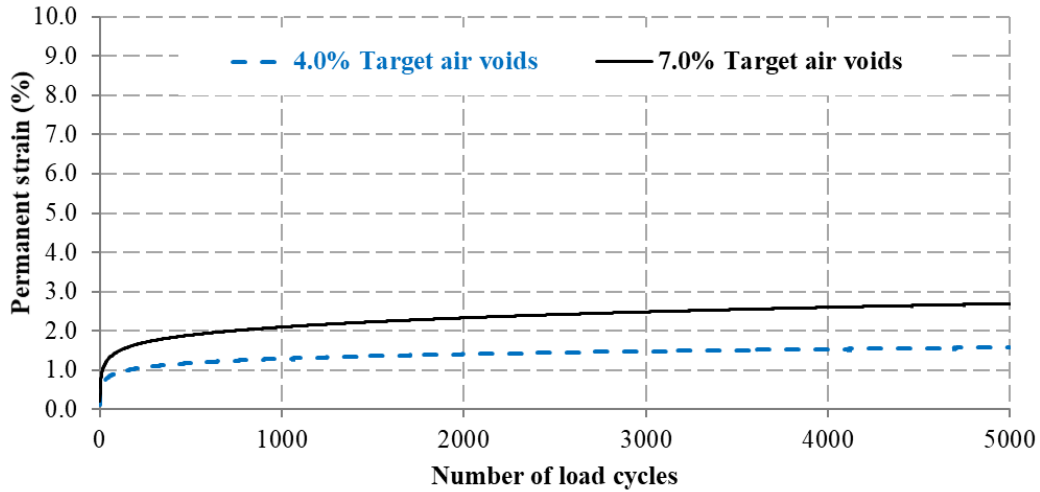


Figure 6.14: UST results – gyratory-compacted samples with a 4% and 7% target air voids content (20 mm NMPS mix)

6.5 Summary

This chapter investigated the influence of the compaction method and density on the rutting resistance of HMA samples. The HMA samples were compacted using two different methods: the gyratory compactor and the slab roller compactor. The rutting resistances of two different HMA mixes (10 mm and 20 mm NMPS) were evaluated using two different rutting tests.

Section 6.2 presented results of comparative evaluation of the two rutting tests at three test temperatures (40, 50 and 60 °C). The results show that the permanent shear strain values increased with a rise in test temperature for both tests, meaning that the higher the temperature, the weaker became the rutting resistance of the HMA mix (which was the expected trend). However, at elevated temperature (i.e., 50 and 60 °C), the permanent shear strain values of the URST test were generally lower than those of the RSST-CH test. This could be due to the differences in the set-up of the two tests and how the shear load was applied.

Section 6.3 presented an analysis of the data obtained from the laboratory experiments carried out to investigate the influence of the compaction method on the HMA rutting resistances. It was found that, despite the HMA samples being compacted to a similar density, HMA samples compacted using the gyratory compactor had better rutting resistance than those compacted with

the slab roller compactor. Therefore, achieving a similar compaction density did not necessarily guarantee that the HMA samples would have equivalent rutting resistance. It was concluded that the compaction method indeed had an influence on the rutting resistance of the HMA samples investigated. The differences in the rutting resistance achieved by the gyratory and the slab roller compactors could be attributed to the differences in the internal structure of the asphalt samples that were produced using each of the two compaction methods. Partl et al. (2007) employed X-ray Computed Tomography in their study to determine the internal structure of asphalt samples compacted using different laboratory methods. They found that different compaction methods produced structurally different asphalt samples, which could influence the mechanical performance (i.e., rutting resistance) of the samples.

Although this aspect of the study focussed on the laboratory compacted HMA samples, the findings can be related to the field compacted HMA samples. This is due to the fact that previous research studies have reported that the gyratory compactor simulates better the field HMA compaction (Khan et al., 1998 AI, 2014; Austroads, 2014; Sabita Manual 35/TRH 8, 2020). It should, however, be pointed out that field compaction is influenced by other factors such as the supporting layer, which could affect the distribution of air voids in the compacted HMA samples, as demonstrated in the discussion provided in Section 5.6. Therefore, such factors need to be considered when evaluating the rutting resistance results of field compacted HMA samples.

Section 6.4 indicated the effect of the compaction density on the rutting resistance of HMA samples. Two HMA mixes (10 mm NMPS and 20 mm NMPS) compacted with a gyratory compactor were investigated. The samples were compacted to two different compaction densities – approximately 4.0% and 7.0%. The 4.0% represented the stable condition of the compacted HMA during most of its design life, while the 7.0% represented the phase immediately after HMA mix paving. The rutting resistance of the compacted HMA samples was evaluated using the RSST-CH and URST tests. The results showed that the rutting resistance of HMA samples compacted to a 4.0% air voids content was better than that of the samples compacted to a 7.0% air voids content, which was expected.

The study found that the difference in the permanent shear strain values between the HMA samples compacted to 4.0% and 7.0% air voids contents was more pronounced for the 10 mm NMPS mix. This indicates that the sensitivity of the HMA mix resistance due to changes in air voids content could be greater for the sand skeleton mix (10 mm NMPS) than for the stone skeleton mix (20 mm NMPS).

7 CONCLUSIONS AND RECOMMENDATIONS

7.1 Introduction

This thesis aimed to relate aggregate packing characteristics with HMA compactability, the resulting volumetric properties of the HMA, as well as rutting resistance of the compacted HMA mixtures. This final chapter discusses the conclusions reached, based on an analysis of the results of the experiments that were carried out to investigate each of the three specific study objectives.

Section 7.2 discusses conclusions of the experiments that were carried out to investigate the influence of aggregate packing characteristics on the compactability of HMA. Section 7.3 discusses the conclusions of the investigation into the spatial distribution of air voids in compacted HMA mixes. Section 7.4 focuses on the influence of the compaction method and compaction density on the HMA rutting resistance, while the recommendations and suggestions for future research work are provided in Section 7.5.

7.2 The influence of aggregate packing characteristics on HMA compactability

The first specific objective of this study was to investigate the influence of aggregate packing characteristics on the compactability of HMA mixes. The experimental work carried out was analysed and discussed in Chapter 4. Aggregate packing analysis was undertaken using six gradation curves – three 10 mm NMPS and three 20 mm NMPS. For each NMPS, the three gradation curves were designed to yield coarse, medium and fine gradation structures. For each gradation structure, eight packing parameters were determined. These included the shape factor (n), gravel-to-sand ratio (G/S), three traditional Bailey ratios (CA , FA_c and FA_f), and three rational Bailey ratios (CA_r , C/F and F_{Armf}). The study established that most of the aggregate packing parameters investigated could distinguish the aggregate gradation structure. However, the rational Bailey ratios provided a better description of the effect that the packing characteristics of the gradation structure had on the macro, midi and micro skeleton matrix levels.

The six gradation curves were used to produce HMA mixes, following which HMA samples were compacted using a gyratory compactor. The gyratory compaction data was analysed to determine five compactability parameters, including locking point (LP); compaction energy index (CEI); traffic densification index (TDI_{300}); compaction slope (CS); and the area under shear stress curve (ASS_{max}). The analysis results showed that the compactability of the HMA mixes is influenced by the NMPS and by the packing characteristics of the gradation structure. Most of the HMA

compactability parameters showed a strong correlation with the rational Bailey ratios, with the TDI_{300} , LP, and CS, relating more logically to the NMPS and aggregate gradation structures.

7.3 The spatial distribution of aggregates in compacted HMA samples

The second specific objective of the study was to investigate the spatial distribution of air voids in compacted HMA. Chapter 5 presented the analysis and discussion of the experiments carried out. A gyratory compactor was used to compact sets of HMA samples at two target sample heights (120 mm and 170 mm) and two target compaction densities (4.0% and 7.0% air voids content). The study also investigated the spatial distribution of air voids in asphalt cores extracted from actual road sections. The results showed that the top and bottom parts of the gyratory-compact samples exhibit a relatively high air voids content (i.e., low density). However, the air voids distribution in the middle part of the HMA samples was fairly uniform, suggesting that HMA specimens for performance testing should ideally be extracted from the middle of the compacted gyratory samples.

The vertical air voids distribution was influenced by both the sample height and the compaction density. The smaller the sample height, the higher was the variation of the vertical distribution of the air voids. Similarly, the higher the compaction density, the higher was the variation of the vertical air voids distribution. One of the implications of this finding is the thin asphalt pavement layers constructed in South Africa could be more prone to the vertical distribution of the air voids content, necessitating the need to exercise stringent quality control and assurance measures.

For the asphalt cores extracted from the actual road sections, the vertical distribution of the air voids of the HiMA mix followed the same trend as the laboratory-compact samples, namely the top and bottom ends exhibited high air voids. However, for the BTB cores, only the bottom part exhibited higher air voids. The radial distribution of air voids was found to be uniform for the gyratory-compact HMA samples and the field-extracted asphalt core samples. Factors such as supporting layer, aggregate segregation and temperature variation with depth during HMA compaction may have contributed to the observed trend and should be further investigated in future studies.

7.4 The influence of compaction method and density on HMA rutting resistance

The third specific objective of the study was to investigate the influence of the compaction method and density on the rutting resistance of HMA samples. Chapter 6 contains the analysis and discussion of the results of experimental work carried out. The first aspect of this specific objective was devoted to a comparative evaluation of the RSST-CH and the URST. The analysis showed that the permanent shear strain values determined with the RSST-CH were generally lower than those determined with the URST. These variations could be attributed to the differences in the set-up and how the shear load was applied in the URST and the RSST-CH. Although the comparative assessment results indicated that the URST has the potential to be used as an alternative to the RSST-CH, further evaluation using different types of South African HMA mixes was recommended.

The second aspect compared the rutting resistance of gyratory- and slab roller-compacted samples. The results showed that the rutting resistance of the HMA samples compacted using the gyratory compactor was better than the resistance of those compacted using the slab roller compactor, regardless of the samples being compacted to a similar density. This is possible because the literature review indicated that different compaction methods could produce HMA specimens that differ in their internal structure (Partl et al., 2007). Although the study focussed on the laboratory compacted HMA samples, the findings could benefit the field compaction, considering that previous research studies have shown that gyratory compactor simulates better the field compaction (Khan et al., 1998 AI, 2014; Austroads, 2014; Sabita Manual 35/TRH 8, 2020).

Lastly, the influence of target compaction density on the HMA's rutting resistance was investigated. Two sets of HMA samples were compacted with a gyratory compactor to a target of air voids content of 4.0% and 7.0% respectively. Both the RSST-CH and URST results showed that the rutting resistance of samples compacted to a 4.0% air voids content was better than that of the samples compacted to a 7.0% air void content.

7.5 Recommendations and suggestions for future research

The current South African asphalt mix design manuals (Sabita Manual 24, 2020; Sabita Manual 35, 2020) recommend using the traditional Bailey ratios to optimise aggregate gradation. The study in hand, however, showed that the rational Bailey ratios give a better description of the

macro, midi and micro levels of the gradation structure. Thus, it was recommended that future revision of the existing asphalt mix design manuals should explore the possibility of also incorporating the rational Bailey ratios. Most of the existing asphalt mix design procedures recommend evaluating at least three gradation structures. Before proceeding with the preparation of mixtures and compaction, the rational Bailey ratios could be determined to assess the packing characteristics of the macro, midi and micro levels of the gradation structure, and thus to assist in identifying the potential HMA mix compaction problems. Full incorporation of the aggregate packing principles into the existing mix design procedures would require further research in order to establish relationships between aggregate packing parameters with other HMA performance attributes such as permeability and moisture damage potential. In South Africa, the SANRAL research programme initiative is envisaged to tackle some of these aspects.

This study used the spatial distribution of air voids to define the internal structure of the compacted HMA. While this provided a clear and logical trend regarding the possible internal structure of the compacted HMA, future research to validate the findings may be required. Such research could explore aspects such as investigating the actual arrangement of aggregate particles by using advanced techniques such as X-ray Computed Tomography scanning, combined with porosity concepts and numerical modelling. It should also be pointed out that the current study investigated only the influence of HMA sample height and target compaction density on the spatial distribution of air voids. Future studies should investigate other factors, such as the effect of variations in the MVD within the sample on the calculation of air voids, as well as the effect of support conditions and temperature variation with depth during field and laboratory HMA compaction. Seeing that the study was limited to a specific type of asphalt mix, it is also recommended that future studies should include other HMA mix types to validate the findings.

The comparison between the rutting resistance results of HMA samples compacted using a gyratory compactor and slab roller compactor showed that the gyratory-compacted sample has better rutting performance. This finding implies that the rutting resistance specification stipulated in the existing guidelines documents may need to be re-examined. For instance, in South Africa, the rutting resistance specification and guidelines provided in the SABITA manuals were developed based on slab roller-compacted samples, despite the fact that the gyratory compactor is currently the most often used equipment in the industry. Thus, the future revision and development of HMA performance specifications should consider the influence of the compaction method on the volumetric and mechanical properties of the resulting HMA samples.

8 REFERENCES

AASHTO T 320. 2011. *Standard Method of Test for Determining the Permanent Shear Strain and Stiffness of Asphalt Mixtures Using the Superpave Shear Tester (SST)*. American Association of State Highway and Transportation Officials (AASHTO).

AI. 2001. Superpave Mix Design. *Superpave Series No. 2 (SP-2)*. Asphalt Institute (AI), Third Edition.

AI. 2014. *Asphalt Mix Design. MS-2*. Asphalt Institute (AI), Seventh Edition.

Anochie-Boateng, J., Denneman, E., O'Connell, J. and Ventura, D. 2010. Test Protocols for determining properties of asphalt materials for SAPDM. *TECHNICAL REPORT No: CSIR/BE/IE/IR/2010/0001/B*, CSIR, Pretoria.

Anochie-Boateng, J., Komba, J., Ventura, D. and Verhaeghe, B. 2011. Effect of sample geometry on bulk relative density of Hot-mix Asphalt mixes. *Proceedings of the 10th Conference on Asphalt Pavements in Southern Africa*. September 2011, KwaZulu-Natal, South Africa.

Anochie-Boateng, J., Komba, J. and Tutumluer, E. 2012. Aggregate Surface Areas Quantified Through Laser Measurements for South African Asphalt Mixtures. *Journal of Transportation Engineering*. 1(137), pp. 1006-1015.

Arasan, S., Yenera, E., Hattatoglu, F., Hınıslıoglu, S. and Akbuluta, S. 2011. Correlation between shape of aggregate and mechanical properties of asphalt concrete. *Road Pavement Material and Design*, 12(2).

ASTM D2493. 2001. *Standard Viscosity-Temperature Chart for Asphalts*. ASTM International, West Conshohocken, PA.

ASTM D 6752. 2004. *Bulk-specific gravity and density of compacted asphalt mixtures using automatic vacuum sealing method*. ASTM International, West Conshohocken, PA.

Austrroads. 2008. *A Review of Austrroads Gyrotory Compaction Research. AP-T94/08*. Austrroads, Sydney, NSW.

Austrroads. 2014. *Guide to Pavement Technology Part 4B: Asphalt. AGPT04B-14*. Austrroads, Sydney, NSW.

Awed, A., Kassel, E., Masad, E. and Little, D. 2015. Method for predicting the laboratory compaction behavior of asphalt mixtures. *Journal of Materials in Civil Engineering*, 27(11).

Bahia, H., Friemel, T., Peterson, P., and Russell, J. 1998. Optimization of constructability and resistance to traffic: A new design approach for HMA using the Superpave compactor. *Journal of the Association of Asphalt Paving Technologists*, 189, 67–98.

Bodin, D., Grenfell, J.R. and Collop, A.C. 2009. Comparison of small and large-scale wheel-tracking devices. *Journal of Road Materials and Pavement Design*, 10, sup1.

Brown, E.R. and Haddock, J.E. 1997. *A Method to ensure Stone-on Stone contact in Stone Matrix Asphalt Paving Mixtures. NCAT Report No-97-2*. National Center for Asphalt Technology of Auburn University. USA.

Burtseva, L. and Werner, F. 2015. *Modelling of spherical particle packing structures using mathematical tessellation*. MSC: 05B45, 05B40, 52B05. Downloadable from www.math.unimagdeburg.de [Accessed on 05 March 2017].

Button, J. W., Perdomo, D., and Lytton, R. L. 1990. Influence of aggregate on rutting in asphalt concrete pavements. *Transportation Research Record 1259*, 141-152. Transportation Research Board, National Research Council, Washington D.C.

Chang, K.G. and Meegoda, J.N. 1997. Micromechanical simulation of hot mix asphalt. *Journal of Engineering Mechanics*, 123, 495–503.

Chen, Y., Ras, R. and Battley, M. 2015. *Modelling of closed-cell foams incorporation cell size and cell wall thickness variations*. 11th World Congress on Computational Mechanics; 5th European Conference on Computational Mechanics; 6th European Conference on Computational Fluid Dynamics; 20th International Conference on Composite Materials, Copenhagen, Denmark 19-24 July 2015.

Chen, J., Huang, B. and Shu, X. 2013. Air-void distribution analysis of asphalt mixture using discrete element method. *Journal of Materials in Civil Engineering*, 25, 1375–1385.

Chen, J.S., Lin, K.Y. and Chang, M.K. 2005. Influence of coarse aggregate shape on the strength of asphalt concrete mixtures. *Journal of the Eastern Asia Society for Transportation Studies*, 6, 1062–1075.

COLTO, 1998. *Standard Specifications for Road and Bridge Works for State Authorities*. SAICE, Midrand, South Africa.

Cox & SONS. 2020. *Kneading Compactor*. Available at: <https://www.jamescoxandsons.com/kneading-compacto/> [Accessed on 27 May 2020].

Crouch, L.K., Copeland, A.R., Walker, C.T., Maxwell R.A., Duncan, G.M., Goodwin, W.A., Badoe, D.A and Leimer, H.W. 2002. Determining air void content of compacted hot-mix asphalt mixes. *Transportation Research Record*, 1813, 39–46.

ELE International. 2020. Hveem Stabilometer - ASTM Type. Available at: <https://www.ele.com/Product/hveem-stabilometer-astm-type/327> [Accessed on 27 May 2020].

FAA. 2013. *Hot-Mix Asphalt Paving Handbook*. US Department of Transportation, Federal Aviation Administration (FAA), Office of Airport Safety & Standards - Airport Engineering Division.

FHWA. 2010. *Superpave Gyratory Compactors*. Technical Brief FHWA THIF T11 T032, US Department of Transportation, Federal Highway Administration (FHWA), Office of Pavement Technology.

FHWA. 2014. *A Study on Intelligent Compaction and In-Place Asphalt Density*. Publication No. FHWA-HIF-14-017, US Department of Transportation, Federal Highway Administration (FHWA).

Fuller, W.B. and Thompson, S.E. 1907. The laws of proportioning concrete. *American Society of Civil Engineers*, LIX (2), 67–143.

Gallivan, V.L., Chang, G.K. and Horan, R.D. 2011. Practical Implementation of Intelligent Compaction Technology in Hot Mix Asphalt Pavements. *Journal of the Association of Asphalt Paving Technologies*, 80.

Gopalakrishnan, K., Shashidhar, N. and Zhong, X. 2006. Study of compaction in hot-mix asphalt using computer simulations. *International Journal of Electrical and Computer Engineering*, 1 (4).

Horak, E., Sebaaly, H., Maina, J. and Varma, S. 2017. Rational Bailey ratios and dominant aggregate size range porosity with rutting and mixture strength parameters. *36th Southern African Transport Conference*. July 2017, Pretoria.

Horak, E. and Cromhout, A. 2018. Permeability potential of asphalt mixes via binary aggregate packing principles applied to Bailey method ratios and porosity principles. *Proceedings of the 2018 SARF/IRF/PIARC*, October 2018, Durban.

Kandhal, P.S. and Koehler, W.C. 1984. Pennsylvania's experience in the compaction of asphalt pavements. *ASTM Special Technical Publication*, 829, 93–106. American Society for Testing and Materials. Philadelphia, PA.

Kennedy, T.W., Roberts, F.L. and McGennis, R.B. 1984. Effects of compaction temperature and effort on the engineering properties of asphalt concrete mixtures. *ASTM Special Technical Publication*, 829, 48–66. American Society for Testing and Materials, Philadelphia, PA.

Khan, Z.A., Al-Abdul Wahab, H.I., Asi, I. and Ramadhan, R. 1998. Comparative study of asphalt concrete laboratory compaction methods to simulate field compaction. *Construction and Building Materials*, 12, 373–384.

Kim, S., Roque, R. and Birgisson, B. 2006. Identification and assessment of the Dominant Aggregate Size Range (DASR) of asphalt mixture. *Journal of the Association of Asphalt Paving Technologists*, 75, 789–814.

Kim, S., Roque, R., Birgisson, B. and Guarin, A. 2009. Porosity of the Dominant Aggregate Size Range to evaluate coarse aggregate structure of asphalt mixtures. *Journal of Materials in Civil Engineering*, 21(1).

Komba, J. 2013. *Analytical and laser scanning techniques to determine shape properties of aggregates used in pavements*. Master's Dissertation. University of Pretoria, South Africa.

Komba, J., Anochie-Boateng, J. and Steyn, J. vd M. 2013. Analytical and laser scanning techniques to determine shape properties of aggregates. *Transportation Research Record*, 2335, 60–71.

Komba, J.J., Maina, J.W., Horak, E. and Steyn, W.J. vd M. 2019a. Relationship between aggregate packing characteristics and compactability of hot-mix asphalt mixes. *Proceedings of the International Airfield and Highway Pavements Conference under the auspices of the Transportation and Development Institute (T&DI) of American Society of Civil Engineers (ASCE)*, Chicago, Illinois, USA July 21-24, 2019.

Komba, J.J., Maina, J.W., Horak, E., Steyn, W.J. vd M. and O'Connell, J. 2019b. Distribution of air voids in compacted Hot-Mix Asphalt samples – laboratory vs field. *Proceedings of the Conference on Asphalt Pavements in Southern Africa (CAPSA)*, Sun City, October 13 – 16, 2019.

Komba J.J., Mataka M., Malisa J.T., Walubita L.F., Maina J.W. 2018. Traffic Data Characterization for Road Rehabilitation: A Case Study of the Korogwe-Mombo Road Section in Tanzania. In: Sevi A., Neves J., Zhao H. (eds) *Enhancements in Applied Geomechanics, Mining, and Excavation Simulation and Analysis*. GeoChina 2018. Sustainable Civil Infrastructures. Springer, Cham.

Komba J.J., Mataka M., Malisa J.T., Walubita L.F., Maina J.W. 2019c. Assessment of Traffic Data for Road Rehabilitation Design: A Case Study of the Korogwe-Mombo Road Section in Tanzania. *Journal of Testing and Evaluation* 47 (3), pp. 1745-1761.

Kumar, V.S. and Santhanam, M. 2003. Particle packing theories and their application in concrete mixture proportioning: A review. *The Indian Concrete Journal*, 77(9), 1324–1331.

Kundhal, P. and Mallick, R. 2001. Effect of mix gradation on rutting potential of dense-graded asphalt mixtures. *80th Annual Meeting of the Transportation Research Board*. Washington, D.C.

Kutay, M.E., Arambula, E., Gibson, N. and Youtcheff, J. 2010. Three-dimensional image processing methods to identify and characterise aggregates in compacted asphalt mixtures. *International Journal of Pavement Engineering*, 11(6), 511–528.

Kutay, M.E., Ozturk, H.I. and Gibson, N. 2010. 3D micromechanical simulation of compaction of hot mix asphalt using real aggregate shapes obtained from X-ray CT. *ASCE Engineering Mechanics Institute's Special Publication, Pavements and Materials, Testing and Modeling in Multiple Length Scales*. Reston, VA.

Kutay, M.E., Varma, S. and Jamrah, A. 2015. A micromechanical model to create digital microstructures of asphalt mastics and crumb rubber-modified binders. *International Journal of Pavement Engineering*.

Laso, M., Karayiannis, N.C.H., Foteinopoulou, K., Mansfield, M.L. and Kröger, M. 2009. Random packing of model polymers: local structure, topological hindrance and universal scaling. *Soft Matter*, 5, 1762–1770.

Leyland, R. 2014. A case study of intelligent compaction used in road upgrades. *Engineering Geology for Society and Territory*, 7, 201–206.

Loseby, M. 2014. *A study of the influence of aggregate grading on concrete penetrability*. Thesis for Master's of Science in Civil Engineering, University of Cape Town, Cape Town SA.

Masad, E. 2004. X-ray computed tomography of aggregates and asphalt mixes. *Materials Evaluation*, 62 (9), 775–783.

Masad, E., Muhunthan, B., Shashidhar, N. and Harman, T. 1999. Quantifying laboratory compaction effects on the internal structure of asphalt concrete. *Transportation Research Record No. 1681*, 179–185.

Micaelo, R., Azevedo, M.C., Ribeiro, J. and Azevedo, N. 2009. Discrete element simulation modelling of field asphalt compaction. *Sixth International Conference on Maintenance and Rehabilitation of Pavements and Technological Control (MAIREPAV6)*. Torino, Italy.

Mollenhauer, K. and Wistuba, M. P. 2016. Influence of asphalt compaction procedure on 3D deformation properties. *International Journal of Pavement Engineering*, 17(1), 5–12.

NCHRP 1-37A. 2004. *Development of the 2002 Guide for the Design of New and Rehabilitated Pavement Structures*.

NCHRP 9-29. 1999. *Simple Performance Tester for Superpave Mix Design*.

Olard, F. 2015. GB5: Innovative design of high-performance asphalt mixes for long-life and cost-effective pavements by optimizing aggregates and using SBS modified bitumen. *Proceedings of the Conference on Asphalt Pavements in Southern African (CAPSA)*. August 2015. Sun City, South Africa.

Oliver, J.W.H., Alderson, A.J. and Luke, R.G. 2000. Comparison between the performance of Servopac and Gyropac gyratory compactors. *APRG document AR 00/06 (MA)*, ARRB Transport Research, Vermont South, Vic.

Pan, T., Tutumluer, E. and Carpenter, H. 2005. Effect of coarse aggregate morphology on the resilient modulus of hot mix asphalt. *TRB 84th Annual Conference*, Washington D.C, USA, January 2005.

Partl, M.N., Flisch, A. and Jönsson, M. 2007. Comparison of laboratory compaction methods using X-ray computer tomography. *Road Materials and Pavement Design*, 8, 39–164.

Pavement Interactive. 2020. *Hveem Mix Design*. Pavement Tools Consortium, (www.pavementinteractive.com), University of Washington, (accessed on 26 May 2020).

Pavement Interactive. 2021. Nuclear Density Gauge. Pavement Tools Consortium, (www.pavementinteractive.com), University of Washington, (accessed on 28 September 2021).

Qasim, Z.I., Abed, A.H. and Almomen, K.A. 2019. Evaluation of Mixing and Compaction Temperatures (MCT) for modified asphalt binders using zero shear viscosity and Cross-Williamson model. *Case Studies in Construction Materials*, 11, 1–12.

Roberts, F.L., Kandhal, P.S., Brown, E.R, Lee, D.Y. and Kennedy, T.W. 1996. *Hot Mix Asphalt Materials, Mixture Design, and Construction*. National Asphalt Pavement Association Education Foundation. Lanham, MD.

Roque, R., Birgisson, S., Kim, S. and Guarin, A. 2006. *Development of Mix Design Guidelines for Improved Performance of Asphalt Mixtures*. Report No. BD545 (RPWO#16). Florida Department of Transportation.

Ruth, B.E., Roque, R. and Nukunya, B. 2002. Aggregate gradation characterization factors and their relationships to fracture energy and failure strain of asphalt mixtures. *Journal of the Association of Asphalt Paving Technologists*, 71.

Sabita Manual 35. 2019. *Manual 35/TRH 8: Design and Use of Asphalt in Road Pavements*. South African Bitumen Association (Sabita), Howard Place, South Africa.

SANS 3001-AS1, 2015. *Civil Engineering Test Methods Part AS1: Making of Asphalt Briquettes for Marshall Tests and other Specialised Tests*. SABS Standards Division, Pretoria, South Africa.

SANS 3001-AS2, 2011. *Civil Engineering Test Methods Part AS2: Determination of Marshall Stability, Flow and Quotient*. SABS Standards Division, Pretoria, South Africa.

SANS 3001-AS10, 2011. *Civil Engineering Test Methods Part AS2: Determination of bulk density and void content of compacted asphalt*. SABS Standards Division, Pretoria, South Africa.

SANS 3001-AS11, 2011. *Civil Engineering Test Methods Part AS2: Determination of the Maximum Void-Less Density of Asphalt Mixes and the Quantity of Binder Absorbed by the Aggregate*. SABS Standards Division, Pretoria, South Africa.

SANS 4001-BT1, 2016. *Civil Engineering Specifications. Part BT1: Penetration Grade Bitumen*. SABS Standards Division, Pretoria, South Africa.

SATS 3208, 2019. *Technical Specification. Performance Grade (PG) Specification for Bitumen in South Africa*. SABS Standards Division, Pretoria, South Africa.

Shashidhar, K. and Gopalakrishnan, K. 2006. Evaluating the aggregate structure in hot-mix asphalt using three-dimensional computer modeling and particle packing simulations. *Canadian Journal of Civil Engineering*, 33, 945–954.

Shen, S. and Yu, H. 2011. Characterize packing of aggregate particles for paving materials: Particle size impact. *Construction and Building Materials*, 25, 1362–1368.

SHRP-A-407. 1994. *The Superpave Mix Design Manual for New Construction and Overlays*. Strategic Highway Research Program (SHRP), National Research Council, Washington, USA.

TRB. 2006. Factors affecting compaction of asphalt pavements. *Transportation Research Circular Number E-C105*. Transportation Research Board (TRB), Washington, USA.

Vallerga, B.A. and Lovering, W.R. 1985. Evolution of the hveem stabilometer method of designing asphalt paving mixtures. *Asphalt Paving Technology: Proceedings*, 54, 243–265. Association of Asphalt Paving Technologists Technical Sessions, 11-13 February 1985. San Antonio, TX.

Williams B.A., Bausano, J.P. and Williams, R.C. 2007. Criterion test for method selection in determining the bulk specific gravity of hot-mix asphalt. *Journal of ASTM International*, 4(1), 1–10.

Yildirim, Y., Solaimanian, M. and Kennedy, T.W. 2000. *Mixing and Compaction Temperature for Hot Mix Asphalt Concrete*. Report No. 1250-5. Center for Transportation Research, the University of Texas at Austin, USA.

Yu, H. and Shen, S. 2013. A micromechanical-based three-dimensional DEM approach to characterize the complex modulus of asphalt mixtures. *Construction and Building Materials*, 38, 1089–1098.

Yue, Z.Q., Bekking, W. and Morin, I. 1995. Application of digital image processing to quantitative study of asphalt concrete microstructure. *Transportation Research Record*, 1492, 53–60.

Vavrik, R.W., Fries, R.J., Carpenter, S.H. and Aho, B.D. 1999. Effect of flat and elongated coarse aggregates on characteristics of gyratory compacted samples. *Transportation Research Record*, 1681, 28–36.

Vavrik, W.R., Huber, G., Pine, W.J., Carpenter, S.H. and Bailey, R., 2002. Bailey method for gradation selection in hot-mix asphalt mixture design. *Transportation Research E-Circular*, E-C044, October 2002, Washington D.C., USA.

Verhaeghe, B., Myburgh, P.A. and Denneman, E. 2007. *Asphalt Rutting and its Prevention*. Presented at the 9th Conference on Asphalt Pavements for Southern Africa. September 2007, Gaborone.

Walubita, L.F., Jamison, B., Alvarez, A.E., Hu, X. and Mushota, C. 2012. Air void characterization of hot mix asphalt gyratory laboratory-molded samples and field cores using X-ray computed tomography (X-ray CT). *Journal of South African Institution of Civil Engineering*, 54 (2), 22–31.

Walubita, L.F., Faruk, A.N.M., Zhang, J., Hu, X. and Lee, S.I. 2016. The Hamburg rutting test – effects of HMA sample sitting time and test temperature variation. *Journal of Construction and Building Materials*, 108, 22–28.

White, T.D. 1985. Marshall procedures for design and quality control of asphalt mixtures. Asphalt paving technology. *Proceedings of the Association of Asphalt Paving Technologists Technical Sessions*, 54, 265–284. 11-13 February 1985. San Antonio, TX.

Xu, Q. and Chang, G.K. 2013. Evaluation of Intelligent Compaction for Asphalt Materials. *Automation in Construction*, 30, 104–112.

9 APPENDIX A: GYRATORY COMPACTION RESULTS

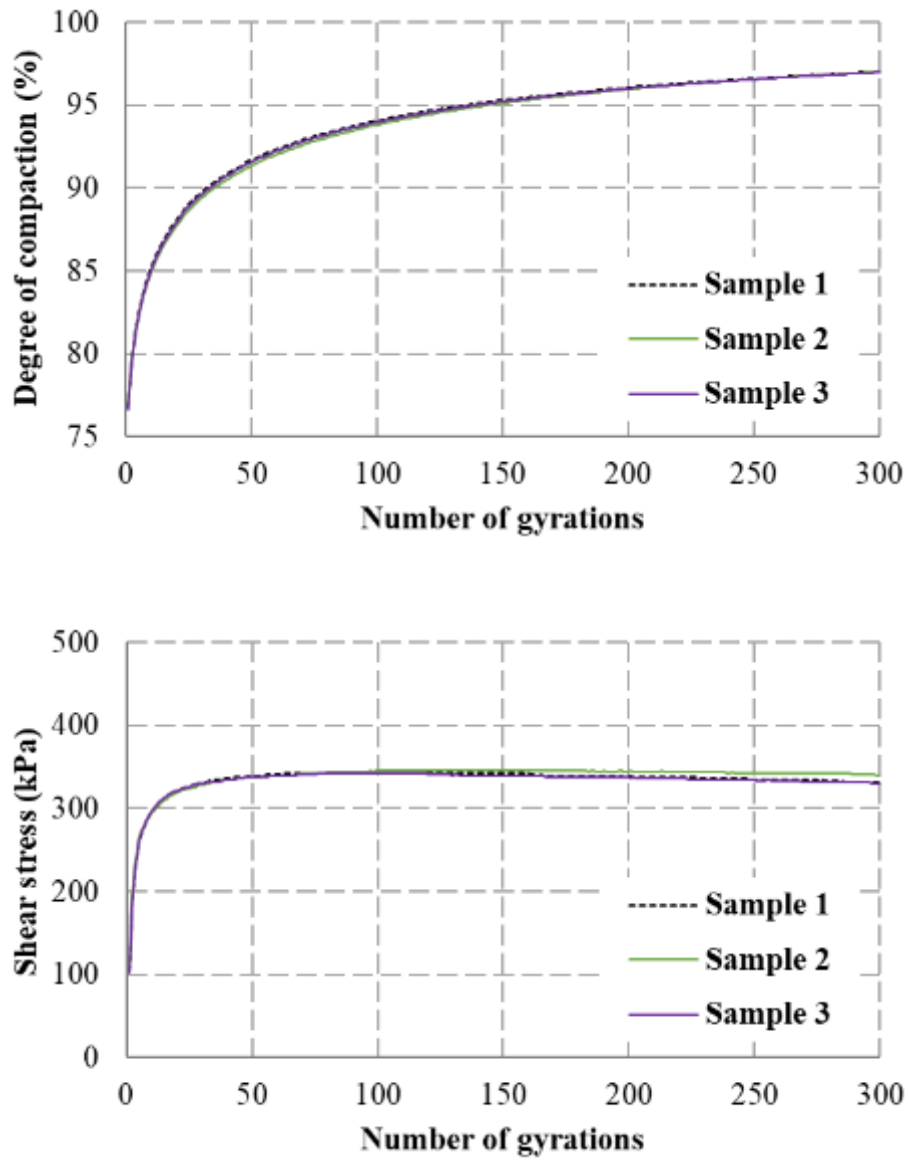


Figure 9.1: Gyration compaction results – 10 mm NMPS coarse gradation structure

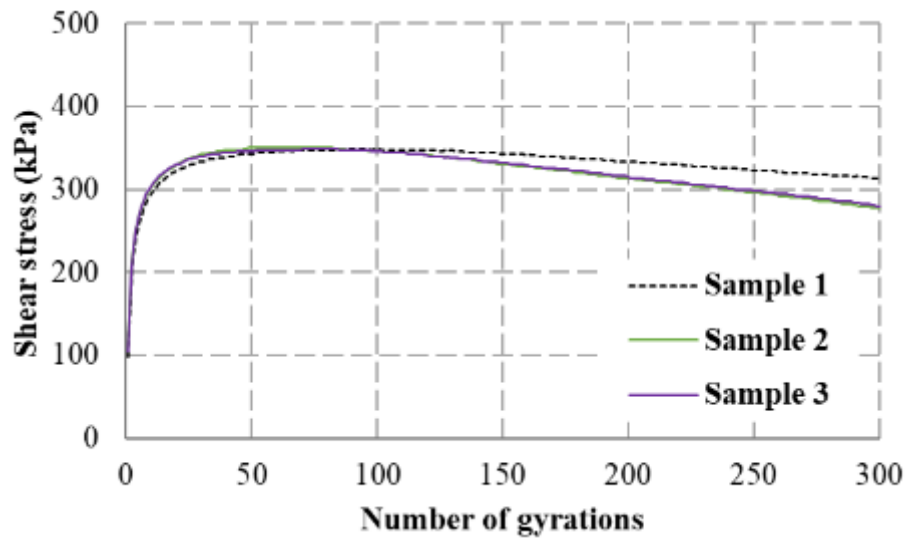
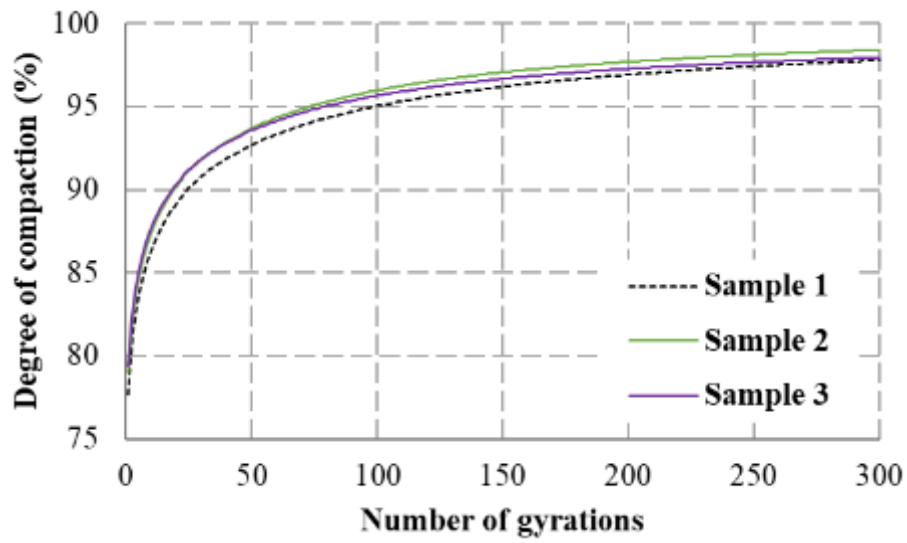


Figure 9.2: Gyrotory compaction results – 10 mm NMPS medium gradation structure

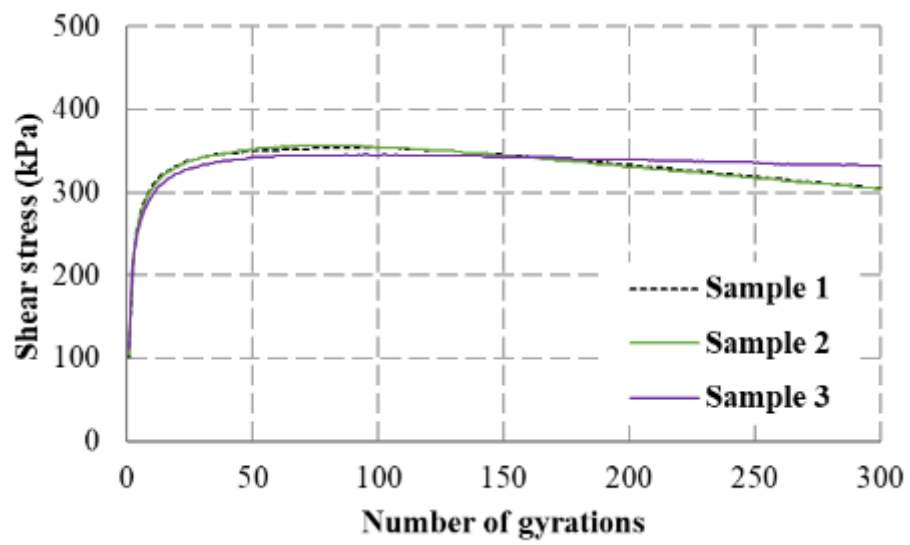
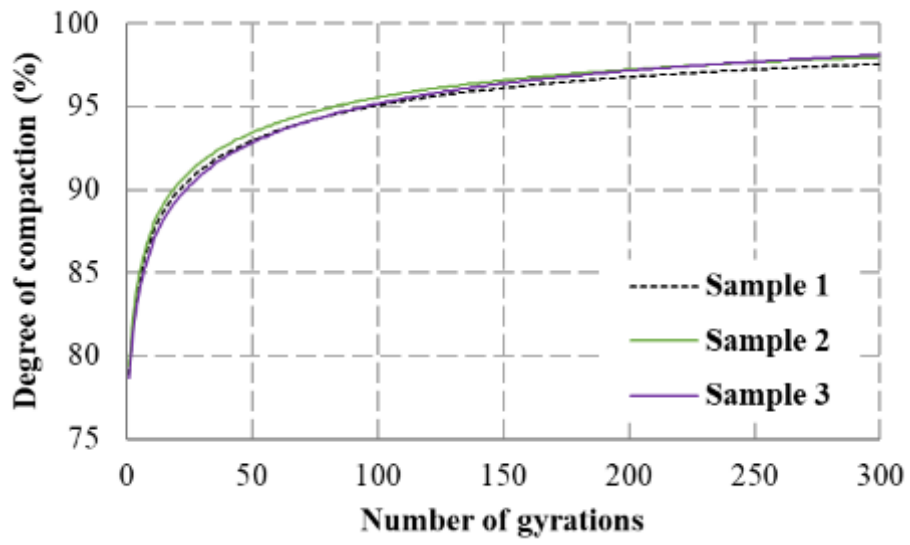


Figure 9.3: Gyrotory compaction results – 10 mm NMPS Fine gradation structure

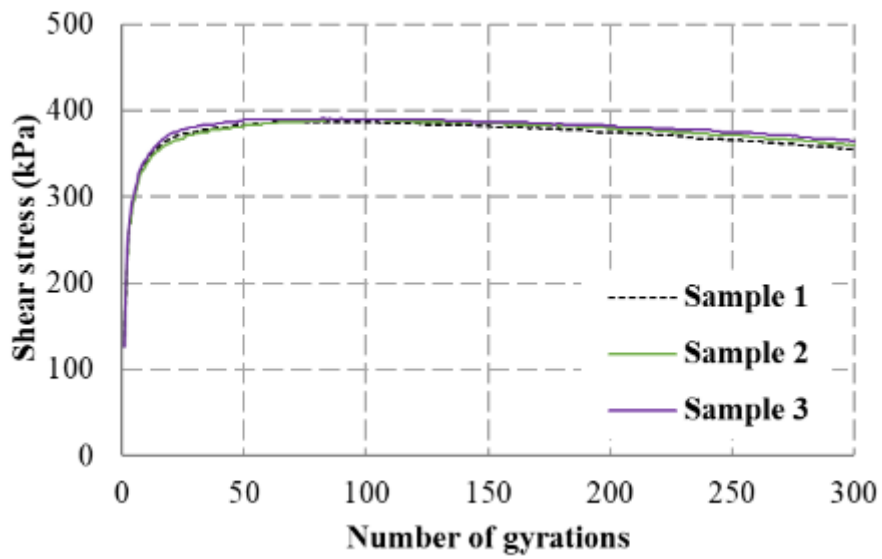
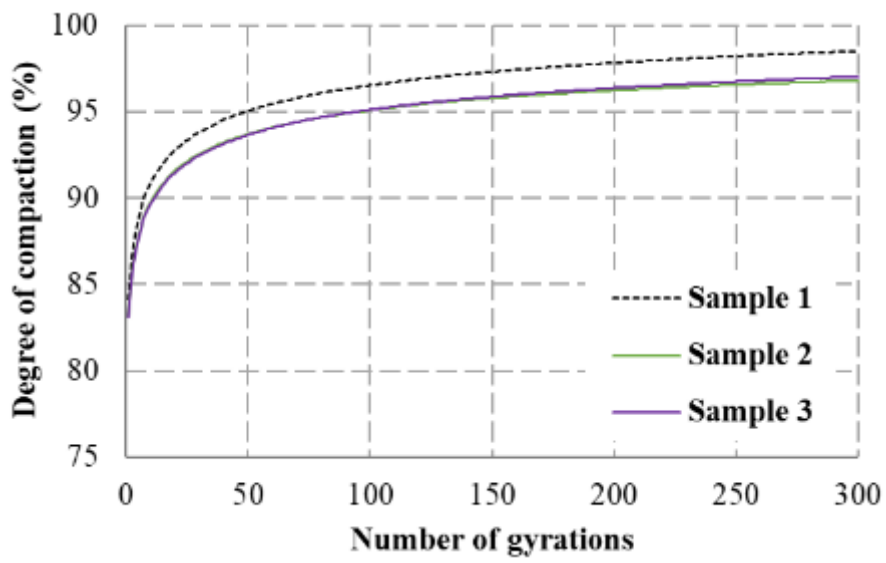


Figure 9.4: Gyrotory compaction results – 20 mm NMPS coarse gradation structure

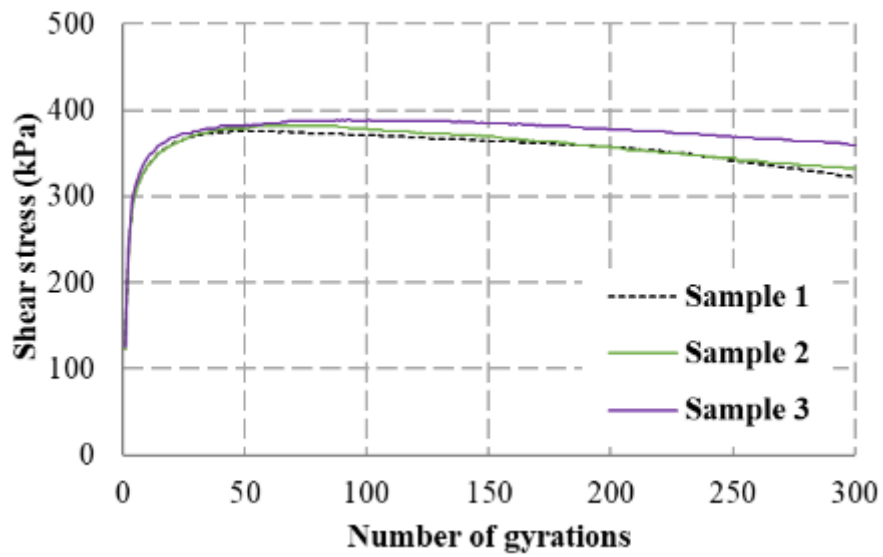
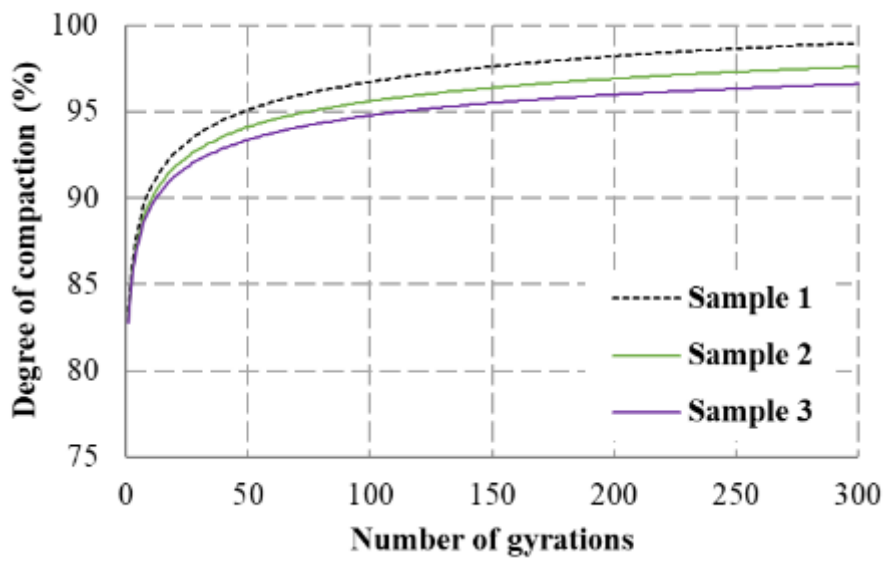


Figure 9.5: Gyrotory compaction results – 20 mm NMPS medium gradation structure

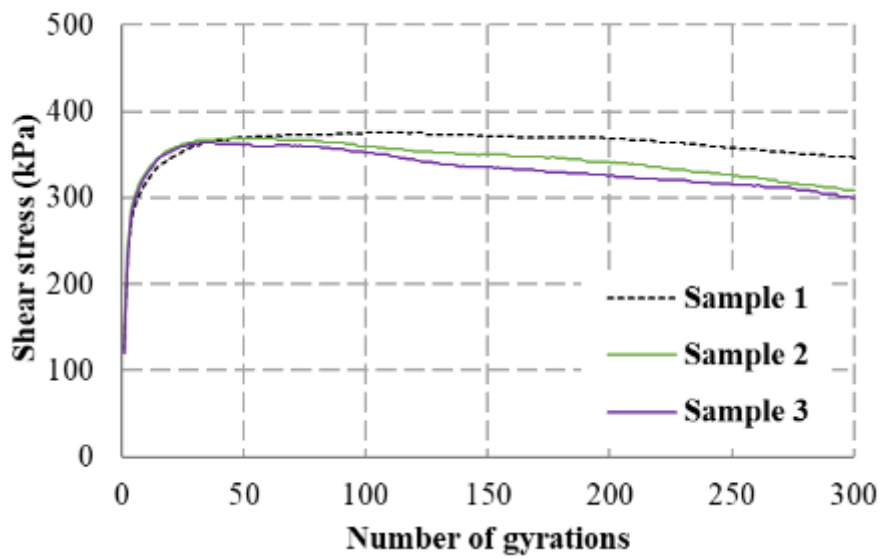
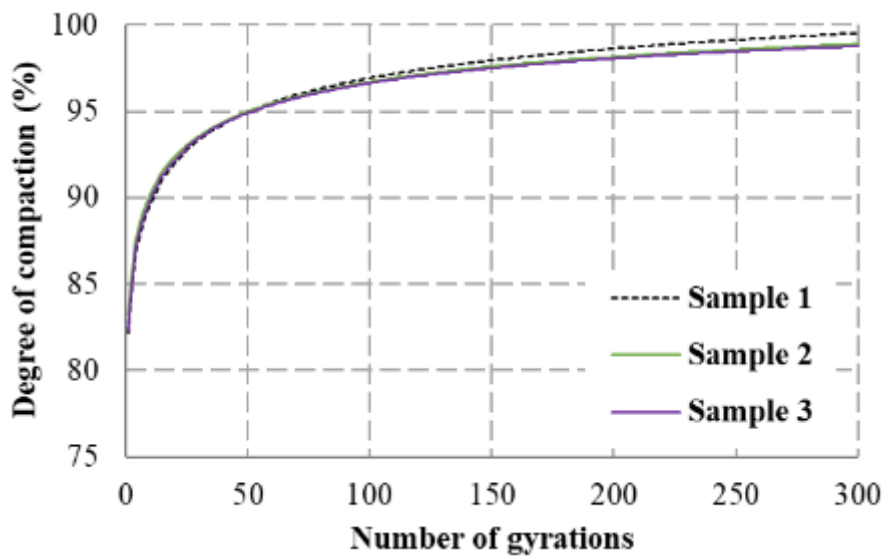


Figure 9.6: Gyrotory compaction results – 20 mm NMPS Fine gradation structure

10 APPENDIX B: SUMMARY OF BULK DENSITY RESULTS

The Maximum Void-less Density (MVD) of the mix was 2622 kg/m³. The tables below present the Bulk Density (BD) results.

10.1 Bulk density of laboratory-compacted samples – investigation into vertical air voids distribution

Table 10.1: Bulk density of 170 mm high samples – vertical distribution

| Repeat | 4.0% target air voids (kg/m ³) | 7.0% target air voids (kg/m ³) |
|--------|--------------------------------------------|--------------------------------------------|
| 1 | 2508 | 2442 |
| 2 | 2508 | 2436 |
| 3 | 2507 | 2444 |

Table 10.2: Bulk density of the top, middle and bottom – 4.0% target air voids, 170 mm high

| Repeat | BD (kg/m ³) | | |
|--------|-------------------------|--------|--------|
| | Top | Middle | Bottom |
| 1 | 2509 | 2512 | 2504 |
| 2 | 2494 | 2527 | 2502 |
| 3 | 2485 | 2521 | 2510 |

Table 10.3: Bulk density of the top, middle and bottom – 7.0% target air voids, 170 mm high

| Repeat | BD (kg/m ³) | | |
|--------|-------------------------|--------|--------|
| | Top | Middle | Bottom |
| 1 | 2443 | 2454 | 2451 |
| 2 | 2438 | 2452 | 2436 |
| 3 | 2454 | 2464 | 2431 |

Table 10.4: Bulk density results of the six parts – 4.0% target air voids

| Repeat | BD (kg/m ³) | | | | | |
|--------|-------------------------|------|------|------|------|------|
| | 1 | 2 | 3 | 4 | 5 | 6 |
| 1 | 2472 | 2536 | 2516 | 2511 | 2540 | 2456 |
| 2 | 2455 | 2529 | 2522 | 2530 | 2550 | 2442 |
| 3 | 2440 | 2526 | 2518 | 2521 | 2544 | 2469 |

Table 10.5: Bulk density results of the six parts – 7.0% target air voids

| Repeat | BD (kg/m ³) | | | | | |
|--------|-------------------------|------|------|------|------|------|
| | 1 | 2 | 3 | 4 | 5 | 6 |
| 1 | 2373 | 2488 | 2459 | 2453 | 2476 | 2421 |
| 2 | 2399 | 2474 | 2444 | 2459 | 2486 | 2373 |
| 3 | 2402 | 2491 | 2471 | 2451 | 2455 | 2393 |

Table 10.6: Bulk density of 120 mm high samples – vertical distribution

| Repeat | 4.0% target air voids (kg/m ³) | 7.0% target air voids (kg/m ³) |
|--------|--------------------------------------------|--------------------------------------------|
| 1 | 2527 | 2452 |
| 2 | 2498 | 2433 |
| 3 | 2496 | 2440 |

Table 10.7: Bulk density of the top, middle and bottom – 4.0% target air voids, 120 mm high

| Repeat | BD (kg/m ³) | | |
|--------|-------------------------|--------|--------|
| | Top | Middle | Bottom |
| 1 | 2493 | 2563 | 2511 |
| 2 | 2454 | 2542 | 2478 |
| 3 | 2467 | 2545 | 2462 |

Table 10.8: Bulk density of the top, middle and bottom - 7.0% target air voids, 120 mm high

| Repeat | BD (kg/m ³) | | |
|--------|-------------------------|--------|--------|
| | Top | Middle | Bottom |
| 1 | 2435 | 2490 | 2418 |
| 2 | 2396 | 2473 | 2419 |
| 3 | 2407 | 2479 | 2433 |

10.2 Bulk density of laboratory-compacted samples – investigation into radial air voids distribution

Table 10.9: Bulk density of 170 mm high – radial distribution (4.0% target air voids)

| Repeat | BD (kg/m ³) | | |
|--------|-------------------------|-------|-------|
| | 100 mm | 78 mm | 54 mm |
| 1 | 2510 | 2518 | 2525 |
| 2 | 2509 | 2513 | 2516 |
| 3 | 2501 | 2505 | 2507 |

Table 10.10: Bulk density of 170 mm high – radial distribution (7.0% target air voids)

| Repeat | BD (kg/m ³) | | |
|--------|-------------------------|-------|-------|
| | 100 mm | 78 mm | 54 mm |
| 1 | 2446 | 2453 | 2450 |
| 2 | 2439 | 2446 | 2453 |
| 3 | 2443 | 2448 | 2449 |

Table 10.11: Bulk density of 120 mm high – radial distribution (4.0% target air voids)

| Repeat | BD (kg/m ³) | | |
|--------|-------------------------|-------|-------|
| | 100 mm | 78 mm | 54 mm |
| 1 | 2527 | 2530 | 2523 |
| 2 | 2513 | 2513 | 2503 |
| 3 | 2517 | 2517 | 2511 |

Table 10.12: Bulk density of 120 mm high – radial distribution (7.0% target air voids)

| Repeat | BD (kg/m ³) | | |
|--------|-------------------------|-------|-------|
| | 100 mm | 78 mm | 54 mm |
| 1 | 2449 | 2456 | 2454 |
| 2 | 2411 | 2414 | 2414 |
| 3 | 2467 | 2471 | 2475 |

11 APPENDIX C: REPEATED SIMPLE SHEAR TEST AT CONSTANT HEIGHT RESULTS

11.1 RSST-CH results of slab roller-compacted samples

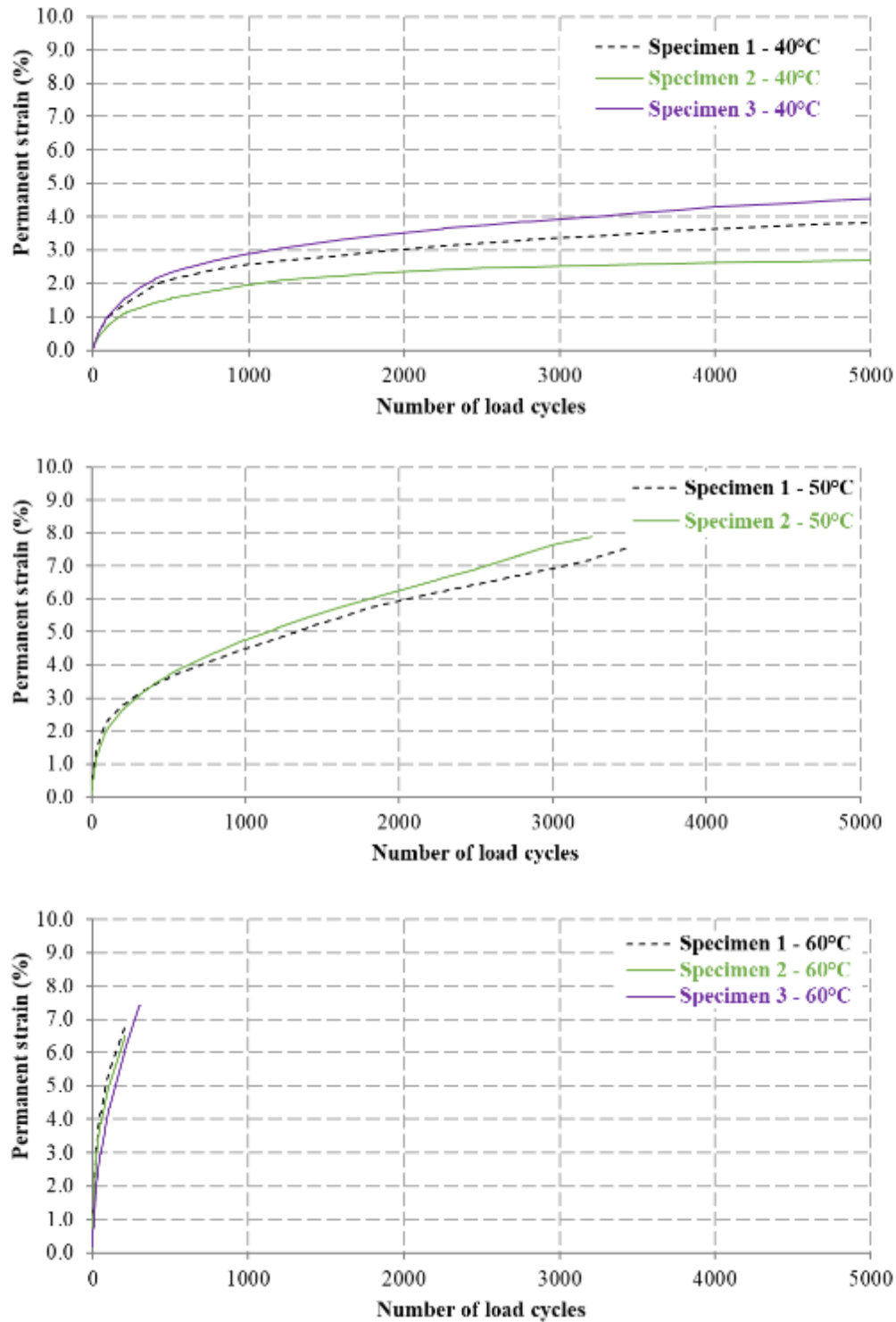


Figure 11.1: RSST-CH results of roller-compacted samples – 10 mm NMPS mix (7% air voids)

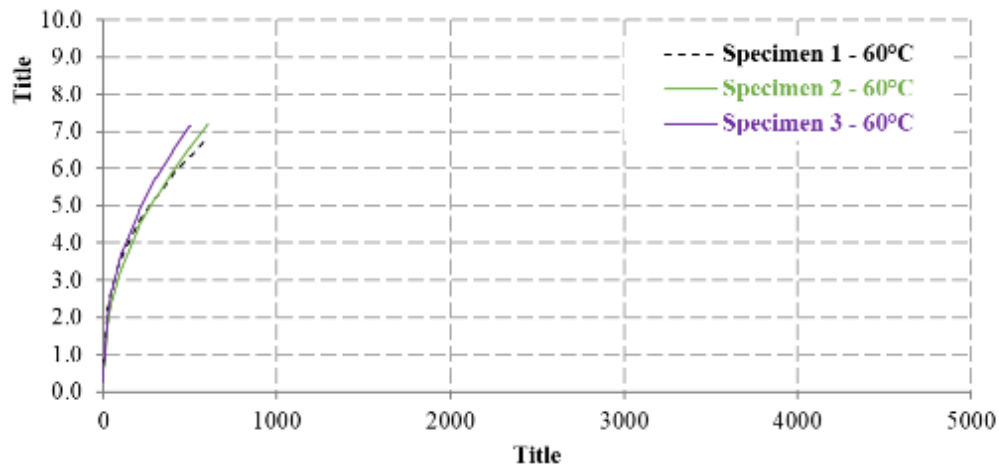
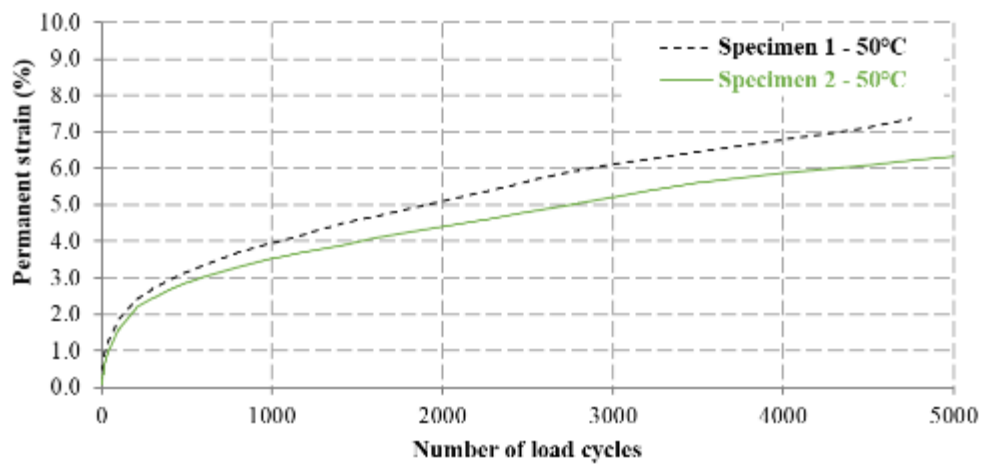
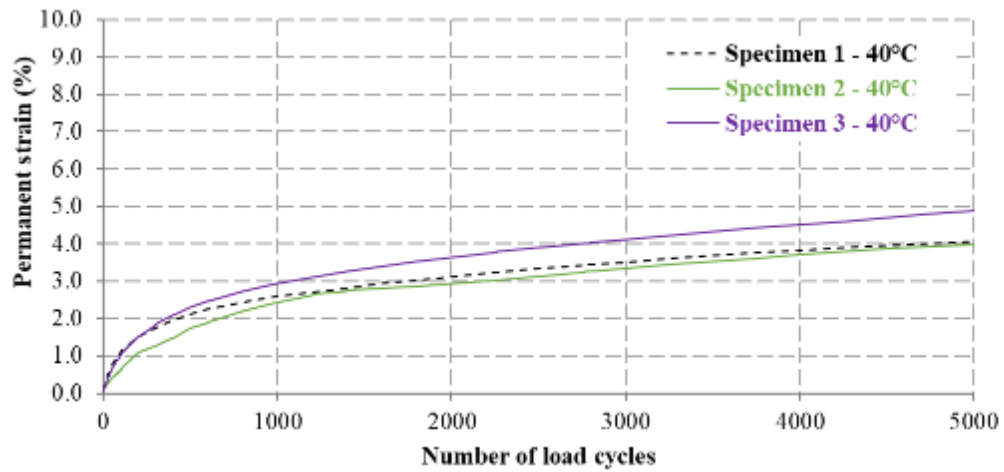


Figure 11.2: RSST-CH results of roller-compacted samples – 20 mm NMPS mix (7% air voids)

11.2 RSST-CH results of gyratory-compacted samples

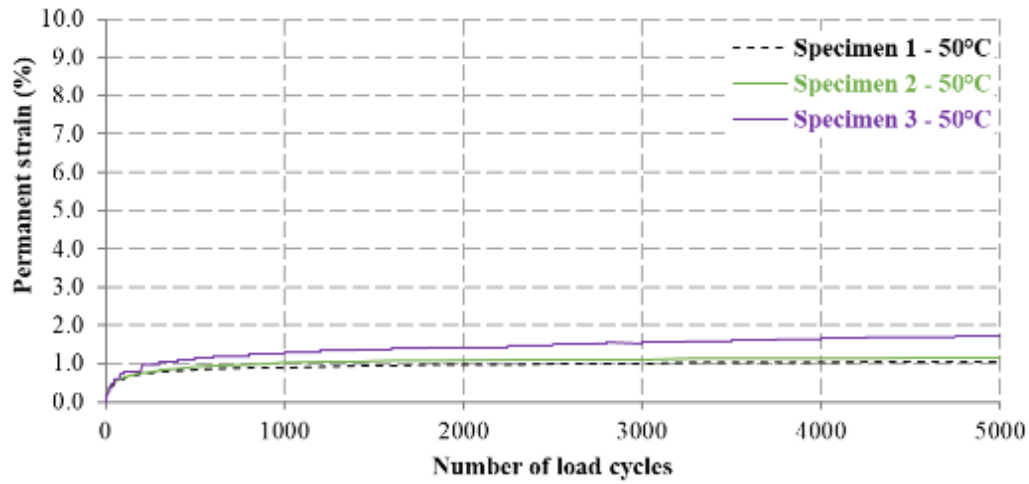


Figure 11.3: RSST-CH results of gyratory-compacted samples – 10 mm NMPS mix (4% air voids)

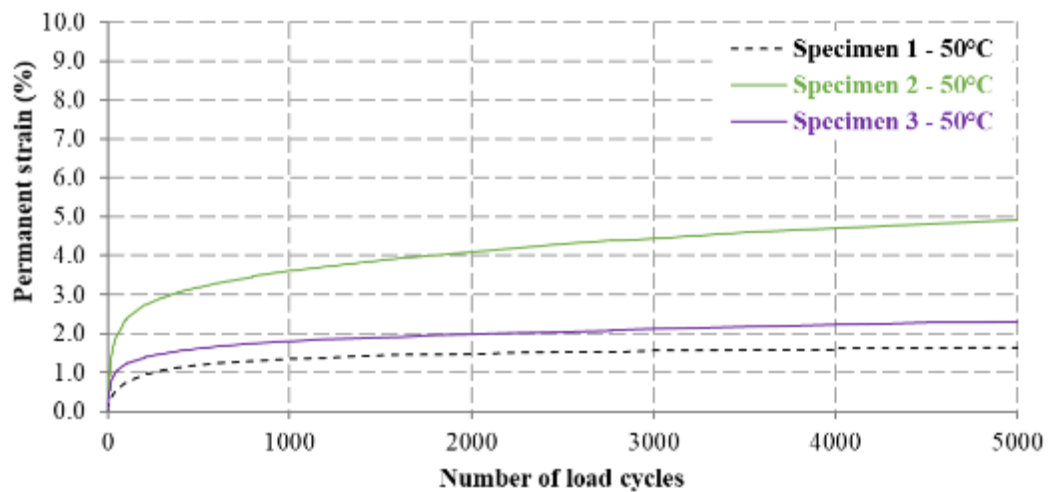


Figure 11.4: RSST-CH results of gyratory-compacted samples – 10 mm NMPS mix (7% air voids)

**Specimen 2 appears to be an outlier.*

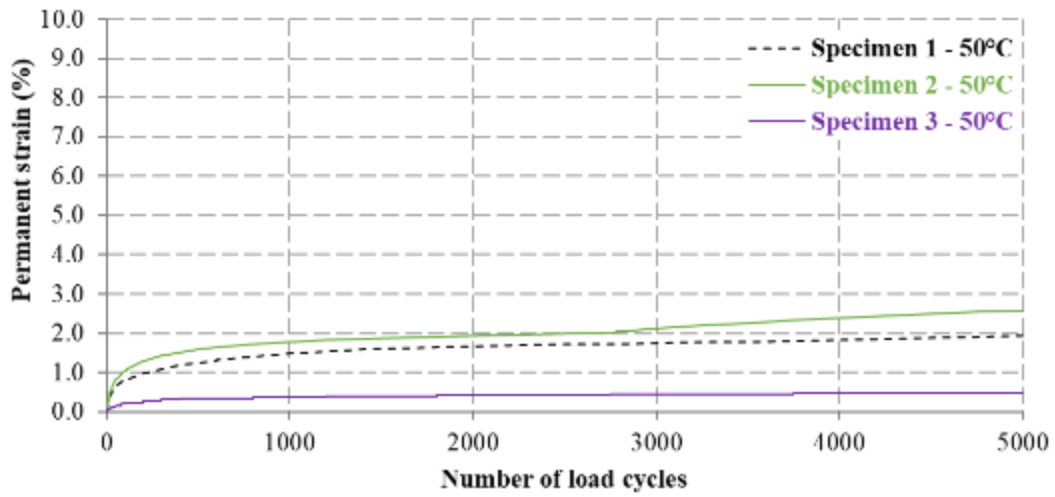


Figure 11.5: RSST-CH results of gyratory-compacted samples – 20 mm NMPS mix (4% air voids)

**Specimen 3 appears to be an outlier.*

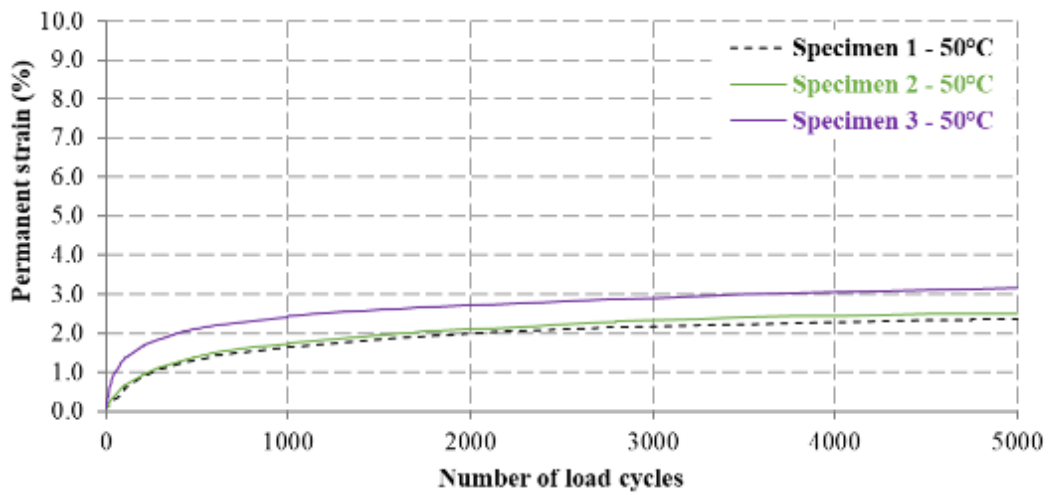


Figure 11.6: RSST-CH results of gyratory-compacted samples – 20 mm NMPS mix (7% air voids)

12 APPENDIX D: UNIAXIAL SHEAR TESTER RESULTS

12.1 URST results of slab roller-compacted samples

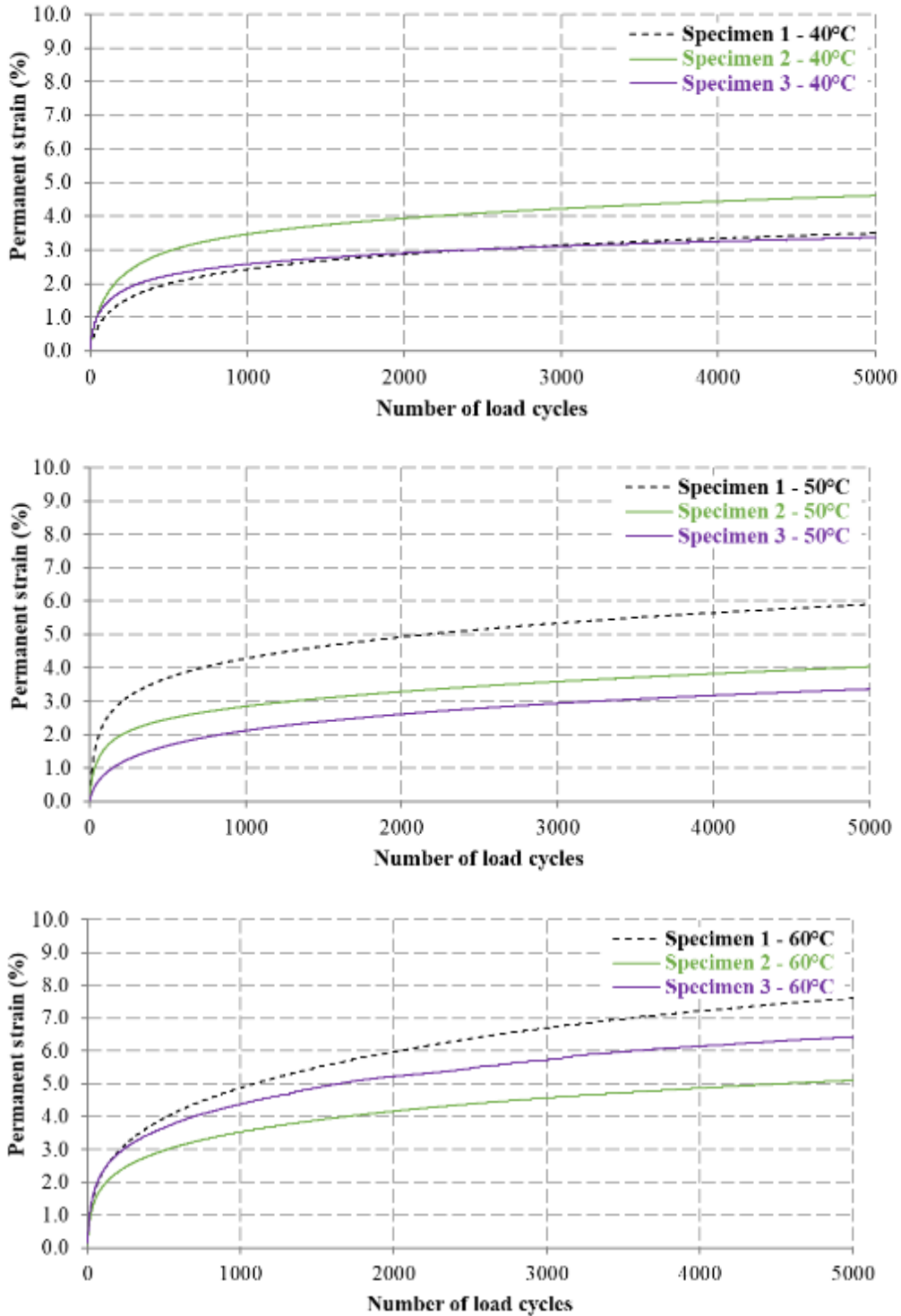


Figure 12.1: URST results of slab roller-compacted samples – 10 mm NMPS mix (7% air voids)

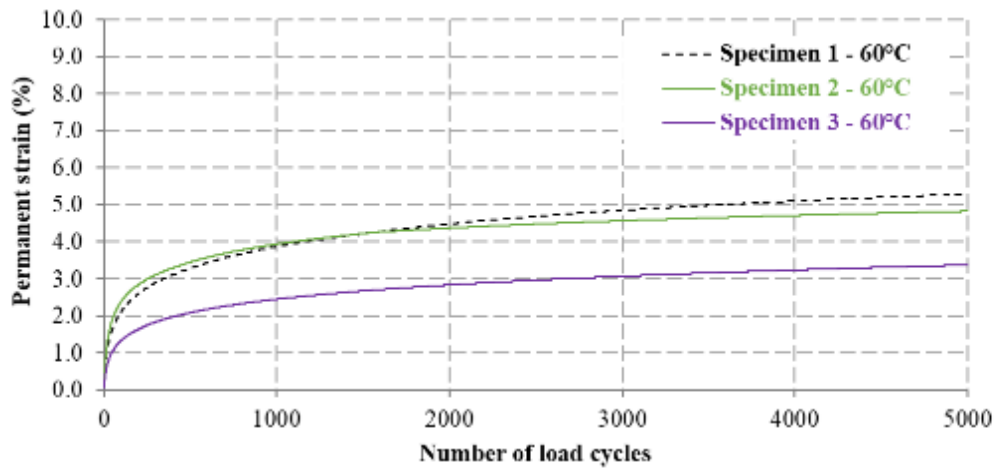
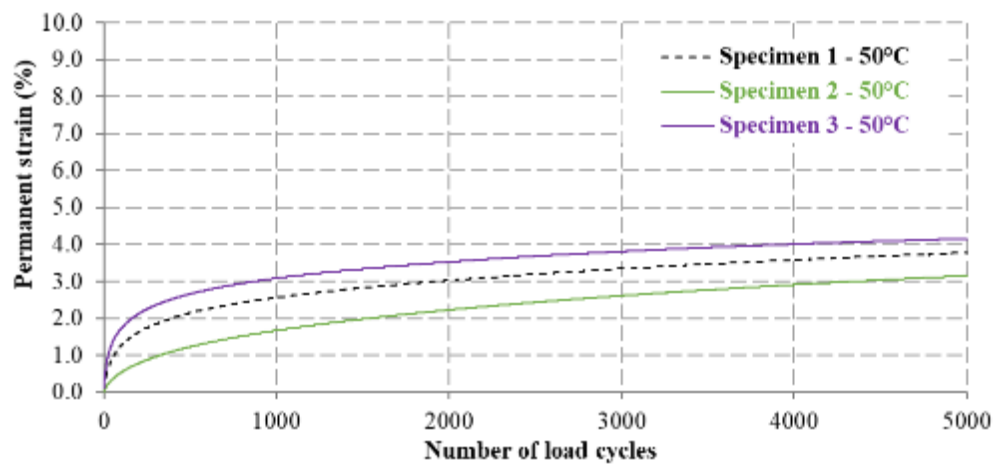
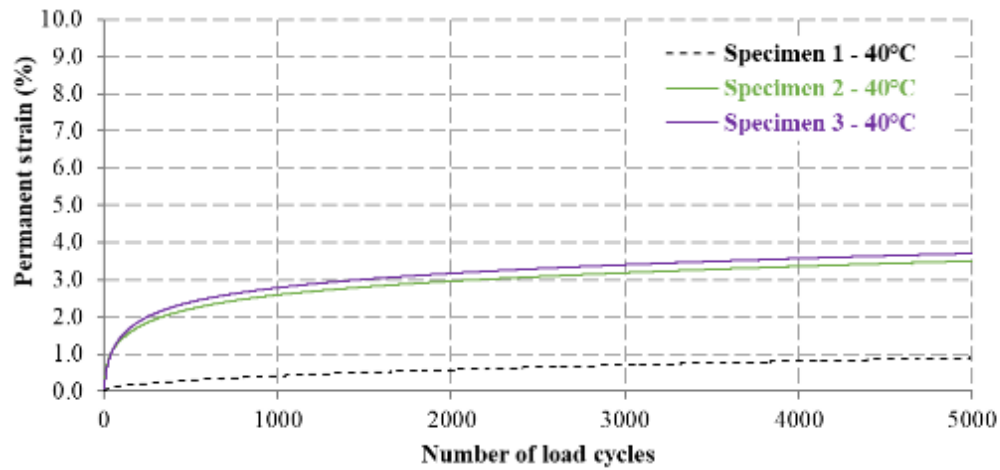


Figure 12.2: URST results of slab roller-compacted samples – 20 mm NMPS mix (7% air voids)

**Specimen 1 at 40 °C and specimen 3 at 60 °C appear to be outliers.*

12.2 URST results of gyratory-compacted samples

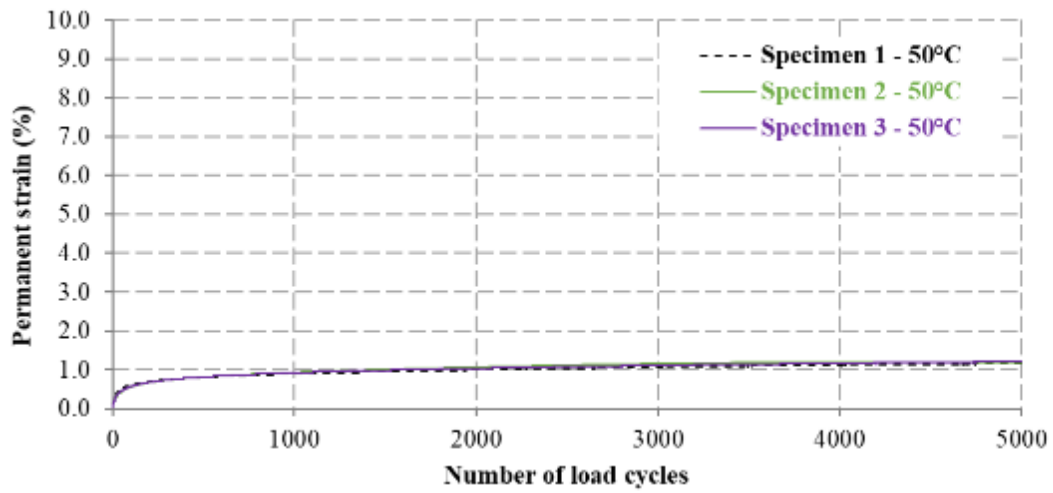


Figure 12.3: URST results of gyratory-compacted samples – 10 mm NMPS mix (4% air voids)

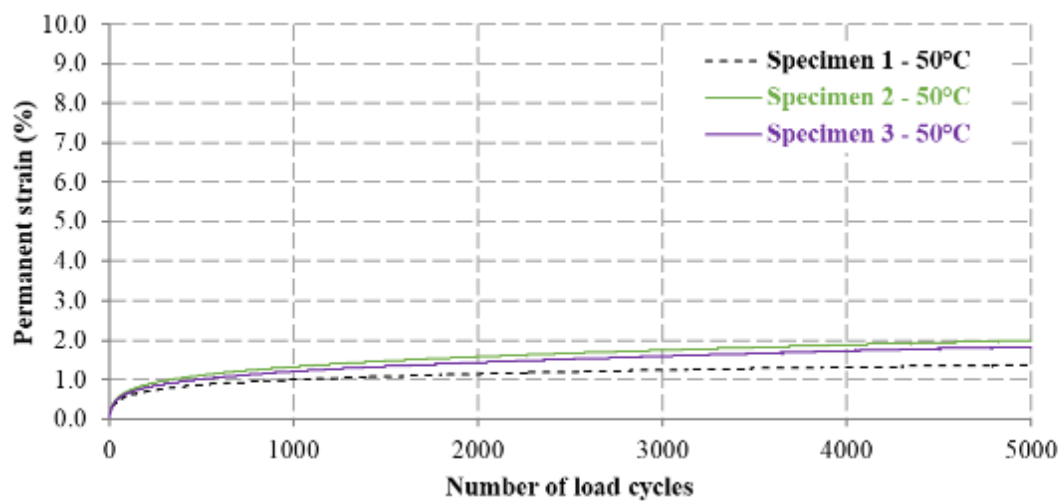


Figure 12.4: URST results of gyratory-compacted samples – 10 mm NMPS mix (7% air voids)

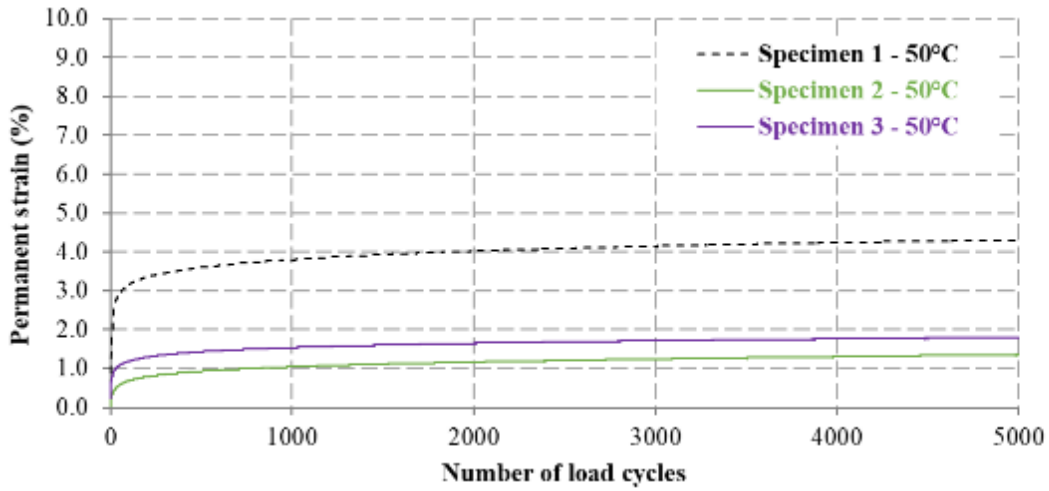


Figure 12.5: URST results of gyratory-compacted samples – 20 mm NMPS mix (4% air voids)
**Specimen 1 appears to be an outlier*

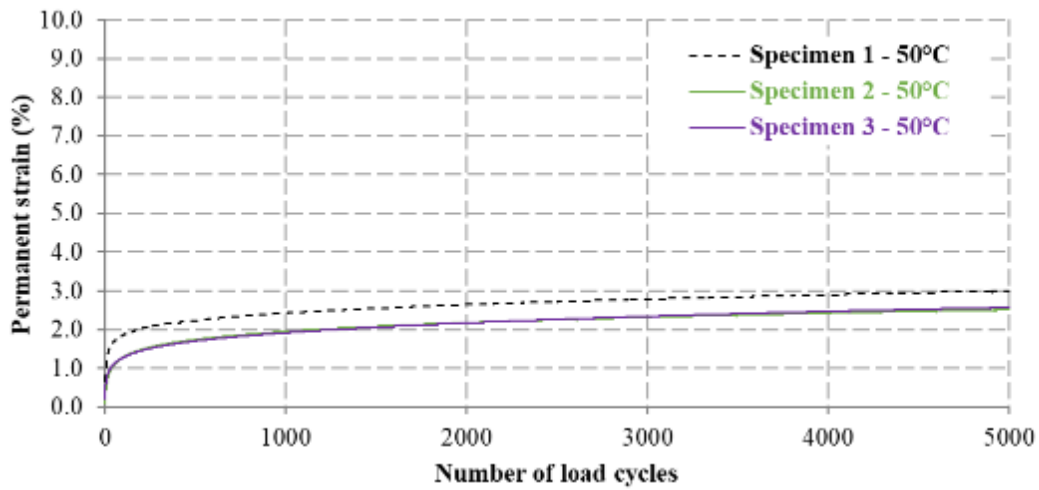


Figure 12.6: URST results of gyratory-compacted samples – 20 mm NMPS mix (7% air voids)